

2010

A Monolithic Spiral Coil Acoustic Transduction Sensor for Chemical and Biological Analytes

Donald F. McCann

Follow this and additional works at: <http://digitalcommons.library.umaine.edu/etd>



Part of the [Electrical and Computer Engineering Commons](#)

Recommended Citation

McCann, Donald F., "A Monolithic Spiral Coil Acoustic Transduction Sensor for Chemical and Biological Analytes" (2010). *Electronic Theses and Dissertations*. 361.

<http://digitalcommons.library.umaine.edu/etd/361>

This Open-Access Dissertation is brought to you for free and open access by DigitalCommons@UMaine. It has been accepted for inclusion in Electronic Theses and Dissertations by an authorized administrator of DigitalCommons@UMaine.

**A MONOLITHIC SPIRAL COIL ACOUSTIC TRANSDUCTION SENSOR
FOR CHEMICAL AND BIOLOGICAL ANALYTES**

By Donald F. McCann

B.S. Cornell University, 2000

B.S. Ithaca College, 2000

M.S. University of Maine, 2008

A THESIS

Submitted in Partial Fulfillment of the

Requirement for the Degree of

Doctor of Philosophy

(in Electrical & Computer Engineering)

The Graduate School

The University of Maine

May, 2010

Advisory Committee:

John Vetelino, Professor of Electrical Engineering, Advisor

David Frankel, Senior Research Scientist

Mauricio Pereira da Cunha, Associate Professor of Electrical Engineering

Ralf Lucklum, Faculty of Electrical Engineering

Rosemary Smith, Professor of Electrical Engineering

DISSERTATION
ACCEPTANCE STATEMENT

On behalf of the Graduate Committee for Donald McCann, I affirm that this manuscript is the final and accepted thesis. Signatures of all committee members are on file with the Graduate School at the University of Maine, 42 Stodder Hall, Orono, Maine.

John Vetelino, Professor of Electrical and Computer Engineering

(Date)

© 2010 Donald F. McCann

All Rights Reserved

LIBRARY RIGHTS STATEMENT

In presenting this thesis in partial fulfillment of the requirements for an advanced degree at The University of Maine, I agree that the Library shall make it freely available for inspection. I further agree that permission for "fair use" copying of this thesis for scholarly purposes may be granted by the Librarian. It is understood that any copying or publication of this thesis for financial gain shall not be allowed without my written permission.

Signature:

Date:

**A MONOLITHIC SPIRAL COIL ACOUSTIC TRANSDUCTION SENSOR
FOR CHEMICAL AND BIOLOGICAL ANALYTES**

By Donald McCann

Thesis Advisor: Dr. John Vetelino

An Abstract of the Thesis Presented
in Partial Fulfillment of the Requirements for the
Degree of Doctor of Philosophy
(in Electrical & Computer Engineering)
May, 2010

Acoustic wave sensor platforms typically consist of piezoelectric materials in which bulk or surface acoustic waves are excited by metallic transducers deposited on the sensing surface of the platform. This type of transduction has limitations. In particular the transducer may limit the type of sensing film that can be used or analyte that can be measured and limit the frequency of operation of the sensor. In this work a novel method of exciting high frequency bulk acoustic waves in piezoelectric sensor platforms has been explored. This technique consists of applying time varying electromagnetic fields to the sensor platform using an antenna in order to excite high order harmonic acoustic waves. This configuration is known as a Monolithic Spiral Coil Acoustic Transduction (MSCAT) device. This technique offers benefits such as a bare sensing surface that allows for the detection of both mechanical and electrical property changes in the film or analyte and is capable of operating at high frequencies by exciting high order harmonics ($> 99^{\text{th}}$ harmonic) in the substrate. The antenna configurations have been experimentally and theoretically examined and an

understanding of how these electric fields excite the acoustic waves in the substrate has been developed. Finally, the MSCAT sensor platform was used to detect real world chemical and biological analytes and found in many cases to be superior to other bulk acoustic wave sensor platforms.

ACKNOWLEDGMENTS

First, I would like to thank my Ph.D. advisor, Dr. John Vetelino, for his great mentorship and patience and for giving me the opportunity to pursue this research. I would also like to thank my advisory committee: Dr. David Frankel, Dr. Mauricio Pereira da Cunha, Dr. Ralf Lucklum, and Dr. Rosemary Smith for their help and guidance. Next I would like to thank my fellow graduate students Mitchell Wark and Lester French for their tremendous help through numerous discussions and hard work over the past few years. In addition, I would like to thank the LASST faculty and staff, in particular George Bernhardt, Paul Millard, and Eric Martin, for their help over the course of this project as well as Joe Arsenault for his help in the derivation of the near fields radiated from a spiral coil antenna. I would also like to thank all of my fellow graduate students and REU students who I have worked with during my time at the University of Maine. I wish to extend a special thanks to Titan Fan at Beacon Analytical for his generous donation of saxitoxin antibodies to help further my research.

I wish to acknowledge the support of my family: my mother, Beth, my children, Hannah and Andrew, and my extended family, Pamela and Norman. I also wish to thank Bill Rushmore for his many insightful comments and suggestions over the years.

Most of all I want to thank my wife, Alisha, for her tremendous encouragement and support and for helping me to maintain perspective through this incredible journey.

TABLE OF CONTENTS

ACKNOWLEDGMENTS	iv
LIST OF TABLES	x
LIST OF FIGURES	xi
1. INTRODUCTION	1
1.1. The Sensor System	1
1.2. Purpose and Objectives	4
1.3. Organization	8
2. BACKGROUND	10
2.1. Sensor Platforms with Photolithographically Deposited Electrodes	10
2.1.1. Quartz Crystal Microbalance (QCM)	10
2.1.2. Thickness Shear Mode (TSM) Resonators with Modified Electrodes on the Sensing Surface	16
2.1.3. Lateral Field Excited (LFE) Sensor Platforms.....	117
2.2. Remotely Excited Bulk Acoustic Wave (BAW) Platforms	22
2.2.1. Electromagnetic Acoustic Transduction (EMAT)	22
2.2.2. Magnetic Acoustic Resonance Sensors (MARS)	25
2.2.3. Electromagnetic Piezoelectric Acoustic Sensors (EMPAS)	28

3. DEVELOPMENT OF THE MONOLITHIC SPIRAL COIL ACOUSTIC TRANSDUCTION (MSCAT) SENSOR.....	35
3.1. The MSCAT platform	35
3.2. MSCAT Sensor Fabrication	37
3.3. Selection of AT-cut Quartz Wafers.....	40
3.4. Resonant Frequency Measurement Setup	49
3.4.1. Lock-in Amplifier Measurement System.....	49
3.4.2. Network Analyzer Based Measurement System.....	52
3.5. Experimental Examination of the MSCAT Spiral Coil Design	57
3.5.1. Alternative Spiral Configurations.....	70
3.6. Finite Element Model of the Electromagnetic Fields Radiated from an MSCAT Spiral Coil	71
3.6.1. MSCAT Behavior Under Liquid Loads.....	72
3.6.2. Near Field Behavior of Spiral Coil Antennas	88
4. MEASUREMENT OF LIQUID MECHANICAL AND ELECTRICAL PROPERTY CHANGES	93
4.1. Introduction	93
4.2. Experimental Description for Liquid Property Measurements	94
4.3. Measurement of Liquid Viscosity Changes	95
4.4. Measurement of Liquid Conductivity Changes	98

4.5. Measurement of Liquid Relative Permittivity Changes	101
4.6. The Measurement of Mechanical and Electrical Property Changes at High Frequencies	104
5. THE MSCAT BIOLOGICAL SENSOR PLATFORM.....	115
5.1. Introduction.....	115
5.2. <i>E. coli</i> Background.....	115
5.3. <i>E. coli</i> O157:H7 Selective Sensing Film.....	117
5.3.1. Verification of the Selectivity of the <i>E. coli</i> O157:H7 Antibodies.....	120
5.3.2. Verification of the Antibody Attachment to the MSCAT Sensor Platform.....	123
5.3.3. Verification of the Effective Binding of <i>E. coli</i> O157:H7 to the MSCAT	127
5.4. MSCAT Response Signature	129
5.5. Determination of Lowest <i>E. coli</i> O157:H7 detection limit	134
5.6. Detection of <i>E. coli</i> O157:H7 in Real World Sensing Environments	140
5.7. <i>Salmonella</i> Background	147
5.8. <i>Salmonella</i> Selective Sensing Film.....	150
5.8.1. Verification of the <i>Salmonella</i> Antibody Attachment to the MSCAT Sensor Platform.....	151

5.9. MSCAT <i>Salmonella</i> Results	153
5.10. Summary	156
6. THE MSCAT CHEMICAL SENSOR PLATFORM	157
6.1. Introduction	157
6.2. Saxitoxin (STX) Background.....	157
6.3. STX Selective Sensing Films	159
6.3.1. Crown Ether (CE) Based Selective Sensing Film.....	159
6.3.2. Antibody Based STX Selective Sensing Film	159
6.3.2.1. Attachment of STX Selective Antibodies to the Sensor Surface	161
6.3.2.2. Verification of STX Antibody Film.....	162
6.4. MSCAT STX Results.....	167
6.4.1. CE Based Selective Sensing Results.....	167
6.4.2. Antibody Based Selective Sensing Results.....	170
6.5. Summary	172
7. SUMMARY, CONCLUSIONS, AND FUTURE WORK	174
7.1. Summary	174
7.2. Conclusions	176
7.3. Future Work	181
REFERENCES	184

APPENDICES

Appendix A. Lateral Field Excited LiTaO₃ High Frequency Bulk Acoustic
Wave Sensors.....198

Appendix B. An Expression for the Electromagnetic Fields Radiated from
a Planar Spiral Coil Antenna224

BIOGRAPHY OF THE AUTHOR.....238

LIST OF TABLES

Table 2.1	Compressed matrix notation	10
Table 3.1	Initial spiral coil parameters to explore the effects of N, W, and S	60
Table 3.2	Additional MSCAT spiral coil parameters.	63
Table 5. 1	MSCAT operating frequency and frequency shift for various concentrations of <i>E. coli</i> O157:H7.....	137
Table A.1	Piezoelectric coupling coefficients for various temperature compensated TSMs in α -quartz	204

LIST OF FIGURES

Figure 1.1. Block diagram of a complete sensor system for the detection of biological or chemical targets	2
Figure 1.2. Diagram of MSCAT sensing element	6
Figure 2.1 AT-cut plate using IEEE (YXwl) notation.	13
Figure 2.2. Top view of a standard QCM sensor	14
Figure 2.3 Geometries of TSM.....	17
Figure 2.4 Top view of a LFE sensor.....	18
Figure 2.5 Configuration for bulk wave EMAT	24
Figure 2.6 Diagram of MARS.....	26
Figure 2.7 Geometry of EMPAS device	29
Figure 2.8 Diagram showing toroid based EMPAS	30
Figure 2.9 Block diagram of EMPAS system	32
Figure 3.1 Diagram of MSCAT sensing	35
Figure 3.2 Glass mask used to fabricate MSCAT sensors.	39
Figure 3.3 Interferometric surface roughness for plano-plano Laptech crystals	42
Figure 3.4 Interferometric surface roughness for plano-convex Sawyer crystals	43
Figure 3.5 Interferometric surface roughness for plano-plano Sawyer crystals	44

Figure 3.6	Interferometric surface parallelism for plano-plano Laptech crystals	46
Figure 3.7	Interferometric surface parallelism for plano-convex Sawyer crystals	47
Figure 3.8	Interferometric surface parallelism for plano-plano Sawyer crystals	48
Figure 3.9	Block diagram of lock-in amplifier based signal designed for the MSCAT.....	50
Figure 3.10	Typical MSCAT resonant signal obtained using the lock-in amplifier based measurement system	51
Figure 3.11	Typical MSCAT impedance spectrum around resonance as measured by a network analyzer.....	54
Figure 3.12	Typical signal used to calculate the resonant frequency of the MSCAT.....	56
Figure 3.13	Geometry of the MSCAT sensor	58
Figure 3.14	[1, 250, 2750] and [2, 250, 2750] MSCATs.....	62
Figure 3.15	Graph showing percentage of crystal covered by spiral coil vs. maximum harmonic that could be excited.....	66
Figure 3.16	Graph showing the resistance of the spiral coils vs. maximum harmonic that could be excited	66
Figure 3.17	3D plot showing the relationship between N, S, and the maximum harmonic that can be excited	67

Figure 3.18 3D plot showing the relationship between N, W, and the maximum harmonic that can be excited.	68
Figure 3.19 3D plot showing the relationship between S, W, and the maximum harmonic that can be excited.	69
Figure 3.20 Alternative spiral configurations.....	70
Figure 3.21 Lateral field coupling coefficients k_{LE} for the TSM , fast quasi-shear mode, and quasi-longitudinal in AT-cut quartz versus electric field angle ψ with respect to the X axis	73
Figure 3.22 MSCAT COMSOL model	75
Figure 3.23 MSCAT voltage distribution calculated using COMSOL	75
Figure 3.24 Segment showing the electrostatic electric field distribution in the MSCAT quartz when the sensor is loaded with DI water and only in air	78
Figure 3.25 Zoomed in region indicated in Figure 3.23 showing the electric field distribution for the MSCAT when it is operated in air.....	79
Figure 3.26 Zoomed in region indicated in Figure 3.23 showing the electric field distribution for the MSCAT when it is loaded with water	80
Figure 3.27 Segment showing the electrostatic electric field distribution in the EMPAS quartz when the sensor is only in air and loaded with DI water	83
Figure 3.28 Zoomed in region indicated in Figure 3.26 showing the electric field distribution for the EMPAS when it is operated in air	84

Figure 3.29	Zoomed in region indicated in Figure 3.26 showing the electric field distribution for the EMPAS when it is operated in water.....	85
Figure 3.30	Diagram showing MSCAT with gold top layer	86
Figure 3.31	MSCAT response in air for bare MSCAT and MSCAT with gold layer	87
Figure 3.32	Magnitude of the thickness component of the electric field in the center of the MSCAT's AT-cut quartz wafer for various electrode geometries.....	91
Figure 3.33	Magnitude of the thickness component of the electric field in the center of the MSCAT's AT-cut quartz	91
Figure 4.1	Sensor response to changes in glycerol concentrations	97
Figure 4.2	Sensor response to changes in NaCl concentration.	100
Figure 4.3	Sensor response to changes in 2-propanol concentration.	103
Figure 4.4	MSCAT frequency shift due to a change of 2.25 cP when operated at elevated frequencies	106
Figure 4.5	MSCAT frequency shift due to a change of 1235 μ S when operated at elevated frequencies	108
Figure 4.6	MSCAT frequency shift due to a change in relative permittivity of 60 when operated at elevated frequencies	111
Figure 4.7	Relative frequency shift to a change in viscosity of 2.25 cP as a function of operating frequency	113
Figure 4.8	Relative frequency shift to a change in conductivity of 1235 μ S as a function of operating frequency.....	114

Figure 4.9	Relative frequency shift to a change in relative permittivity of 60 as a function of operating frequency.....	114
Figure 5.1	Schematic of antibody/antigen immobilization for <i>E. coli</i> O157:H7 selective film.....	119
Figure 5.2	<i>E. coli</i> O157:H7 slide under normal light and fluorescence.....	122
Figure 5.3	<i>E. coli</i> K-12 slide under normal light and fluorescence.....	122
Figure 5.4	<i>P. fluorescens</i> slide under normal light and fluorescence.....	123
Figure 5.5	Photograph of MSCAT sensor with the <i>E. coli</i> antibody film after the introduction of Amplex Red.....	125
Figure 5.6	Photograph of the control MSCAT sensor without the <i>E. coli</i> antibody film after the introduction of Amplex Red	126
Figure 5.7	<i>E. coli</i> bound to MSCAT <i>E. coli</i> O157:H7 selective sensing film.....	129
Figure 5.8.	The MSCAT sensor response to the layers of the bio-film and <i>E. coli</i> O157:H7 in solution.....	130
Figure 5.9	Diagram showing sensor substrate, linker, and sensing film molecule during oscillation.....	133
Figure 5.10	Typical growth curve for <i>E. coli</i> O157:H7.....	135
Figure 5.11	MSCAT sensor's response to a liquid sample containing 10^4 microbes/mL of <i>E. coli</i> O157:H7 when operated at the 59 th harmonic	137
Figure 5.12	MSCAT sensor's response to well water.	141

Figure 5.13 MSCAT sensor's response to well water inoculated with <i>E. coli</i> O157:H7	142
Figure 5.14 MSCAT's sensor response to apple juice.....	145
Figure 5.15 MSCAT sensor's response to apple juice inoculated with <i>E. coli</i> O157:H7	146
Figure 5.16 Schematic of <i>Salmonella</i> Selective Sensing Film.....	151
Figure 5.17 <i>Salmonella</i> bound to the MSCAT's surface	152
Figure 5.18 Bare MSCAT with no <i>Salmonella</i> bound to the MSCAT's surface.....	153
Figure 5.19 The MSCAT sensor response to <i>Salmonella</i>	155
Figure 6.1 CE Film attached to the bare quartz surface of an LFE sensor platform.....	160
Figure 6.2 Schematic of Antibody Based STX Sensing Film.....	162
Figure 6.3 Photograph of MSCAT sensor with the STX antibody film after the introduction of Amplex® Red	165
Figure 6.4 Photograph of the control MSCAT sensor without the STX antibody film after the introduction of Amplex® Red	166
Figure 6.5 Differential sensor response to various concentrations of STX.....	168
Figure 6.6 STX dose response curve for CE MSCAT	169
Figure 6.7 Antibody Based MSCAT STX Response to STX	171
Figure A.1 Top view of a standard QCM sensor	200
Figure A.2 IEEE Standard on Piezoelectricity coordinate system used to calculate acoustic mode data.....	202

Figure A.3	LFE sensor notation system for electric field direction relative to the crystallographic axes.....	203
Figure A.4	Lateral field coupling coefficients for -32.25° and 50.3° rotated-Y cuts of quartz versus electric field angle w.r.t. the X axis	205
Figure A.5	Lateral field coupling coefficients for -16.5° and -83.4° rotated Y cuts of lithium tantalate versus electric field angle w.r.t. the X axis	207
Figure A.6	Coordinate system with respect to the crystal face used in XRD measurements and calculations	208
Figure A.7	LTO LFE test crystal with dimensions	209
Figure A.8	X'Pert Texture generated experimental pole figure of the $\langle 202 \rangle$ plane	213
Figure A.9	Experimental temperature behavior for (YXwl) -16.5° LTO	215
Figure A.10	Sensor response to change in corn syrup	216
Figure A.11	Sensor response to changes in NaCl	218
Figure A.12	Sensor response to changes in 2-propanol concentration	221
Figure B.1	Geometry of rectangular spiral coil problem solved by Ballantyne	225
Figure B.2	Diagram showing a two turn spiral coil made up of four semi-circles	227
Figure B.3	Coordinate system used in near field spiral coil calculations	227

Figure B.4	Three-dimensional normalized patter of normalized θ component of the electric field as a function of θ	236
Figure B.5	Three-dimensional normalized patter of normalized ϕ component of the electric field as a function of θ	237

1 INTRODUCTION

1.1. The Sensor System

Bulk Acoustic Wave (BAW) sensors have been used for over 50 years for a variety of physical, chemical, and biological sensing applications. Often a BAW sensor platform is referred to simply as a “sensor” although this can lead to confusion in the case of chemical or biological sensing applications. For the purposes of this work each component of a BAW sensor system will be defined with a particular emphasis on chemical and biological sensing applications.

The first component of a sensor system consists of preparing and delivering a sample to the sensor element (Figure 1.1). Examples of sample preparation include particulate filtering and chemical or biological filtering to remove the analyte from solution or separate the analyte from interferences. Additionally, the sample preparation phase of a sensor system could include the pre-concentration of a large, dilute sample into a measurable aliquot. This preparation component of the overall system is generally developed after the sensing element has been finalized since the effectiveness of the sample preparation depends upon the requirements of the sensing element.

Although the sensor platform is an integral part of the complete sensor system it must be integrated with other critical components. When a BAW sensor platform is used to detect physical changes on the sensor surface (mass, viscosity, electrical properties, etc.) no sensing film is necessary and the sensor platform is simply the sensor element. When a BAW sensor platform is used in a chemical or biological

sensor system (Figure 1.1), however, the sensor element consists of two components, the target selective biological or chemical film and the sensing platform. The sensor platform typically provides sensitivity to the sensor system while the film provides selectivity.

In the case of detecting biological analytes the film provides selectivity and often is designed to detect only one biological analyte. An example is a monoclonal antibody selective only to specific pathogenic bacteria such as *E. coli* O157:H7. For chemical films the selectivity may not be as high and often one must resort to doping of the chemical film and/or operating the sensor platform at temperatures appropriate for the film to react with the chemical analyte.

In the case of chemical or biological sensing applications, the sensing platform is typically the substrate upon which one deposits the biological or chemical

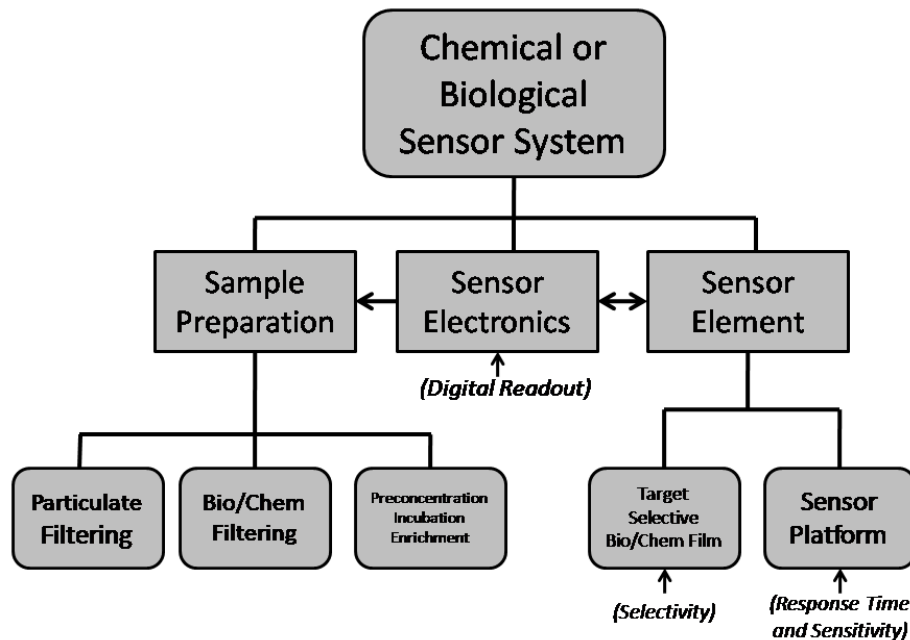


Figure 1.1 Block diagram of a complete sensor system for the detection of biological or chemical targets

selective film. As the biological or chemical film interacts with the target analyte changes occur in the film that may be electrical, chemical, and/or mechanical. In particular the electrical property changes include conductivity and/or dielectric constant changes while the mechanical changes include mass, elasticity, and/or viscosity changes. The sensing platform must be able to detect these changes sensitively and rapidly (*in situ*). Finally, the output from the sensing element must be interfaced to appropriate electronics that will provide a digital readout and display the presence or absence of the target analyte or the relative concentration of the target analyte. Often the electronic part of the sensor system is embedded in a laboratory-based instrument that is non-portable. Ideally in order to realize a complete *in situ* sensor system that satisfies the criteria of selectivity, high sensitivity, and portability it must be possible to integrate the sensor platform and electronics into a small portable unit.

Critical to the development of a small portable unit is the appropriate technology employed for the sensing platform. Ideally this technology should be very sensitive and capable of detecting both electrical and mechanical property changes in the target film due to the interaction between the target analyte and the film. Sensing platforms based on optical technology typically utilize optical fibers or surface plasmon resonance (SPR) and employ spectroscopy or fluorescence to examine the reflection or absorption of light on a target film. Optically based sensing platforms primarily detect electrical property changes in the target film and cannot detect some mechanical property changes such as mass and viscosity. Although optical sensing platforms are sensitive and selective, when interfaced with

the necessary electronics systems they are generally non portable and require specialized training to operate. Electrochemical based sensing elements measure a change in voltage, current, or conductance of a target film. One of the most popular electrochemical based sensing platforms consists of a semiconducting metal oxide (SMO) film deposited on an insulating substrate. This sensing element is very sensitive but does not have a high level of selectivity due to the fact that most selective sensing films cannot be applied to the sensor's surface and it measures only electrical property changes. Piezoelectric sensing platforms may employ surface bound acoustic waves or bulk acoustic waves. In the case of the former, surface acoustic wave (SAW) and acoustic plate mode (APM) sensing platforms may be realized. Although these sensing platforms have been shown to be quite sensitive, the platforms are limited to a single operating frequency. When using this sensing platform it is also necessary to isolate the electrodes from the sample and the sensing film. Recently BAW sensors that utilize spiral coils to excite acoustic waves have been designed. The sensors have been shown to operate over wide frequency ranges but suffer from relatively weak excitation efficiencies when compared to other BAW sensors and often require specialized electronic systems in order to excite and measure changes in resonant modes. More details on these sensor platforms are presented in Chapter 2.

1.2. Purpose and Objectives

The purpose of this work is to develop a novel BAW sensor platform that has a bare sensing surface and is capable of operating over a wide frequency range. The

bare sensing surface is desirable because it allows both mechanical and electrical property changes caused by a target analyte to be detected. In addition, when quartz is used as the sensor substrate, a bare sensing surface allows the use of silica based surface chemistries to attach selective sensing films to the sensor's surface. As will be shown later, if the sensor platform is capable of operating over a wide frequency range, significant improvements in sensor sensitivity can be achieved for some applications. In order to achieve these goals the following tasks need to be accomplished:

- Review previous work on BAW sensors in order to identify possible avenues for achieving the goals of this work.
- Design a novel sensor platform that has a bare sensing surface and is capable of operating over a wide frequency range.
- Develop a theoretical understanding of the sensor platform operation.
- Determine if the new sensor platform is capable of detecting both mechanical and electrical property changes in liquids.
- Determine if the new sensor platform is capable of detecting both chemical and biological analytes of interest.

Through the course of performing these tasks the Monolithic Spiral Coil Acoustic Transduction (MSCAT) sensor (Figure 1.2) was developed. The MSCAT has electrodes removed from the sensing surface and is capable of operating over a wide frequency range. In order to operate over a wide frequency range the MSCAT utilizes a photolithographically deposited antenna on the surface of a piezoelectric material opposite to the sensing surface. Although there are limitless numbers of

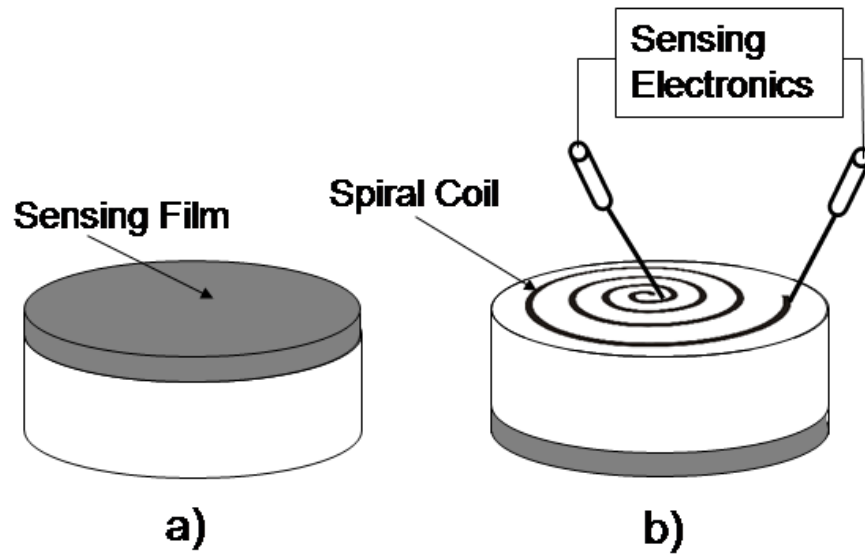


Figure 1.2 Diagram of MSCAT sensing element. a) Top view showing target selective sensing film b) bottom view showing electrical connections to sensing electronics

antenna configurations that are used for various applications, this thesis focuses on a spiral coil antenna. The antenna configuration for the MSCAT was not chosen arbitrarily. Most antenna designs are based on the wavelength of the electromagnetic wave that is to be excited and therefore only operate efficiently at a single frequency. There is, however, a class of antennas known as frequency independent spiral antennas that are capable of operating over a wide frequency range. Due to the ability to miniaturize these antennas and the fact that they operate efficiently over a wide frequency range a spiral coil antenna was chosen as the antenna type for the MSCAT.

The MSCAT sensor platform utilizes a photolithographically deposited spiral coil to excite acoustic waves in piezoelectric materials. The coil on the MSCAT sensor is an antenna that radiates a time varying electric field that penetrates the piezoelectric wafer when the coil is excited by an RF source. As a result of the

piezoelectric effect, the time varying electric field sets up a time varying stress in the wafer. Depending on the wafer thickness and the frequency of excitation, resonant acoustic waves at the fundamental or higher order harmonic frequencies are excited. The measurable output of the MSCAT sensor is a change in its resonant frequency due to changes in the surrounding medium or sensing film caused by the measurand.

Although the MSCAT's spiral coil antenna can be deposited on any piezoelectric substrate, AT-cut quartz is used in the present work. As will be discussed in the following chapters, when the sensor substrate is AT-cut quartz, the MSCAT excites the pure transverse shear mode (TSM) in the substrate. The TSM has mechanical displacements that are perpendicular to the propagation direction and parallel to the crystal surface which minimizes acoustic losses in liquid sensing applications. The AT-cut is particularly attractive for sensing applications due to the fact that a pure, temperature compensated TSM may be excited.

The MSCAT has a number of advantages over other BAW sensor platforms. The MSCAT has a bare sensing surface and is capable of operating over a wide frequency range . The bare sensing surface allows the MSCAT to detect both mechanical and electrical property changes in liquids and allows for the use of silica based chemistries when developing chemically or biologically selective sensing films. The geometry of MSCAT's photolithographically deposited spiral coil antenna can easily be modified which can lead to significant increases in the range of frequencies that can be excited in the device. The spiral coil antenna on the MSCAT is also in direct contact with the substrate which leads to significantly higher excitation efficiencies in comparison to some other BAW sensor platforms. In addition, the

MSCAT does not require specialized electronics and tuning capacitors, unlike some other BAW devices. The MSCAT also has the added advantage of operating at a number of different frequencies which can lead to significant decreases in both detection time and detection limit in comparison to other BAW sensor platforms as will be shown later.

In this work it is shown that the MSCAT is in fact capable of exciting up to the 99th harmonic in AT-cut quartz. An expression for the near-field electric fields radiated from a spiral coil antenna has been derived and finite element modeling has been performed in order to gain insight into how the MSCAT's spiral coil antenna excites the TSM in AT-cut quartz. It has also been found that the MSCAT is capable of detecting both electrical and mechanical properties in liquids. Finally, it has been shown that the MSCAT is capable of detecting both biological and chemical analytes of interest.

1.3. Organization

This thesis is organized into nine chapters, the first of which is the Introduction. The second chapter details the previous work performed on the development of BAW sensor platforms and identifies possible avenues for improvement. The third chapter describes development of the MSCAT sensor platform and provides a theoretical understanding of how the MSCAT operates. The fourth chapter presents the experimental work relating to the use of the MSCAT sensor to detect mechanical and electrical property changes in liquids. The fifth chapter details the use of the MSCAT platform as a biological sensor element. Chapter 6 presents a proof of concept on the use of the MSCAT platform as a

chemical sensing element. The seventh chapter presents the summary, conclusions, and potential future work. Appendix A describes the development of an alternative BAW sensor platform, a Lateral Field Excited (LFE) sensor platform fabricated on LiTaO_3 , which is also capable of operating at high frequencies by exciting high harmonics in the device. The final chapter, Appendix B details the derivation of the near fields for planar spiral coil antennas.

2 BACKGROUND

Bulk acoustic wave (BAW) devices by definition utilize acoustic waves that propagate through the interior of the device's substrate. A BAW device's resonant frequency is dependent on both the velocity of the acoustic wave and the thickness of the substrate. Most BAW devices utilize the piezoelectric effect in order to produce standing acoustic waves in the device. In a piezoelectric material, an electric potential is produced when a mechanical stress is applied (direct piezoelectric effect). The reverse is also true for piezoelectric materials, an applied mechanical stress will produce an electric potential (reverse piezoelectric effect). When a BAW device is used as a sensor, changes in the acoustic wave's velocity or amplitude as the wave interacts with the surrounding medium are monitored. The resonant frequency of BAW sensors is directly related to the velocity of the acoustic wave and therefore the resonant frequency is often used as the measurable output of the sensor. In this chapter previous work on BAW sensors is reviewed in order to identify possible avenues for achieving the goals of this work outlined in Chapter 1.

2.1. Sensor Platforms with Photolithographically Deposited Electrodes

2.1.1 The Quartz Crystal Microbalance (QCM)

The most popular and well-known BAW sensor platform is the quartz crystal microbalance (QCM) which utilizes the piezoelectric properties of AT-cut quartz crystals. For piezoelectric materials the constitutive equations describe the

relationship between stress (T), strain (S), electric field (E), and electric displacement (D) [1, 2] as follows:

$$T_{ij} = c_{ijkl}^E S_{kl} - e_{kij} E_k \quad (2.1)$$

and

$$D_i = e_{ikl} S_{kl} + \epsilon_{ik}^S E_k \quad (2.2)$$

Where e_{kij} describes the piezoelectric constant tensor of the material, c_{ijkl}^E describes the elastic stiffness constant tensor at a constant electric field, and ϵ_{ik}^S describes the dielectric permittivity tensor measured at a constant strain. The subscripts i, j, k , and have values of 1, 2, or 3 and indicate the three Cartesian coordinates of the crystal axis ($x = 1, y = 2, z = 3$). Repeated indices indicate a summation. For example:

$$u_i v_i = u_1 v_1 + u_2 v_2 + u_3 v_3 \quad (2.3)$$

and

$$u_{ii} = u_{11} + u_{22} + u_{33} \quad (2.4)$$

In order to simplify (2.1) and (2.2) a compressed Voigt notation is often used where ij or kl are replaced by p or q . In this case p or q can have the values of 1, 2, 3, 4, 5, or 6 as seen in Table 2.1.

Table 2.1 Compressed matrix notation

ij or kl	p or q
11	1
22	2
33	3
23 or 32	4
31 or 13	5
12 or 21	6

In this case (2.1) and (2.2) become:

$$T_p = c_{pq}^E S_q - e_{kp} E_k \quad (2.5)$$

$$D_i = e_{iq} S_q + \epsilon_{ik}^S E_k \quad (2.6)$$

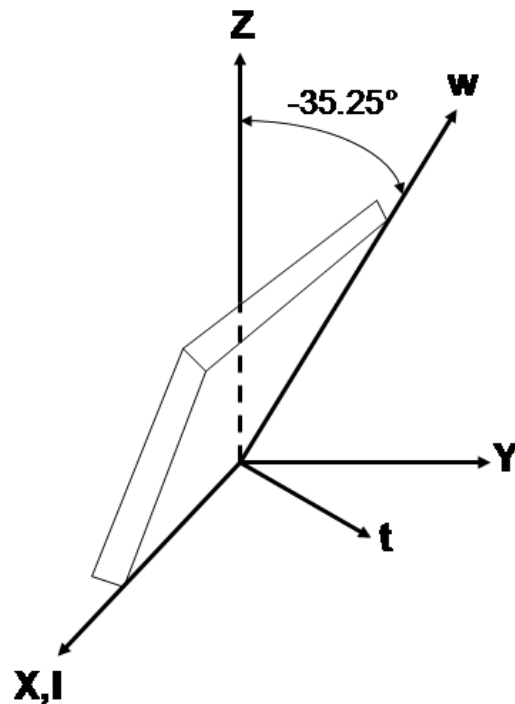


Figure 2.1 AT-cut plate using IEEE (YXwl) notation.

AT-cut quartz is a singly rotated Y-cut of quartz (Figure 2.1) that is commonly used for sensor and resonator applications due to its frequency stability to changes in temperature around room temperature (25° C). The most common electrode geometry of the QCM sensor is shown in Figure 2.2. The metalized region on the opposite surface (reference side) is outlined with dashed lines. The tab of the electrode on the sensing side wraps around the edge of the crystal to the reference side so that both electrodes can be contacted on the reference side. QCM rate monitors have a slightly different electrode configuration with the sensing electrode covering almost the entire surface and no electrode wrap-around [3]. In the QCM sensor an electrical signal is delivered to the QCM via two leads that contact the back surface or reference surface of the crystal. Since the electrode on the sensing side is on the side opposite to the

reference electrode, the applied electric field is primarily perpendicular to the surface of the crystal. This method of excitation is known as thickness field excitation (TFE). For the QCM rate monitor, leads are attached to both crystal surfaces, also resulting in thickness field excitation. The application of a high frequency electrical signal excites the resonant thickness shear mode (TSM) in the crystal. The TSM has mechanical displacements that are perpendicular to the propagation direction and parallel to the crystal surfaces. When a mechanical change (mass, viscosity, or elasticity) occurs on the sensor surface, the resonant frequency of the device changes [4]. A more detailed analysis of the relative sensitivity of the QCM compared to other BAW sensors can be found in Chapter 4.

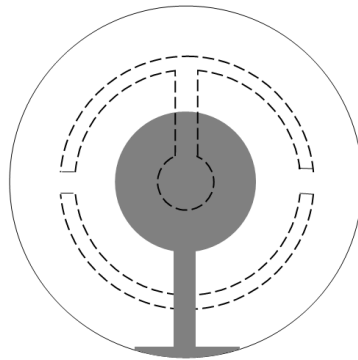


Figure 2.2 Top view (sensing surface) of a standard QCM sensor. Shaded and dotted regions are gold. Dotted regions indicate reference (bottom) side while shaded regions indicate sensing (top) side.

Although the QCM rate monitor is the standard for monitoring thin film thicknesses in deposition systems, there are disadvantages associated with the QCM sensor platform. For chemical or biological sensing the gold electrode on the sensing surface of the QCM necessitates using techniques such as the Langmuir-Blodgett Method [5] to attach the selective chemical or biological film to the sensor surface instead of the silica based surface chemistries that are most often used in chemical and

biological sensing applications. Further, the electric field associated with the TSM cannot penetrate into the measurand or sensing layer due to the conducting electrode on the sensing surface. Therefore, electrical property changes to the permittivity and/or conductivity of the adjacent liquid or chemi- or bioselective film caused by the target analyte cannot be detected with the standard QCM sensor. Although the measurement of electrical property changes is not always advantageous, for some applications such as biological or chemical sensing the ability to monitor electrical property changes can offer additional information about analyte interactions with the sensing film. Another drawback of the QCM is the fact that the operating fundamental resonant frequency is typically only between 3 and 20 MHz due to the thicknesses of the piezoelectric plates which limits the sensitivity [6]. Although QCM sensors may be operated at elevated harmonics [7], efficiently exciting above the 7th harmonic is difficult due to the relatively low piezoelectric coupling of quartz [8] and the fact that the transducer configuration results in a large parallel capacitance. These limitations, however, can be overcome.

As will be described in the remainder of this chapter, novel acoustic wave platforms with various transducer configurations have been developed that improve upon the QCM sensor platform. In these sensor platforms the exciting transducers can be external to the sample or photolithographically deposited on the sample. In most, but not all, cases the sample is AT-cut quartz due to the fact that the TSM in AT-cut quartz is temperature compensated around room temperature.

2.1.2. Thickness Shear Mode (TSM) Resonators with Modified Electrodes on the Sensing Surface

In order to measure electrical properties of a medium or sensing layer several researchers have examined modifying the electrode geometry of the QCM. Josse *et al.* [9, 10] modified the size and shape of the sensing electrode and found that it was possible to detect conductivity and permittivity changes in liquids. In particular they investigated decreasing the size of the sensing electrode (Figure 2.3a) and also used a ring-shaped sensing electrode (Figure 2.3b) to detect electrical properties in liquid environments. They found that resonators with these modified electrodes were in essence capacitance sensors. They also noted that one could measure the static capacitance changes due to changes in the liquid environment through measurement of the changes in the anti-resonant frequency of the device. They concluded that these devices combine the advantages of a mass-sensitive QCM with a capacitive sensor.

Zhang and Vetelino [11, 12] also examined the resonators with small sensing electrodes (Figure 2.3a), ring-shaped sensing electrodes (Figure 2.3b), and an open ring electrode (Figure 2.3c). They performed extensive experiments characterizing these modified electrode resonators to liquid loads with changing viscosity, conductivity, and permittivity. They found that as the overlap between the sensing electrode and the reference electrode was minimized, the sensitivity of the TSM resonator to liquid electrical property changes was almost 25 times greater than for the standard QCM electrode. Specifically, the results obtained when the devices were exposed to various concentrations of NaCl in solution showed the decreased size and

open ring sensing electrodes to have much higher frequency shifts than the standard QCM.

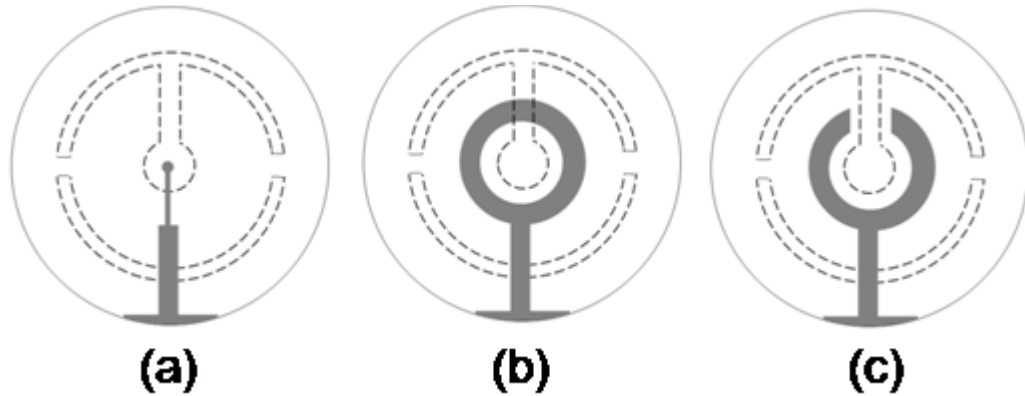


Figure 2.3 Geometries of TSM resonators with a (a) small sensing electrode, (b) ring-shaped sensing electrode, and (c) open ring sensing electrode.

Although the TSM resonators with small sensing electrodes have been shown to be capable of detecting liquid property changes they are not capable of operating at elevated frequencies. In addition they still have electrodes on their sensing surface which can limit the type of sensing film that can be used. In order to develop a BAW sensor platform with a bare sensing surface, researchers have recently developed the lateral field excited (LFE) sensor platform.

2.1.3. Lateral Field Excited (LFE) Sensors

The TSM can also be excited in an AT-cut quartz disc by the application of an electric field parallel to the surfaces. This excitation is called lateral field excitation (LFE) and has primarily been used to drive piezoelectric plates as resonant filters

[13]. Although Vig and Ballato [14, 15] suggested the possibility of LFE devices as sensors, Vetelino *et al.* [16- 18] were the first to use LFE devices as sensors.

In an LFE sensor platform both electrodes are placed on the surface opposite the sensing medium (Figure 2.4) while still exciting a thickness shear mode [16]. In this case, the sensing surface of the device is bare and one can either expose this surface directly to a measurand or attach a chemiselective or bioselective layer directly on the bare crystal surface. The bare quartz sensing surface allows the electric fields associated with the TSM to probe the measurand, allowing the LFE sensor platform to detect both electrical and mechanical property changes in the analyte or sensing film. Recently Hempel *et al.* [19] have shown that changes in the electrical properties of the analyte causes a redistribution of the electric field direction inside the crystal. This redistribution results in piezoelectric stiffening (see equations 2.1 and 2.2) which produces a change in the velocity of the acoustic wave. Thus the bare quartz sensing allows the LFE sensor platform to detect both electrical and mechanical property changes in the analyte or sensing film.

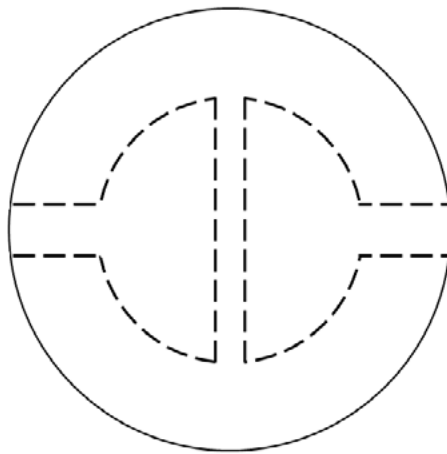


Figure 2.4 Top view (sensing surface) of a LFE sensor. Dotted regions are gold and indicate reference (bottom) side.

Hu *et al.* [18] characterized the responses of a range of LFE devices with varying gap widths to changes in liquid properties. The LFE sensor resonant frequency responses were compared with the resonant frequency responses of sensors having a small electrode, a closed ring electrode, an open ring electrode geometries, and a standard QCM. The liquid environments included media with varying conductivity, permittivity, and viscosity. The results of these tests showed that in addition to being extremely sensitive to electrical property changes, (conductivity and relative permittivity); the LFE is also capable of detecting mechanical property changes (viscosity). The LFE was also shown to be approximately twice as sensitive as the modified electrode devices to changes in both electrical and mechanical property changes. In the cases of conductivity and viscosity the resonant frequency shift of the LFE sensor was negative while for the dielectric constant it increased as the relative dielectric constant decreased. In all cases the LFE sensor frequency shift was larger than the corresponding frequency shift of the QCM.

The use of other piezoelectric materials other than AT-cut quartz for LFE sensors also been explored. McCann *et al.* [20] performed a theoretical search and experimental measurements to identify the existence of high frequency temperature compensated TSMs in LiTaO₃ (See Appendix A). Recently Wang *et al.* [21] also performed a similar search in LiNbO₃ and identified possible orientations that may be suitable for sensor applications.

In order to demonstrate the applicability of the LFE sensing platform, responses to chemical and biological target analytes in liquid solutions have been examined. The LFE sensing platform has been used in the detection of

organophosphates in solution [22]. The LFE sensing platform was coated with a polyepichlorohydrin (PECH) film, which selectively sorbs phosmet ($C_{11}H_{12}NO_4PS_2$), a pesticide widely used on fruits and vegetables. The sensitivity, reproducibility, and response time of the resulting LFE sensing element was obtained and compared to similar results obtained with a QCM sensor element. The LFE sensing element was found to exhibit significantly higher sensitivity than the QCM even though it was exposed to lower concentrations of phosmet. The responses were found to be reproducible and the response times shorter than those of the QCM.

Relative to biological sensing, the LFE sensing platform was used to selectively detect *E. coli* O157:H7 in water [23]. *E. coli* is one of the leading causes of food borne illnesses [24]. There are many strains of *E. coli* and although most are harmless to humans, some strains such as the 3 serotype O157:H7 can cause serious illnesses [25]. A biochemical film based on work performed by Berkenpas [26] that is selective to *E. coli* was attached to the LFE platform's surface and changes in the resonant frequency of the resulting element were monitored [23]. More information on the selective sensing film is given in Chapter 5. When compared to results obtained with a QCM sensor element, the sensitivity was about 5 times greater although the LFE's detection limit was still only 10^8 microbes/mL.

Recently, the LFE platform has been used in the detection of the chemical analyte saxitoxin (STX), the most dangerous neurotoxin associated with paralytic shellfish poisoning (PSP). Shellfish containing STX, a product of a harmful algal bloom (HAB) such as red tide, is one of the primary causes of PSP in humans. The current Association of Official Analytical Chemists (AOAC) accepted method to

detect STX is the mouse bioassay. This method is a long lab-based test with both technical and ethical limitations. In this procedure samples are extracted from shellfish meat and then injected into mice. The time of death is noted and, using a standard table, the toxin level in the sample is estimated [27].

A sensing film based on an 18-crown-6 ether (CE) molecule, which has been reported to sensitively sorbs STX, was developed and covalently bound to the LFE sensing surface [28]. As described in Chapter 6, the selectivity of CE to STX is not as high as was reported in [28]. Preliminary tests have shown that a differential LFE STX sensor element is highly sensitive to STX. The differential LFE STX sensing element's response was determined by subtracting the resonant frequency shift of the control sensor from that of the CE-coated sensor. The LFE STX sensing element exhibited a differential resonant frequency shift of 27 Hz to 1 μ M STX in water. With the use of the neutral sensor the differential resonant frequency shift is due to the interaction of STX with the CE film while discounting other non-specific environmental interactions. The response time of the differential LFE STX sensor element is approximately 5-7 minutes as compared to the mouse bioassay which can have a response time on the order of days.

Recently it was found that the LFE electrode configuration plays a significant role in the nature of anharmonic modes that are excited [29]. As is the case with the QCM, it was also found that when curved substrates were used the quality factor (Q), effective coupling, and mode spectrum were improved [29, 30]. It was also shown that etching the surface of LiTaO₃ LFE sensors improved the mode spectrum by decreasing or eliminating spurious modes that were excited.

Although the LFE has a bare sensing surface and has been shown to be more sensitive than both the standard QCM and QCM sensors with modified electrodes, it is unable to operate at elevated frequencies which can limit its sensitivity in biological and chemical sensing applications. Recently researchers have begun to explore BAW sensing platforms that have the exciting electrode completely removed from the sensor substrate which can more useful for certain sensing applications such as harsh environment sensing.

2.2. Remotely Excited Bulk Acoustic Wave Sensor Platforms

2.2.1. Electromagnetic acoustic transducer (EMAT)

Electromagnetic acoustic transducers (EMATs) have been in use for the nondestructive evaluation (NDE) of materials for over 50 years [31]. Randall *et al.* first used EMATs to measure internal friction due to intercrystalline thermal currents in brass bars [32]. It was not until the early 1970's that EMATs were used for practical sensing purposes. EMATS were first utilized to estimate steel sheet formability [33] and for the detection of stress corrosion cracks in buried gas pipelines [34]. More recently EMATs have been used in a variety of applications including inspecting the welds of sheet metal in a rolling mill, railroad rail inspection, and a thickness gage for seamless stainless steel tubing [34]. EMAT transducers have also been used to extract the material constants of piezoelectric materials [35]. In this work a longitudinal EMAT (L-EMAT) was developed and used to calculate the phase velocities and stiffness coefficients of various piezoelectric materials and found to

agree with the values reported in literature to within 0.1%. In contrast to the earlier EMAT applications, which were on the macro scale, in the past five years EMAT applications have been used on a micro scale for a broad array of sensing applications, which include biosensors [36] and liquid sensors [37].

A typical bulk wave EMAT is shown in Figure 2.5 and consists of a spiral coil and a pair of permanent magnets [38]. Eddy currents in the metal sample are induced by the RF current in the coil elements. Lorentz forces are generated in the metal due to the interaction of these eddy currents with the externally applied DC magnetic field. The Lorentz forces can create a spectrum of acoustic modes in metals which depend on the magnet and coil configurations [31, 39]. A pulse-echo configuration is then used to monitor the acoustic mode properties for the nondestructive evaluation (NDE) of materials [40]. As Hirao and Ogi discuss [31] the primary advantages of EMAT techniques are (1) non contact excitation, (2) easy generation and reception of the shear wave, (3) ability to operate in applications up to 1000°C, (4) ability to detect anisotropic elastic constants with polarized shear waves while the disadvantages include (1) low transfer efficiency compared to piezoelectric transducers and (2) inapplicability to non-metallic materials. More recently the EMAT approach has been modified for use on the micro scale to produce acoustic wave sensors as described in the following section.

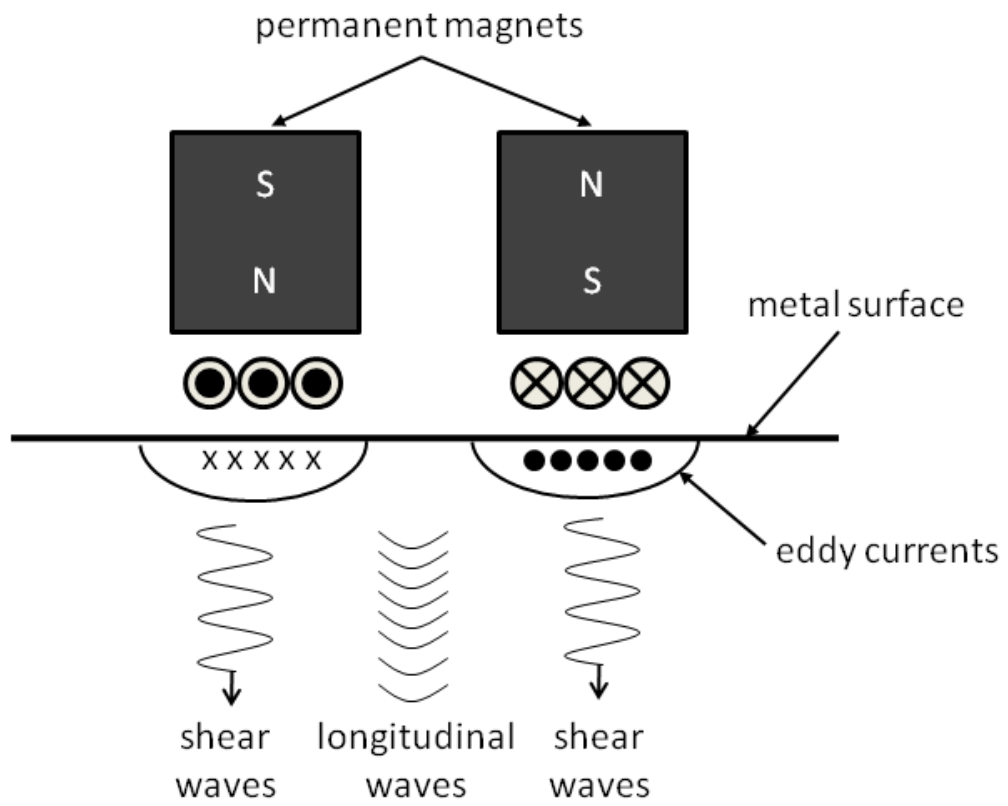


Figure 2.5 Configuration for bulk wave EMAT [31].

2.2.2. Magnetic Acoustic Resonance Sensors (MARS)

Stevenson and Lowe [41] modified the EMAT configuration on the micro scale to excite high Q resonances in silica glass. Instead of being used on the macro scale, the MARS utilizes the same basic configuration as EMATs but applies it on the micro scale to produce an acoustic wave sensor [41]. In the MARS configuration, an electrically excited hand wound spiral coil is placed near a metalized substrate that is exposed to the DC magnetic field from a single permanent magnet (Figure 2.6). The spiral coil produces electromagnetic fields that induce eddy currents on the thin metal layer that is attached to the substrate according to Lenz's law. The permanent magnet produces static magnetic fields that couple with the time-varying eddy currents to produce Lorentz forces. These time varying forces produce time varying stresses and hence acoustic waves. As with other acoustic wave sensors the resonant frequency of the device shifts with changes on its surface [42]. Unlike other acoustic wave sensors however, the MARS configuration has the advantage of being capable of utilizing non-piezoelectric substrates.

The term MARS can lead to some confusion. Stevenson and Lowe also use MARS to describe a different sensor configuration where no permanent magnet is used and a piezoelectric wafer is used as the sensor substrate [43]. Others refer to this configuration as the Electromagnetic Piezoelectric Acoustic Sensor (EMPAS) and this term will be used in this work to avoid further confusion. The details of the EMPAS sensor platform is given in section 2.2.3.

Initially Stevenson and Lowe [41] deposited a thin layer of metal onto glass plates in which the Lorentz forces were generated. Using a single permanent magnet

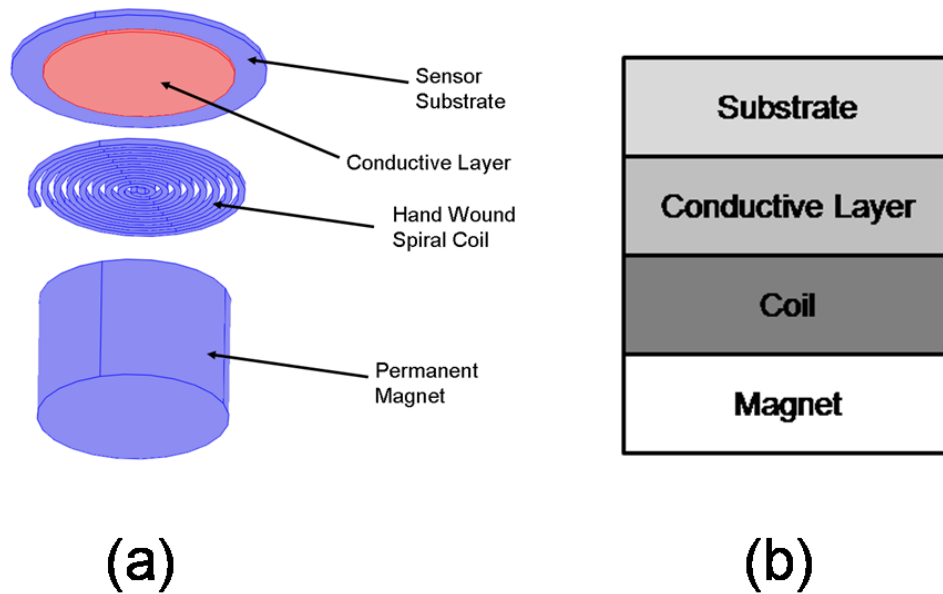


Figure 2.6 Diagram of MARS device showing (a) layout of sensor substrate (usually non-piezoelectric), conductive layer, hand wound spiral coil, and permanent magnet and (b) the four layers of the device.

they generated radially polarized shear waves. These shear waves then propagated through the thickness of the glass sample to the sensing surface. They were able to resolve resonances up to the 34th harmonic in a 530 μm thick aluminized silica plate. An acoustic Q factor as high as 7×10^5 was measured with this configuration. They also found that the sensor's response to mass loading exhibited Sauerbrey-like behavior [6] similar to the QCM.

Stevenson and Lowe also examined other sensor substrates for use in MARS devices [41]. Stainless steel, aluminum, silica glass, fused quartz, sapphire, and diamond were examined. They found that although diamond had the highest shear velocity and sapphire produced the clearest resonant peaks, silica glass had the best combination of shear velocity and clear resonant peaks. When used as a sensor, the

silica glass based MARS was shown to be more sensitive than the standard QCM when measuring mass and liquid viscosity.

In collaboration with Thompson, [44] Stevenson and Lowe found that it was possible to silinize the silica based MARS device creating a hydrophobic surface that resulted in sensors that exhibited smaller frequency shifts when immersed in water than untreated devices. They were able to measure a frequency shift with only minimal damping of the sensor response when an aluminized silica sample was loaded with water. They also showed that it when the silica based MARS device was used to detect protein absorption it exhibited a Sauerbrey-like behavior [45].

Recently Lucklum *et al.* [46-50] have performed extensive research on the MARS. They have simulated and designed the MARS with different RF coil geometries and magnet arrangements to generate thickness shear [46, 50], flexural [47, 49, 50], and face shear [47- 50] modes. They have demonstrated the applicability of the MARS for liquid property sensing and mass detection. It was found that sensors exhibited sensitivity that was similar to the QCM for mass sensing applications [46]. The advantage of the sensor for liquid property sensing is that the resonator element can be completely immersed in the liquid, while the electrical apparatus for excitation and detection is outside. It was found that circular face shear modes were more sensitive to liquid density and viscosity changes while radial flexural plate modes were better suited to detecting liquid level. Although a comparison to other BAW sensors was not performed it was demonstrated that aluminum [48] and silicon [49] based MARS devices were capable of detecting changes in liquid viscosity ranging from 1-11 mPas. Lucklum and Jakoby have also extended a single MARS into a MARS array

on a single substrate of metalized silicon [50], where each sensor of the array can be designed to operate in distinct vibration modes. Prototypes of the MARS array have been fabricated in brass, successfully exciting different modes in individual sensors in the array. One potential shortcoming of the MARS is that the lower detection efficiency compared to conventional piezoelectric transducers requires the use of dedicated sensor electronics [49]. In addition, these sensors have not been shown to be capable of operating at frequencies in excess of a few MHz or detecting changes in liquid electrical property changes.

2.2.3. Electromagnetic Piezoelectric Acoustic Sensor (EMPAS)

Stevenson and Lowe in collaboration with Thompson modified the MARS configuration to take advantage of the temperature stability of AT-cut quartz [44, 51]. This new device will be referred to as the Electromagnetic Piezoelectric Acoustic Sensor (EMPAS). The EMPAS shown in Figure 2.7 uses only a piezoelectric crystal and a hand wound spiral coil that is separated by a small air gap (~ 0.30 mm) [51]. The hand wound spiral coil produces electric fields that penetrate the piezoelectric material to excite acoustic waves. The EMPAS has the advantage of being capable of exciting high order harmonics in AT-cut quartz wafers without the need for electrical contacts to the wafer.

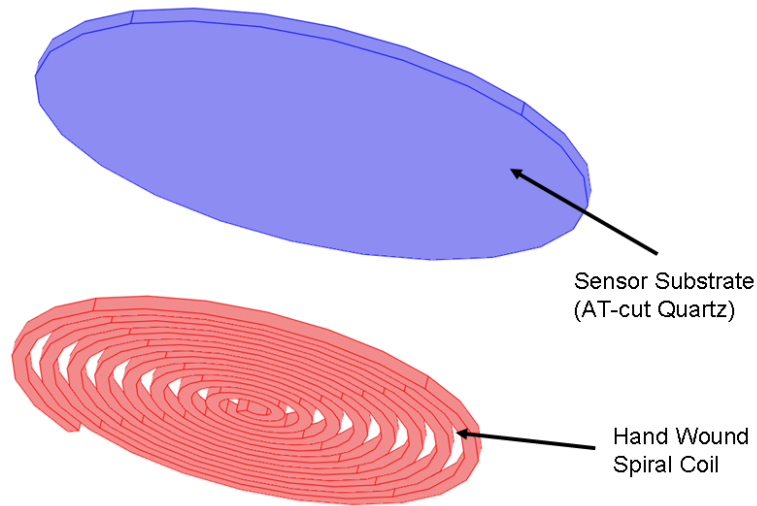


Figure 2.7 Geometry of EMPAS device.

Stevenson and Lowe first used the EMPAS to measure the attachment of Immunoglobulin G (IgG), a monomeric immunoglobulin commonly used to bind antibodies to a surface [51]. They found that the EMPAS did not exhibit frequencies predicted by Kanazawa [52] for BAW sensors. They also found that they were able to distinguish chemical changes when the device was operated at two different frequencies that were not apparent when the device was operated at a single frequency [53]. In these tests they were able to excite up to the 49th harmonic in the device. In later experiments they were able to excite acoustic waves up to 1 GHz using thin AT-cut quartz wafers although the signal-to-noise ratio (SNR) was reduced significantly at these frequencies.

More recently alternative EMPAS configurations have been examined. Stevenson and Lowe examined using ferrite-supported toroids [54] as the excitation mechanism for EMPAS devices (Figure 2.8a). The toroids were designed so that their resonant frequency matched the fundamental frequency of the AT-cut quartz wafers

(6.6 MHz). They found that the toroid based EMPAS could excite shear acoustic waves in liquid although the maximum operating frequency of the device was only 33 MHz. More significantly, they were able to excite acoustic waves when the toroid was separated from the quartz wafer by a water filled beaker (Figure 2.8b).

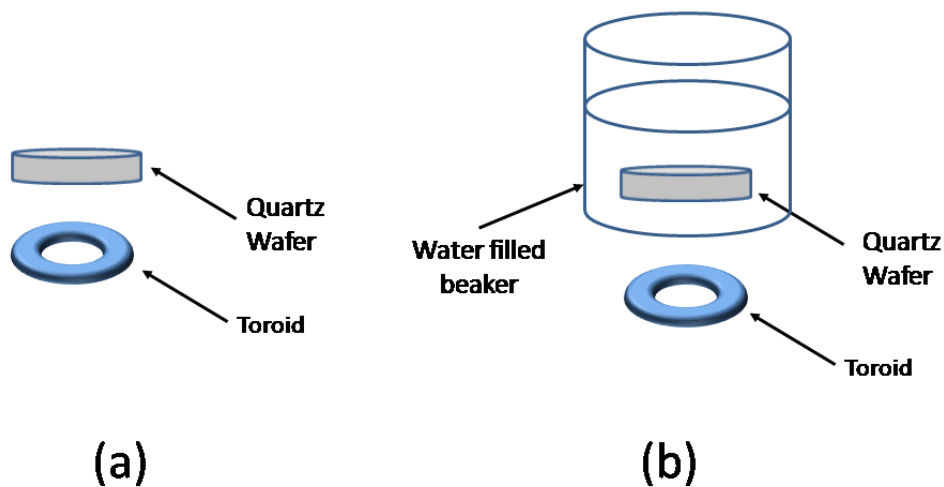


Figure 2.8 Diagram showing (a) toroid based EMPAS and (b) quartz wafer immersed in water.

Stevenson and Lowe also explored using small piezoelectric chips for the EMPAS substrate [55]. An AT-cut quartz wafer was cleaved into millimeter sized chips of various shapes. They found that these non-symmetrical chips had the benefit of more clearly defined resonance peak than a 12 mm diameter quartz wafer. The authors postulate that this is due to the non-parallelism of the larger wafer.

Araya-Kleinstueber *et al.* utilized the EMPAS as a bimolecular sensor in a technique they termed magnetic acoustic resonance immunoassay (MARIA) [57]. They explored two methods for attaching antibodies onto the quartz surface of an

EMPAS. The first technique was direct adsorption of the antibody onto the bare quartz surface and found that this technique resulted in poor attachment and low antibody surface density when goat IgG antibodies were used. The second technique used covalent immobilization technique developed by Cass [58] that utilized a trimethoxysilylpropylethylene diamine modified surface coupled with glutaraldehyde to attach the antibodies to the sensor surface. They found that this approach yielded higher antibody surface densities and larger sensor responses the binding of goat IgG. They postulate that the ability of the EMPAS to operate over a wide range of frequencies may allow one to distinguish between interactions on the sensing film from viscosity changes in the liquid medium due to the ability to match the acoustic wavelength of the sensor to the film thickness. They believe that any interactions from viscosity changes in the liquid medium would not be measured by the sensor in this case because the acoustic wave would not penetrate past the sensing layer.

Ballantyne and Thompson [59] were able to excite acoustic waves up to the 75th harmonic in AT-cut quartz using the EMPAS configuration although the signal was not useful at these frequencies due to poor signal quality-factor (Q). In a subsequent publication they state that the 49th harmonic is the upper limit on the EMPAS device [60]. Vasilescu *et al.* examined using gallium phosphate (GaP₀₄) as the sensor substrate for the EMPAS instead of AT-cut quartz. They found that neutravidin chemisorbed to the bare GaP₀₄ sensor surface without the need for the amine layer to link the neutravidin to the sensor surface that is needed with the QCM.

Ballantyne [8] compared the EMPAS to the QCM in the detection of the protein neutravidin. The QCM was operated at its fundamental frequency (9 MHz)

while the EMPAS was operated at its 47th harmonic (453 MHz). He found that the EMPAS exhibited a seven times larger signal to noise ratio in these tests. He also used both devices to monitor the interaction of tat protein to a trans-activation responsive region Ribonucleic acid (TAR RNA) and found that the EMPAS was three times more sensitive than the QCM.

Although the separation of the spiral coil from the piezoelectric crystal allows for remote interrogation of the sensor, the resonant responses from these devices tend to be relatively weak and require specialized electronics and tuning circuits to operate efficiently [8, 53-61] (Figure 2.9). The system seen in Figure 2.9[8] utilizes a signal generator, lock-in amplifier, and handmade electronics (AM diode detector, preamplifier, and parallel RLC circuit) to monitor the resonant frequency of the EMPAS. More details on the operating principles of the system can be found in

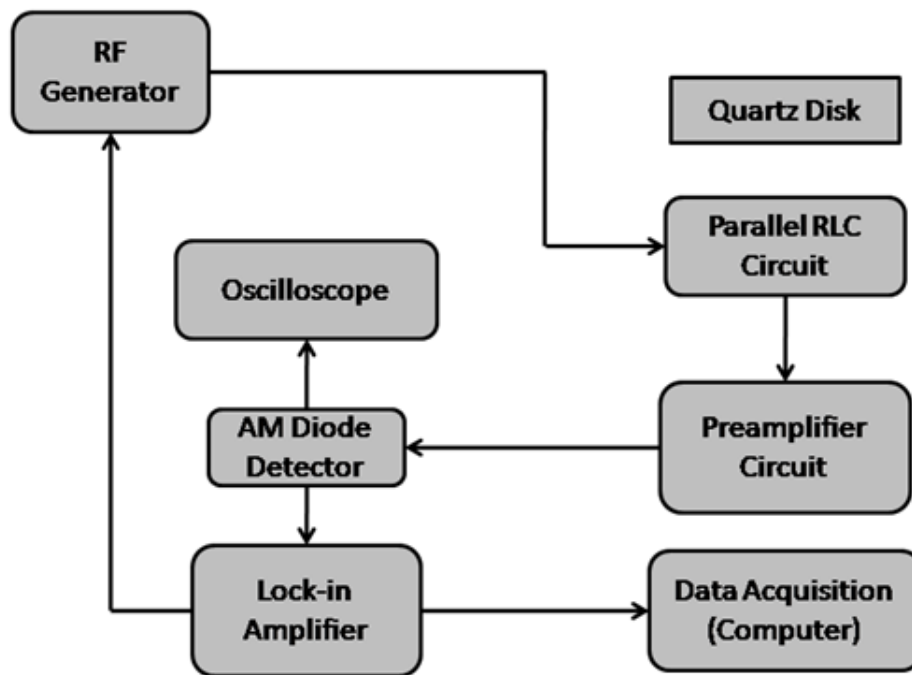


Figure 2.9 Block diagram of EMPAS system.

Chapter 3. Although the lock-in amplifier based system is capable of monitoring the resonant frequency of an EMPAS device, it does have several limitations. Besides the complexity and cost of this system, resonance sweeps take a significant amount of time due to the necessity of letting the output of the signal generator settle after each change in signal frequency. A single sweep to monitor the harmonics of an EMPAS from 6 MHz to 600 MHz takes approximately 20 hours [53]. Stevenson *et al.* developed a technique called frequency hopping to reduce this time to 30 minutes [53]. In this technique computer software was used to tune the signal generator to the resonant peak of each harmonic and scan over a limited range and then “hop” to the next resonant peak. Additionally, due to the hand-made nature of the spiral coils, reproducibility from device to device can be poor [61].

Lee *et al.* [61] further modified the EMPAS system to enhance high frequency operation. They characterized the impedance of two different spiral coil configurations (3mm and 5 mm in diameter) and found that the larger spiral coil had undesirable parasitic capacitance. They also found that the length of the coaxial cable used to join the spiral coil to the AM-detector is of critical importance. They found that when the cable was a quarter of a wavelength long the system was able to achieve the highest resonant frequencies (650 MHz). Researchers in Magdeburg, Germany are developing a compact impedance measurement system [62] that may be applicable to the EMPAS.

Although the EMPAS has a bare sensing surface and is capable of operating at elevated harmonics, the EMPAS does have some limitations. As will be shown later, because the spiral coil is separated from the sensor substrate the majority of the electric field radiated from the spiral coil is trapped in the air gap between the spiral

coil and the sensor substrate leading to weak resonances in the substrate. In order to monitor the resonant frequency shifts of an EMPAS it is necessary to utilize complex electrical systems such as a lock-in amplifier system described in Chapter 3. These measurement systems are extremely slow and it takes over 30 minutes to perform a single frequency sweep which limits the sensor's ability to quickly detect changes in the target analyte or sensing film. In addition, the necessary electronics systems are large and difficult to miniaturize for non-lab based applications. In order to develop a sensor platform that had a bare sensing surface and was capable of operating over a wide frequency range but without the limitations of the EMPAS device, a different approach was undertaken.

3 DEVELOPMENT OF THE MONOLITHIC SPIRAL COIL ACOUSTIC TRANSDUCTION (MSCAT) SENSOR

3.1 The MSCAT Platform

In this work a new BAW sensor platform that builds on the work done on previous BAW sensor platforms, in particular the LFE and EMPAS has been developed. As will be shown in the following sections, the monolithic spiral coil acoustic transduction (MSCAT) platform (Figure 3.1) can excite the TSM in AT-cut quartz like other BAW platforms such as the QCM and LFE. The MSCAT sensor, which uses a gold, photolithographically-deposited, spiral coil, has been developed to improve upon the best aspects of the standard QCM sensor while integrating the positive features of other acoustic wave sensors such as the LFE and EMPAS. The coil on the MSCAT sensor is an antenna that radiates a time-varying electric field that penetrates the AT-cut quartz wafer. As a result of the piezoelectric effect, the time

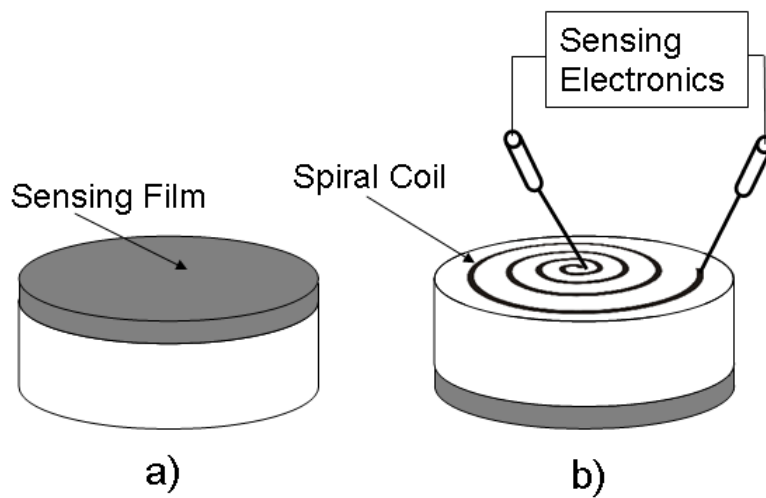


Figure 3.1 Diagram of MSCAT sensing element a) top view showing target selective sensing film b) bottom view showing electrical connections to sensing electronics

varying electric field sets up a time-varying stress in the wafer. Depending on the wafer thickness and the frequency of excitation, resonant acoustic waves at the TSM fundamental and higher order harmonic frequencies are excited. Like the LFE and QCM, the measurable output of the MSCAT sensor is a change in the TSM resonant frequency due to changes in the surrounding medium or sensing film caused by the measurand. As will be discussed later, like the LFE and EMPAS the MSCAT only operates efficiently when it has a liquid on its sensor surface due to the electrical boundary conditions and is not applicable to gas sensing applications. This limitation, however, can be overcome.

As will be shown later, because the MSCAT's spiral coil is in direct contact with the piezoelectric wafer the MSCAT excites acoustic waves in a different manner than the EMPAS. This leads to significantly stronger resonances in the AT-cut quartz wafer which allows the MSCAT to operate at significantly higher harmonics than the EMPAS and does not require specialized electronics or manual tuning for each measurement. The author has been awarded a British patent [63] for the MSCAT sensing platform and currently has US [64], German [65], and Japanese [66] patents pending.

The antenna configuration for the MSCAT was not chosen arbitrarily. Most antennas such as dipoles are designed to operate at a single frequency. With a dipole based antenna a fraction of the wavelength (λ) (typically $\lambda/2$ or $\lambda/4$) is a critical part of the antenna design. These designs are not practical in a BAW sensor platform due to the size of BAW devices. A typical AT-cut quartz BAW sensor that has a fundamental frequency of 5 MHz has a thickness of 0.33 mm and a diameter of 25.4

mm. If one wanted to operate the device at a high frequency, for example 500 MHz, using a dipole based antenna one would need a dipole of length 300 mm ($\lambda/2$) or 150 mm ($\lambda/4$), far larger than the sensor. In addition, the sensor would only operate at a single frequency. There is, however, a class of antennas that are capable of operating over a wide frequency range that are known as frequency independent spiral antennas [67]. Due to the ability to miniaturize these antennas and the fact that they operate efficiently over a wide frequency range a spiral coil antenna was chosen as the antenna type for the MSCAT. As will be shown later, this antenna configuration is capable of exciting the TSM in AT-cut quartz.

3.2 MSCAT Sensor Fabrication

The cleanroom facility at the Laboratory for Surface Science and Technology (LASST) (University of Maine) was utilized to fabricate all MSCAT platforms for this work. Glass masks were created for each spiral coil configuration. Since the mask maker at LASST is only able to produce rectangles, a C program was written that creates the spirals from a series of rectangles. Figure 3.2 shows a typical MSCAT glass mask.

Initially an etch procedure was used where gold was deposited on AT-cut quartz wafers and the desired spiral coil pattern was exposed onto photoresist that was spun onto the gold layer. Finally, the unwanted gold was removed through an etching process. Gold was used due to the fact that it is chemically inert and has a high conductivity. In order to attach the gold to the quartz surface a 200 Å chromium adhesion layer was used. It was found, however, that for smaller feature sizes (less

than $\sim 20 \mu\text{m}$) the etch process did not produce reproducible patterns. During the etch process the chromium layer could be undercut by the etchant if the sensor was left in the etchant too long resulting in the spirals peeling off from the quartz. Based on these results a liftoff technique was developed.

The spiral coil patterns were fabricated on the AT-cut quartz wafers by spin coating lift-off resist and photoresist on the crystal before the gold and chromium layers were deposited. MicroChem LOR5B lift-off resist was first spun onto the bare surface of the wafer for 40 seconds at 2,500 RPM. The wafer was then placed on a preheated hotplate (115°C) and the temperature was ramped up to 190°C to avoid thermally shocking the crystal. The wafer was baked at 190°C for 10 minutes to harden the lift-off resist. The crystal was allowed to cool for 5 minutes and then Rohm Haas S1813 photoresist was spun on top of the LOR5B for 40 seconds at 3500 RPM. The wafer was baked at 115°C for 3 minutes to harden the photoresist.

In order to produce the desired spiral coil pattern a glass mask with the desired pattern was utilized and the desired pattern was exposed under UV light for 45 seconds. The pattern was developed by first using a 1:5 solution of Rohm Haas MF351 to remove the photoresist layer and then a 1:2 solution of Rohm Haas MF319 was used to remove the LOR5B layer that was exposed by the removal of the S1813. A 200 \AA chromium adhesion layer and then the gold layer (usually 2000 \AA) were deposited on the element using magnetron sputtering. Finally, a lift-off procedure was used to remove the unwanted gold and chromium leaving the desired spiral coil pattern on the AT-cut quartz wafer.

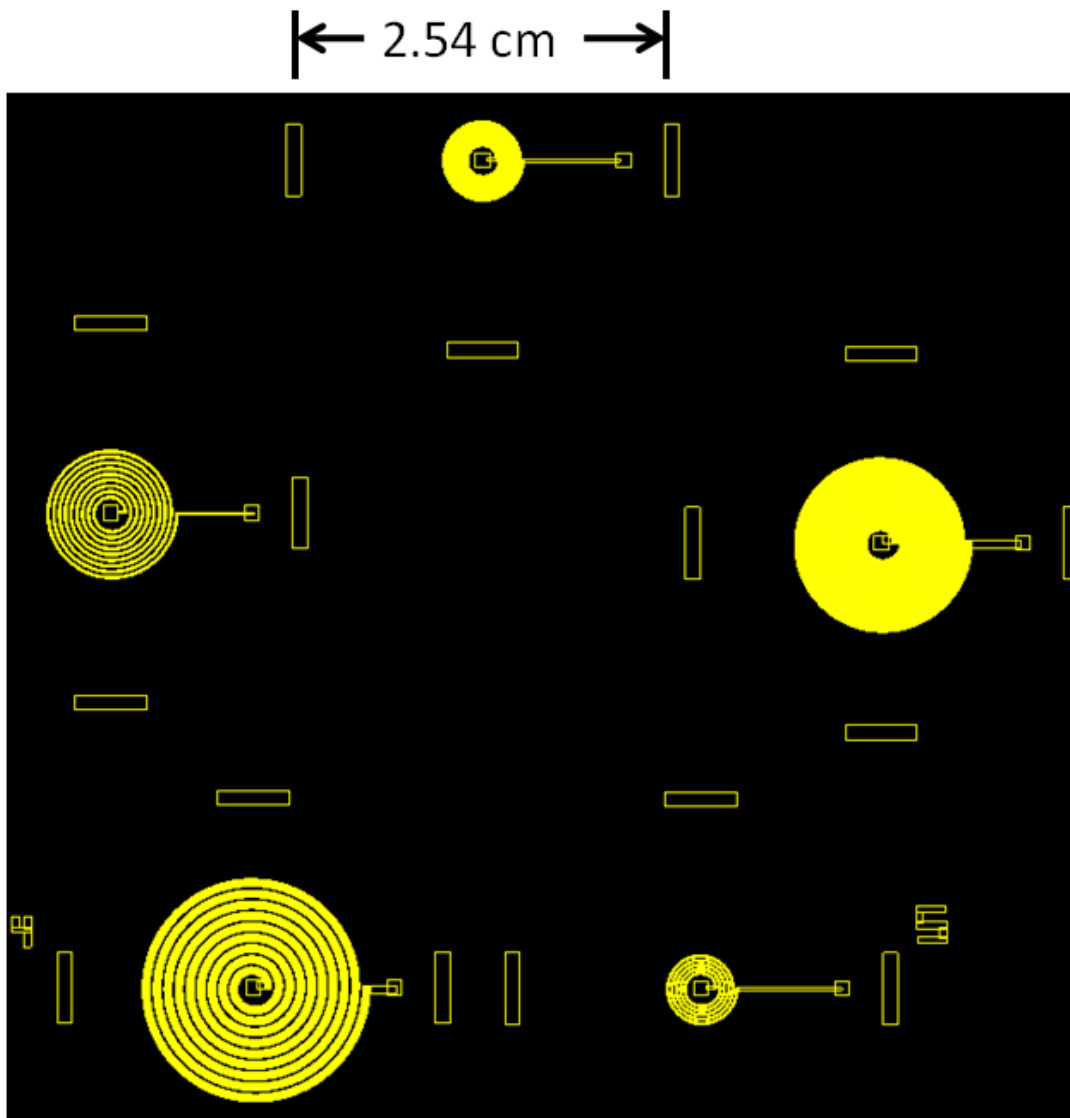


Figure 3.2 Glass mask used to fabricate MSCAT sensors. The rectangles are alignment marks and are not part of the final spiral deposited on the quartz. The spiral geometries are [N, S (μm), W (μm)] clockwise from the top: [8, 50, 150], [8, 250, 50, 515], [4, 150, 150], [8, 250, 515], and [8, 250, 150]

3.3 Selection of AT-cut Quartz Wafers

Initially, MSCAT sensor elements were fabricated using 1” diameter 5MHz AT-cut quartz wafers obtained from Sawyer Technical Materials, LLC (Eastlake, OH). These wafers were intended for use in QCM fabrication. Although it was possible to excite up to the 9th harmonic in these devices it was found that they were not capable of high-order harmonic operation. It was found that these quartz wafers had a convex surface as they were originally intended for use in QCM fabrication and the convex surface aids in energy trapping of the acoustic wave. Additional 5 MHz quartz wafers were purchased from Sawyer Technical Materials, LLC that were plano-plano (both sides parallel to each other). Although MSCATs fabricated on these wafers were able to operate at higher frequencies, up to the 11th harmonic, even higher operating frequencies was desired. In order to achieve even higher operating frequencies, AT-cut quartz wafers were obtained from Lap-Tech (Bowmanville, Ontario, Canada) with an optical polish on both sides and the surfaces parallel to within 4 light bands (~ 1 μ m). Devices fabricated on these wafers were able to operate up to the 99th harmonic, significantly higher than the Sawyer crystals. Based on these results the Laptech crystals were chosen for all further MSCAT designs.

In order to gain an understanding of the differences in the crystals that could explain the significant differences in performance; parallelism and surface roughness tests were performed on samples of each type of crystal using a Laser Fizeau interferometer (Zygo, Middlefield, CT). The surface roughness measurements were performed on a 100 μ m x 100 μ m square in the center of each crystal while the parallelism measurements were performed across the entire crystal.

As can be seen from Figure 3.3-Figure 3.5 there is only a small difference in surface roughness between the Laptech and plano-plano Sawyer crystals. The Laptech and plano-plano Sawyer crystals both had surface roughness's of approximately 3 nm. The plano-convex Sawyer crystals were slightly rougher with surface roughness up to 8 nm, most likely due to the fact that they were not optically polished. Given that the plano-plano Sawyer crystals and the Laptech crystals both had roughly the same surface roughness it was concluded that that differences in surface roughness does not explain the differences in performance between the Laptech and Sawyer crystals.

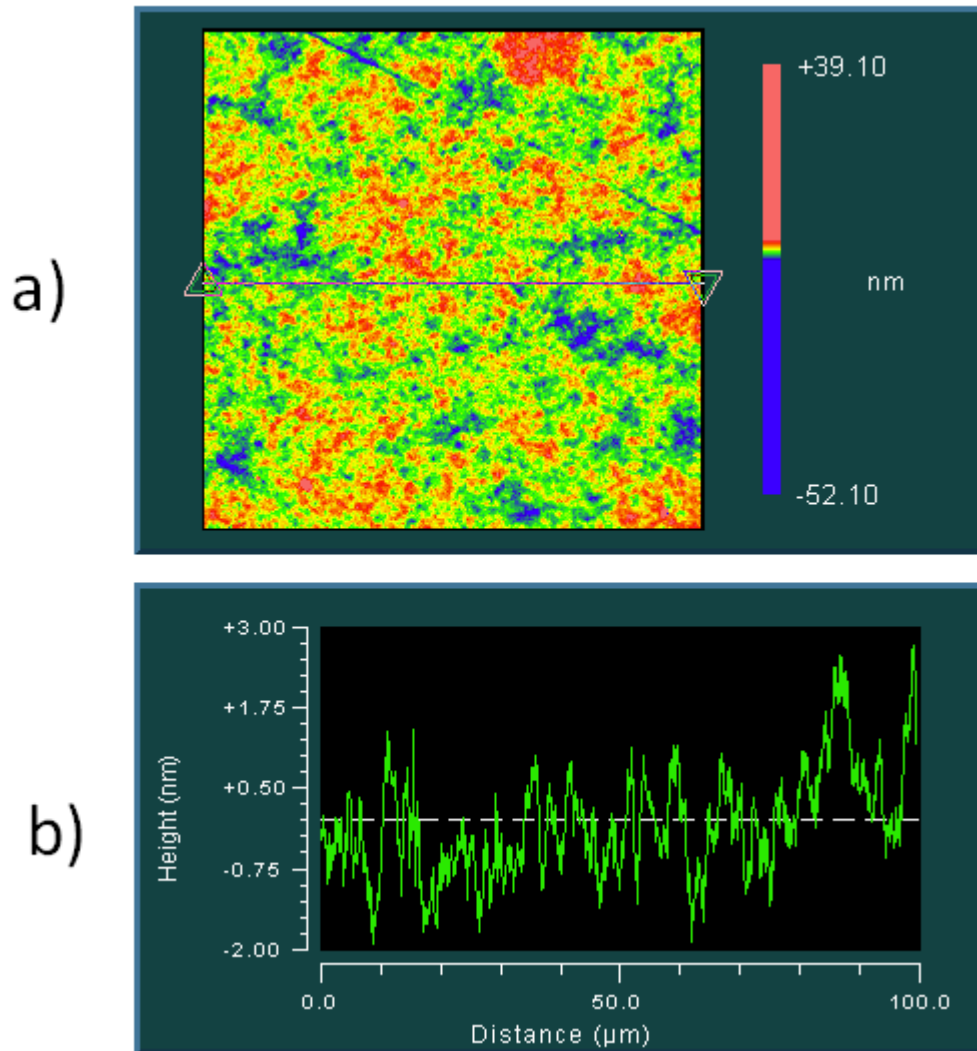


Figure 3.3 Interferometric surface roughness for plano-plano Laptech crystals a) crystal surface and b) plot of height over line seen in (a).

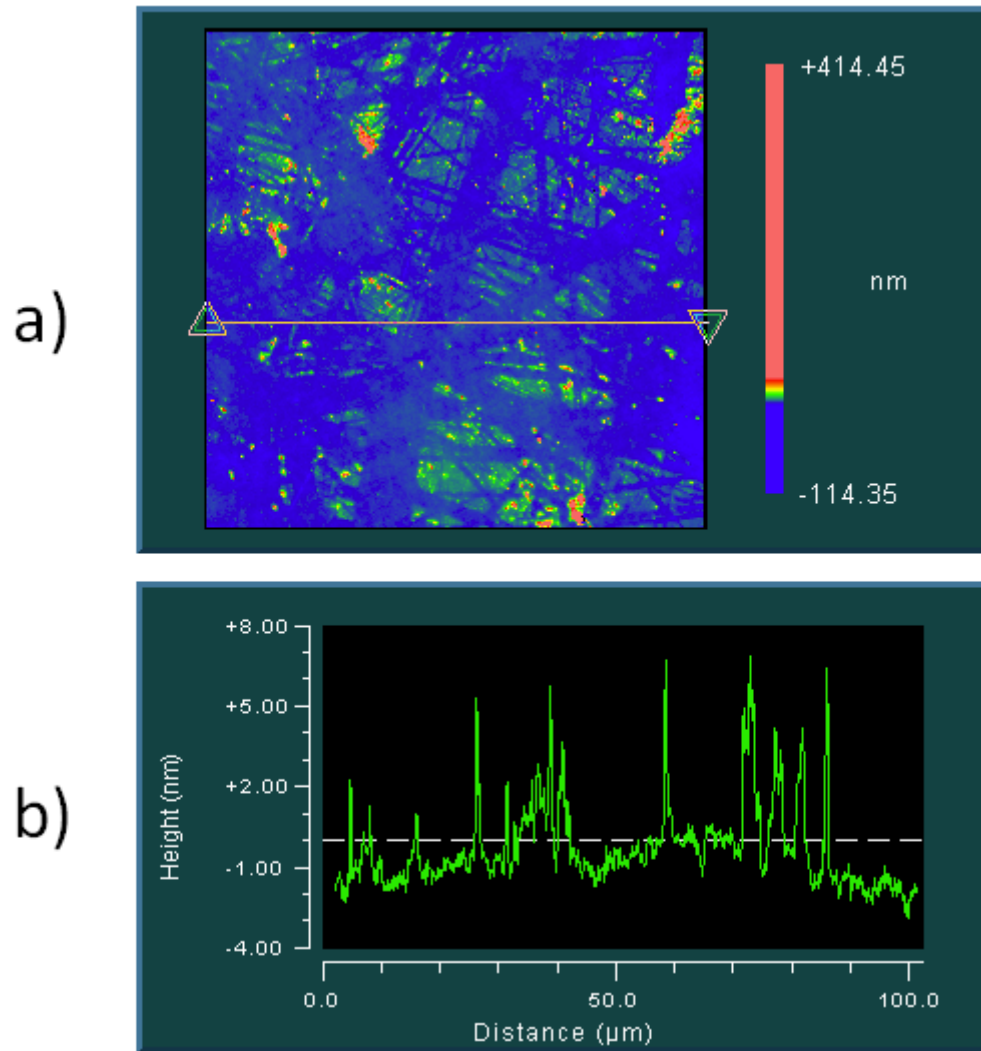


Figure 3.4 Interferometric surface roughness for plano-convex Sawyer crystals a) crystal surface and b) plot of height over line seen in (a).

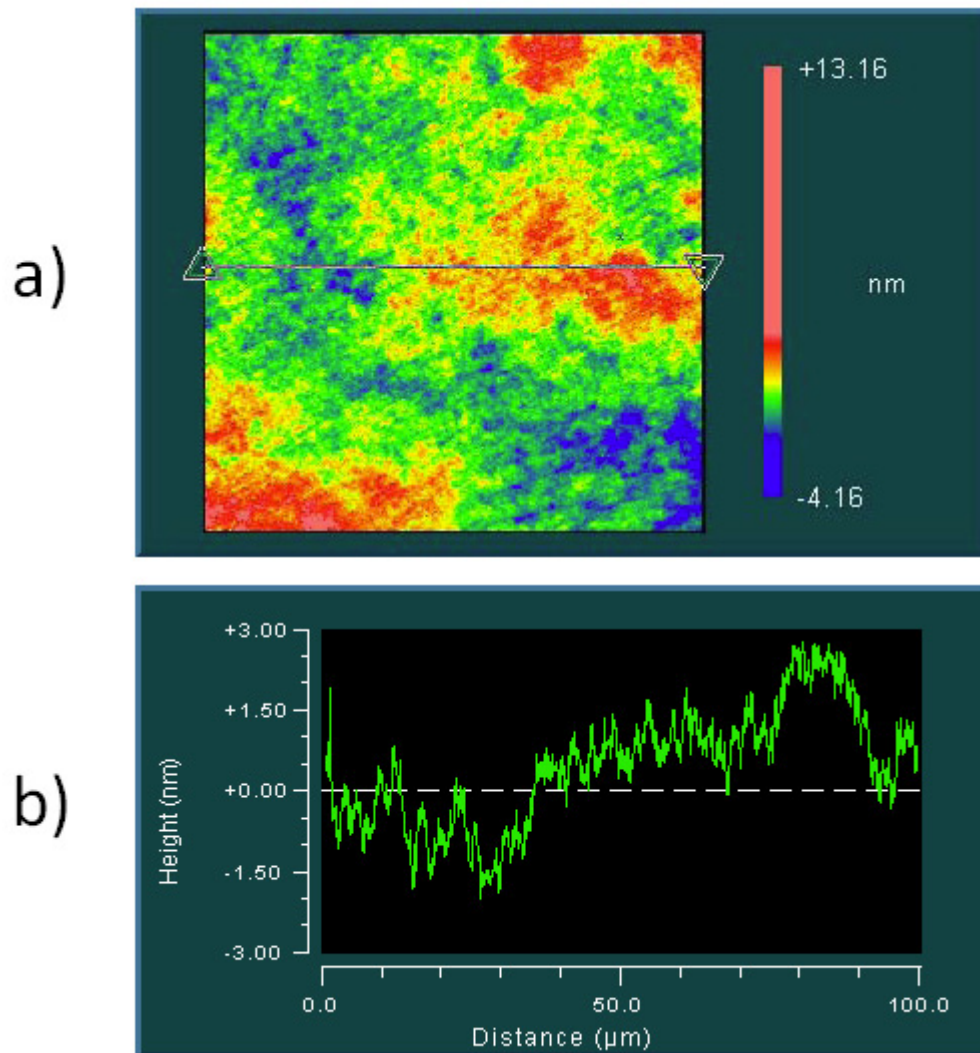


Figure 3.5 Interferometric surface roughness for plano-plano Sawyer crystals a) crystal surface and b) plot of height over line seen in (a).

As will be described later, for high frequency applications it is desirable for the crystal faces to be as parallel as possible. As can be seen in Figure 3.6-Figure 3.8 there are significant differences in the parallelism between the three crystals. Figure 3.6b-Figure 3.8b show the change in distance between the two faces of the crystal. If the faces were perfectly parallel, the height distance would be 0. As can be seen in Figure 3.6a the Laptech crystals were highly parallel throughout the most of the crystal with surface parallelism within 10 nm through the middle of the crystal. The edges are slightly less parallel but still within 30 nm. The plano-plano Sawyer crystals were significantly less parallel with surface parallelism ranging approximately 200 nm across the crystal. As can be seen in Figure 3.8a, the surface of the plano-plano Sawyer crystal was also much less uniform. Not surprisingly, the surface of the plano-convex Sawyer crystal was not parallel. Based on these results it was concluded that the parallelism of the crystal face was critical in order to operate the MSCAT at elevated harmonics. This is because the wavelength of the standing wave that is setup between the faces of the crystal decreases with increasing frequency. At 5 MHz the acoustic wavelength is approximately 660 μm , however at 500 MHz the wavelength decreases to approximately 6.6 μm . If the crystal faces are not parallel or if the surfaces are not flat destructive interference will not allow a standing wave to form at higher harmonics.

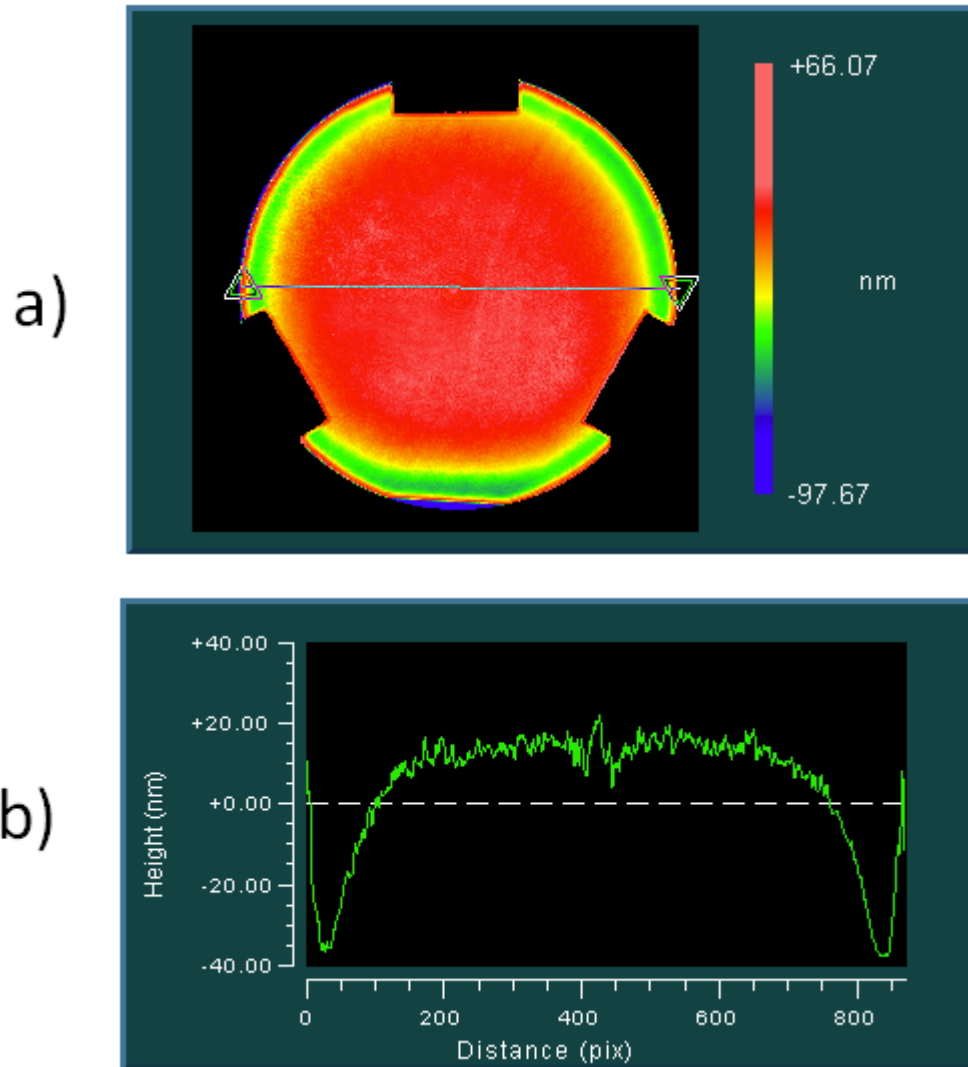


Figure 3.6 Interferometric surface parallelism for plano-plano Laptech crystals a) crystal surface and b) plot of height over line seen in (a).

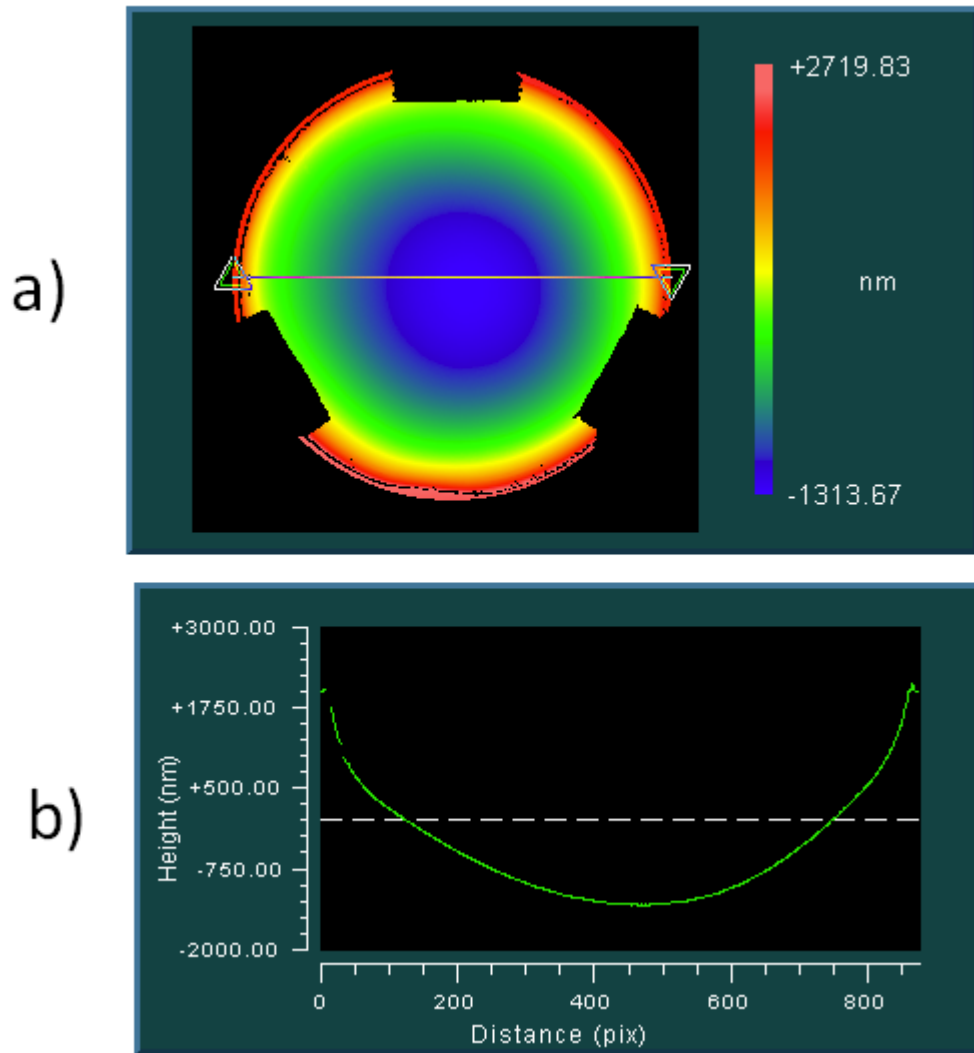


Figure 3.7 Interferometric surface parallelism for plano-convex Sawyer crystals a) crystal surface and b) plot of height over line seen in (a).

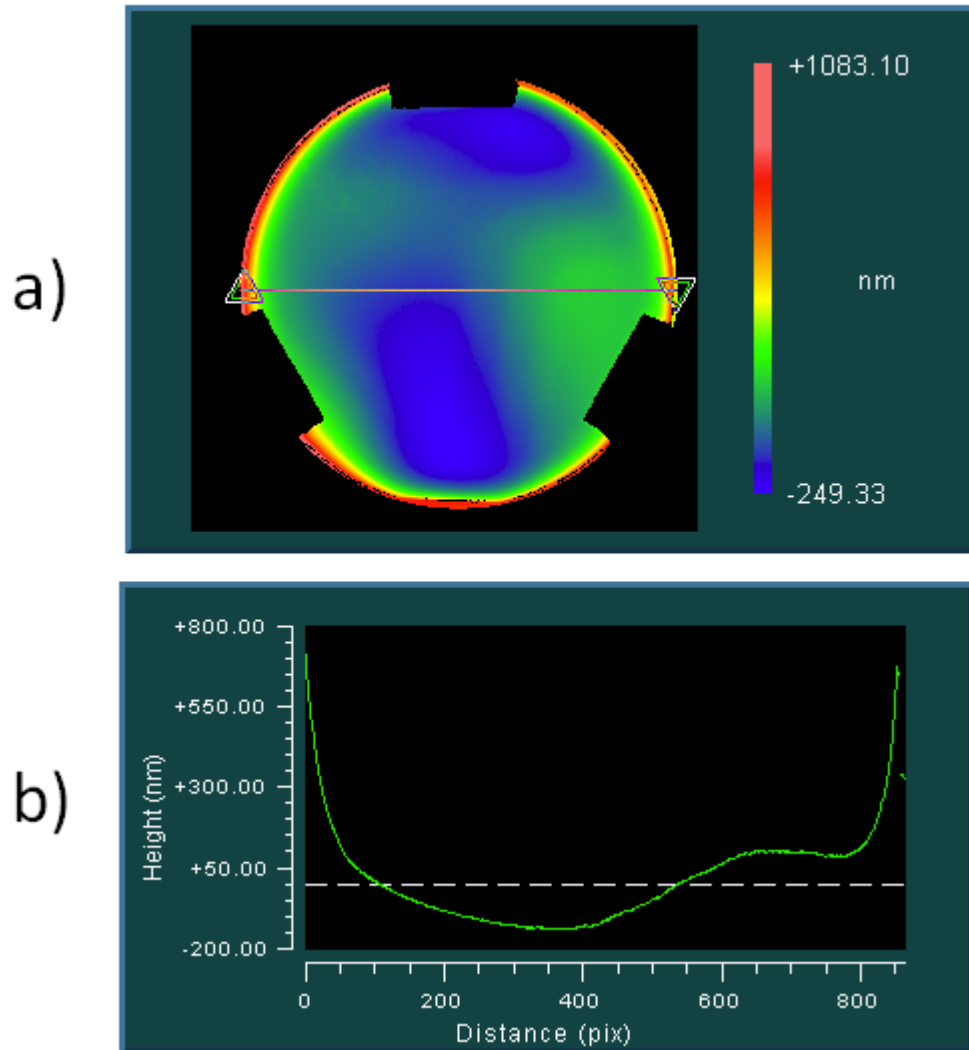


Figure 3.8 Interferometric surface parallelism for plano-plano Sawyer crystals a) crystal surface and b) plot of height over line seen in (a).

3.4 Resonant Frequency Measurement Setup

Several different measurement setups that allowed the measurement of the resonant frequency of MSCAT devices were explored. In initial tests a measurement setup based on a lock-in amplifier similar to the system that was developed for the EMPAS was explored. Subsequently tests were performed using a network analyzer.

3.4.1 Lock-in amplifier measurement system

As was described in Chapter 2, Ballantyne [68] utilized a signal generator, lock-in amplifier, and handmade electronics (AM diode detector, preamplifier, and parallel RLC circuit) to monitor the resonant frequency of the EMPAS. As will be discussed later in this chapter, it is much harder to excite and detect resonances in the EMPAS than it is for the MSCAT. For the EMPAS, it is necessary to monitor very weak resonances; therefore a highly sensitive electronics system must be used. A similar setup was built and evaluated for the MSCAT (Figure 3.9).

The lock-in system is built around a highly sensitive lock-in amplifier. Although the lock-in amplifier is highly sensitive, it is only capable of measuring low frequency signals (kHz range) while it is desirable to monitor the resonant frequency of the MSCAT in the MHz range. In order to overcome this limitation a signal generator (controlled by LabVIEW) produces a carrier signal near the expected resonant frequency of the device. This signal is modulated with a low frequency signal that can be read by the lock-in amplifier. The frequency of the signal from the signal generator was swept over the expected resonant frequency range of the device being tested. As the frequency of the signal generator is swept through the expected

resonant frequency of the MSCAT, the amplitude of the signal increases when the sensor resonates. This amplitude change is extracted from the signal using an amplitude modulation (AM) diode detector circuit. The AM detector circuit demodulates the signal and filters out the high frequency components. The lock-in amplifier monitors the amplitude changes in the low frequency signal. If the resonant frequency of the device is within the selected frequency range, the amplitude will be highest at that frequency. The voltage output of the lock-in amplifier is monitored by a data acquisitions card in the computer. The computer then displays or saves the resonance envelope of the device. This system is necessary for EMPAS devices because the resonances are very weak and difficult to detect and it is necessary to use a device (lock-in amplifier) capable of detecting very small signal changes. A typical resonant signal for an MSCAT can be seen in Figure 3.10.

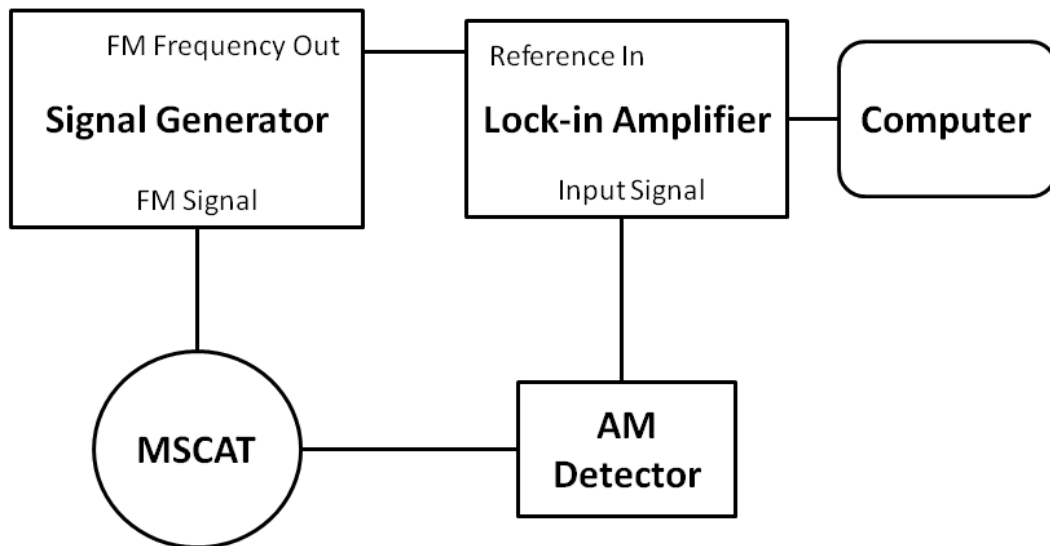


Figure 3.9 Block diagram of lock-in amplifier based signal designed for the MSCAT.

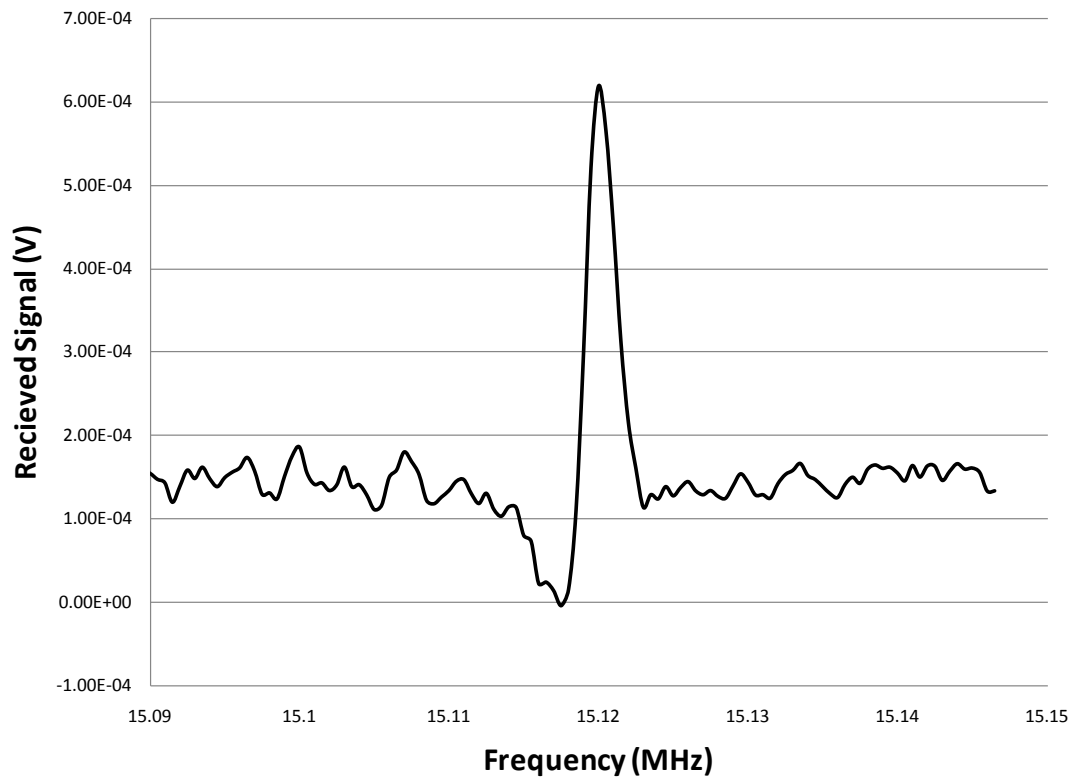


Figure 3.10 Typical MSCAT resonant signal obtained using the lock-in amplifier based measurement system.

Besides the complexity, large size, and cost of this system, resonance sweeps take a significant amount of time due to the necessity of letting the output of the signal generator settle after each change in signal frequency. As described earlier, a single sweep to monitor the harmonics of a device from 6 MHz to 600 MHz takes approximately 20 hours. Due to these limitations, an alternative measurement approach was utilized.

3.4.2 Network Analyzer based measurement system.

Based on the limitations of the lock-in amplifier system a network analyzer (HP 5617A) was used for subsequent tests. A network analyzer has the advantage of being capable of operating over a wide frequency range and having quick data acquisition times. It is also possible to miniaturize network analyzers for BAW sensor applications [70, 71]. For a one port device, a network analyzer sends a voltage at the frequency of interest into the device and then measures the reflected signal [69]. From this, the reflection coefficient, Γ , can be calculated. From Γ one can calculate the impedance (and therefore admittance) of the device using the following relationship:

$$Z_L = Z_o \frac{1 + \Gamma}{1 - \Gamma} \quad (3.1)$$

where

Z_L = the impedance of the device being tested

and

Z_o = the input impedance of the network analyzer (50 Ω)

In order to determine the resonant frequency of the MSCAT being tested, the peak of the admittance was monitored. The particular network analyzer used has a built in feature that can automatically convert Γ into the admittance of the device. Figure 3.11 shows a typical MSCAT admittance spectrum around resonance as measured by the network analyzer. It should be noted that, like the LFE, at the fundamental frequency there is a second mode that is excited approximately 15 kHz higher in frequency than the pure TSM. This second mode is not present, however at higher frequencies.

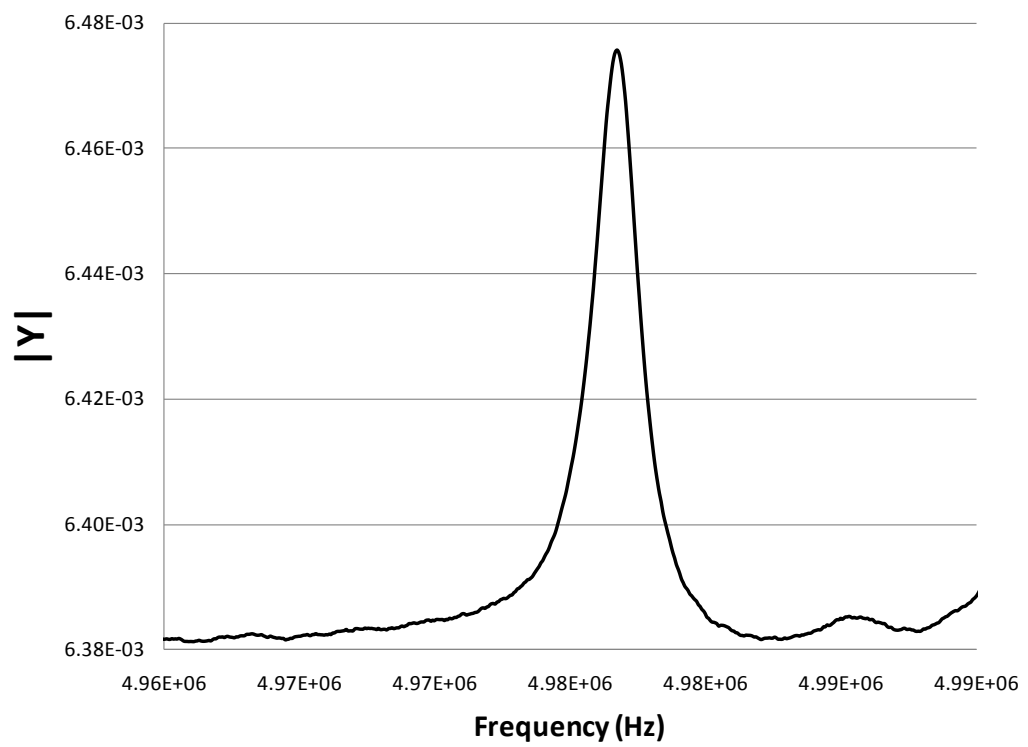


Figure 3.11 Typical MSCAT impedance spectrum around resonance as measured by a network analyzer.

The particular network analyzer used, however, does have one limitation. It is only able to save 801 data points. Therefore resolution of the resonant frequency of the device can be lost unless the frequency span is small enough. In order to overcome this limitation the network analyzer was setup to only monitor the frequency region of the very peak of the admittance in order to get the maximum possible resolution. The width of the frequency region that was monitored depended on the bandwidth of the resonant frequency being monitored which increases with operating frequency. For measurements of the fundamental frequency (5 MHz), 801 Hz was typically used. For the 99th harmonic, 100 kHz was typically used. In order to minimize the effects of noise on the signal, a quadratic function was fitted to the sensor response. The resonant frequency of the MSCAT was taken to be the maximum value of this quadratic function (value of the frequency when the derivative was set equal to zero). A MATLAB program was written to perform the calculations for each data file. Figure 3.12 shows a typical MSCAT response and corresponding fitted line. It was found that this technique decreased the measured resonant frequency noise by approximately a factor of 5 compared to simply taking the frequency at the maximum value of the raw admittance data as the resonant frequency.

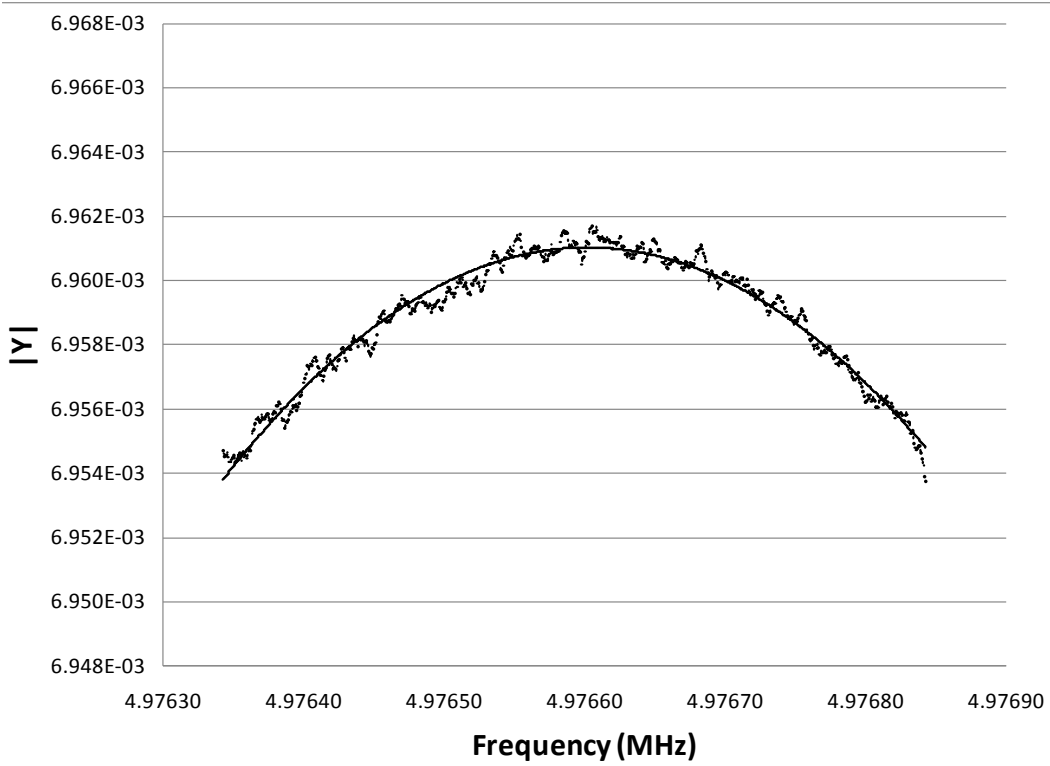


Figure 3.12 Typical signal used to calculate the resonant frequency of the MSCAT.
The dots are the raw data and the solid line is the fitted line.

Recently researchers at the University of Magdeburg have developed a portable RF impedance spectrum analyzer [70, 71]. This impedance analyzer is small and has been optimized to track the resonant frequency of BAW sensors, particularly the QCM and LFE. Preliminary tests have shown that this impedance analyzer can also be used with the MSCAT; however the analyzer is not commercially available and therefore was not used for the work described in this thesis. Future work could also include developing a miniaturized oscillator circuit for use with the MSCAT.

3.5 Experimental Examination of the MSCAT Spiral Coil Design.

Based on the work described in Appendix B to calculate the near-field electric fields radiated from a spiral coil antenna it is clear that the antenna design plays a role in the form of the radiated field. The expressions for the field are too complex, however, to be used to fully understand the effects of the antenna parameters on the sensors performance. Therefore over 40 antenna geometries were designed, fabricated, and experimentally tested for use in the MSCAT. As shown in Figure 3.13, there are three geometric parameters that may be varied with a spiral coil antenna: the numbers of turns (N), spacing widths (S), and line widths (W). In this work the notation $[N, S (\mu\text{m}), W (\mu\text{m})]$ will be used to describe the geometry of the various MSCAT spirals. A fourth parameter, the thickness of the spiral may also be changed but experimental measurements have shown that varying the thickness of the antenna between 1000 and 10,000 Å has no significant effect on the sensor's performance although the thinner antennas (1000Å), however, tended to scratch easily and therefore 2000 Å was chosen as the thickness for all subsequent MSCATs.

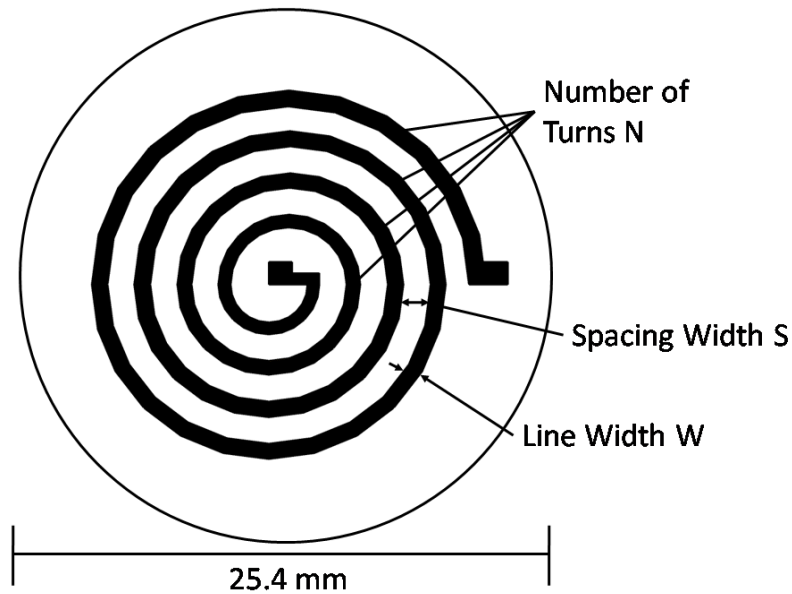


Figure 3.13 Geometry of the MSCAT sensor. The spiral coil is on the reference surface and the sensing surface is void of metal

In order to gain an understanding of the overall effect of each spiral parameter on the MSCAT's performance, MSCAT sensors with spiral coil antenna designs that varied in N , W , and S were initially designed. The highest possible operating frequency of each device was examined. The highest operating frequency was defined as the frequency where the resonance peak was at least 5 times larger than the signal noise. Fifteen spiral antenna designs were fabricated on identical 1" AT-cut quartz wafers obtained from Laptech (5 MHz fundamental frequency) with N values ranging from 16 to 64, S values ranging from 50 μm to 400 μm , and W values ranging from 50 μm to 400 μm (see Table 3.1). The N and S values were chosen as they are the values that are typically used for the hand wound spiral coils used for the MARS and EMPAS [72, 73]. Since the MARS and EMPAS use hand wound spiral coils, the W value is set by the wire being used (50 - 100 μm). The MSCAT uses a photolithographical process and therefore the value of W can be changed. In the

initial study, the values of W were selected for the N and S values chosen (Table 3.1) such that the spiral did not cover more than 50% of the crystal, the largest area covered by typical EMPAS spiral coil designs. In order to aid in comparison, the percentage of the total crystal area (5 cm^2) that was covered by each spiral coil was also calculated. Initially it was believed that spirals with the largest number of turns would provide the best results as Ballantyne [68] hypothesized that the total electric field radiated from a spiral would be a superposition of each field produced from a single turn of the spiral. This, however, proved not to be the case.

Table 3.1 Initial spiral coil parameters to explore the effects of N, W, and S.

Varying **N** with W and S constant

N	S (μm)	W (μm)	Area (%)	Max Harm.
16	50	50	4.519809	7
28	50	50	9.430219	9
40	50	50	16.12623	9
52	50	50	24.60785	11
64	50	50	34.87507	7

Varying **S** with N and W constant

N	S (μm)	W (μm)	Area (%)	Max Harm.
16	10	50	2.529853	7
16	108	50	8.423706	5
16	206	50	17.75926	7
16	304	50	30.5365	7
16	402	50	46.75544	7

Varying **W** with N and S constant

N	S (μm)	W (μm)	Area (%)	Max Harm.
16	50	10	2.529853	7
16	50	108	8.423706	11
16	50	206	17.75926	13
16	50	304	30.5365	63
16	50	402	46.75544	93

In order to gain insight on the overall importance of each of the three spiral coil parameters when the MSCAT was operated in a liquid environment, the fifteen sensors were tested with 1 mL of de-ionized water on their surface to determine their maximum operating frequency. It was found in the initial experiments that the most important spiral coil parameter for achieving the highest possible operating frequency among the devices tested is the width of the spiral, W . In fact, varying the number of turns, N , or the space between the coils, S , had almost no effect on the maximum operating frequency of the device. The device that operated at the highest frequency in these tests was a [16, 50, 402]. This device was able to operate at the 93rd harmonic (approximately 465 MHz). Since the performance of the MSCAT seemed to increase with large W values and therefore lower coil resistance, MSCATs with very large W values ([1, 250, 3750] and [2, 250, 2750]) were designed and fabricated (Figure 3.14). It was found that neither of these spirals could operate above the fundamental frequency and both exhibited poor (noisy) resonances leading to the conclusion that the width of the spirals was not the only factor in determining the optimum spiral configuration.

Based on these results 18 additional spirals were designed and tested (Table 3.2). It was found that a [8, 250, 515] spiral configuration was superior to all other designs examined (capable of operating at ~500 MHz) and it was selected for the tests described in chapters 4-6. As will be described in the remainder of this section, more work is required in order to fully optimize the MSCAT's spiral coil geometry. It should be noted that the LiTaO₃ LFE sensor described in Appendix A was capable of operating at the 269th harmonic.

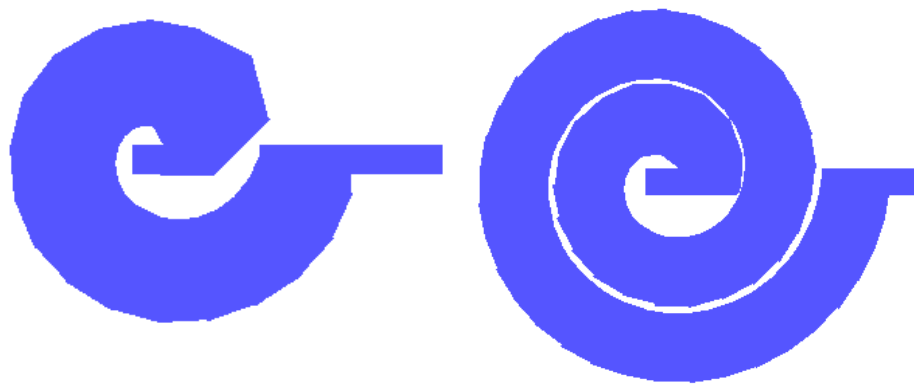


Figure 3.14 [1, 250, 3750] (left) and [2, 250, 2750] (right) MSCATs.

Table 3.2 Additional MSCAT spiral coil parameters.

N	S (μm)	W (μm)	Area (%)	Max Har.
4	50	333	5.27	3
4	250	333	9.50	5
8	50	150	4.86	7
4	150	150	3.88	7
8	150	150	8.49	7
8	250	150	13.12	23
8	50	515	22.96	25
12	150	150	14.89	25
4	150	515	11.60	25
12	150	515	57.68	27
12	50	333	22.16	27
9	150	350	22.32	30
8	150	333	17.73	35
9	200	400	30.38	44
14	250	333	58.88	59
10	500	500	89.28	61
10	250	515	54.96	63
12	250	333	45.63	69
10	250	333	34.07	87
8	250	515	38.55	99

No clear pattern in the relationship between the maximum harmonic and the spiral parameters N, S, W can be seen in Table 3.2. It can, however, be noted that the spiral coil designs that operated at the highest frequencies generally had larger W and covered a larger surface area of the crystal while many of the devices that were not able to operate at high frequencies had lower N and S values. As can be seen in Figure 3.15 there is no clear relationship between the percentage of the crystal covered by the spiral coil and the maximum harmonic that can be excited a general statement can be made that in order to achieve higher operating frequency the spiral should cover 30%-60% of the crystal. This is most likely due to energy trapping as the electrodes on the QCM are designed such that the electrodes are thicker in the center thereby confining displacement to the center of the crystal and minimizing damping effects when the crystal clamped around its outer edges in a holder [74]. The resistance of each coil was also calculated based on the overall length of each spiral. As can be seen in Figure 3.16 all of the MSCAT designs that were capable of achieving higher operating frequencies had resistances ranging between 40 Ω and 150 Ω . This is most likely due to impedance matching, if the impedance of the coil is very small or large it will effectively act as a short circuit or an open circuit and therefore only weakly radiate electric fields.

In order to determine if there was a clear relationship between two of the spiral coil parameters (N, S, W) and the maximum operating frequency of the MSCAT, 3D plots were created for every combination of two spiral coil parameters versus the maximum harmonic that could be excited. These results can be seen in

Figure 3.17-Figure 3.19. Again, no concrete conclusions can be drawn from these figures but some overall comments can be made. As can be seen in Figure 3.17 when comparing N and S all of the devices that operated at elevated frequencies had N values between 8 and 14 and the majority had S values between 250 μm and 300 μm . From Figure 3.18 it can be seen that when comparing N and W that all of the devices that operated at elevated frequencies had N values less than 16 and W values between 300 μm and 515 μm . From Figure 3.19 it can be seen that when comparing S and W all of the devices that operated at elevated harmonics had W values above 333 μm and spacing values between 200 μm and 300 μm . It is clear from these results that no single parameter independently affects the maximum harmonic that can be excited in the MSCAT and more work is needed to fully develop a model for the MSCAT. Although these results do not allow a concrete conclusion to be drawn, it can generally be said that for high frequency operation the MSCAT spiral coil design should have N values between 8 and 14, S values between 300 μm and 515 μm , W values above 300 μm , cover 30-60% of the crystal surface, and have a spiral resistance of 40 – 150 Ω .

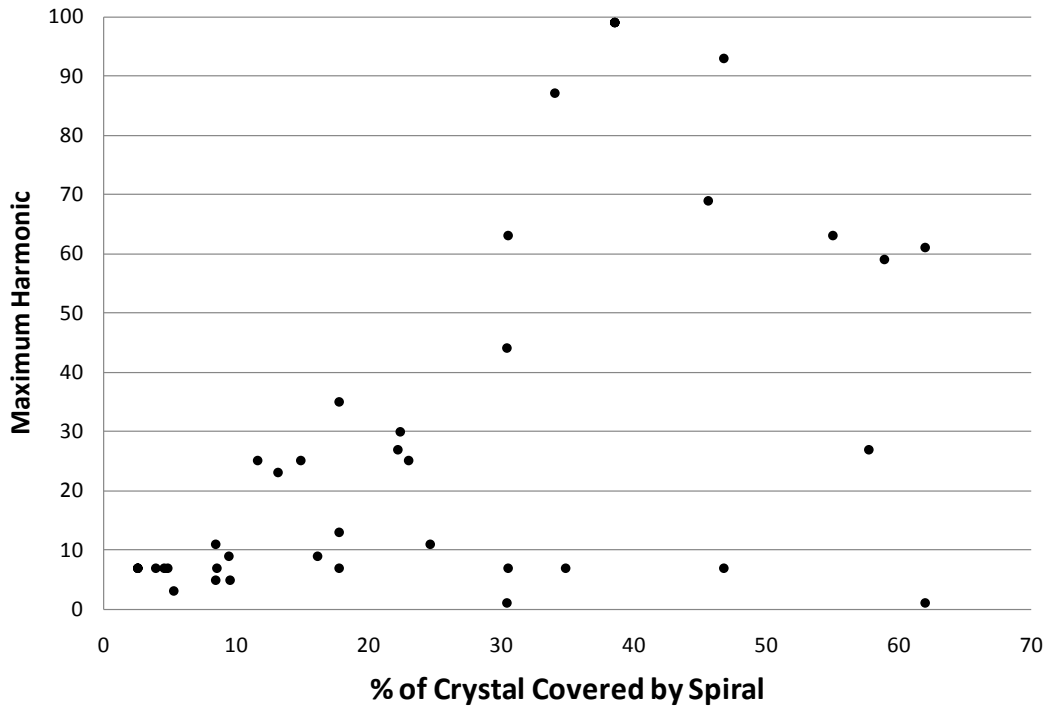


Figure 3.15 Graph showing percentage of crystal covered by spiral coil vs. maximum harmonic that could be excited.

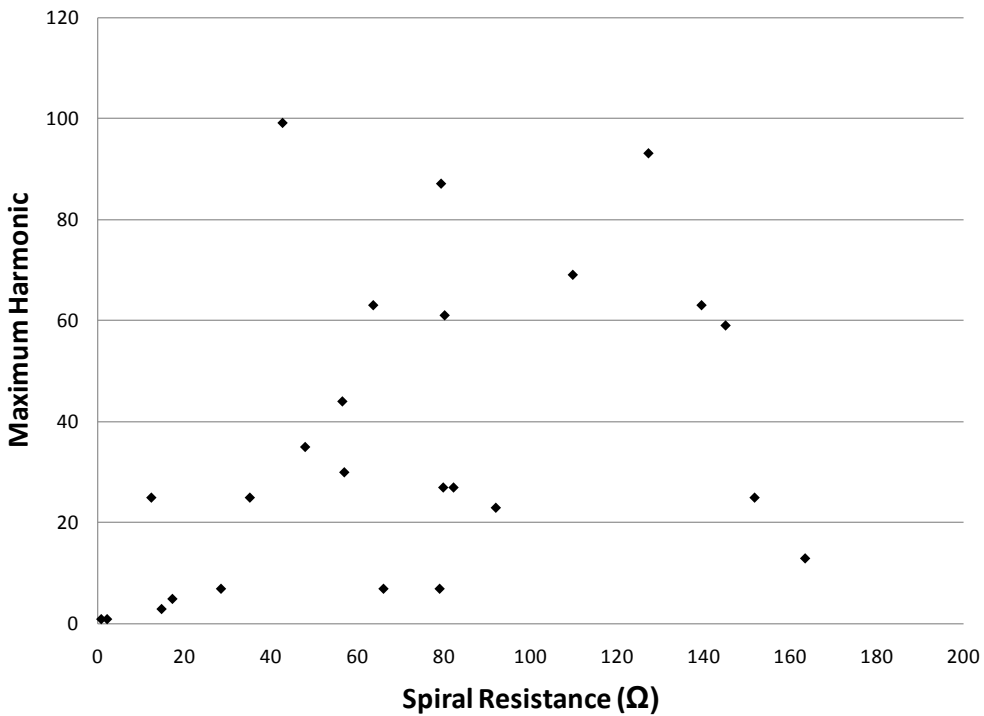


Figure 3.16 Graph showing the resistance of the spiral coils vs. maximum harmonic that could be excited.

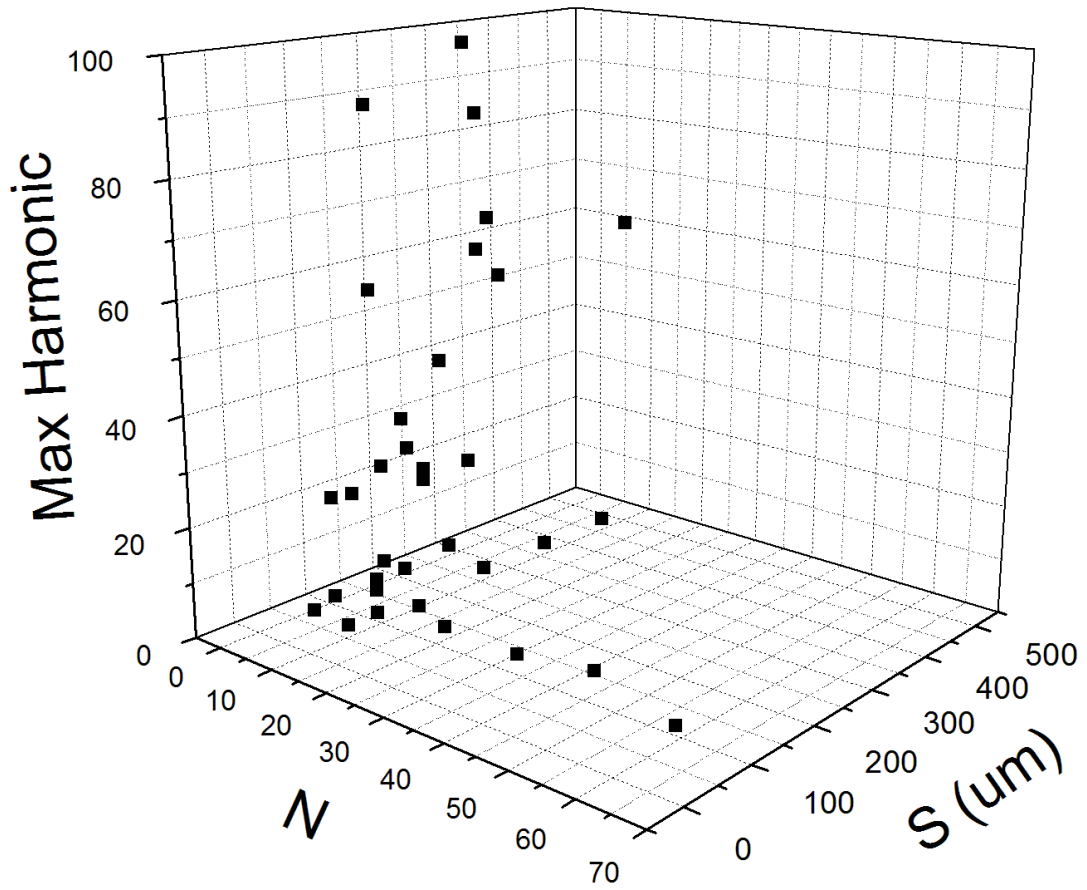


Figure 3.17 3D plot showing the relationship between N, S, and the maximum harmonic that can be excited.

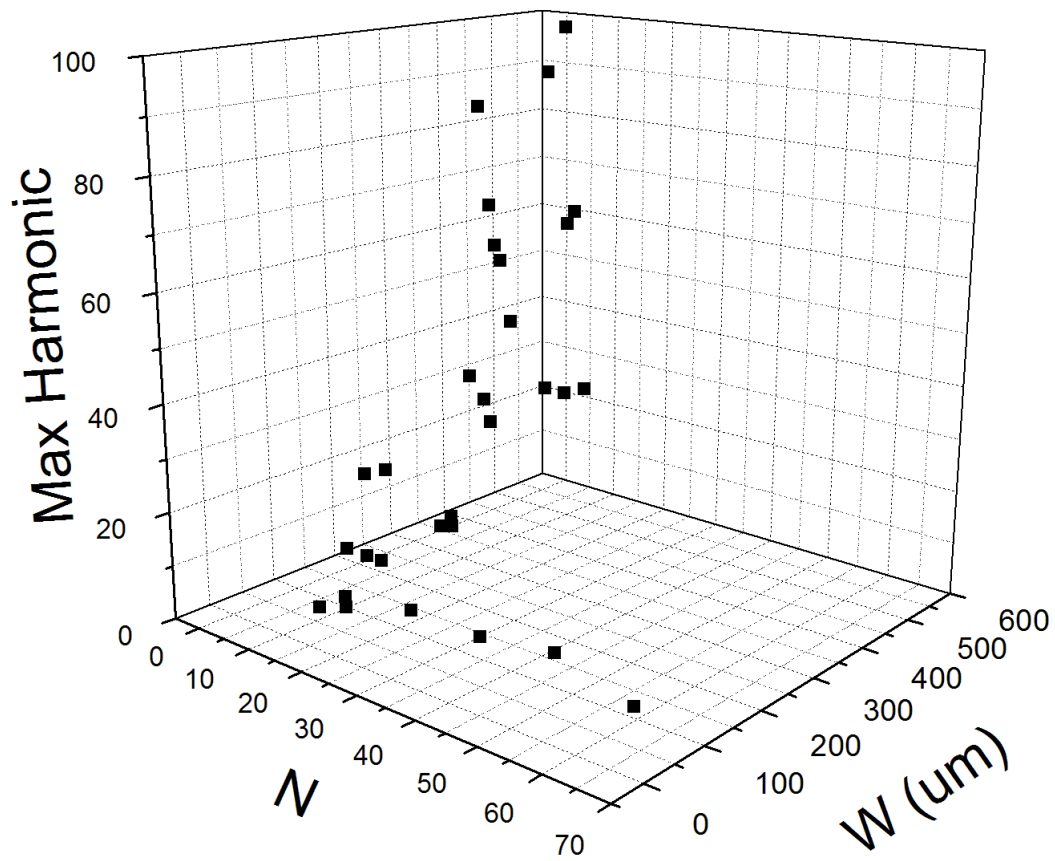
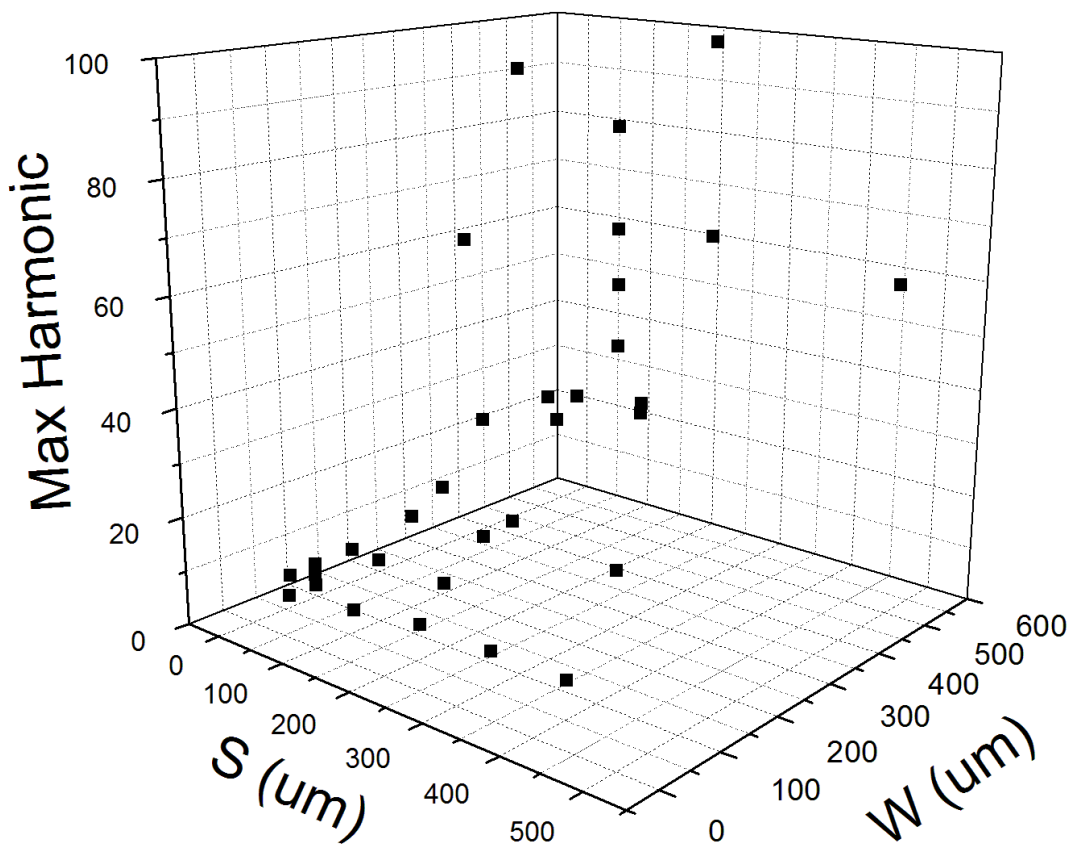


Figure 3.18 3D plot showing the relationship between N, W, and the maximum harmonic that can be excited.



3.5.1 Alternative spiral configurations

Although circular spiral loop antennas are typically used for wireless applications, three other configurations were also examined, namely, a square spiral (Figure 3.20a), a triangular spiral (Figure 3.20b), and a dual arm circular spiral antenna (Figure 3.20c). The square and triangular designs were tested to determine if they were able to excite higher harmonics than the circular spiral coil. The dual arm spiral coil antenna is an alternative configuration for frequency independent antennas that is occasionally used for some applications [75]. The dual arm spiral coil is different than the other spiral coil designs that were tested because current on adjacent turns of the spiral will travel in different directions. All three spirals were [8, 250, 515]. These were tested to determine if the circular spiral was the best shape for the MSCAT. It was found that the square [8, 250, 515] spiral was able to operate

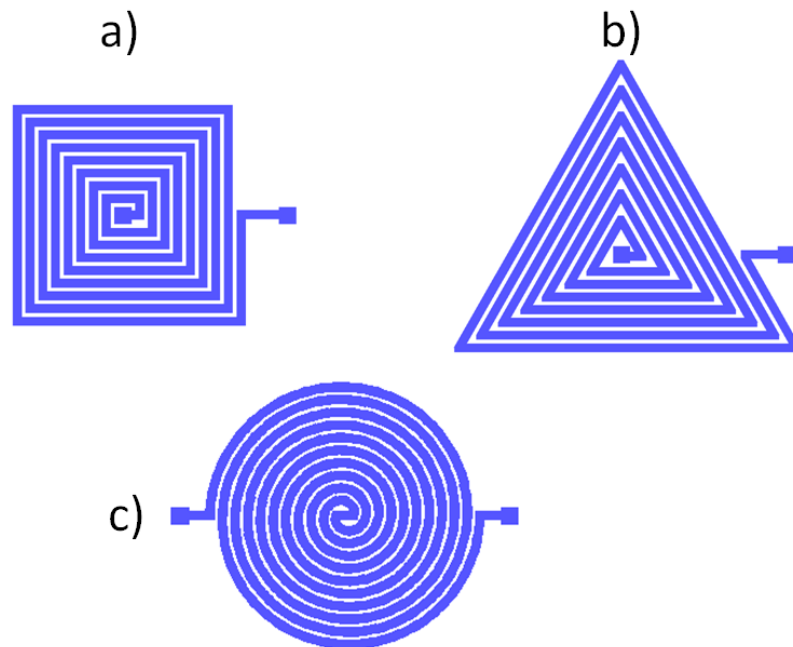


Figure 3.20 Alternative spiral configurations.

up to the 89th harmonic while the triangular [8, 250, 515] MSCAT was able to operate up to the 95th harmonic. The dual arm [8, 250, 515] MSCAT was only able to operate up to the 9th harmonic with poor Q. Based on these results the circular spiral coil described earlier was chosen for the tests described in Chapters 5 & 6.

3.6 Finite Element Model of the Electromagnetic Fields Radiated From a MSCAT

Although equations for the near and far field electric fields radiated by the MSCAT spiral coil antenna were derived (see Appendix B), the form of the equations are too complicated to be of significant use. In order to gain an understanding of how the fields generated by the spiral coil excite the acoustic waves in the MSCAT finite element analysis (FEA) was used to obtain the electromagnetic fields radiated by the spiral coil antenna deposited on AT-cut quartz. The theoretical results were compared to experimental measurements for specific spiral coil geometries.

Two phenomena were explored utilizing the Comsol Multiphysics' finite element analysis (FEA) software package [76]. The first phenomenon that was analyzed involved the behavior of MSCAT sensors under liquid loads. This aspect of the work was motivated by the fact that when operated in air, MSCAT sensors exhibit very weak resonances while a much stronger resonance is observed when a liquid is placed on the sensor surface [77]. The second phenomenon that was explored involved the specific spiral coil antenna configuration. This part of the work was motivated by the fact that the highest harmonic that can be excited in MSCAT sensors

appeared to be strongly dependent on the antenna configuration as described in section 3.5.

3.6.1 MSCAT Behavior Under Liquid Loads

The TSM may be excited in AT-cut quartz using electric fields in the thickness direction of the plate (TFE). In the case of TFE, the piezoelectric coupling coefficient k_{TE} is 8.8% [78]. The TSM may also be excited using lateral field excitation (LFE). In this case, the degree of piezoelectric coupling (k_{LE}) to the TSM as well as the quasi-shear and longitudinal modes are dependent on the orientation of the electric field relative to the x-axis of the crystal (Figure 3.21). If the applied electric fields are not oriented properly (90° relative to the x-axis), other modes may be excited leading to spurious modes.

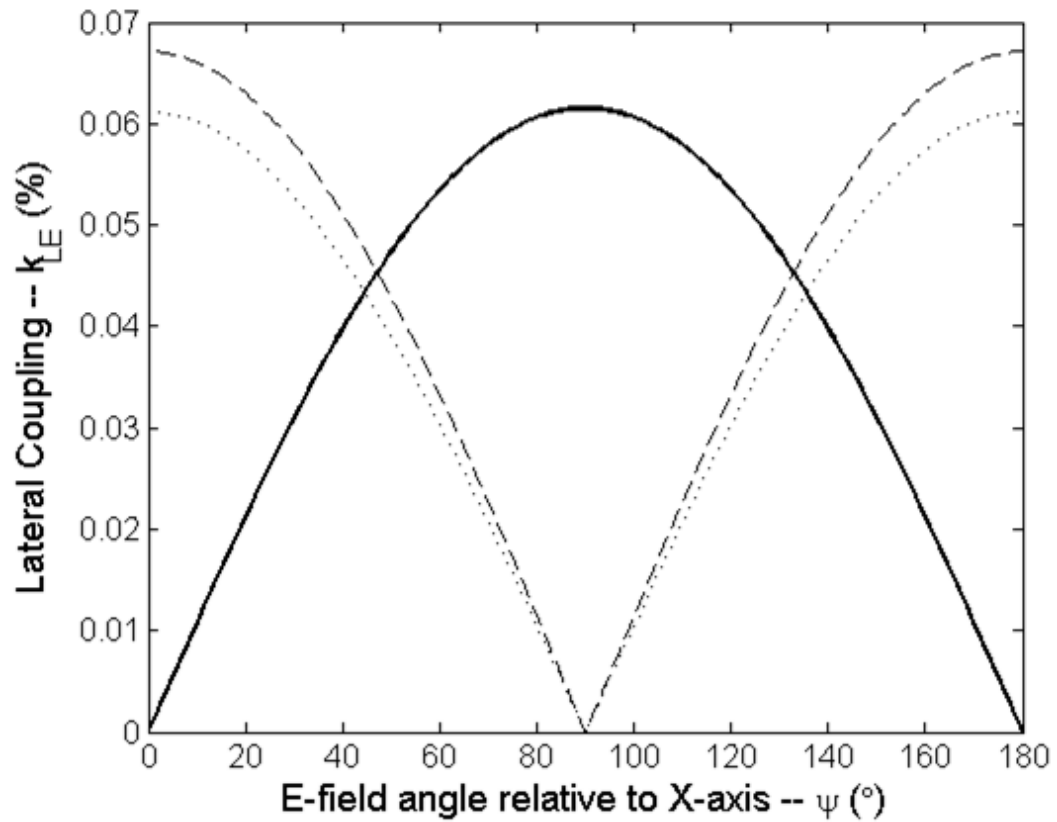


Figure 3.21 Lateral field coupling coefficients k_{LE} for the TSM (solid line), fast quasi-shear mode (small dotted line), and quasi-longitudinal mode (large dotted line) in AT-cut quartz versus electric field angle ψ with respect to the X axis.

Although the TSM may be excited in air using a MSCAT the resonances are relatively weak. Once the sensor surface is covered by a liquid, however, the resonance becomes much stronger. In order to explore this phenomenon FEA modeling is needed. The model seen in Figure 3.22 was constructed consisting of a gold [8, 250, 515] circular spiral coil on the back side (non-sensing surface) of a quartz wafer. Piezoelectric effects were not considered in this model. A medium was then placed on the sensor surface. Since the MSCAT is excited using sinusoidal signals, a potential was assumed between the inner terminal and outer terminal of the spiral coil (Figure 3.23). The voltage distribution on the spiral was calculated for the electrostatic case and the electric field was calculated from the gradient of the voltage. The model was analyzed for two electrostatic cases: when only air was present on the sensor surface and when DI water was on the sensor surface.

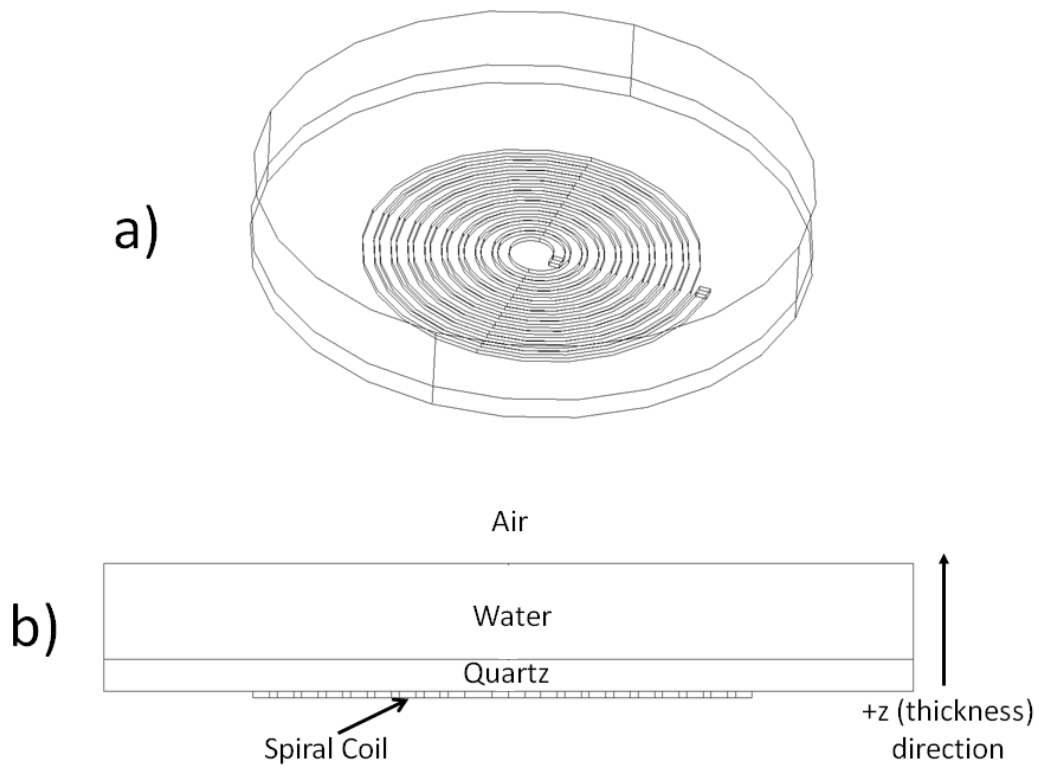


Figure 3.22 MSCAT COMSOL model a) 3D view and b) side view.

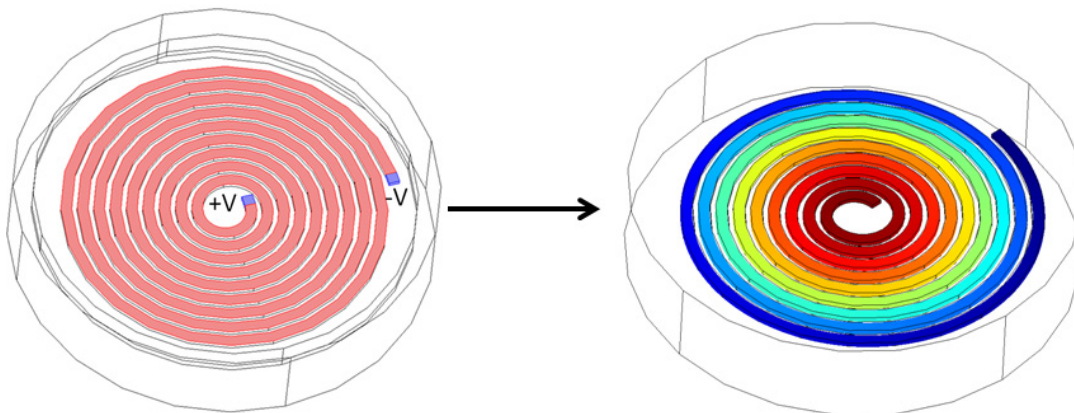


Figure 3.23 MSCAT voltage distribution calculated using COMSOL.

Figure 3.24 shows the electric field in the cross section of the MSCAT when the sensor surface is in air only and when the sensor has DI water on its surface. Figure 3.25 and Figure 3.26 show a zoomed in view of the electric field distribution for the indicated sections. From these figures it is clear that when the MSCAT is operated in air the electric fields inside the quartz are in both the lateral direction and thickness direction, and relatively weak. For the air case the magnitude of the thickness component of the electric field in the region shown in Figure 3.25 is only approximately 3 times larger than the lateral component. This will lead to the excitation of modes other than the TSM such as the quasi-shear and longitudinal modes in the crystal and helps to explain why the MSCAT does not operate well in air.

When the MSCAT is loaded with water the electric field is trapped inside the quartz. In this case the boundary conditions change from the air case and the electric fields are stronger and primarily in the thickness direction. In this case the magnitude of the thickness component of the electric field in the region shown in Figure 3.26 is approximately 800 times larger than the lateral component while the overall magnitude of the electric field inside the quartz is approximately 10 times larger than the air case. It is also interesting to note that the lateral component of the electric field for the water case is approximately 30 times smaller than the air case. The thickness component is approximately 10 times larger in the water case when compared to the air case. This leads to the conclusion that thickness electric fields are primarily responsible for exciting the TSM in the MSCAT when it is under liquid loads. It can also be concluded that the relative weakness of the thickness electric

field and the lateral component of the electric field which is not oriented only at 90° relative to the x-axis (see Figure 3.21) is primarily responsible for the MSCAT's inability to operate efficiently in air.

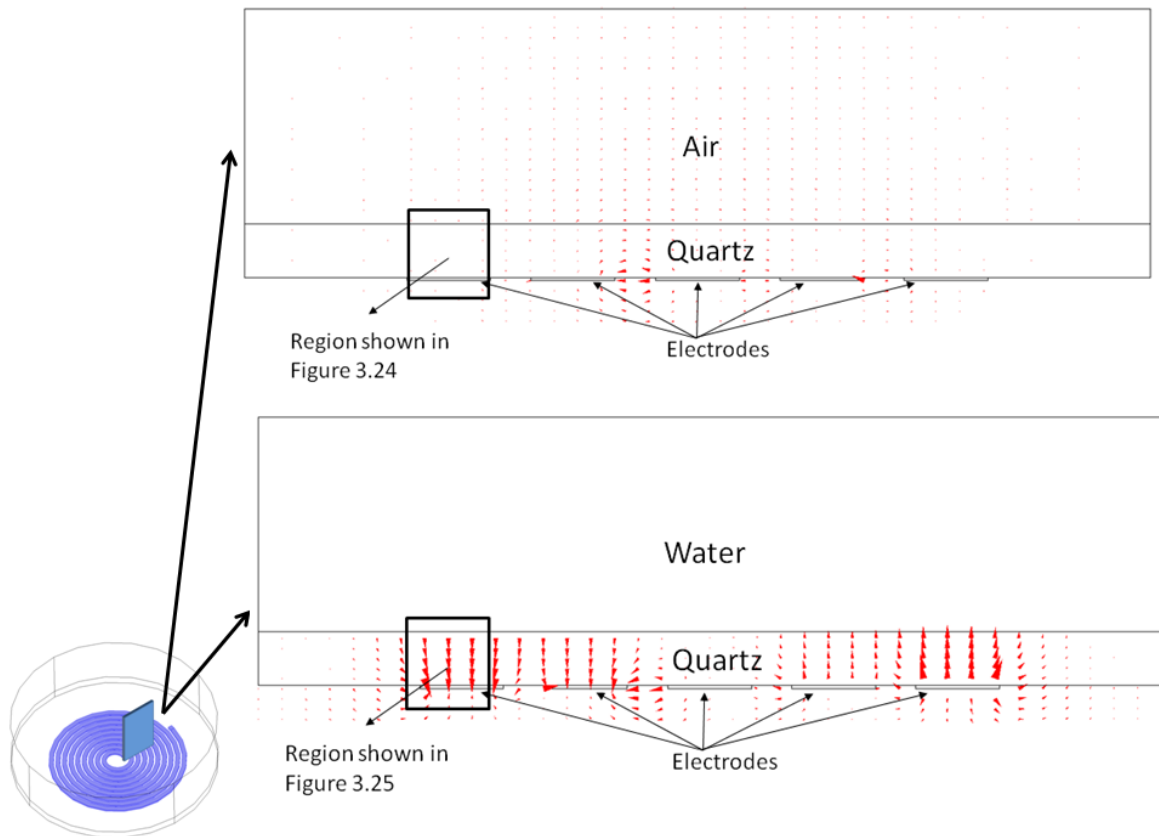


Figure 3.24 Segment showing the electrostatic electric field distribution in the MSCAT quartz when the sensor is only in air (top) and loaded with DI water (bottom). The size of the arrows represents the relative magnitude of the electric field at the base of the arrow and the direction of the arrow indicates the direction of the electric field. Figures 3.24 and 3.25 show an enlarged view of the indicated sections.

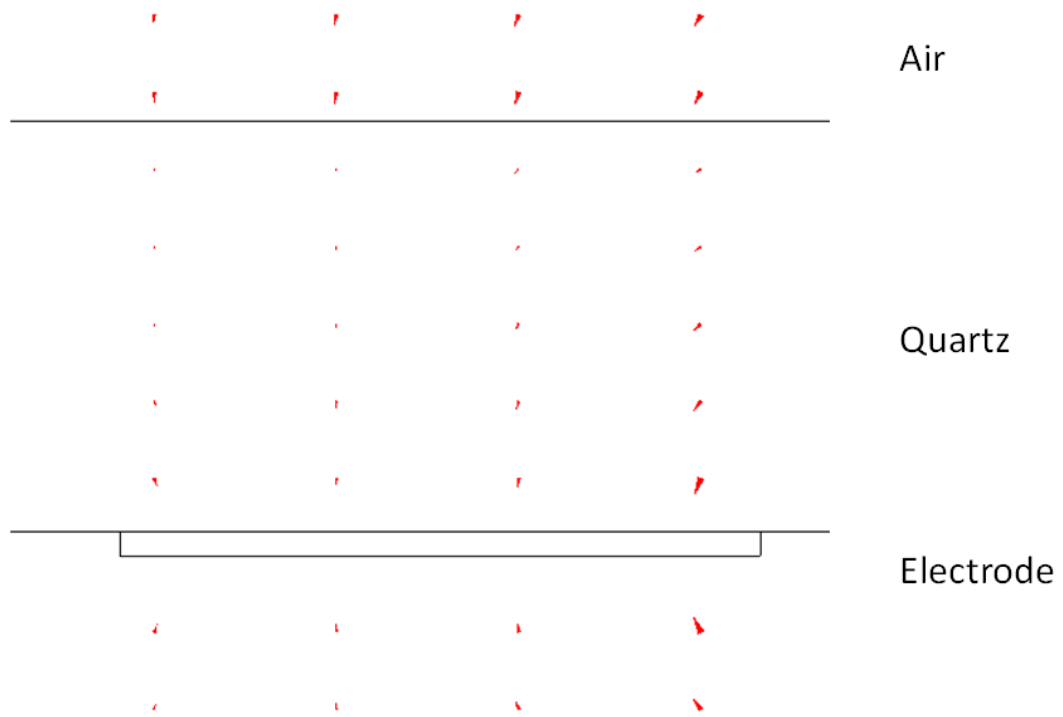


Figure 3.25 Zoomed in region indicated in Figure 3.23 showing the electric field distribution for the MSCAT when it is operated in air.

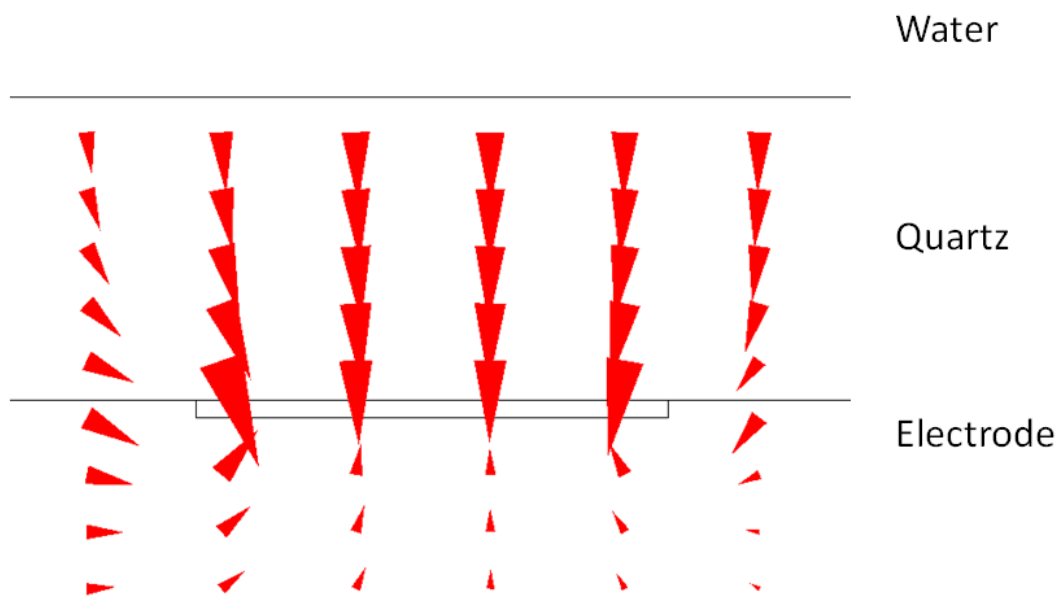


Figure 3.26 Zoomed in region indicated in Figure 3.23 showing the electric field distribution for the MSCAT when it is loaded with water.

It is interesting to note that because the spiral coil of the EMPAS is separated from the quartz the electric field behavior is significantly different than for the MSCAT. It is important to note that it has previously been reported that the EMPAS is unable to operate in air [68]. Figure 3.27 shows the electric field distribution for the EMPAS for both the air and water case. For this model the spiral coil was the same [8, 250, 515] spiral used for the MSCAT model in order to allow for a direct comparison. The coil was separated from the quartz substrate by 200 μm , roughly the distance of a typical teflon o-ring that is used to separate the coil from the quartz in the EMPAS configuration. Figure 3.28 and Figure 3.29 show zoomed in views of the indicated areas. These results show that like the MSCAT, when the EMPAS is loaded with water the electric fields redistributes and is primarily in the thickness direction while the electric field is comparatively weak in air which explains why the EMPAS is unable to operate in air but is capable of operating in liquid environments.

For the air case the magnitude of the thickness component of the electric field in the region shown in Figure 3.28 is approximately the same as the lateral component unlike the MSCAT where the thickness electric field is larger. As with the MSCAT, this will lead to the excitation of modes other than the TSM such as the quasi-shear and longitudinal modes in the crystal; however the fact that the thickness and lateral components of the electric field have approximately the same magnitude in the air case may explain why the EMPAS does not operate at all in air.

Like the MSCAT, when the EMPAS is loaded with water the electric field is trapped inside the quartz. In this case the magnitude of the thickness component of the electric field in the region shown in Figure 3.29 is approximately 50 times larger

than the lateral component while the overall magnitude of the electric field inside the quartz is approximately 3 times larger than the air case. It is also interesting to note that the lateral component of the electric field is for the water case is approximately 10 times smaller than the air case while the thickness component is approximately 4 times larger in the water case when compared to the air case. A more significant issue, however, is that for the EMPAS the electric field is primarily trapped in the air gap between the spiral coil and the quartz while the electric fields inside the quartz are weak in comparison to the MSCAT (Figure 3.24). Compared to the MSCAT, the thickness component of the electric field for the EMPAS in the water case is approximately 5 times smaller while it is approximately 50% smaller for the air case.

These results show that the magnitude of the thickness component of the electric field inside the EMPAS is much smaller than the MSCAT while the difference in magnitude between the thickness and lateral components of the electric field is not as large as the MSCAT. This helps to explain why the resonances in the EMPAS are relatively weak and difficult to detect which results in the need for specialized electronics such as the lock-in amplifier setup described earlier while the MSCAT does not.

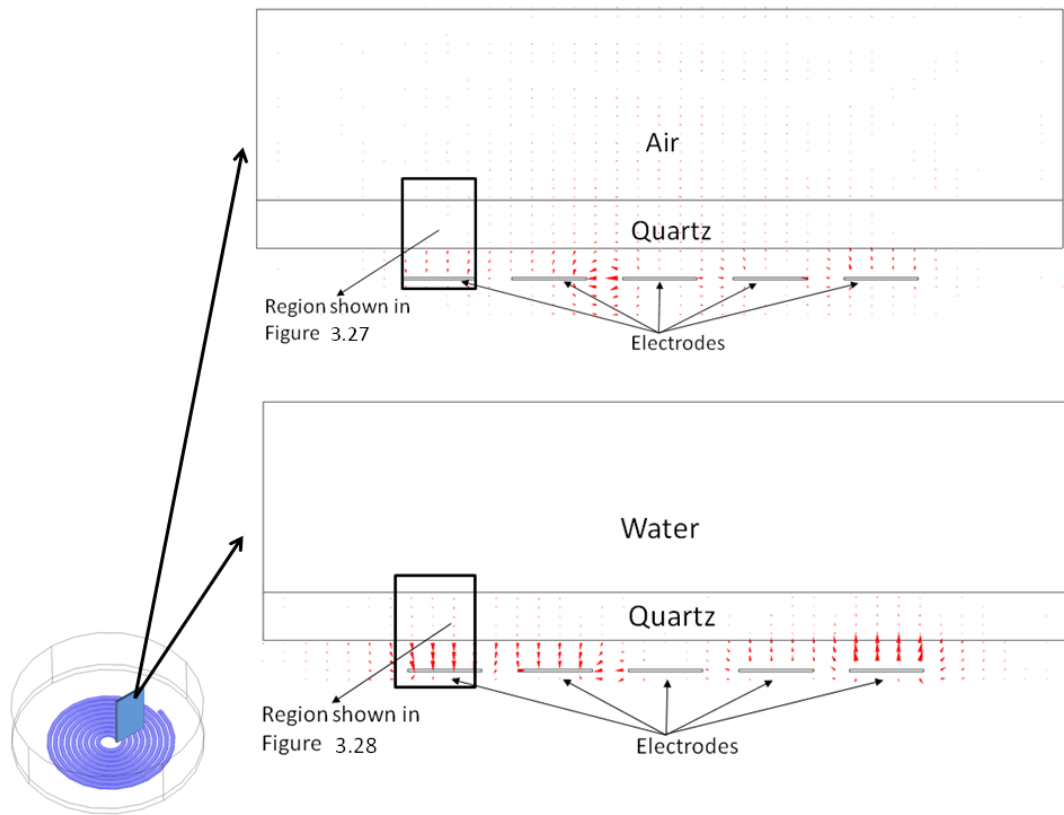


Figure 3.27 Segment showing the electrostatic electric field distribution in the EMPAS quartz when the sensor is only in air (top) and loaded with DI water (bottom). The size of the arrows represents the relative magnitude of the electric field at the base of the arrow and the direction of the arrow indicates the direction of the electric field. Figures 3.27 and 3.28 show an enlarged view of the indicated sections.

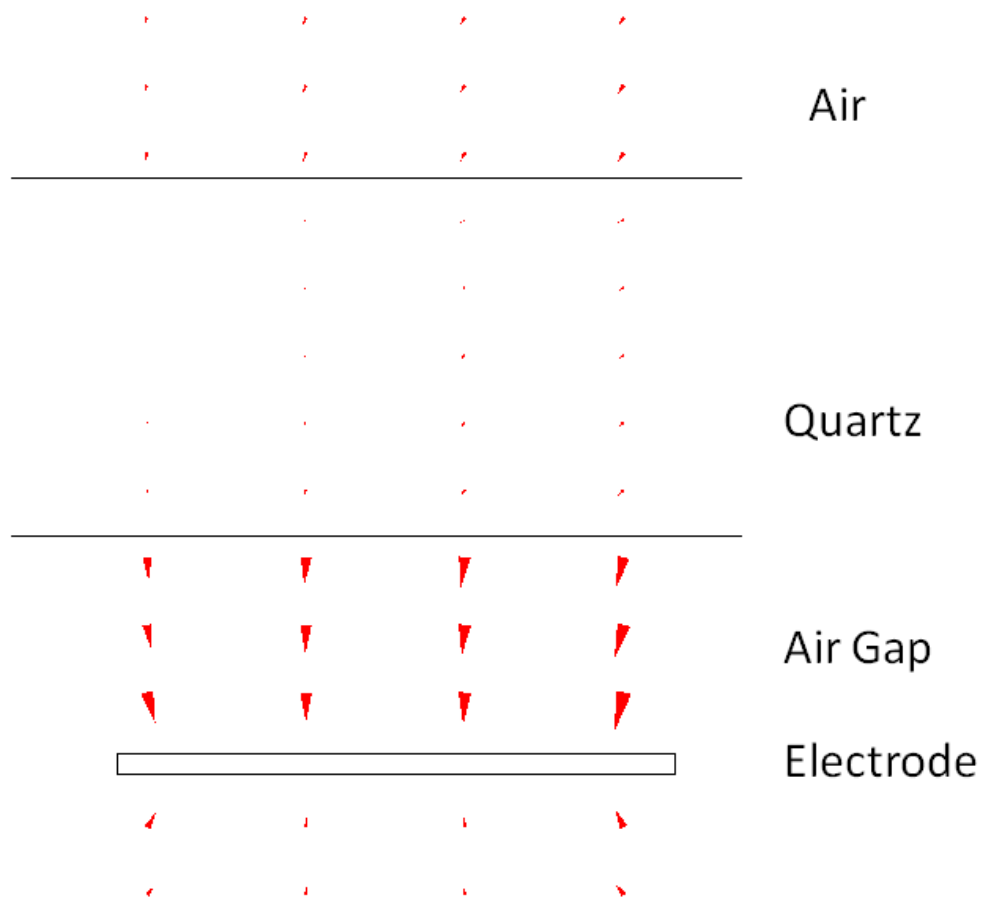


Figure 3.28 Zoomed in region indicated in Figure 3.26 showing the electric field distribution for the EMPAS when it is operated in air.

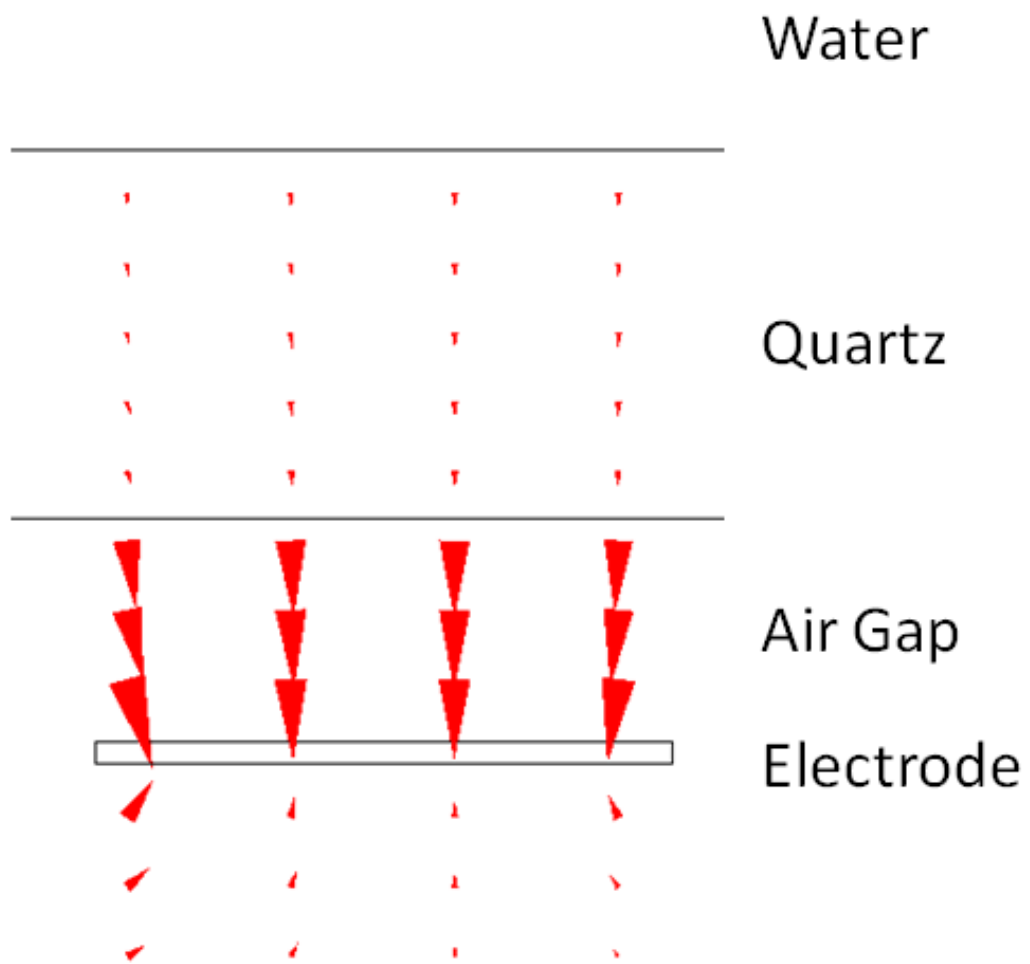


Figure 3.29 Zoomed in region indicated in Figure 3.26 showing the electric field distribution for the EMPAS when it is operated in water.

As was previously discussed, the MSCAT's resonances in air are weak and it cannot be operated at elevated harmonics. In order to replicate the boundary conditions that exist when water is placed on the sensor's surface, a thin (2000 Å) gold layer was deposited on the MSCAT to mimic the boundary conditions of the liquid case. The bottom spiral was [8, 250, 515]. It was found that the MSCAT with a gold layer placed on the sensing surface was able to operate in air with much stronger resonances than a [8, 250, 515] MSCAT (Figure 3.31). The gold MSCAT was able to operate up to the 61st harmonic. It is possible that this new sensor may be useful for gas sensing application. Although this work utilized a gold layer, it is possible that utilizing materials with higher dielectric constants than quartz ($\epsilon_r \sim 4$) as the top layer may also be useful for gas sensing applications. Future work could include optimizing the overall MSCAT design (N , S , W , σ , ϵ_r) for a particular sensing application.

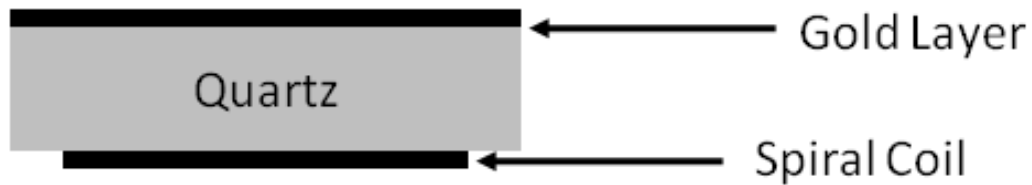


Figure 3.30 Diagram showing MSCAT with gold top layer.

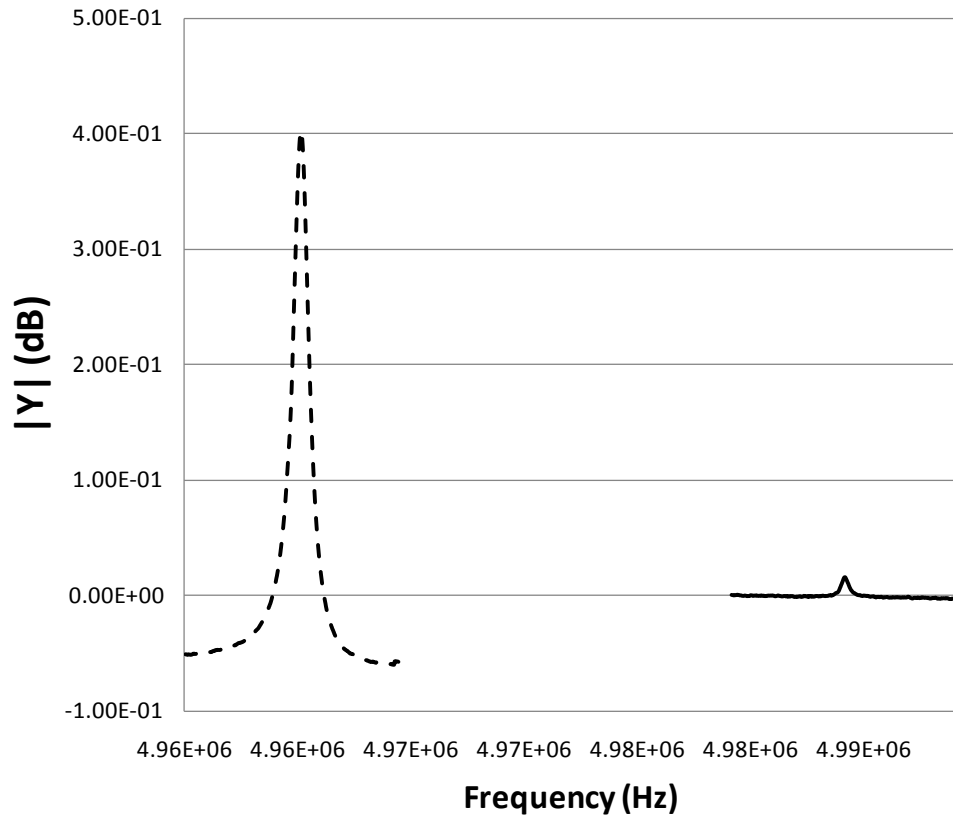


Figure 3.31 MSCAT response in air for bare MSCAT (solid line) and MSCAT with gold layer (dashed line).

3.6.2 Near Field Behavior of Spiral Coil Antennas

The far-field radiation characteristics of spiral coil antennae in air are well understood and they are known to operate over a wide frequency range [67], however the near-field radiation characteristics have not been studied in detail. Since the MSCAT's spiral coil antenna is operated in the near-field it is important to understand how the electric fields radiated by the antenna behave in the near-field. It was expected that the electric fields produced from the MSCAT antenna will vary depending on the design of the coil, however this has not been shown previously.

As described in Chapter 5, it was found that for biological applications utilizing antibody based sensing films, an operating frequency of approximately 300 MHz is optimum due to the dimensions of the sensing film [79, 80]. A number of different antenna configurations were experimentally examined as explained previously and it was found that an antenna design consisting of [8, 250, 515] provided the greatest sensitivity in the detection of *E. coli* O157:H7 [80] and was capable of operating as high as 495 MHz (99th harmonic). In order to gain insight into the effects varying spiral coil geometry has on the radiated electric fields, three other designs were also examined and compared to the [8, 250, 515] design. As shown previously, a [10, 500, 500] design was capable of operating up to 305 MHz (61st harmonic). This design was chosen for further study due to the fact that it was able to operate at frequencies in excess of most designs but still nearly 200 MHz short of the [8, 250, 515] design. A number of MSCAT antenna designs were found to be incapable of operating at significantly high frequencies. Two of these designs, namely [8, 150, 150] (maximum excitable harmonic the 23rd) and [8, 250, 150]

(maximum excitable harmonic was the 7th) were also chosen for further study. In order to gain an understanding of the form of the radiated electric field for different antenna configurations at different operating frequencies, COMSOL's RF module was utilized.

Since it has been shown that the thickness (z-direction) component of the electric field is responsible for exciting the TSM in the MSCAT sensor platform, the z-component of the electric field was chosen for further study. Each MSCAT described above was modeled over a frequency range of 65 MHz – 365 MHz. Due to the complexity of the model it was not possible to analyze frequencies in excess of 365 MHz or incorporate the effects of piezoelectricity without the use of a supercomputer or running multiple processors in parallel. A sinusoidal voltage was applied between the inner and outer terminals and the resulting electric field was calculated for all points in the model. The magnetic vector potential \mathbf{A} due to a current source that generates a current density \mathbf{J} may be calculated from the solution to the inhomogeneous vector wave equation and the electric field \mathbf{E} may be calculated from \mathbf{A} [67] as follows:

$$\mathbf{A} = \frac{\mu}{4\pi} \iiint \mathbf{J} \frac{e^{-jkR}}{R} dv \quad 3.2$$

and

$$\mathbf{E} = -j\omega\mu\mathbf{A} - j\frac{1}{\omega\epsilon}\nabla(\nabla \cdot \mathbf{A}) \quad 3.3$$

where

μ = permeability

ϵ = dielectric constant

ω = angular frequency

k = wave number

R = point of interest

Since the electric field inside the AT-cut quartz crystal is of primary interest, the point at the center of the crystal was chosen for further study. Figure 3.32 shows the magnitude of the resulting electric field for each design in the center of the crystal. As can be seen in Figure 3.32, the [8, 250, 515] MSCAT produced a much stronger thickness direction electric field which explains why it was able to operate the most efficiently. The [10, 500, 500] MSCAT also produced a much stronger electric field than the [8, 250, 150] and [8, 150, 150] MSCATs as the later two designs exhibited very weak thickness electric fields in comparison to the first two designs. As can be seen in Figure 3.33 the [8, 250, 150] design did produce an electric field that was approximately twice as strong as the [8, 150, 150] design which explains why it was able to operate at higher frequencies than the [8, 150, 150] design. Although the [8, 250, 515] design was experimentally found to be the best design tested it is possible that further work may uncover an even better design. It is clear, however, that more work is necessary in order to understand what aspects of the spiral coil design lead to stronger near-field electric field (see Appendix B).

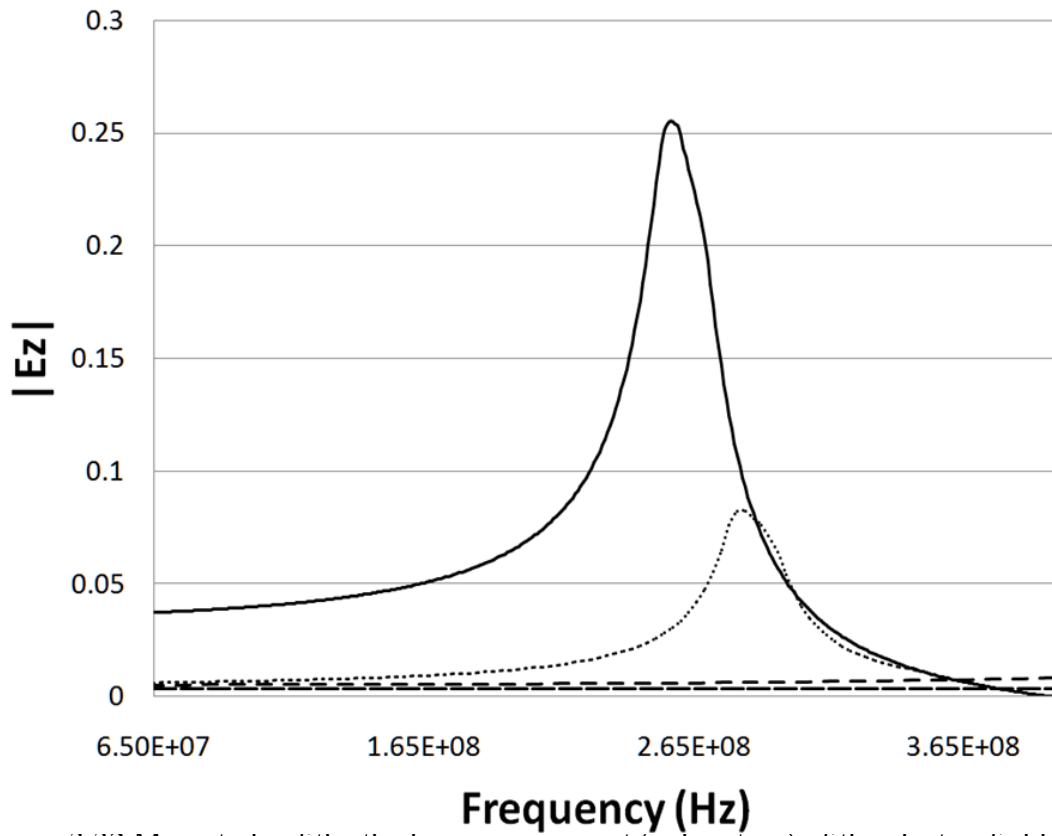


Figure 3.32 Magnitude of the thickness component (z direction) of the electric field in the center of the MSCAT's AT-cut quartz wafer for various electrode geometries: [8, 250, 515] (solid line), [10, 500, 500] (small dotted line), [8, 250, 150] (medium dotted line), and [8, 150, 150] (large dotted line).

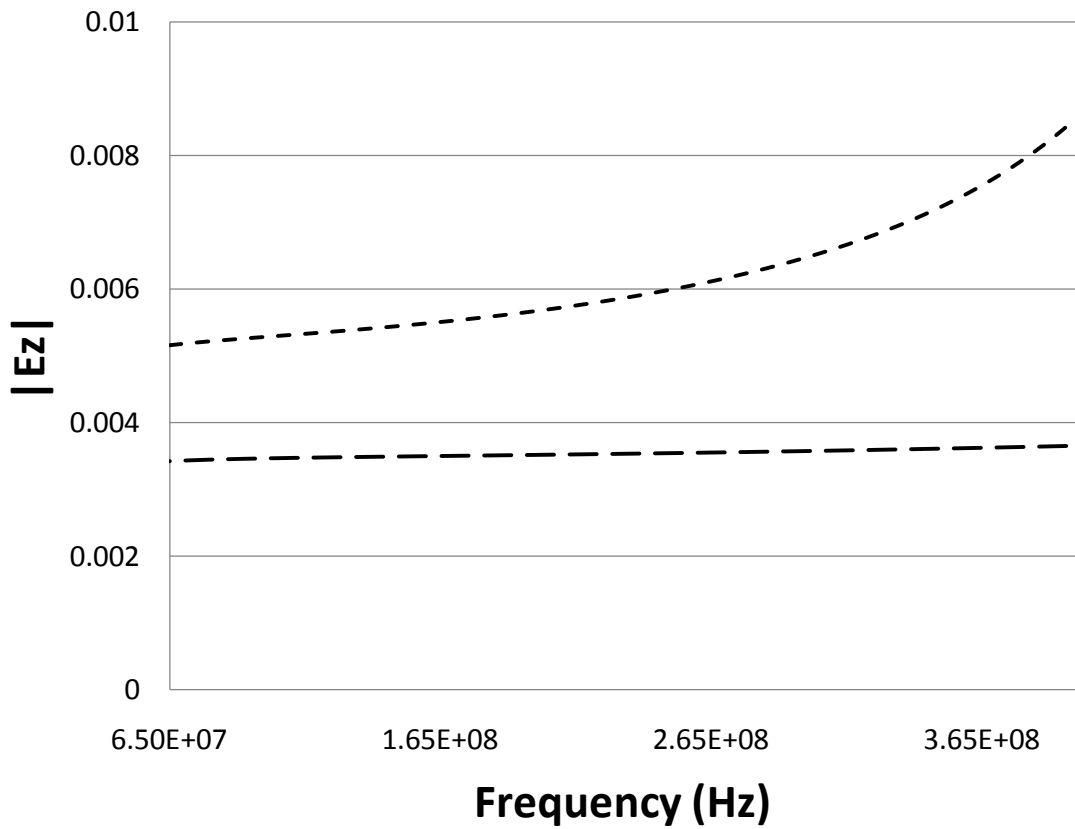


Figure 3.33 Magnitude of the thickness component (z direction) of the electric field in the center of the MSCAT's AT-cut quartz wafer for the electrode geometries: [8, 250, 150] (medium dotted line), and [8, 150, 150] (large dotted line).

4 MEASUREMENT OF LIQUID MECHANICAL AND ELECTRICAL PROPERTY CHANGES

4.1. Introduction

Since a QCM has electrodes on the top and bottom surface, the electric field cannot penetrate into the measurand or sensing layer due to the conducting electrode on the sensing surface. Therefore, electrical property changes to the conductivity and/or permittivity of the adjacent liquid or chemi- or bioselective film caused by the target analyte cannot be detected with the standard QCM sensor. Previous work has shown that the LFE sensor platform is able to detect both electrical and mechanical property changes due to the fact that it does not have an electrode on its sensing surface [81]. In order to determine if the MSCAT is also capable of measuring both mechanical and electrical property changes in liquids, MSCAT sensors were used to monitor both mechanical (viscosity/density) and electrical (conductivity, relative permittivity) properties in liquids.

Based on the results described in Chapter 3, several MSCAT geometries were chosen for these tests and compared to QCM and LFE sensors. Although the MSCAT is capable of operating at high frequencies by exciting high-order harmonics in the device, the MSCATs were operated at their fundamental frequency (5 MHz) to allow direct comparison to the QCM and LFE sensors which were also operated at their fundamental frequency (5 MHz). In subsequent tests, the frequency response of the MSCAT when it was operated at elevated harmonics was examined.

4.2. Experimental Description for Liquid Property Measurements

Each sensor was clamped in a cylindrical 3 mL liquid cell holder that is 1.27 cm in diameter. For each test, 1 mL of liquid was placed on the sensor's surface using a Thermo Scientific 200-1000 μL variable Finnpiquette pipetter. The change in resonant frequency for each solution from the resonant frequency when only de-ionized (DI) water was present was measured for each device. After each test the sensor was rinsed 10 times with DI water and then dried with nitrogen. Each test was repeated five times.

One of the challenges in measuring liquid mechanical and electrical property changes using BAW sensors is that there are no candidate liquid solutions in which only a single parameter (viscosity and density, conductivity, relative permittivity) changes. Typically, solutions are selected where one variable changes significantly with only small variations in the other two parameters [81]. The solutions described in [81] were chosen for the liquid property measurements in this work.

The viscous liquids used for the tests were created by mixing various ratios of DI water and glycerol in ratios between 0% and 30% wt. glycerol. A Cannon Fenske Routine Viscometer was used to measure the viscosity of each liquid and was found to range between 0.97 and 3.2 cP. The square root of the density-viscosity product is typically used when reporting BAW sensor data due to the fact that it is not possible to separate the effects of each parameter individually. The square root of the density viscosity product ranged between 0.97 and 1.88 $\sqrt{\text{g}\cdot\text{cm}^{-3}\cdot\text{mPas}\cdot\text{s}}$. The conductivity of each solution was measured using an Oakton CON 11 conductivity meter and found to vary by no more than 40 μS between all of the solutions. The relative

permittivity of the solutions is reported in [82] to vary by 8 (80 for the DI water and 72 for the 30% wt. glycerol solution).

For changes in liquid conductivity measurements, NaCl- water solutions in the range of 0 to 0.06 wt% NaCl was used. The conductivity of each solution was measured using an Oakton CON 11 conductivity meter and found to range between 1.7 and 1235 μS . Since the resonant frequency change of the MSCAT sensor is due to both mechanical and electrical property changes in the liquid, the NaCl concentrations chosen for this experiment (0 to 0.06% wt) have very small variations in mechanical property changes such as density and viscosity. The viscosity of each solution was measured using the Cannon Fenske routine viscometer and the square root of the density-viscosity product was found to be nearly the same as the DI water used in the tests ($0.97 \sqrt{(\text{g}\cdot\text{cm}^{-3}\cdot\text{mPas}\cdot\text{s})}$ for DI water and $1.0 \sqrt{(\text{g}\cdot\text{cm}^{-3}\cdot\text{mPas}\cdot\text{s})}$ for the 0.06 wt% solution). The relative permittivity of these solutions is reported to vary by approximately 2 [84].

Liquid solutions with varying relative permittivity were created by mixing solutions of DI water and 2 – propanol mixtures in 2-propanol concentrations between 0 wt% ($\epsilon_r = 80$) and 100 wt% ($\epsilon_r = 20$). Although the conductivity of each solution varies only slightly (less than 2 μS), the square root of the density-viscosity product varies between 0.94 and $1.27 \sqrt{(\text{g}\cdot\text{cm}^{-3}\cdot\text{mPas}\cdot\text{s})}$.

4.3. Measurement of Liquid Viscosity Changes

A [8, 250, 515] MSCAT was compared to the performance of standard QCM and LFE sensors, both fabricated on AT-cut quartz with a fundamental frequency of

approximately 5 MHz as seen in Figure 4.1. In order to aid in comparison, the theoretical frequency shift for the QCM was calculated using the relationship developed by Kanazawa and Gordon [83].

As can be seen in Figure 4.1 the MSCAT sensor was capable of monitoring the changes in the liquid viscosities and exhibited nearly identical frequency shifts when compared to the LFE sensor. As is discussed in Appendix A, a LFE fabricated on LiTaO_3 that is capable of operating at elevated harmonics also exhibited similar sensitivity levels when compared to a LFE fabricated on AT-cut quartz. The MSCAT exhibited a slightly larger frequency shift than the QCM, however. This may partly be due to the fact that the conductivity and relative permittivity of the liquids varied slightly between solutions (approximately $40 \mu\text{S}$ for the conductivity and 8 for the relative permittivity). It should be noted that the conductivity of the solutions changed by approximately $40 \mu\text{S}$ within the first four data points and was constant for the remaining data points which helps to explain why the MSCAT and LFE had higher sensitivities for the first four solutions. As shown later, the [8, 250, 515] MSCAT with a gold layer placed on its sensing surface is significantly less sensitive to electrical property changes than the standard MSCAT or LFE. In Figure 4.1 it can be seen that the gold layered MSCAT exhibited larger frequency shifts than the QCM but smaller frequency shifts than the standard MSCAT or LFE. This result strengthens the theory that the increased frequency shift exhibited by the MSCAT and LFE is at least partly due to changing electrical properties of the liquids. A triangular [8, 250, 515] MSCAT was also tested and found to exhibit frequency shifts that were almost identical to the standard [8, 250, 515] MSCAT.

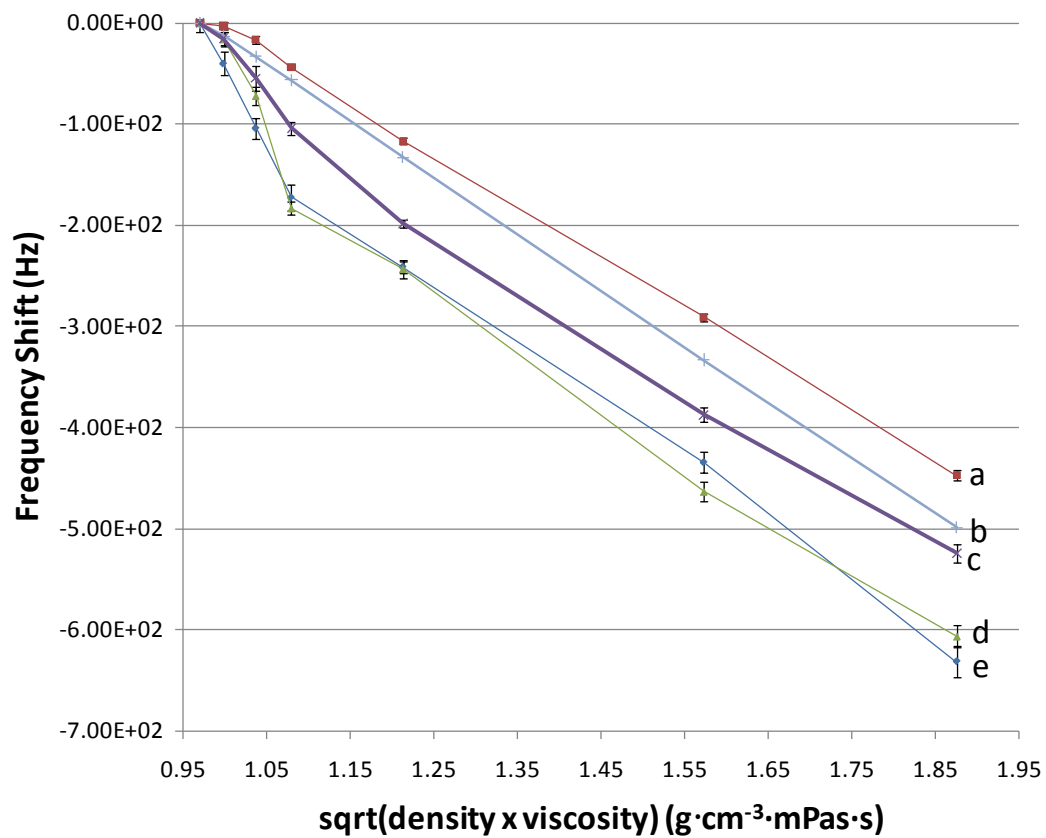


Figure 4.1 Sensor response to changes in glycerol concentrations: (a) QCM; (b) theoretical frequency shift; (c) [8, 250, 515] MSCAT with gold top layer; (d) LFE, and (e) [8, 250, 515] MSCAT.

4.4. Measurement of Liquid Conductivity Changes

The MSCAT sensor was also tested to determine its response to electrical property changes in liquids. The resonant frequency changes of the sensors with respect to their resonant frequencies in DI water as a function of the solution conductivity is shown in Figure 4.2. As can be seen in Figure 4.2 the QCM and MSCAT with the gold top layer exhibited very small changes to the changes in liquid conductivity. This is due to the fact that both sensors have a gold top layer which keeps the boundary conditions constant and therefore the electric field inside the sensor substrate will not vary significantly with changes in the electrical properties. This result indicates that an MSCAT with a gold layer on the sensing surface may be used for applications where it is not desirable for the sensor to be as sensitive to electrical property changes.

There were, however, significant changes in the resonant frequency of both the standard and triangular MSCATs indicating that they were both capable of monitoring liquid electrical property changes while the QCM could not. It is interesting to note that the triangular MSCAT was more sensitive than the standard MSCAT even though its spiral coil covered a surface area approximately 35% smaller than the standard MSCAT. This may be due to the fact that the triangular MSCAT has sharp angles in its electrode while the standard circular MSCAT does not. It is common practice in printed circuit board (PCB) design to avoid right angles in signal traces due to the fact that charge can build up at the sharp angles leading to reflection problems [85]. The added sensitivity of the triangular MSCAT may be due to charge build up at its sharp angles. The frequency change of the LFE was more than twice as

large as the MSCAT sensors. Hempel has shown that changes in liquid electrical properties causes a redistribution of the electric field inside the LFE's quartz wafer which results in a piezoelectric stiffening effect which in turn changes the resonant frequency of the device [86]. Although the LFE is highly sensitive to conductivity changes, its dynamic range is limited as its resonant frequency does not vary significantly for solutions above 500 μS . Hempel has postulated that for the LFE the rate of piezoelectric un-stiffening is only significant for low electrolytic solutions and is less pronounced for higher electrolytic solutions. Although the MSCAT is less sensitive to changes in conductivity than the LFE its dynamic range is larger. It is likely that the difference in the electric field distribution produced by each electrode geometry plays a significant role in the sensitivity of each device to changes in liquid electrical property changes.

Previous work has shown that varying the LFE electrodes results in varying sensitivity to electrical property changes [81]. In addition, Peters has shown that the material properties of the resonator material also impact the sensitivity of LFE sensors to electrical property changes [87]. It is clear that if it is desirable to achieve the highest possible sensitivity to electrical property changes then more work is needed to optimize both the electrode configuration and sensor substrate material for these applications. Peters also developed a method to distinguish between changes in the density-viscosity product and relative permittivity in liquids using an LFE. However a significant amount of work remains in order to separate the changes in both conductivity and relative permittivity in a solution.

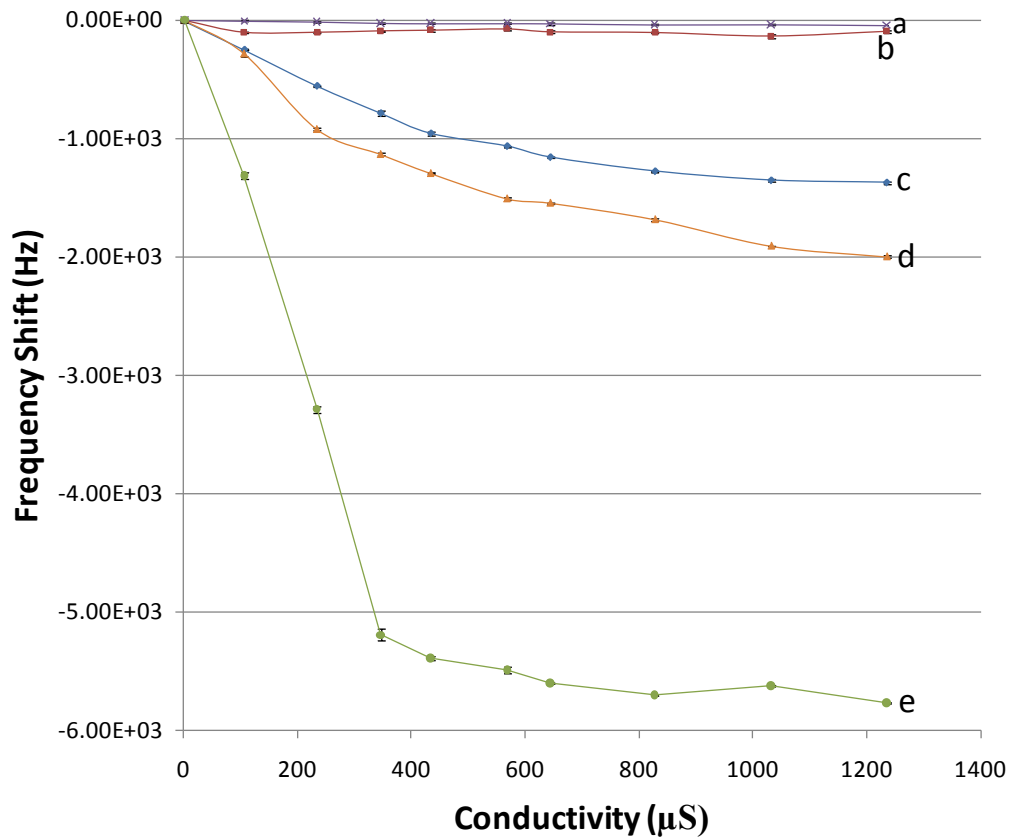


Figure 4.2 Sensor response to changes in NaCl concentration for: (a) QCM, (b) [8, 250, 515] MSCAT with gold top layer, (c) standard [8, 250, 515] MSCAT, (d) triangular [8, 250, 515], and (e) LFE.

4.5. Measurement of Liquid Relative Permittivity Changes

In order to determine the MSCAT's sensitivity to changes in relative permittivity the solutions 2-propanol solutions described earlier were used. The resonant frequency changes of the sensors with respect to their resonant frequencies in DI water as a function of the solution relative permittivity is shown in Figure 4.3. As can be seen in Figure 4.3 the standard MSCAT, triangular MSCAT, and LFE exhibited positive frequency shifts with increasing concentrations of 2-propanol (lower ϵ_r). The QCM exhibited a negative frequency shift as its resonant frequency was affected only by changes in the density-viscosity product of the solution. The triangular MSCAT was slightly more sensitive than the standard MSCAT while the LFE was approximately twice as sensitive. It is interesting to note that the MSCAT with a gold layer on its surface exhibited a negative frequency shift for the lower 2-propanol concentration solutions as its response was dominated by the viscosity of the solutions but it exhibited a positive frequency shift for the higher concentration solutions. These results further indicate that although the gold layered MSCAT is significantly less sensitive to electrical property changes than the standard MSCAT its frequency response is still influenced by the electrical properties of the liquid.

From these results it is clear that the MSCAT is capable of detecting both mechanical (density/viscosity) and electrical (conductivity and relative permittivity) changes in liquid solutions. It was found that the triangular MSCAT was more sensitive to electrical property changes than the standard MSCAT while the MSCAT with the gold top electrode was less sensitive to electrical property changes. It was also found that the MSCAT was less sensitive to electrical property changes than the

LFE when both devices were operated at their fundamental frequency (5 MHz). It is obvious from the results, however, that more work is required in order to develop a model that can distinguish between mechanical and electrical liquid property changes using a BAW sensor.

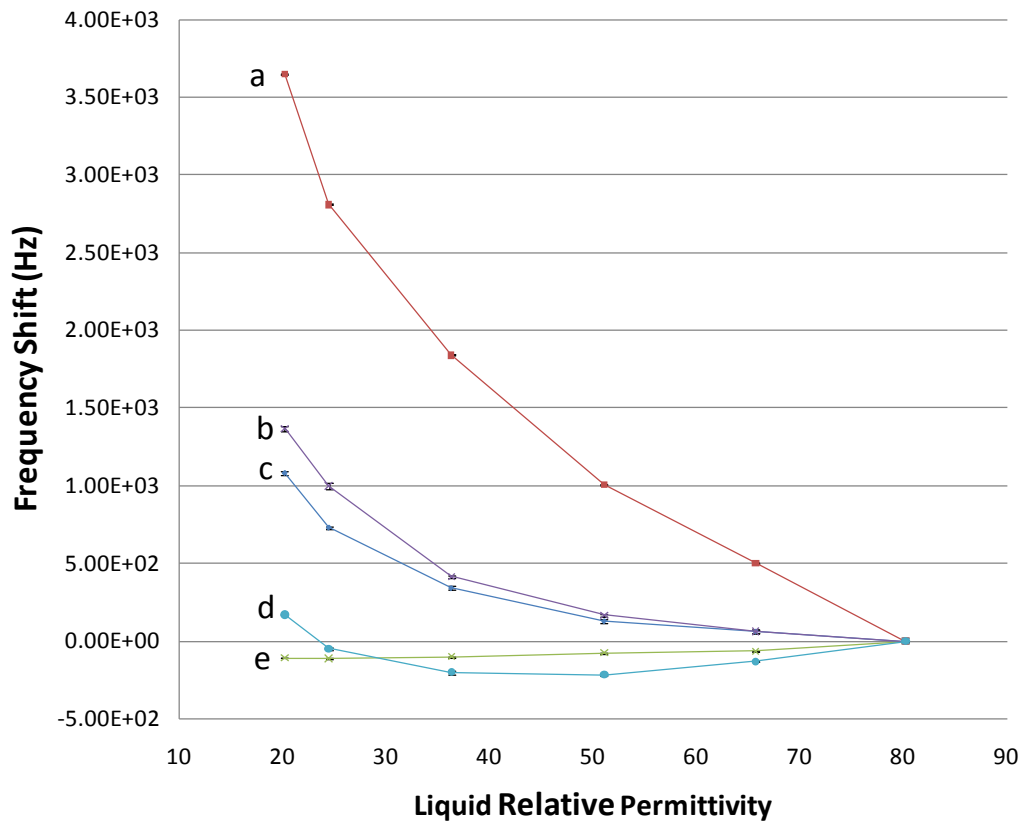


Figure 4.3 Sensor response to changes in 2-propanol concentration for: (a) LFE, (b) triangular [8, 250, 515] MSCAT (c) standard [8, 250, 515] MSCAT, (d) [8, 250, 515] MSCAT with gold top layer, and (e) QCM.

4.6 The Measurement of Mechanical and Electrical Property Changes at High Frequencies

As was discussed in Chapter 3, the MSCAT is able to operate at high frequencies by exciting high order harmonics in the substrate. In order to examine the MSCAT's behavior at elevated frequencies, the MSCAT was operated at elevated harmonics and used to measure mechanical and electrical property changes of liquids. A [8, 250, 515] MSCAT was operated at harmonics ranging from its fundamental (approximately 5 MHz) and the 99th harmonic (approximately 495 MHz).

In order to examine the MSCAT's behavior to changes in liquid viscosity at elevated frequencies, the change in frequency from when the MSCAT was loaded with 1mL of DI water (0.95 cP) to when it was loaded with 1 mL of 30% wt glycerol solution (3.2 cP) was measured at various harmonics. As before, each test was run 5 times. As can be seen in Figure 4.4, the MSCAT exhibited much larger frequency changes when operated at elevated harmonics (approximately 600 Hz at the fundamental frequency and 120 kHz at the 99th harmonic). The frequency shift increased in a nearly linear fashion between 5 and 300 MHz. No significant increase in frequency shift was observed for higher frequencies.

The TSM has mechanical displacements that are perpendicular to the propagation direction and parallel to the crystal surfaces. When the MSCAT is liquid loaded the boundary conditions dictate that the displacements be continuous at the crystal/electrode and electrode/liquid interface. However, the viscous nature of most liquids results in damping of the shear wave a short distance from the crystal surface which results in a decrease in resonant frequency. The distance that the wave travels

is dependent on the operating frequency of the device. As Kanazawa and Gordon have shown [83] the resonant frequency decrease for a QCM is proportional to the square root of the density-viscosity product. It has been shown, however, that this relationship does not apply at higher frequencies [88]. Although the exact mechanism is unknown it is postulated that changes in the complex acoustic impedance of the viscous liquid may play a role in relative frequency shifts observed at higher frequencies.

The dramatic increase in the frequency shift observed for the MSCAT when it is operated at elevated harmonics may have applications where it is desirable to monitor changes in liquid viscosities. One such application is the food industry. There is a need to sensitively measure the viscosity of foods in an in-line manner that provides measurements in real-time and is non-intrusive. Current in-line viscometers for the food industry include the Brookfield SST-100 In-Line Viscometer, the Endress & Hauser Promass I, the Cambridge Applied Systems SPC/L301 Inline Viscometer and the Dynatrol Viscosity Measurement Probe. Most of these viscometers use pistons, a rotating cylinder, or vibrations to measure viscosity that may mix the fluid of interest in a non-desirable fashion. Optical type viscometers are unable to measure the viscosity of opaque or clear liquids. Another problem with the current technology is that they may be intrusive to the food making process and their installation would require an additional FDA inspection. A sensitive in-line viscometer that provides real-time measurement, has no moving parts, is capable of measuring opaque or clear liquids, and would be non-intrusive is needed. The MSCAT is a device that is capable of fulfilling all of these requirements.

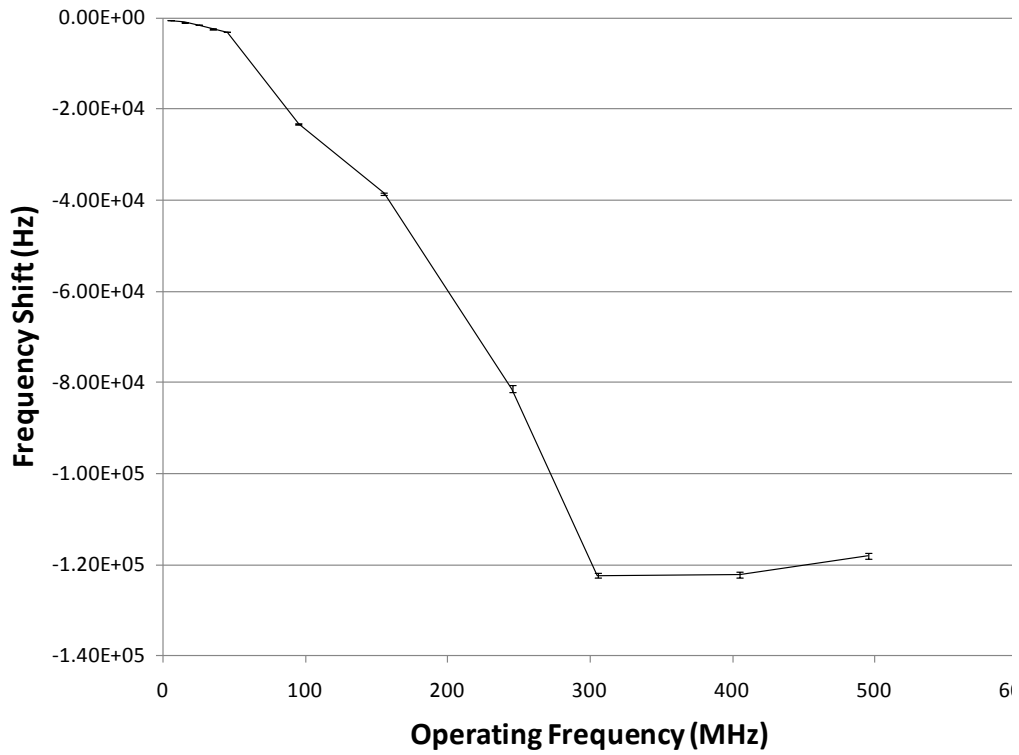


Figure 4.4 MSCAT frequency shift due to a change of 2.25 cP when operated at elevated frequencies.

In order to examine the MSCAT sensor's behavior to changes in electrical property changes at elevated frequencies, the change in frequency from when the sensor was loaded with only DI water ($1.6 \mu\text{S}$, $\epsilon_r = 80$) was compared to when the MSCAT was loaded with a 0.06% wt NaCl solution ($1235 \mu\text{S}$) and when the MSCAT was loaded with a 100 wt% 2-propanol ($\epsilon_r = 20$) was measured at various harmonics. As before, each test was run 5 times.

As was the case with viscosity, the MSCAT exhibited much larger frequency changes to changes in liquid electrical property changes when operated at elevated harmonics. As can be seen in Figure 4.5 the MSCAT frequency shift was approximately 2.000 Hz at the fundamental frequency and 120,000 Hz at the 99th harmonic for the 0.06 wt% NaCl solution. As was the case with the viscosity measurements, no significant increase in frequency shift was observed for higher frequencies.

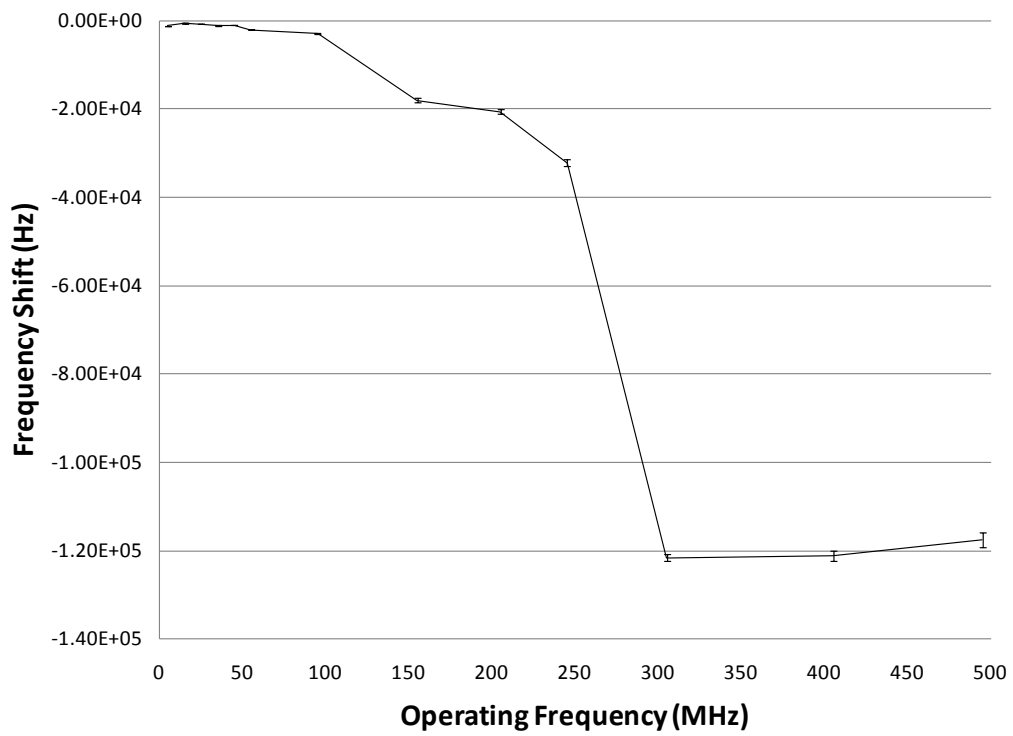


Figure 4.5 MSCAT frequency shift due to a change of 1235 μ S when operated at elevated frequencies.

From Figure 4.6 it can be seen that the resonant frequency of the MSCAT to changes in liquid relative permittivity initially increased in a nearly linear fashion until approximately 200 MHz. From approximately 200 – 350 MHz the resonant frequency shift continued to increase, but at a much slower rate. Above 350 MHz, however, the frequency shift increased dramatically. As was stated previously, although the conductivity of the 2-propanol solutions does not vary significantly, the density-viscosity product varies by approximately 25% between the solutions. From Figure 4.4 it can be seen that the magnitude of the resonant frequency shift to changes in liquid viscosity increase rapidly between 200 and 300 MHz. The frequency shift, however, is negative. Since the MSCAT exhibits a positive frequency shift to changes in relative permittivity the response to viscosity changes “dampens” the MSCAT’s response to the liquid permittivity changes over this frequency range. Above 300 MHz, however, the resonant frequency changes due to changes in liquid viscosity do not vary significantly. This helps to explain why the MSCAT exhibits increased sensitivity to changes in relative permittivity at higher frequencies. Based on these results, if it is desirable to monitor relative permittivity changes in liquids in which the density and viscosity also change, then the MSCAT should be operated at frequencies over 300 MHz to minimize the effects of liquid viscosity changes on the resonant frequency of the sensor.

It should also be noted that the frequency changes of the MSCAT due to liquid permittivity changes are an order of magnitude smaller than the frequency changes due to viscosity and conductivity changes when the MSCAT is operated at

elevated harmonics. As can be seen from Figure 4.1-Figure 4.3 the resonant frequency changes are the same order of magnitude for changes in viscosity, conductivity, and relative permittivity when the MSCAT is operated at the fundamental frequency. The lower frequency shifts to changes in 2-propanol solutions can at least partly be explained by the significant effect changes in viscosity has on the MSCAT's frequency response for the 2-propanol solutions. The change in viscosity significantly masks the changes in relative permittivity at some frequencies.

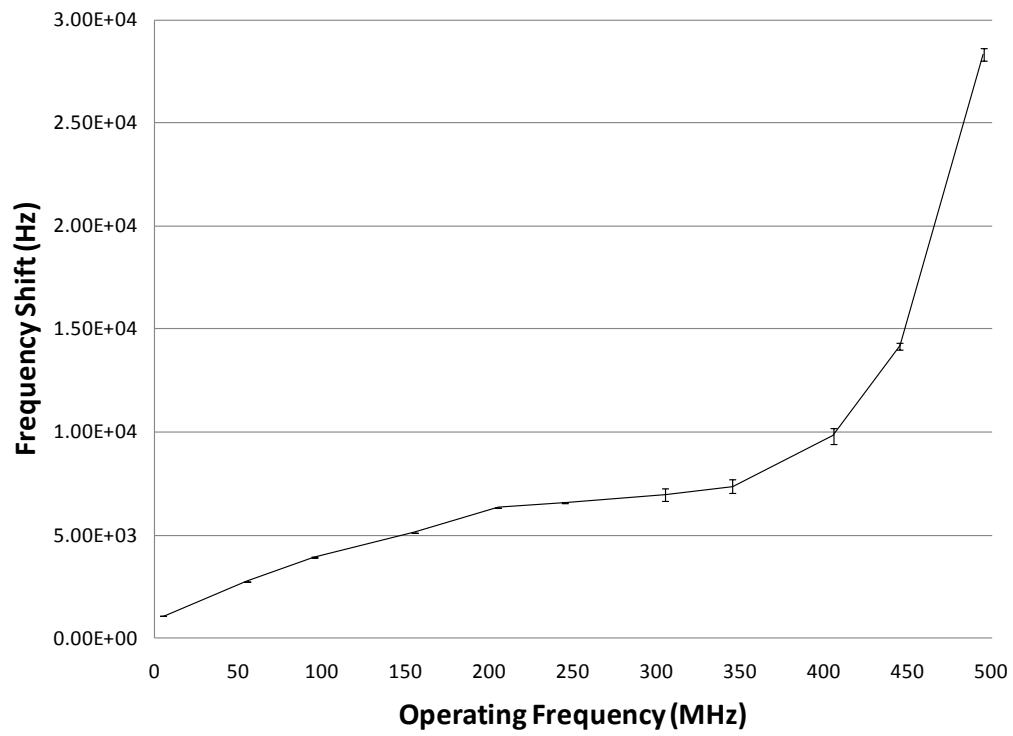


Figure 4.6 MSCAT frequency shift due to a change in relative permittivity of 60 when operated at elevated frequencies.

Figure 4.7-Figure 4.9 show the relative frequency shift ($\Delta f/f$) for changes in the square root of the density viscosity product, conductivity, and relative permittivity. As can be seen in Figure 4.7 and Figure 4.8 the MSCAT has the largest relative frequency shift to changes in viscosity and conductivity when it is operated at approximately 300 MHz. It is interesting to note that the magnitude of the relative frequency shift decreases initially as the operating frequency increases. As can be seen in Figure 4.9 the MSCAT has the largest relative frequency shift to changes in relative permittivity at 500 MHz although the relative frequency shift at 500 MHz is only approximately 15% larger than when the MSCAT was operated at its fundamental frequency. These results show that the sensitivity to mechanical and electrical property changes is dependent on the operating frequency of the device and the highest possible operating frequency does not necessarily result in the highest level of sensitivity. This result may offer a possible avenue to solving the problem of separating liquid mechanical and electrical property changes using a BAW sensor.

As Hempel and Peters have shown for the LFE, the theory developed for the QCM such as the Sauerbrey and Kanazawa equation do not apply to BAW sensors with no gold top electrode [86, 87]. It is clear that a significant amount of work is required to theoretically predict the frequency change of the LFE and MSCAT sensors resulting from both mechanical and electrical property changes in liquids. Peters has performed some promising work on the LFE by monitoring parameters such as the series and parallel resonance frequencies, the maximum of the conductance spectrum, and the half bandwidth and was able to differentiate between electrical and mechanical property changes in liquids. Based on the results shown in

Figure 4.4 - Figure 4.9 it is likely that operating an MSCAT at a wide range of frequencies will provide additional acoustic impedance information about the mechanical and electrical properties of a liquid sample as the sensitivity of the MSCAT to each liquid property changes depending on the operating frequency and may be helpful in separating liquid mechanical and electrical property changes. However, in order to utilize the MSCAT as a sensitive liquid property sensor, it will first be necessary to develop a strategy to separate the effects of liquid mechanical and electrical property changes from the MSCAT's sensor response.

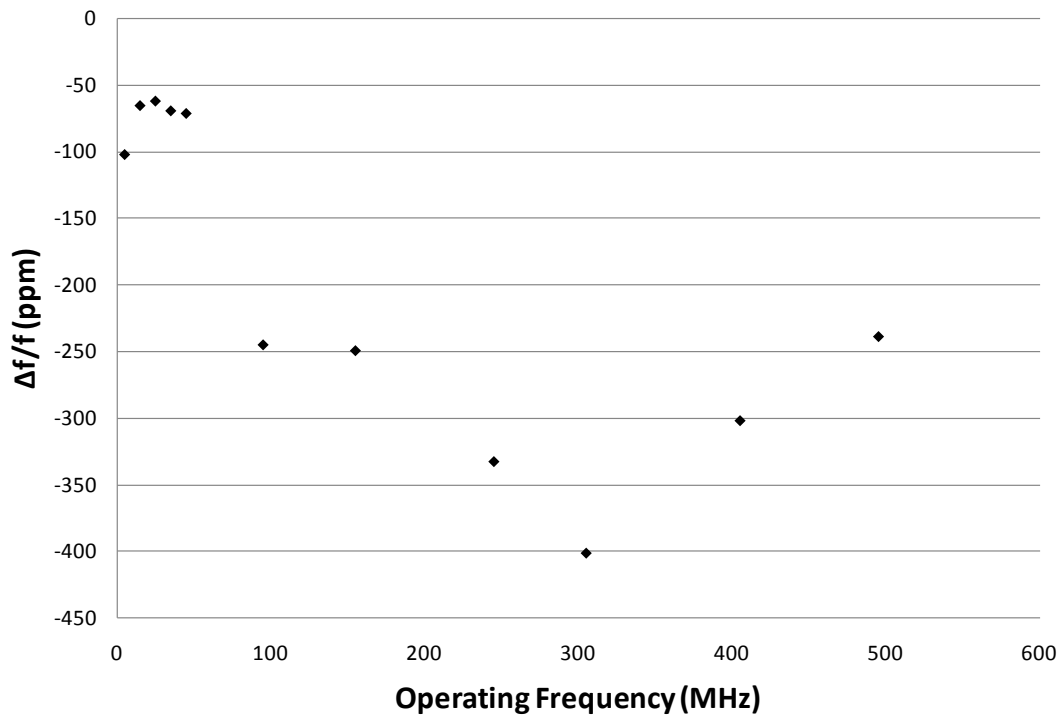


Figure 4.7 Relative frequency shift to a change in viscosity of 2.25 cP as a function of operating frequency.

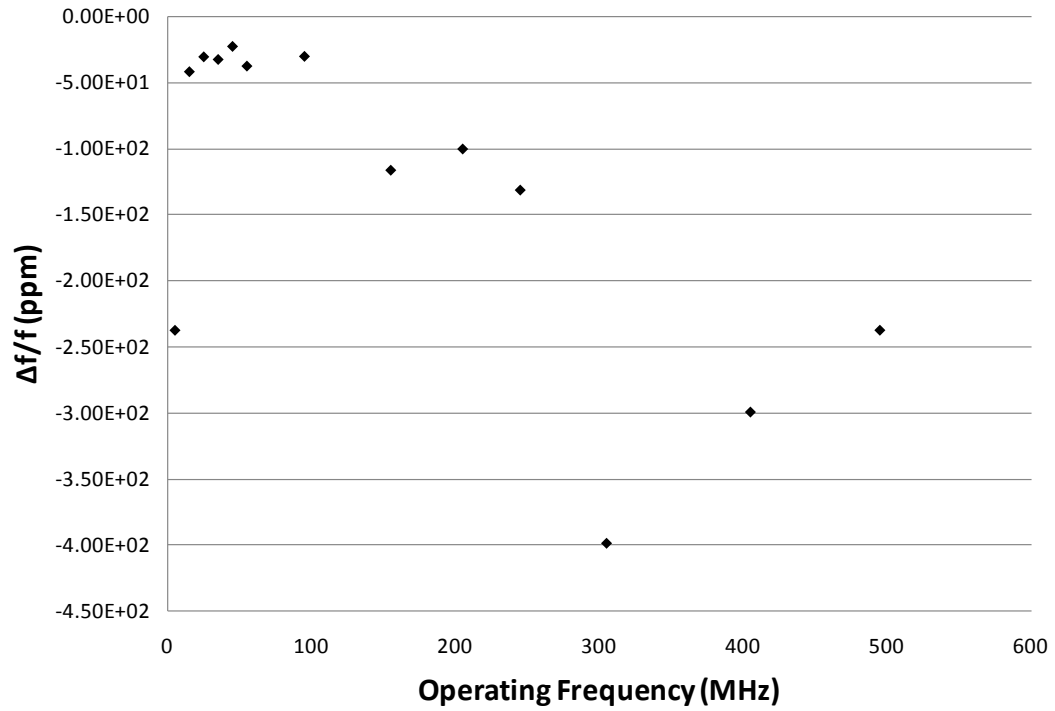


Figure 4.8 Relative frequency shift to a change in conductivity of 1235 μS as a function of operating frequency.

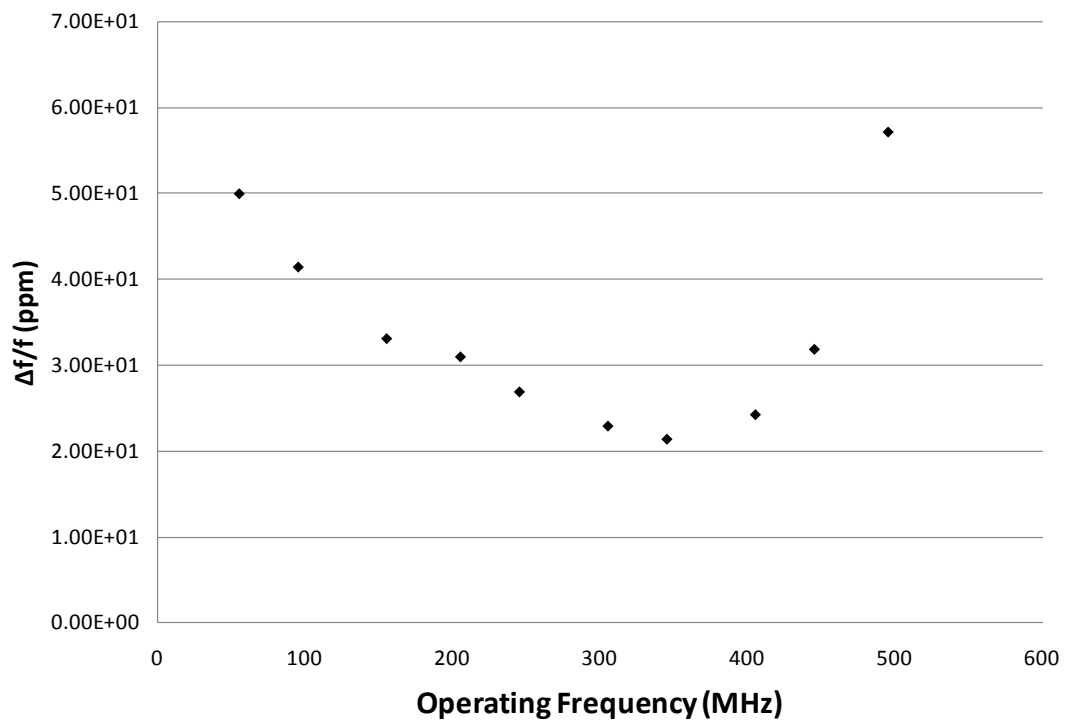


Figure 4.9 Relative frequency shift to a change in relative permittivity of 60 as a function of operating frequency.

5 THE MSCAT BIOLOGICAL SENSOR PLATFORM

5.1. Introduction

As described in Chapter 1, when a BAW sensor platform is used in a biological sensor system the sensor element consists of two components, the target selective biological film and the sensing platform. The development of the MSCAT sensor platform has been described in the previous chapters. In order to demonstrate the applicability of the MSCAT platform, it was used to detect two biological analytes which are the leading causes of foodborne illness. The detection of the first biological analyte using an MSCAT sensor platform, *Escherichia coli* (*E. coli*) O157:H7, was explored in detail while a “proof of concept” was performed for the detection of the second analyte, *Salmonella*. In this chapter background on *E. coli* as well as the current methods of detection is described. Next, the development and verification of the target selective biological sensing film that can be attached to the MSCAT sensor is presented followed by the MSCAT *E. coli* O157:H7 results. Finally, the background, current detection methods, development and verification of the target selective biological sensing film, and the MSCAT results are presented for the case of *Salmonella*.

5.2. *E. coli* Background

E. coli is one of the leading causes of food borne illnesses [89]. There are many strains of *E. coli* and although most are harmless to humans, some strains such as serotype O157:H7 can cause serious illnesses [90]. Severe cases of *E. coli*

O157:H7 exposure can cause severe intestinal cramps, diarrhea, and fever lasting up to 8 days, [90] can involve renal failure and, in small children and the elderly, death. Although *E. coli* is only one part of the fecal coliform group that can cause illness in humans it is commonly used as an indicator for fecal contamination in drinking water and food due to its ability to survive outside of the body [90].

Current methods of evaluating drinking water or food for microorganisms involve collecting samples and transporting them to a central laboratory for analysis. The samples are processed and incubated for 24 to 48 hours before the presence or absence of *E. coli* can be determined [91]. For example, the Maine Health and Environmental Testing Laboratory uses IDEXX Colilert® and Colisure® products for detecting *E. coli* O157:H7 [92]. These products are the only commercially available water tests for microbiological methods included in the Standard Methods for Examination of Water and Waste Water (20th Ed.). [93].

Recent advances in chemical and biosensor technologies have offered possible approaches for *in situ* identification and quantification of specific contaminants in water. Molecular recognition such as antibody-antigen reactions integrated with an appropriate sensing platform such as a semiconductor, a piezoelectric crystal, carbon nanotubes, nano-/microcantilevers and polymerase chain reaction (PCR) technology are currently being researched [94]. However, none of these sensing devices have been accepted as a standard method for evaluating drinking water or food samples. Clearly there is a need for a more rapid detection system for *E. coli* O157:H7.

One comparatively simple sensor that can identify and quantify specific contaminants in situ is a piezoelectric sensing platform which has been coated with a target selective chemical or biological film. In order to test the MSCAT platform as a sensor for *E. coli* O157:H7 it was necessary to develop a target selective sensing film that could be attached to the sensor surface of the MSCAT.

5.3. *E. coli* O157:H7 Selective Sensing Film

An *E. coli* O157:H7 selective sensing film based on *E. coli* O157:H7 antibodies was developed by Wark [95, 96]. Antibody based sensing films are appealing for biological agent detection because they are highly specific and can be attached to a quartz surface. Antibodies are widely used in Enzyme-linked immunosorbent assay (ELISA) tests for bacteria and have been shown to be highly selective [97], especially when a selective growth medium is used [98].

It has recently been shown that it is possible to weakly bind antibodies to bare quartz surfaces [99], however the antibodies are easily rinsed off and therefore simply putting antibodies on to the MSCAT's quartz surface is not a viable approach to produce a robust sensing film. It was therefore necessary to develop a technique for chemically attaching the *E. coli* O157:H7 selective antibodies to the quartz surface of the MSCAT.

Wark initially attempted to modify an antibody based *E. coli* O157:H7 sensing film that Berkenpas developed for a gold coated shear horizontal SAW sensor fabricated on langasite [100-105]. In this work Berkenpas found that the SAW sensor was only capable of detecting *E. coli* O157:H7 concentrations of 10^9

microbes/mL, a significantly higher concentration than the detection limit of some BAW sensors as will be described later [105]. These tests also utilized a method known as "dip-and-dry" in order to increase the sensitivity of the sensor. In a dip-and-dry test the liquid being tested is added to the sensor's surface and allowed to evaporate causing anything in the solution to dry onto the sensor's surface. The sensor's surface is then rinsed to remove anything that was not bound to the sensor's surface. The dip-and-dry method is undesirable to the food industry, however, as this method increases the risk of incidental binding of proteins that cannot be easily rinsed when they are dry such as myoglobin that is found in ground beef leading to false positives. In addition, the sensing film developed by Berkenpas was for a gold sensing surface, not a quartz surface.

Wark [96] developed a procedure to attach the *E. coli* O157:H7 selective antibodies to the MSCAT's surface utilizing an amine layer and avidin/biotin interactions. It is possible to attach amine groups directly to quartz and it is also possible to attach biotin to the amine groups. Finally biotinylated antibodies can be attached to the biotin. In order to build the *E. coli* O157:H7 selective sensing film the following procedures were undertaken (see [96] for a detailed description of the procedure). It should also be noted that this sensing film could be applied to any acoustic wave sensor with a quartz sensing surface such as an LFE or SAW.

The surface of the MCAT sensors was first thoroughly cleaned by using a Piranha cleaning procedure (a combination of sulfuric acid and hydrogen peroxide). A standard liquid silanization procedure utilizing (3-Aminopropyl) triethoxysilane was performed to produce an amine-derivatized surface on the MSCAT. The

MSCAT was then incubated for 4 hours in a 10 μ M solution of NHS-LC-LC biotin in Phosphate buffer saline (PBS) solution. PBS is a buffer solution that is often using in biological testing as helps to maintain a constant pH. The N-Hydroxysuccinimide (NHS) esters react with the amine groups on the MSCAT's surface resulting in the attachment of biotin to the amine groups. The surface of the sensor was then rinsed with a solution of 10 mM of glycine in PBS to deactivate any NHS-esters that may remain on the sensor's surface. The sensors were then incubated in a 0.33 μ M solution of NeutrAvidinTM binding protein in blocker for 1 hour. The sensors were then rinsed with blocker to fill any remaining free binding sites and then incubated for one hour in a solution of 20 μ g/ml of biotinylated *E. coli* O157:H7 antibodies in blocker. A schematic of the resulting film can be seen in Figure 5.1.

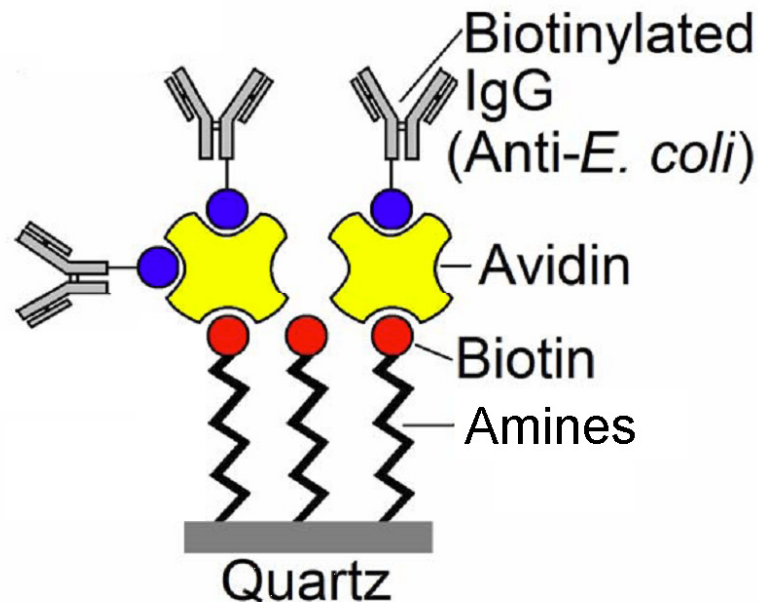


Figure 5.1 Schematic of antibody/antigen immobilization for *E. coli* O157:H7 selective film

5.3.1. Verification of the Selectivity of the *E. coli* O157:H7 Antibodies

To analyze the selectivity of the *E. coli* O157:H7 antibodies employed in the sensing film for the MSCAT *E. coli* O157:H7 sensor, an immunofluorescence assay was performed. The antibodies were tested against three different bacterium: *E. coli* O157:H7, *E. coli* K-12, and *Pseudomonas fluorescens* (*P. fluorescens*). *E. coli* K-12 and *P. fluorescens* were chosen as candidate interferents because they represent bacteria that are commonly found in food. Unlike *E. coli* which is an enteric bacteria (a bacteria which is found in the intestines), *P. fluorescens* is a non-enteric bacteria that is harmless to humans and often present on plants and sometimes used to make yogurt. *E. coli* K-12 is a serotype of *E. coli* that is closely related to *E. coli* O157:H7 and like *E. coli* O157:H7 is an enteric bacteria that is commonly found in food. Unlike *E. coli* O157:H7, however, *E. coli* K-12 is harmless to humans and its detection in food is not necessary.

In order to analyze the selectivity of the chosen antibodies, an assay was performed by exposing suspensions of each bacteria to the selected anti- *E. coli* O157:H7 antibodies (primary). After each bacteria was allowed to react with the selective antibodies for fifteen minutes the solution was centrifuged. This separated the much larger bacteria from the smaller antibodies that did not bind to the bacteria. The separated bacteria were then re-suspended in blocking buffer. Goat anti-mouse IgG-Alexa 488 which was conjugated with Alexa-488 fluorophore was then added to each suspension. The goat anti-mouse IgG antibodies will bind to the biotinylated IgG *E. coli* O157:H7 antibodies. The Alexa-488 fluorophore will fluoresce with a green wavelength when excited. Therefore if the *E. coli* O157:H7 antibodies bound to

the bacteria of interest, green fluorescence will be visible when the solution is excited.

This solution was centrifuged again to remove any unbound goat anti-mouse IgG antibodies and the remaining bacteria were again suspended in blocking buffer. Microscope slides were prepared for each sample and a fluorescent study using a Olympus BX51 optical microscope was performed to determine if the *E. coli* O157:H7 selective antibodies bound to each bacteria. The results of the study can be seen in Figure 5.2-Figure 5.4. In these figures, the presence of a fluorescent signal (green light) indicates that the *E. coli* O157:H7 selective antibodies did in fact bind to the given bacterial. The absence of a green fluorescent signal indicates that the antibodies did not bind to the bacteria.

As can be seen in Figure 5.2, the *E. coli* O157:H7 did in fact bind to the antibodies as a fluorescent signal was observed. As can be seen in Figure 5.3 and Figure 5.4, however, no fluorescent signal is present. This indicates that the selected antibodies did not bind to these two bacteria.

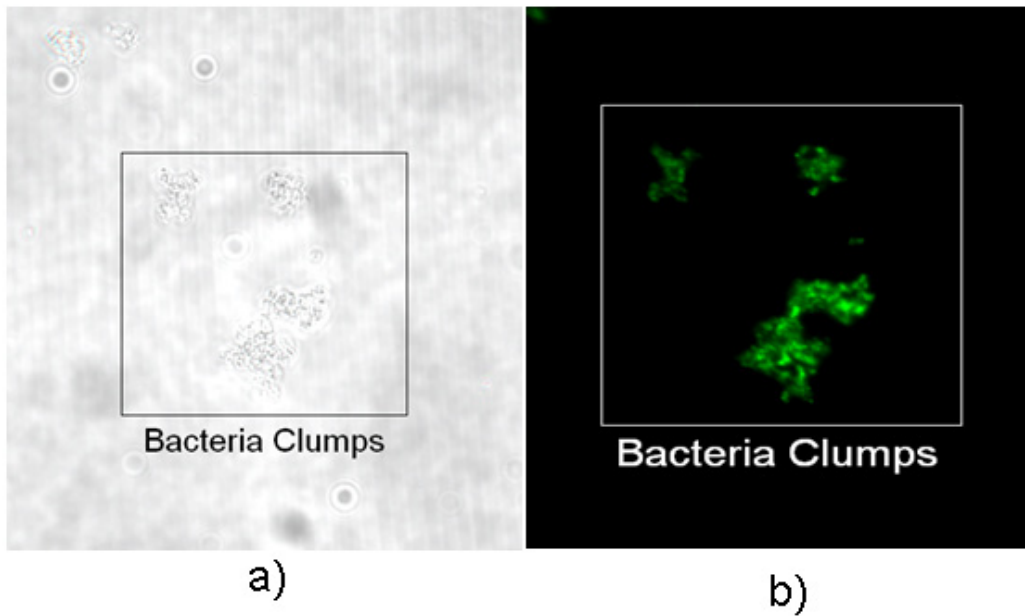


Figure 5.2 *E. coli* O157:H7 slide under a) normal light and b) fluorescence. (400x magnification)

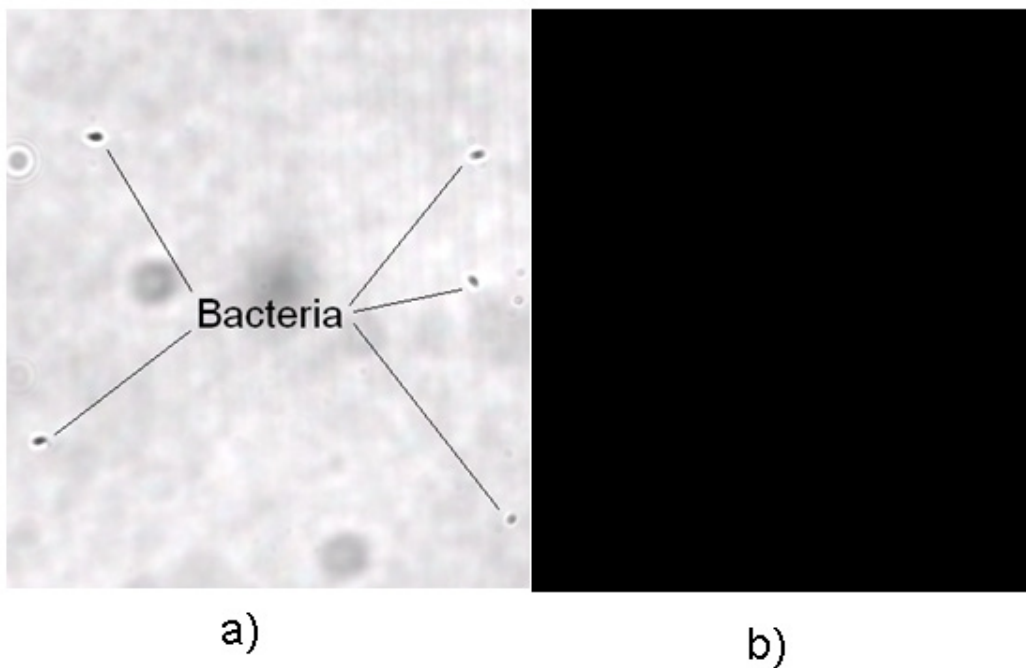


Figure 5.3 *E. coli* K-12 slide under a) normal light and b) fluorescence. (400x magnification)

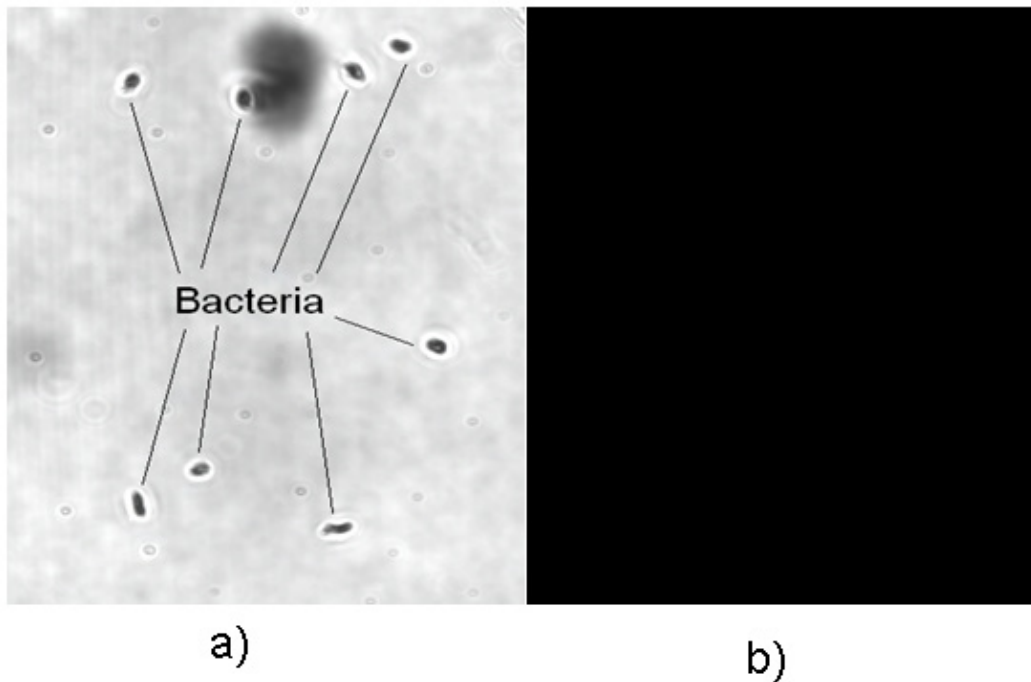


Figure 5.4 *P. fluorescens* slide under a) normal light and b) fluorescence. (400x magnification)

5.3.2. Verification of the Antibody Attachment to the MSCAT Sensor Platform

Once the *E. coli* antibodies were verified to be selective to the serotype of *E. coli* of interest, *E. coli* O157:H7, it was necessary to verify that the antibodies could in fact be bound to the MSCAT's surface using the procedure that was developed. An Amplex® Red based immunoassay was performed to verify that the *E. coli* O157:H7 selective antibodies were bound to the MSCAT's surface. Amplex® Red produces the highly fluorescent compound resorufin that fluoresces at wavelengths of approximately 550 nm when it reacts with hydrogen peroxide (H₂O₂) and can be easily detected using spectrophotometer [106]. Amplex® Red by itself has a very low background fluorescence.

Goat anti-Mouse Immunoglobulin G (IgG) horseradish peroxidase (HRP) secondary antibodies were used in conjunction with Amplex® Red to verify the attachment of the primary *E. coli* antibodies. The secondary antibodies will theoretically bind to only to the primary antibodies [96]. However, it has recently been shown that it is possible to weakly bind antibodies to bare quartz surfaces [99]. In order to remove the possibility of the secondary antibodies to non-specifically bind to empty spots on the sensor surface, the sensors were placed in bovine serum albumin (BSA) after the sensing film was placed on the MSCAT's surface. BSA will attach to any free binding sites eliminating the possibility of non-specific secondary antibody attachment. A control sensor was also used that was only exposed to BSA. The BSA would fill any available binding sites on the control MSCAT eliminating the possibility of secondary antibodies attaching to the sensor surface.

After rinsing both MSCAT's surfaces, the secondary antibodies were applied and allowed to sit for one hour then the sensors' surfaces were rinsed again. The sensors were then placed PBS. Amplex® Red was then added to the sensors. If the secondary antibodies were bound to the MSCAT's surface the Amplex® Red and HRP will produce resorufin and fluoresce at approximately 550 nm (red).

As can be seen in Figure 5.5 and Figure 5.6 the MSCAT with the primary *E. coli* antibody film produced a strong red response while the control did not. These tests were performed twice yielding similar results each time.



Figure 5.5 Photograph of MSCAT sensor with the *E. coli* antibody film after the introduction of Amplex Red.

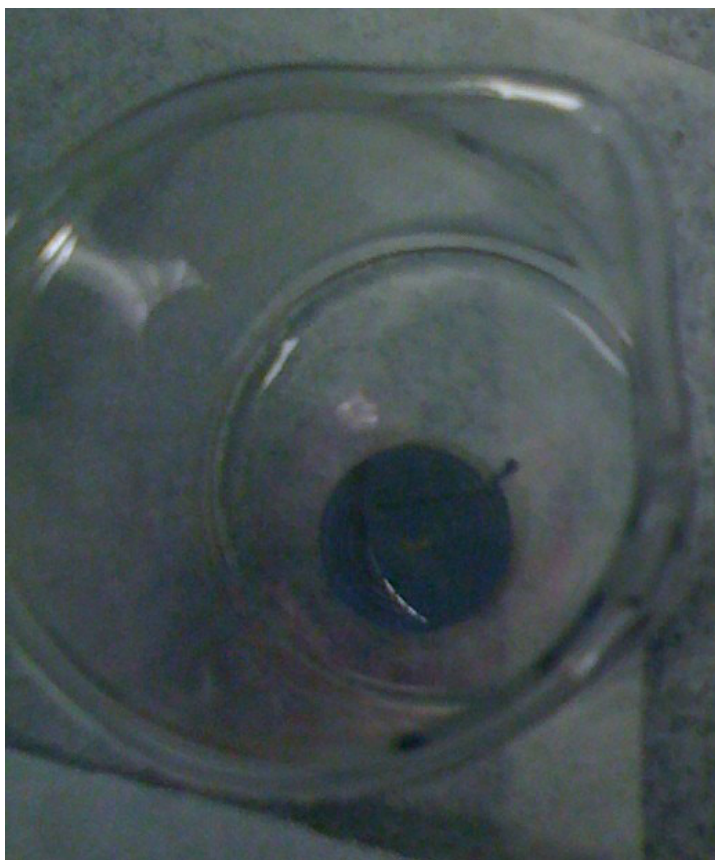


Figure 5.6 Photograph of the control MSCAT sensor without the *E. coli* antibody film after the introduction of Amplex Red.

5.3.3. Verification of the Effective Binding of *E. coli* O157:H7 to the MSCAT

Once it was verified that the *E. coli* O157:H7 selective film was attached to the MSCAT's surface it was necessary to verify that *E. coli* O157:H7 did in fact bind to the sensing film. A MSCAT sensor had the sensing film deposited on its sensing surfaces using the procedure outlined in section 5.3. A control sensor was left with a bare surface. One mL of *E. coli* O157:H7 in PBS was then applied to each sensor's surface and allowed to sit for one hour. The concentration of the *E. coli* O157:H7 was approximately 10^8 microbes/mL. Each sensor was then lightly rinsed with PBS to remove any unbound *E. coli* O157:H7. The sensors' surfaces were then placed in a 1 mL solution of Mouse anti-*E. coli* IgG fluorescein. The Mouse anti-*E. coli* IgG fluorescein is an antibody selective to *E. coli* that has a fluorescein attached to it. The fluorescein will fluoresce under 480 nm wavelength light. The sensors' surfaces were then rinsed again with PBS to remove and Mouse anti-*E. coli* IgG fluorescein that was not attached to *E. coli*. Each sensor was then viewed under an Olympus BX51 optical microscope under 480 nm wavelength light. The control MSCAT's did not exhibit any fluorescence; however it is clear from Figure 5.7 that the *E. coli* bound to the MSCAT sensors with the selective sensing film on their surface.

In order to approximate the number of *E. coli* O157:H7 that could be bound to the surface of the MSCAT the number of possible antibody binding sites were first calculated. In the MSCAT *E. coli* O157:H7 tests a cylindrical 3 mL liquid cell holder that is 1.27 cm in diameter was used. Each antibody covers an area of approximately 75 nm^2 (15 nm x 5 nm). The IgG antibodies used each have two binding sites,

therefore if the MSCAT's sensing surface is uniformly covered with antibodies there would be approximately 3.4×10^{12} binding sites. It should be noted that approximately 4×10^{14} antibodies were applied to the MSCAT's surface during deposition of the sensing film. An *E. coli* O157:H7 bacterium is approximately $1 \mu\text{m}^2$ ($2 \mu\text{m} \times 0.5 \mu\text{m}$). Given the area of the sensing surface, approximately 1.27×10^8 *E. coli* O157:H7 bacteria could be bound to the sensing surface if it is assumed that the bacteria bind in a single, flat layer. From these approximations it can be concluded that the number of antibody binding sites is not a limiting factor in the number of *E. coli* O157:H7 that can be bound to the sensor's surface. It must be stressed, however that these are only approximate values as the antibodies do not always sit in a uniform layer and the *E. coli* O157:H7 do not necessarily lie flat on the sensor's surface.

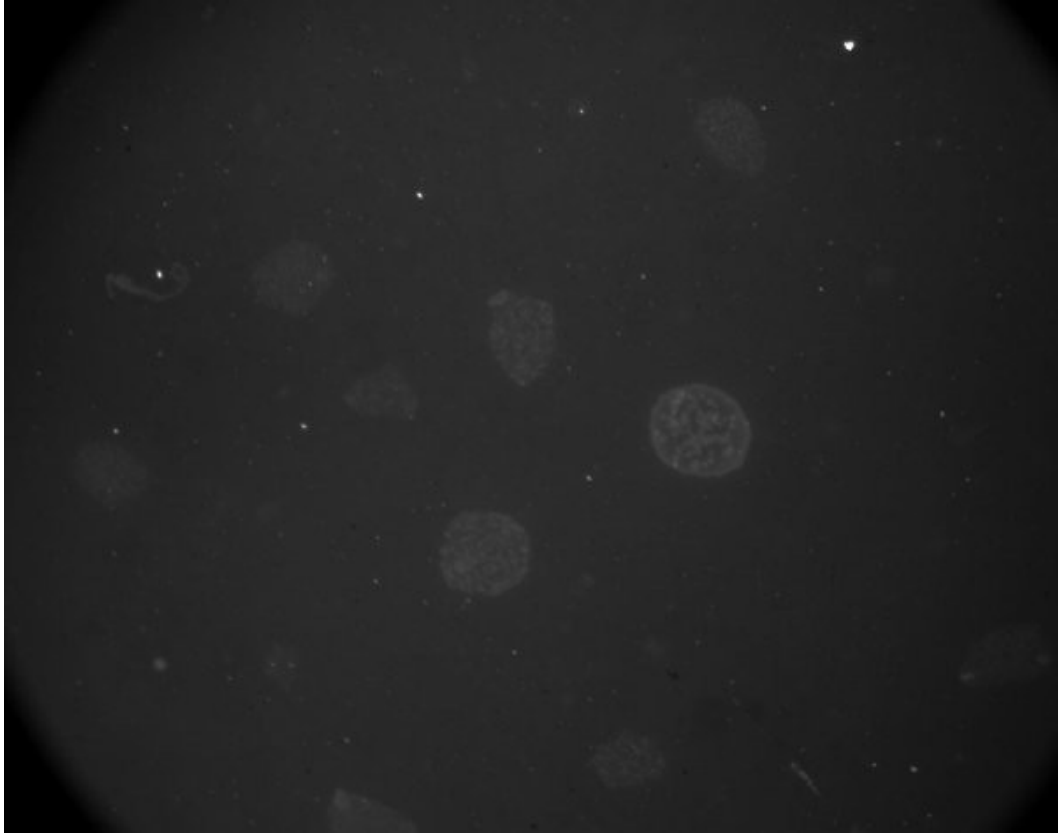


Figure 5.7 *E. coli* bound to MSCAT *E. coli* O157:H7 selective sensing film (400x magnification).

5.4. MSCAT Response Signature

The MSCAT's frequency response signature to *E. coli* is different than a typical mass loading response. It has been shown that classical BAW sensor theory such as the Sauerbrey [107] and Kanazawa [108] equations do not apply to complex liquid phase sensing problems [109]. In order to utilize MSCAT sensors for the detection of *E. coli* O157:H7 it was first necessary to determine the nature of the MSCAT response when *E. coli* O157:H7 attached to the sensing film.

MSCAT sensors were functionalized for the detection of *E. coli* O157:H7 by first vigorously cleaning the bare sensing surface of each of the platforms using a Piranha cleaning procedure (a combination of sulfuric acid and hydrogen peroxide). A [8, 250, 515] spiral coil design as described in Chapter 3 was used for these tests. The *E. coli* O157:H7 selective film described in section 5.3 was applied to the MSCAT's surface. A 1.27 cm diameter liquid cell holder that is capable of holding 3 mL was clamped onto the MSCAT sensor. For the avidin and antibody layers 1 mL of liquid was placed on the sensor surface. The sensors were then exposed to 1 mL liquid samples containing suspensions of non-pathogenic *E. coli* O157:H7 bacteria in PBS. The concentration of these samples was approximately 10^8 microbes/mL. The

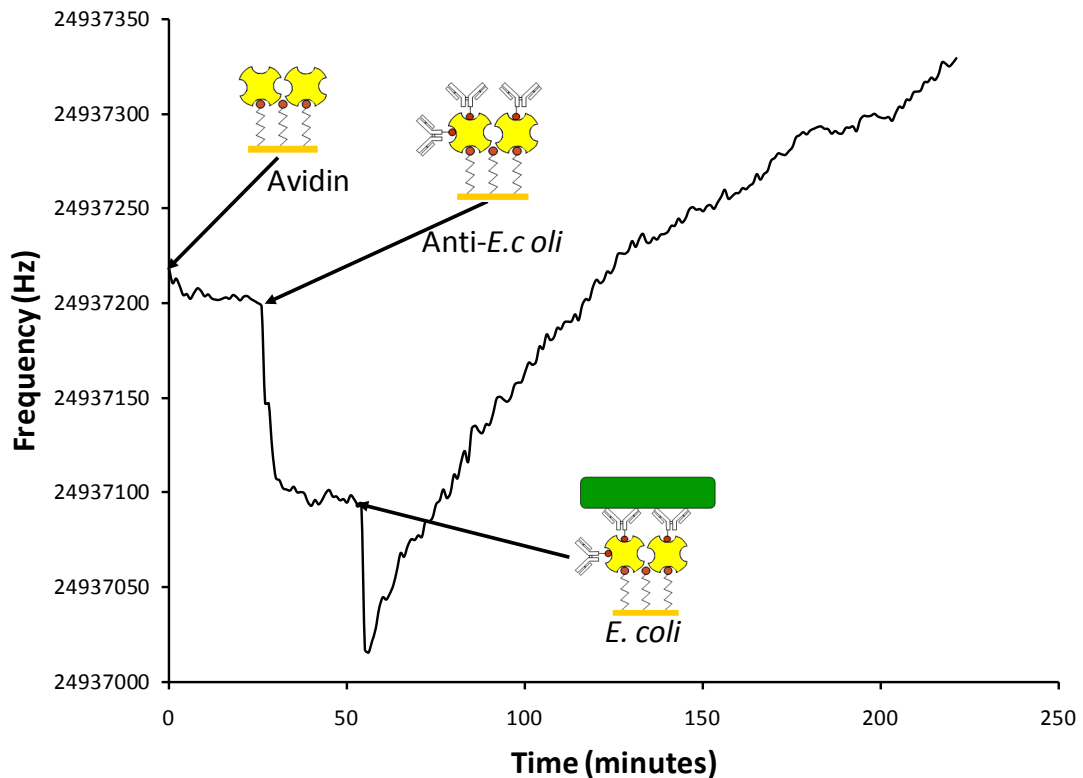


Figure 5.8. The MSCAT sensor response to the layers of the bio-film and *E. coli* O157:H7 in solution

frequency response of the MSCAT was recorded over time and a response signature was obtained for the MSCAT sensor of which a representative signature is shown (Figure 5.8).

The MSCAT response signature shown in Figure 5.8 displays the typical mass-loading responses usually recorded from an acoustic wave sensor for the avidin and antibody layers. The response from the addition of *E. coli* O157:H7 is different. The initial downward trend of the response after *E. coli* O157:H7 is introduced is followed by a positive resonant frequency shift over time. It was this positive frequency shift that was used for the MSCAT sensor's response signature. When *E. coli* O157:H7 is bound to the sensor surface it not only effectively increases the thickness of the film but also changes the elastic properties of the film. The positive resonant frequency shift observed in the sensor upon exposure to *E. coli* may be explained by the visco-elastic effects of the biological film on the sensor's surface which hide any mass-loading response [110], however the BAW detection mechanism for antibody based sensing films is not well understood. Optical tests using a microscope at 400x magnification performed on MSCAT sensors exposed to *E. coli* O157:H7 confirmed that the *E. coli* O157:H7 had in fact bound to the sensor surface and the sensor's response was not due to the film being removed from the sensor surface.

Recently Cavic *et. al.* have introduced the idea of "apparent slip" to explain a similar positive frequency shift observed in BAW sensors when used for the detection of biological analytes [111]. If it is assumed that the sensing layer is rigidly bound to the substrate's surface than any addition to the sensing film would result in the

effective thickness of the transducer increasing and therefore an increase in the effective wavelength of the acoustic wave and an overall resonant frequency decrease. In actuality, however, the sensing layer is not rigidly bound to the sensor surface but connected by linkers such as amines and biotin/avidin (see Figure 5.1). In this case the bonds can rotate or bend. During the course of the sensor's oscillation the surface of the substrate will reverse direction at the end of each oscillation (Figure 5.9). As the substrate surface reverses direction the sensing film continues in its original direction due to its momentum until it is "pulled back" by its attachment to the sensor substrate leading to the phenomenon known as "apparent slip" - there is a lag time between when the substrate changes direction at the end of the oscillation and when the sensing film changes its direction. If the properties of the sensing film changes due to the attachment of *E. coli*, then the degree of apparent slip of the film will change which can prevent the substrate surface from transmitting energy as far into the sensing film. This would result in the apparent thickness of the transducer decreasing and thus increasing the resonant frequency of the device.

It should be noted that the LFE exhibited the same positive frequency shift as the MSCAT when it was used to detect *E. coli* O157:H7 [112]. Although the concept of "apparent slip" does offer some insight into the mechanism behind the MSCAT's response to the addition of *E. coli* O157:H7 there is currently no concrete theory that can predict the optimum operating frequency for a given sensing film. Therefore it was necessary to experimentally determine the optimum operating frequency of the MSCAT for the detection of *E. coli* O157:H7 with the *E. coli* O157:H7 selective sensing film described in section 5.3.

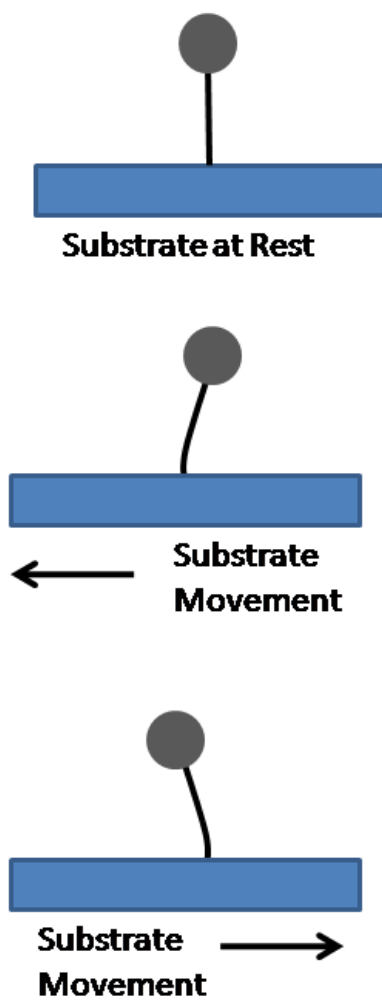


Figure 5.9 Diagram showing sensor substrate (rectangle), linker (line), and sensing film molecule (sphere) during oscillation. There is a lag between the time when the substrate changes directions and the film changes directions leading to "apparent slip."

5.5. Determination of Lowest *E. coli* O157:H7 detection limit.

The United States Food and Drug Administration (FDA) recommended detection limit for *E. coli* O157:H7 detection is 1 microbe/mL. In order to achieve this very high level of sensitivity it is usually necessary to incubate the sample for a given amount of time to grow the *E. coli* O157:H7 population to a detectable level. Therefore the overall detection time is a function not only of the actual detection time of the sensor to a given *E. coli* O157:H7 concentration but also the time to incubate the sample to the minimum detection limit of the sensor.

Current testing methods take approximately 24 hours which means that in a food processing facility the food must be held for an entire day before it can be shipped. If a testing method could be developed, however, that would allow the food processing facility to detect the presence of a single *E. coli* O157:H7 bacterium in less than 12 hours (a typically work shift) then the food could be tested and shipped in the same day, significantly reducing costs as well as the risk of food spoilage and contamination.

Wark measured the number of *E. coli* O157:H7 during their incubation and produced the *E. coli* O157:H7 growth curve seen in Figure 5.10 [96]. It should be noted that this test was performed under optimal conditions (nutrients, temperature) to promote *E. coli* O157:H7 growth and *E. coli* O157:H7 colonies obtained from food samples may grow slower. Typically, the *E. coli* O157:H7 initially experience a lag phase where the growth is slow. Typically a few hours after the lag phase starts the *E. coli* O157:H7 growth enters the log phase where the bacteria multiply rapidly. After 3-8 hours the *E. coli* O157:H7 enter the stationary phase where the nutrients in

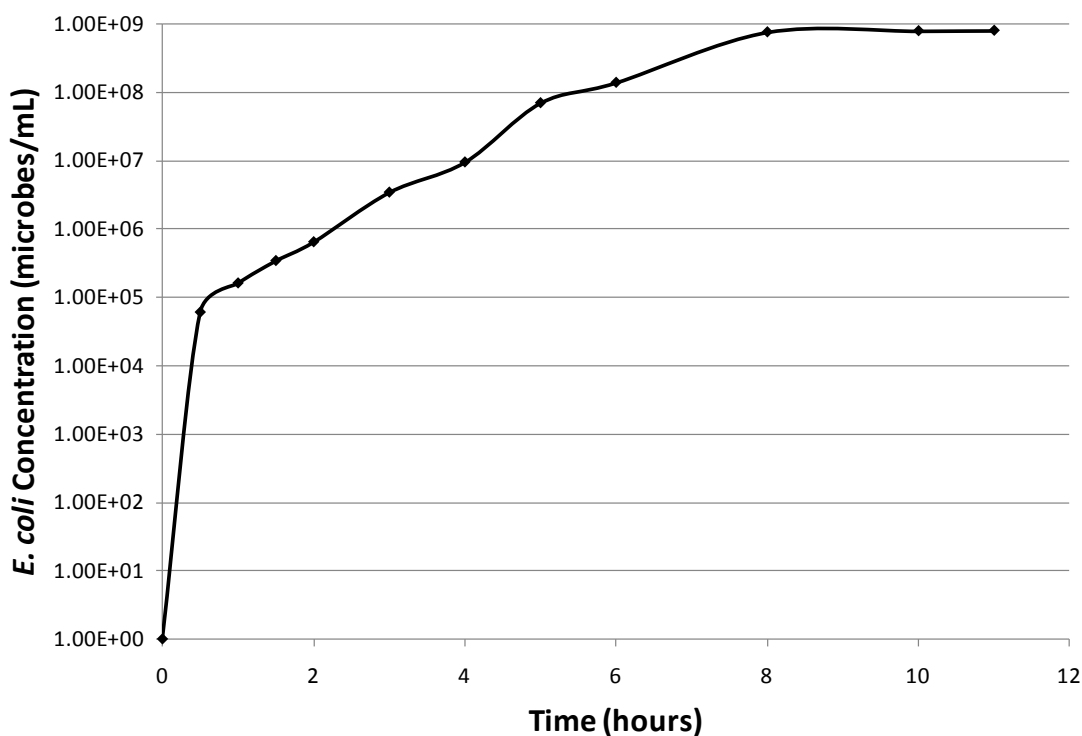


Figure 5.10 Typical growth curve for *E. coli* O157:H7 (log scale).

the solution decrease and the number of bacteria stabilizes. In order to minimize the overall detection time (incubation time + sensor response time) it is desirable to not only minimize the sensor's response time but to also achieve the lowest possible *E. coli* O157:H7 detection limit which will minimize the required incubation time.

Initially it was believed that a MSCAT operating at the highest possible operating frequency would provide the highest level of sensitivity as classical BAW theory such as the Sauerbrey [107] and Kanazawa [108] equations predict that BAW sensor sensitivity increases with operating frequency. This, however, proved not to be the case. In order to determine the lowest detection limit of the MSCAT, it was necessary to develop an approach that minimized the number of tests due to the time and cost required for each test. Initially, an MSCAT sensor was coated with the

biological film described in section 5.3. The sensor was operated at its 3rd harmonic and exposed to a 1 mL liquid sample containing suspensions of non-pathogenic *E. coli* O157:H7 bacteria starting at a concentration of 10⁸ microbes/mL in PBS, the lowest detection limit of the LFE sensor with the same fundamental frequency of the MSCAT (5 MHz) and using a very similar sensing film [112]. Since the MSCAT's frequency response is recorded using a network analyzer and then analyzed after the test, it is necessary to select a detection time before the starting the test. It should be noted that the detection time for the LFE sensor in these tests was 8 hours instead of the 4 hours used in the MSCAT tests. If the sensor was able to detect the *E. coli* O157:H7 within 4 hours, the sensing film was removed from the sensor's surface by piranha cleaning the sensor and the sensing film was reapplied. The MSCAT was considered to have detected *E. coli* O157:H7 if the sensor's response increased by at least a factor of five above the sensor response noise within the four hour detection window. The sensor was then exposed to a liquid sample containing concentrations of *E. coli* O157:H7 ten times lower than the previous sample. If the sensor was unable to clearly detect the *E. coli* O157:H7 within 4 hours, it was operated at the next odd harmonic. This process was repeated until the lowest detection limit for the MSCAT sensor was obtained. Each test was performed at least twice. Table 5.1 shows the lowest frequency at which the detection of *E. coli* O157:H7 was achieved. As can be seen in Table 5.1, the MSCAT sensor was able to detect *E. coli* O157:H7 at concentrations as low as 10⁴ microbes/mL when operated at its 59th harmonic (295 MHz), 4 orders of magnitude lower than the detection limit of the LFE sensor. Figure 5.11 shows a typical frequency response of the MSCAT sensor in these tests.

Table 5.1 MSCAT operating frequency and frequency shift for various concentrations of *E. coli* O157:H7

<i>E. coli</i> Concentration (microbes/mL)	MSCAT Frequency (MHz)	Frequency Shift (Hz)
10^8	15	620
10^7	15	391
10^6	55	71
10^5	105	433
10^4	295	1340

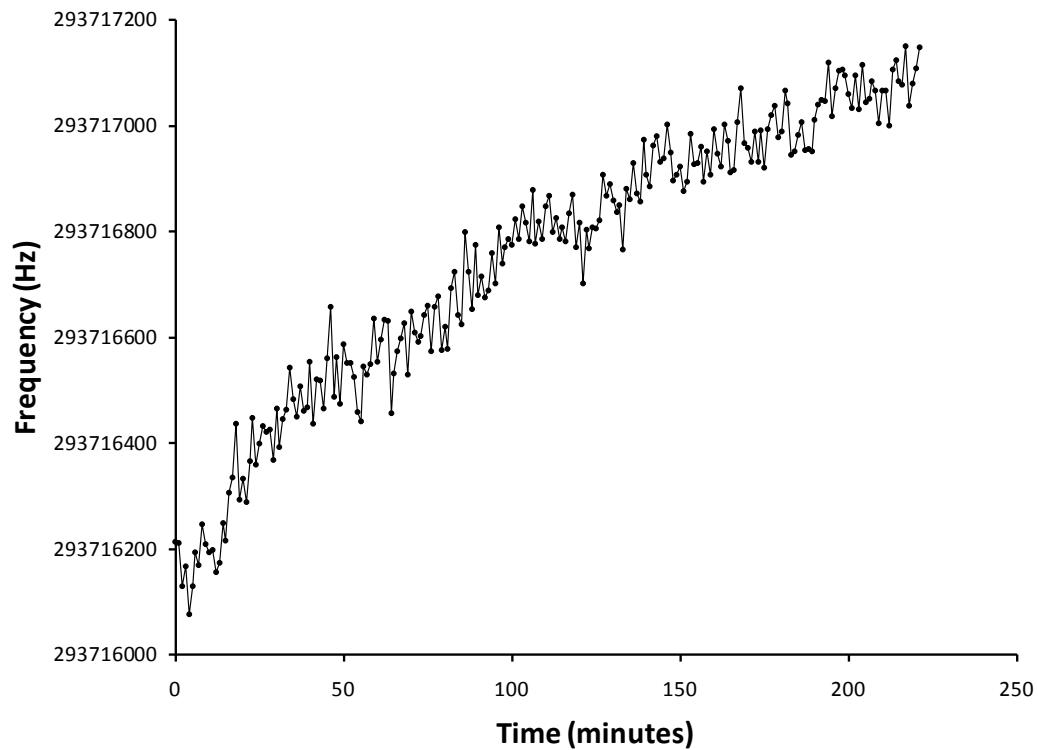


Figure 5.11 MSCAT sensor's response to a liquid sample containing 10^4 microbes/mL of *E. coli* O157:H7 when operated at the 59th harmonic.

Although there are many factors that affect the growth rate of *E. coli* O157:H7 including the nutrient level in the medium, temperature, and health of the starting *E. coli* O157:H7 colony [113], a conservative estimate is that it takes approximately 3 hours of incubation after a 2 hour lag phase for a single bacterium colony of *E. coli* O157:H7 to reach a concentration level of 10^4 microbes/mL for a total incubation time of 5 hours. Thus the response time of the MSCAT is conservatively predicted to be about 9 hours for the single bacterium case, allowing for the current 4 hour sensor response time as well as the 2 hour lag time and 3 hour incubation time. This response time is a vast improvement over the more than 24 hour response time of FDA approved methods and would allow food processor to test and ship food in a single 12 hour work shift. Based on the *E. coli* O157:H7 growth experiments performed by Wark (Figure 5.10), under ideal conditions a concentration level of 10^4 microbes/mL can be reached in under an hour of incubation time. It should be noted that in these tests, the MSCAT's sensor response was recorded for the four hour detection window before it was analyzed. As can be seen in Figure 5.11 the MSCAT's resonant frequency increase by approximately 100 Hz within the first hour, well above the signal noise. It is likely that the detection time could be decreased significantly once electronics systems such as an oscillator circuit are developed that allow real-time monitoring of the MSCAT's frequency response.

Even though the MSCAT sensors used in these test were able to operate at 465 MHz with good signal strength and Q, subsequent increases in the MSCAT sensor's operating frequency did not allow lower concentrations of *E. coli* O157:H7 to be detected and in fact the magnitude of the frequency response decreased. Section

5.4 describing the "apparent slip" effect provides some insight into this phenomenon. It has also recently been shown that for many acoustic wave biological sensing applications proper selection of the sensor operating frequency is critical due to the fact that the depth that the acoustic wave penetrates the sensing layer depends on the operating frequency of the sensor [114]. It was also shown in this work that approximately 300 MHz was the optimum operating frequency for antibody/antigen type sensing films which is further confirmed by this study which found that 295 MHz is the optimum operating frequency for the sensing film. This highlights one of the main strengths of the MSCAT: the ability of the MSCAT sensor to operate at a wide range of frequencies by exciting high order harmonics allows one to tune the MSCAT's operating frequency to the optimal frequency for a given sensing application.

The MSCAT also provides the mechanism for "acoustic spectroscopy." The potential benefits of acoustic spectroscopy were first postulated by Araya-Kleinstuber *et. al* [99]. The fundamental concept of acoustic spectroscopy is that if a sensor platform was developed that could operate over a wide range of frequencies it would be possible to "probe" the sensing film at many different frequencies possibly leading to increased sensitivity and selectivity in complex sensing environments where many different analytes of interest may be present due to the fact that the sensor would be most sensitive to different analytes at different frequencies. Chapter 4 discusses the potential use of acoustic spectroscopy to separate the effects liquid mechanical and electrical property changes have on a BAW sensor's frequency response.

5.6. Detection of *E. coli* O157:H7 in Real World Sensing Environments

In order to test the MSCAT *E. coli* O157:H7 sensor in real-world sensing environments, two sensing scenarios were selected. In the first, untreated well water obtained from a local Maine source was inoculated with *E. coli* O157:H7. The *E. coli* O157:H7 selective sensing film was attached to a MSCAT sensor as described in section 5.3 and the sensor was exposed to the inoculated well water. The MSCAT was operated at its 5th (approximately 25 MHz) harmonic in these tests. The MSCAT was first tested by placing 1 mL of well water with no *E. coli* O157:H7 present on the sensors surface to insure that sensor did not react to any chemical or biological interferences that may be present in the sample. As can be seen in Figure 5.12 the MSCAT's frequency response was stable during this test. The well water was removed from the sensor's surface and 1 mL of well water inoculated with *E. coli* O157:H7 (10^8 microbes/mL of well water) was then applied to the sensor's surface. As seen in Figure 5.13, the MSCAT was able to detect the *E. coli* O157:H7 in the well water and the sensor's frequency shift over time from when the liquid was introduced exhibited the characteristic increase in resonant frequency when *E. coli* O157:H7 is present. From these results it can be concluded that the MSCAT is capable of detecting *E. coli* O157:H7 even in drinking water that may contain chemical or biological interferences.

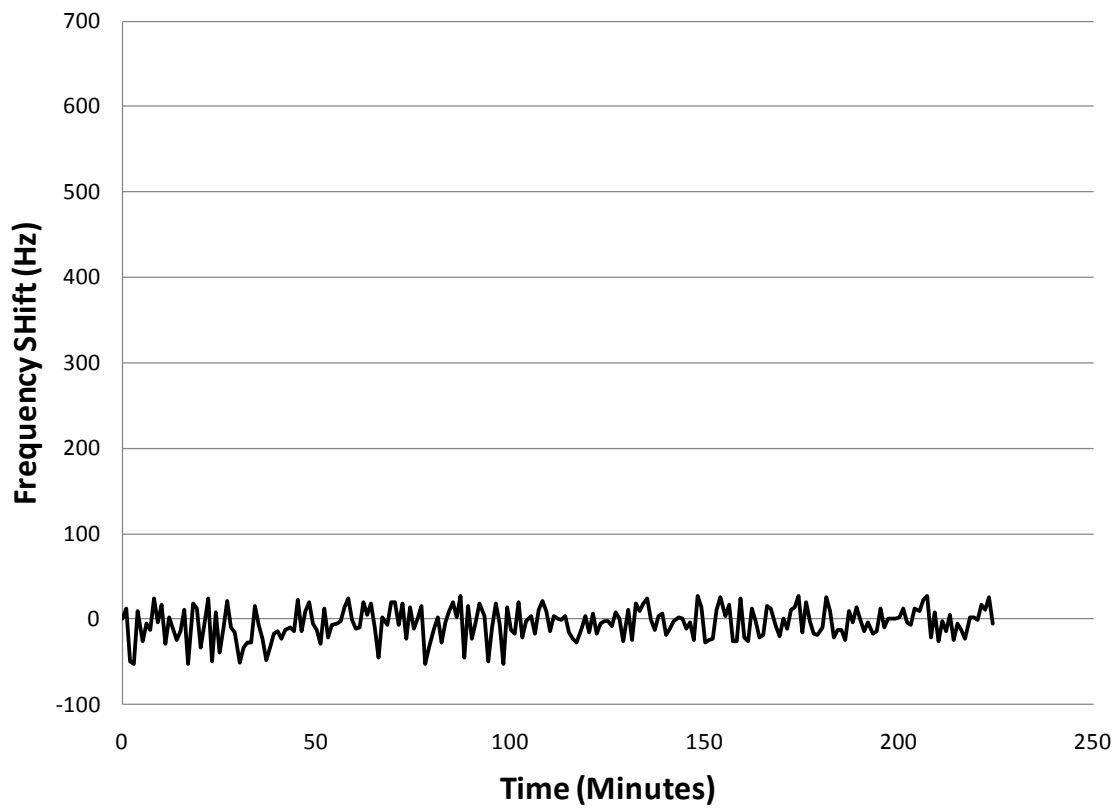


Figure 5.12 MSCAT sensor's response to well water.

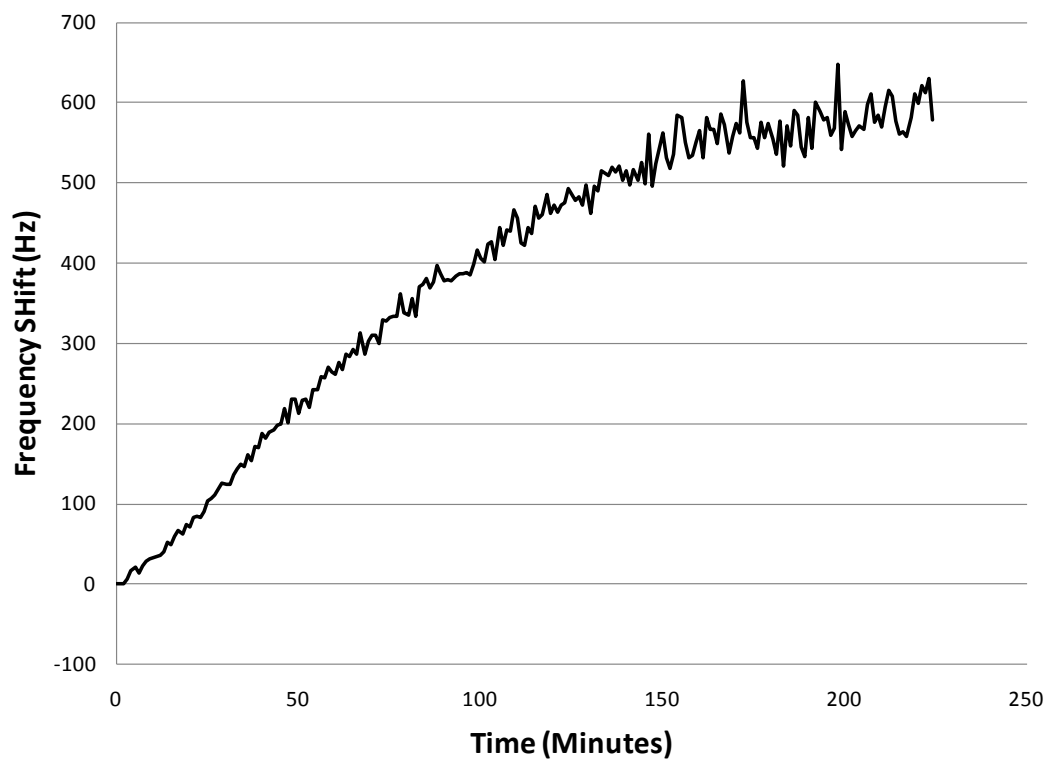


Figure 5.13 MSCAT sensor's response to well water inoculated with *E. coli* O157:H7.

Based on the promising results obtained for well water, apple juice was chosen as a model food item. Pasteurized apple juice was inoculated with *E. coli* O157:H7 and a MSCAT sensor had the *E. coli* O157:H7 selective sensing film attached to its surface as described in section 5.3 above. The sensor was operated at its 5th harmonic in these tests. The MSCAT was first tested by placing 1 mL pasteurized apple juice with no *E. coli* O157:H7 present on the sensors surface to ensure that sensor did not react to any chemical or biological interferences that may be present in the food sample. As can be seen in Figure 5.14 the MSCAT's frequency response was relatively stable during this test although it exhibited slightly more drift than the well water tests. The apple juice was removed from the sensor's surface. One mL of apple juice inoculated with *E. coli* O157:H7 (10^8 microbes/mL of apple juice) was then applied to the sensor's surface. The sensor's frequency response can be seen in Figure 5.15. As was the case with the well water, the MSCAT was able to detect the *E. coli* O157:H7 in the apple juice and the sensor's frequency shift over time from when the liquid was introduced exhibited the characteristic increase in resonant frequency when *E. coli* O157:H7 is present while the MSCAT sensor's frequency did not change when a sample containing only the apple juice that was not inoculated with *E. coli* O157:H7. It should be noted, however, that the frequency response for the apple juice inoculated with *E. coli* O157:H7 was approximately half as large as response for the well water inoculated with *E. coli* O157:H7 indicating that the apple juice may inhibit the binding of *E. coli* O157:H7 to the sensing film. One possible explanation for this is that the pH level varies significantly between water (~7) and apple juice (~3). It has been shown that pH level can affect antibody

binding [115]. Based on these results it may be necessary to adjust the pH level of a food sample before it is introduced to the MSCAT sensor in order to maximize the sensor's sensitivity.

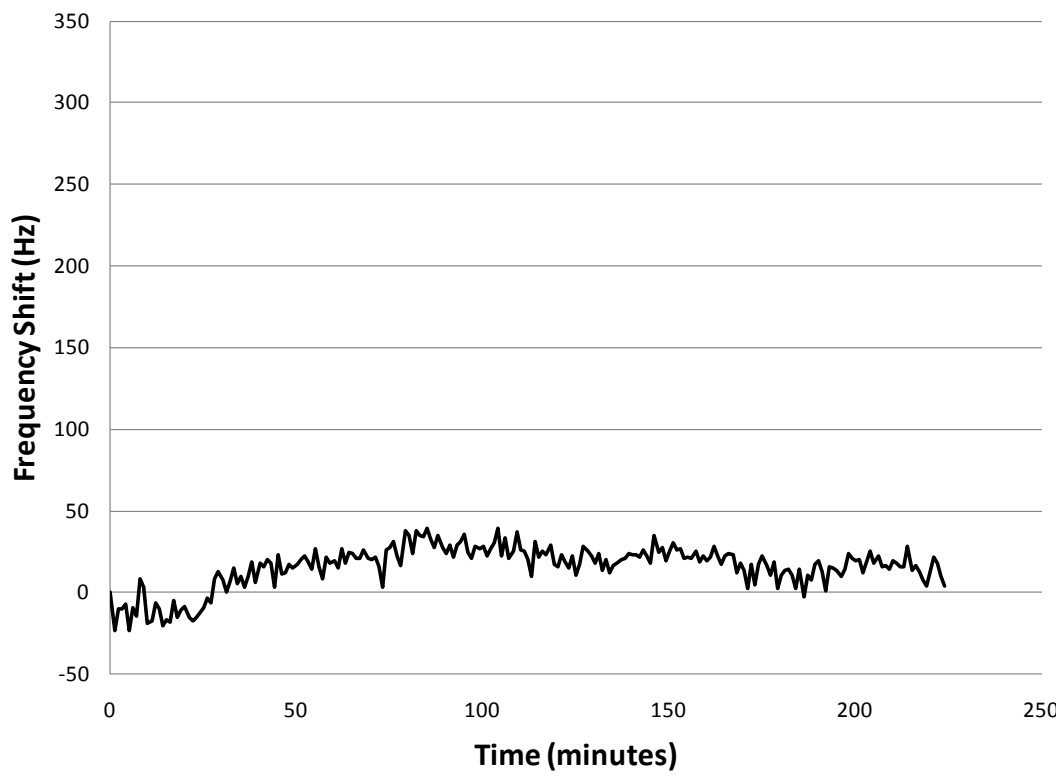


Figure 5.14 MSCAT's sensor response to apple juice.

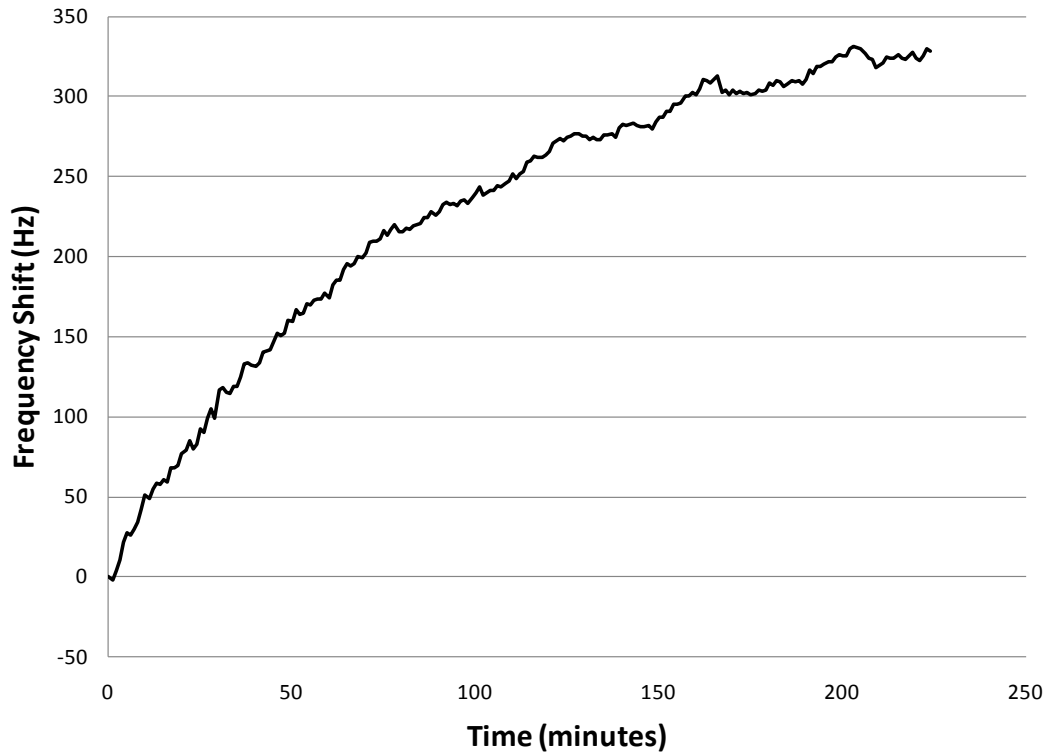


Figure 5.15 MSCAT sensor's response to apple juice inoculated with *E. coli* O157:H7.

In order to realize an MSCAT *E. coli* O157:H7 sensor system that can be used in real-world applications several tasks must be accomplished including: utilize an incubation process to improve the sensitivity and response time of the MSCAT immunosensor to *E. coli* O157:H7, possibly developing a method to adjust the pH of the sample, develop the electronics to collect, process, and store the sensor response, develop the overall sensor system (integration of sample preparation, pre-filtration, sensing element, electronics), and test the sensor system in the lab and in the field, comparing the results with established products such as Colilert (IDEXX Laboratories, Westbrook, ME). Based on the promising results obtained for *E. coli* O157:H7, the detection of a second biological analyte using the MSCAT was explored.

5.7. *Salmonella* Background

The promising results obtained for *E. coli* O157:H7 resulted in preliminary research being undertaken to determine if the MSCAT coated with a *Salmonella* selective antibody based film could be used to detect *Salmonella*. There are approximately 2400 serotypes of *Salmonella* bacteria, 500 of which are of concern for the food industry due to the possibility of negative health effects in humans [116]. The two most common serotypes in the United States are Typhimurium and Enteritidis [117]. *Salmonella* Typhimurium DT104 is especially dangerous as it is highly virulent and resistant to a number of antibiotics [117].

The US FDA method to detect *Salmonella* is outlined in the Bacteriological Analytical Manual (BAM) [118]. This method can take up to 4 days and involves an enrichment and isolation procedure using Buffered Pepton Water (BPW)

Tetrathionate (TT) enrichment broth followed by plating on three different agar plates; Brilliant green novobiocin (BGN) agar, Xylose lysine Tergitol 4 (XLT-4) agar, and Bismuth sulfite (BS) agar. Samples are incubated in the TT enrichment broth for 24 hours and the agar plates are then streaked and incubated for an additional 24 hours. 5 typical colonies are selected from each plate and incubated on TSI and LIA slants for another 24 hours. If *Salmonella* is present, the TSI slant will turn red or yellow while the LIA slant will turn purple. Clearly this is a time and labor intensive sensing approach that is not practical for rapid, large volume screening of food samples.

The concern for consumer safety in foods has resulted in research on sensor systems which can rapidly detect pathogens. In contrast to the BAM approach, practically all rapid detection methods are focused on the detection of a low number of targets. This approach is ideal for screening large numbers of food or liquid samples necessary for quality control.

BioControl's Association of Official Analytical Chemists (AOAC) certified Assurance[®] Gold EIA and VIP *Salmonella* tests utilize enzyme immunoassays based on antibodies selective to *Salmonella*. Although results may be read visually or instrumentally within 10 minutes after introducing an enriched sample with a microplate reader, the tests still require a 24+ hour incubation. In addition they also require complex, hands on lab based procedures to prepare the sample for each test. Neogen's Gene-Trak[®] *Salmonella* Assays which utilize kinetic-based DNA hybridization to selective detect *Salmonella* in food samples are another AOAC certified test currently available on the market. Like the BioControl tests, however,

Gene-Trak[®] *Salmonella* tests require lengthy (40-48 hour) incubations and complicated, hands-on lab based test procedures that are estimated by the manufacturer to take approximately 2 hours [119]. DuPont also markets a AOAC certified *Salmonella* test, the BAX[®] System PCR Assay. This test is based on polymerase chain reaction (PCR) analysis of *Salmonella* - specific DNA fragments. Although the BAX[®] tests require minimal hands-on sample preparation, they do require the same lengthy incubation step as the other tests as well as a 4 hour processing in the required automated testing unit. Head to head tests that have compared the BAM method with the BAX, Gene-Trak, and Gold EIA tests have found that although the BAX tests have the lowest detection limit, they had an unacceptably high false negative rate of nearly 10% [120]. Strategic Diagnostics, Inc. has recently introduced an AOAC validated *Salmonella* test, the RapidChek[®]. These tests utilize a proprietary bacteriophage which selectively infect the bacteria as the selective agent. Although the RapidChek[®] tests are capable of detecting one *Salmonella* cell in a 25 g food sample, these tests still require the use of a proprietary enrichment broth followed by a 24 sample incubation. Although there are tests on the market that are capable of detecting small amounts of *Salmonella* in food, they are all lab based, require complex testing procedures, and require at least a 24 hour incubation time. Clearly there is a need for a more rapid testing method in order to minimize the time food must be held before it goes to market.

5.8. Salmonella Selective Sensing Film

A *Salmonella* selective sensing film based on *Salmonella* antibodies was developed by Wark [96] using a similar approach to the approach described previously for *E. coli* O157:H7. Due to the fact that the *Salmonella* antibodies were not biotinylated it was necessary to use aldehyde to bind the antibodies to the MSCAT's surface. The antibodies were covalently bound to the quartz of the MSCAT sensor platforms by first silanizing the sensor surface with 3-Aminopropyltriethoxysilane, leaving a primary amine group-terminated surface. Unlike the *E. coli* O157:H7 sensing film, an aldehyde layer is used to bind the *Salmonella* selective antibodies to the quartz surface of the MSCAT. A free carbonyl group on the aldehyde binds to the amines. After the amine layer was deposited, the sensors were then incubated in a 5% glutaraldehyde solution for 1 hour. A solution containing the *Salmonella* antibodies in the same concentration as the *E. coli* antibodies (approximately was 4×10^{14} antibodies) then added and allowed to incubate for 12 hours. The amine terminated antibodies were bound to a free carbonyl group on the aldehyde. Figure 5.16 shows a diagram of the *Salmonella* selective sensing film.

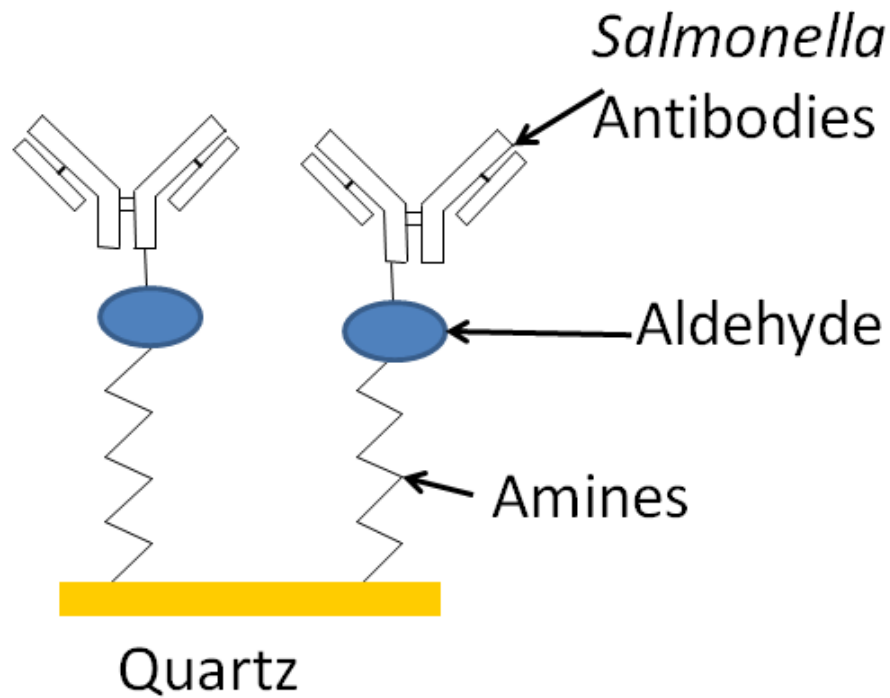


Figure 5.16 Schematic of *Salmonella* Selective Sensing Film

5.8.1. Verification of the *Salmonella* Antibody Attachment to the MSCAT Sensor Platform

In order to verify that *Salmonella* was in fact binding to the MSCAT's surface, the same procedure described in section 5.3.2. was performed. Two MSCAT sensors had the sensing film deposited on their sensing surfaces using the procedure outlined in section 5.8. A bare control sensor with no *Salmonella* selective sensing film was also used. Each sensor was exposed to 1 mL of *Salmonella* for four hours. The concentration of the *Salmonella* was approximately 10^9 microbes/mL. Each sensor was then lightly rinsed with PBS to remove any unbound *Salmonella*. Each sensor

was examined under an Olympus BX51 optical microscope. Figure 5.17 shows the *Salmonella* bound to the MSCAT that had the sensing film while Figure 5.18 shows that *Salmonella* did not bind to the bare MSCAT.



Figure 5.17 *Salmonella* bound to the MSCAT's surface (800x magnification)



Figure 5.18 Bare MSCAT with no *Salmonella* bound to the MSCAT's surface (800x magnification)

5.9. MSCAT *Salmonella* Results

The *Salmonella* selective sensing film described previously was applied to a MSCAT sensor. A [8, 250, 515] spiral coil design as described in Chapter 3 was used for these tests and the sensor was operated at its fundamental frequency. The MSCAT was allowed to stabilize for 80 minutes in PBS buffer and then *Salmonella* (approximately 10^9 microbes/mL in PBS buffer) was applied to the sensor surface. The MSCAT's response signature seen in Figure 5.19 is similar to the MSCAT's response to *E. coli* O157:H7 (see Figure 5.8), however the sensor response exhibits considerably more noise with the *Salmonella* selective film than with the *E. coli*

O157:H7 selective film. The cause of this additional noise is not known at this point but it is believed that it is caused by the *Salmonella* selective sensing film which utilizes aldehyde instead of avidin and biotin.

Although these *Salmonella* results are promising and demonstrate that it is possible to develop MSCAT sensors for a wide range of pathogenic bacteria a significant amount of future work remains. The chemistry to attach non-biotinylated antibodies to the quartz MSCAT surface should be further developed to minimize the noise exhibited by the MSCAT's frequency response. In addition, it will be necessary to determine the optimum operating frequency of the MSCAT for this new film. Finally the new *Salmonella* sensor should be tested to determine its lowest detection limit and to verify that it is able to detect *Salmonella* in real-world sensing environments.

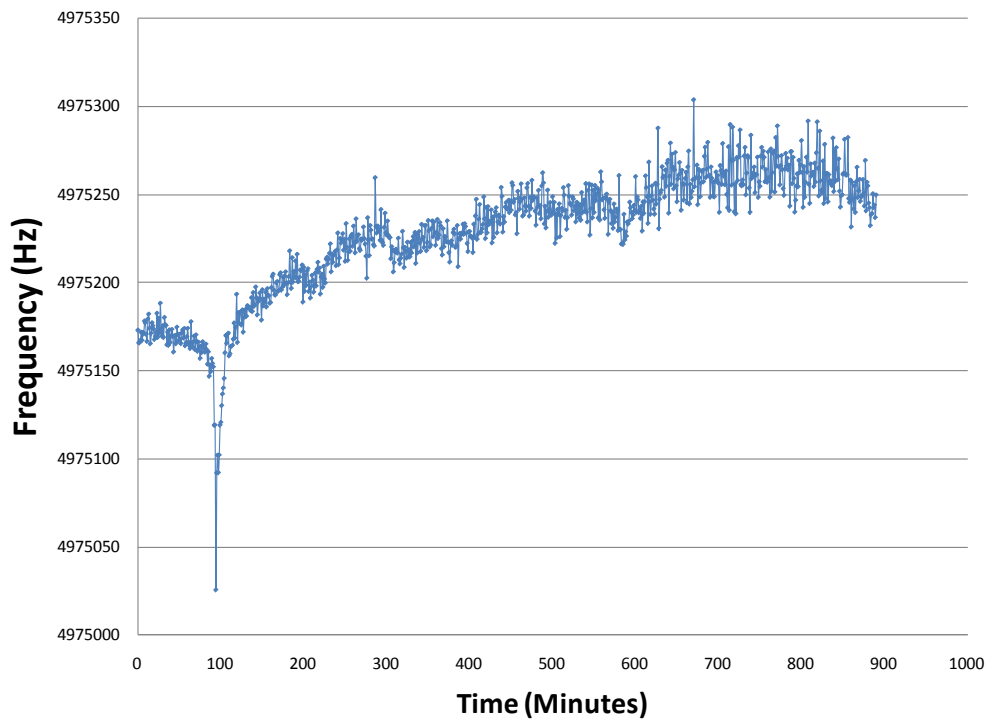


Figure 5.19 The MSCAT sensor response to *Salmonella*. *Salmonella* was added after the 80th minute.

5.10. Summary

In order to demonstrate the applicability of the MSCAT platform as a sensor, it was used to detect two biological analytes which are the leading causes of foodborne illness. The first biological analyte was *Escherichia coli* (*E. coli*) O157:H7, one of the leading causes of food borne illnesses. There are many strains of *E. coli* and although most are harmless to humans, some strains such as serotype O157:H7 can cause serious illnesses. An *E. coli* O157:H7 selective sensing film that can be attached to the MSCAT's quartz surface was developed by Wark. The optimum operating frequency of the MSCAT was determined and found to be approximately 295 MHz. At this frequency the MSCAT was capable of detecting 10^4 microbes/mL within 4 hours.

The second biological analyte examined was *Salmonella*. There are approximately 2400 serotypes of *Salmonella* bacteria, 500 or which are of concern for the food industry due to the possibility of negative health effects in humans. A *Salmonella* selective sensing film was developed for the MSCAT by Wark and the MSCAT sensing element was tested to and found to be capable of detecting *Salmonella* in concentrations of 10^9 microbes/mL.

6 THE MSCAT CHEMICAL SENSOR PLATFORM

6.1. Introduction

In order to demonstrate the applicability of the MSCAT platform as a chemical sensor, it was used to detect the paralytic shellfish toxin (PST) saxitoxin (STX). In this chapter background on STX as well as the current methods of detection is described. Next, the development of two target selective sensing films that can be attached to the MSCAT sensor is presented followed by the MSCAT STX results.

6.2. Saxitoxin (STX) Background

Algal blooms commonly occur in marine environments when a particular algal species reproduces quickly due to changes in nutrient level, water quality, sunlight, or temperature. Although many algal blooms are harmless, a harmful algal bloom (HAB) produces toxins that can be dangerous to other organisms. Often a HAB in a coastal region is referred to as "red tide" due to the fact that the algal species associated with these outbreaks are often red or brown in color. Although lab based analytical tests for red tide exist [121], more recently satellite imagery has been used to monitor red tide outbreaks [122, 123]. One hazard of a HAB outbreak that is of particular concern is paralytic shellfish poisoning (PSP) which results from the ingestion of toxic shellfish meat containing algal bloom toxins by humans.

Bivalve mollusks, the main vectors of PSTs, acquire their toxicity by suspension-feeding on toxigenic dinoflagellates (*Alexandrium* spp. in North America)

which causes the PSTs to bioaccumulate in the mollusk. When the toxic mollusks are ingested by humans, PSP can be contracted, constituting a public health hazard and additionally can cause severe economic losses when areas are closed to commercial fishing. The main toxin responsible for PSP is saxitoxin (STX) [124].

The current AOAC Official Method of Analysis for PST detection is the mouse bioassay [125] which requires 10 mice for standardization as well as 2 or 3 for each actual test. In this procedure samples are extracted from shellfish meat and then injected into mice. The time of death is noted, and using a standard table, the toxin level in the sample is estimated [126]. The AOAC also mandates that these mice must be maintained at a weight between 19 and 21 g. The death time of the mouse is used to calculate the amount of toxin present, with any amount greater than 80µg toxin/100g meat considered unsafe. When one includes the time of standardization, the mouse bioassay test takes approximately 2 days. In addition to the inherent problems and limitations of mammalian bioassays, the high cost of maintaining a healthy mouse colony for the assay and the controversial issue of using mammals for medical testing encourages the development of alternative assays.

There are some alternatives to the mouse bioassay for the detection of STX in shellfish meat on the market such as High Pressure/Performance Liquid Chromatography (HPLC) and Liquid chromatography-Mass Spectrometry (LCMS) which are very expensive laboratory-based tests and a “dip-stick” test (Jellet, Canada) which can provide a colormetric yes or no result. The Lawrence HPLC test has been accredited by the AOAC, but still requires significant laboratory equipment and time. The Jellet Rapid Test for STX detects toxin levels to 40µg/100g (approximately 1.5

μM if the STX is in water) quickly and *in situ*, but this level is fairly close to the $80\mu\text{g}/100\text{g}$ deadly level and the result given by the test is qualitative and suffers from a high false positive rate [127]. A third and even less used method is the Garthwaite Enzyme-Linked Immunosorbent Assay (ELISA). Although some alternatives to the mouse bioassay exist, all of the currently available tests to detect STX are expensive, slow, sometimes non-quantitative, and do not allow the detection of PSTs directly in seawater. Therefore a need exists for a method of detecting STX which can provide fast and accurate *in situ* results.

6.3. STX Selective Sensing Films

A STX selective sensing film based on crown-ether (CE) molecules was first developed and tested. Based on these results a second sensing film based on STX selective antibodies was also developed and tested.

6.3.1. Crown Ether (CE) Based Selective Sensing Film

It has been reported that an 18-crown-6 ether (CE) molecule has cationic affinity to STX compared to other common cations while remaining insensitive to sodium, potassium, and calcium ions in solution [128]. Additionally when CE is integrated into a 4-(monoaza-18-crown-6-methyl)-7- octadecanoylamino coumarin (ODAC) film deposited onto a quartz surface, it has been reported1233333333333333 that STX is absorbed into the film [132]. Therefore CE can thus be theoretically attached to the quartz surface of an MSCAT sensor platform, making a sensitive sensor element selective for STX and insensitive to common ions found in a marine

environment. An STX selective sensing film based on CE molecules was developed by Wark [129] and will be briefly described here.

Each MSCAT sensor platform was cleaned in a Piranha solution. Each cleaned substrate was then incubated in a 5 mM solution of 3-Aminopropyltrimethoxysilane (APTMS) in acetone resulting in a silanized quartz surface. Three mg of the crown ether chemical 18-Crown-6-2,3,11,12-tetracarboxylic acid was dissolved in 5 ml of the solvent N,N-Dimethylformamide (DMF) with 20 mg of the coupling agent N,N-Dicyclohexylcarbodiimide (DCC) added. The silanized quartz substrates were then incubated in the Crown/DMF/DCC solution for 24 hrs. This procedure resulted in the STX sensitive crown ether bound to the quartz surface of the MSCAT sensor platform (see Figure 6.1).

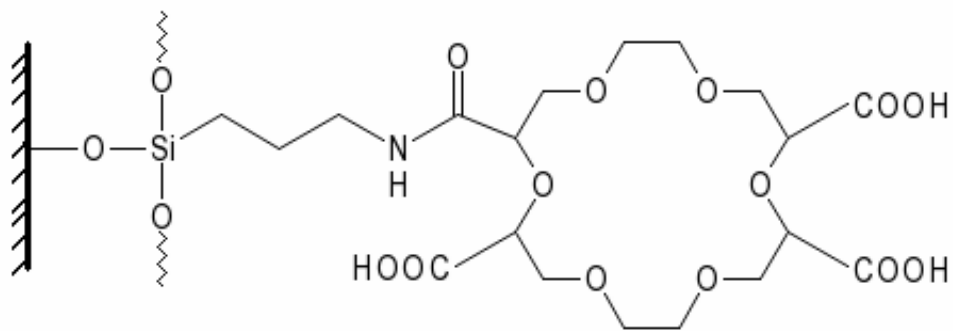


Figure 6.1 CE Film attached to the bare quartz surface of an MSCAT sensor platform

6.3.2. Antibody Based STX Selective Sensing Film

Based on the successful results of the MSCAT *E. coli* sensor, an antibody based sensing film selective to STX was also developed by Wark [129] and Hunter [130]. A small sample of antibodies selective to STX was obtained from Beacon Analytical (Portland, ME) [131]. Due to the small amount of antibodies available, it was only possible to perform a "proof of concept" study on using a MSCAT sensor platform coated with an antibody based sensing film to detect STX. It is not possible to purchase commercial STX antibodies and Beacon is currently one of the only companies who have developed an ELISA based STX test. In order to attach the STX selective antibodies to the quartz surface of the MSCAT a chemical procedure was first developed by Wark and Hunter.

6.3.2.1. Attachment of STX Selective Antibodies to the Sensor Surface

The antibodies were covalently bound to the quartz of the MSCAT sensor platforms by first silanizing the sensor surface with 3-Aminopropyltriethoxysilane, leaving a primary amine group-terminated surface. The sensors were then incubated in a 5% glutaraldehyde solution for 1 hour and then a solution containing the STX antibodies were added and allowed to incubate until the sensor's response stabilizes (indicating that binding is no longer occurring). The antibody solution contained approximately 4×10^{14} antibodies in the 1 mL solution. A schematic of the sensing film can be seen in Figure 6.2.

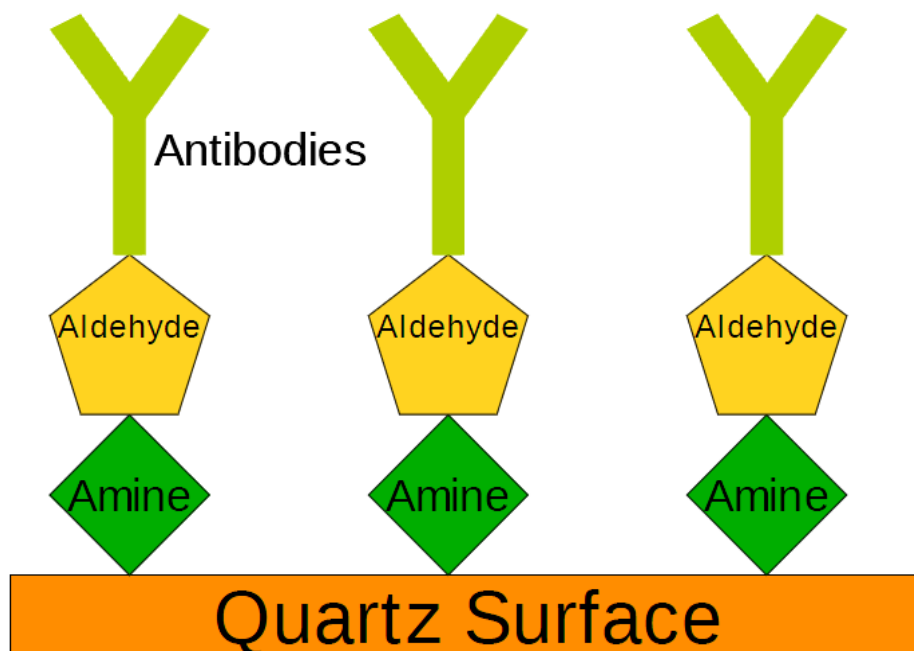


Figure 6.2 Schematic of Antibody Based STX Sensing Film

6.3.2.2 Verification of STX Antibody Film

In order to verify the attachment of the primary STX selective antibodies, an Amplex® Red immunoassay was performed using Goat anti-Rabbit IgG HRP. The immunoassay was performed in separate beakers from the film deposition process to avoid contamination. 12Goat anti-Rabbit Immunoglobulin G (IgG) horseradish peroxidase (HRP) secondary antibodies were used in conjunction with Amplex® Red to verify the attachment of the primary STX antibodies. The secondary antibodies theoretically bind to only to the primary antibodies; however, it has recently been

shown that it is possible to weakly bind antibodies to bare quartz surfaces [132]. In order to remove the possibility of the secondary antibodies to non-specifically bind to empty spots on the sensor surface the sensors were placed in bovine serum albumin (BSA) after the sensing film was placed on the MSCAT's surface. BSA attaches to any free binding sites eliminating the possibility of non-specific secondary antibody attachment. A control sensor was also used that was only exposed to BSA. The BSA would fill any available binding sites on the control MSCAT eliminating the possibility of secondary antibodies attaching to the sensor surface.

Each sensor was silanized to form the amine layer and then glutaraldehyde was added and allowed to sit for one hour to form the aldehyde layer. The STX selective antibodies were then added to phosphate buffered saline (PBS) to produce a solution with a concentration of 5 $\mu\text{L}/\text{mL}$. The antibody solution was then added to the sensors and allowed to sit for 8 hours to ensure complete binding of the antibodies to the aldehyde layer. The sensor surface was then gently rinsed to remove any free antibodies and BSA blocker was added and allowed to sit for one hour in order to block any free binding sites not occupied by antibodies.

After rinsing both MSCAT's surfaces, the secondary antibodies were applied and allowed to sit for one hour then the sensors' surfaces were rinsed again. The sensors were then placed in PBS. PBS is a buffer solution that is often used in biological testing because it helps to maintain a constant pH. Amplex® Red was then added to the sensors. If the secondary antibodies were bound to the MSCAT's surface the Amplex® Red and HRP will produce resorufin and fluoresce at approximately 550 nm (red).

As can be seen in Figure 6.3 and Figure 6.4 the MSCAT with the primary STX antibody film produced a strong red response while the control did not. These tests were performed twice yielding similar results each time. It should be noted that this sensing film could be applied to any acoustic wave sensor with a quartz sensing surface such as an LFE or SAW.



Figure 6.3 Photograph of MSCAT sensor with the STX antibody film after the introduction of Amplex® Red.



Figure 6.4 Photograph of the control MSCAT sensor without the STX antibody film after the introduction of Amplex® Red.

6.4. MSCAT STX Results

After each film was developed, the sensing films were applied to MSCAT platforms. Each film was tested to determine if the MSCAT sensing element was capable of detecting STX.

6.4.1. CE Based Selective Sensing Results

Based on results obtained for LFE sensors for the detection of STX [134], two MSCAT sensors were used in a differential sensing pair for the detection of STX in water. One sensor, referred to as the CE MSCAT, had a film of CE molecules covalently bound to its sensing surface as described in previously. The second sensor in the differential pair, referred to as the APTMS MSCAT, was functionalized with 3-Aminopropyl-trimethoxysilane (APTMS) as described in section 6.3.1, leaving positively charged groups on its sensing surface. These groups resist the binding of positively charged STX molecules while detecting non-specific mechanical and electrical changes in the fluid environment not associated with STX binding to the CE MSCAT sensor.

The differential sensing pair was exposed to varying 1 mL concentrations of STX in de-ionized (DI) water. Both sensors were operated at their fundamental frequency (approximately 5 MHz). The CE MSCAT sensor exhibited a change (shift) in its resonant frequency due to mechanical and electrical changes in the CE film from STX binding. This sensor, however, also responds to non-specific changes such as the conductivity in the fluid medium. Therefore, the total response of the differential sensor pair is obtained by subtracting the resonant frequency change of

the APTMS MSCAT from that of the CE MSCAT, leaving a net frequency change principally due to STX binding to the CE film as seen in Figure 6.5. A dose response curve for the data shown in Figure 6.5 can be seen in Figure 6.6.

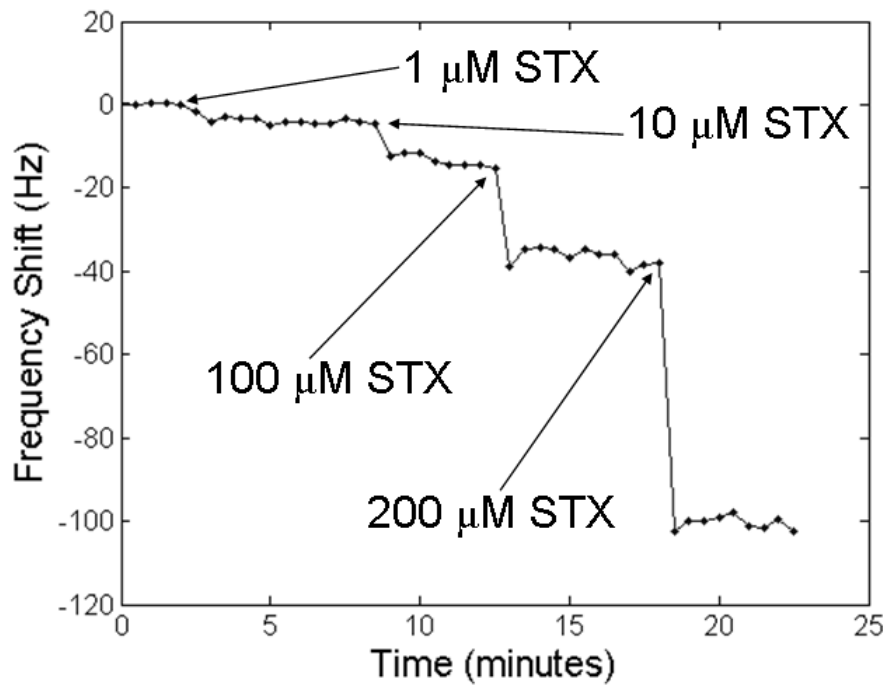


Figure 6.5 Differential MSCAT sensor response to various concentrations of STX

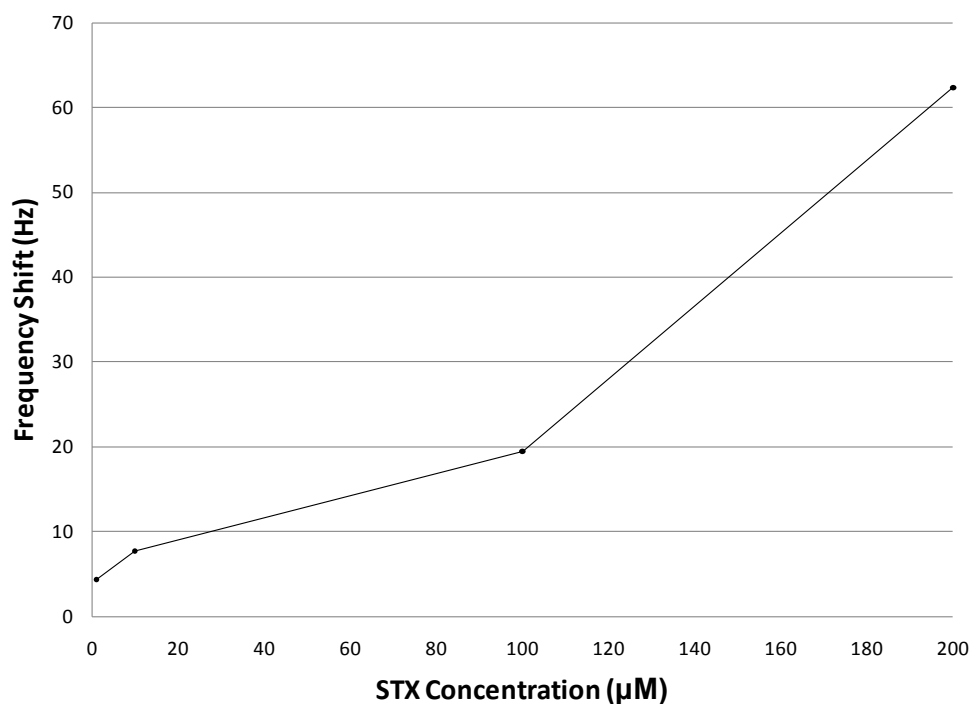


Figure 6.6 STX dose response curve for CE MSCAT.

The differential MSCAT sensing pair for STX in DI water is a quantitative *in situ* monitor for STX with a sensitivity of about 1 µM, which is significantly more sensitive than the mouse bioassay. In addition, the sensor's response time was approximately 1 minute, significantly shorter than the response time for other sensing technologies like the mouse bioassay which takes 48 hours. The differential sensing pair's performance in non-ideal environments, however, was less than ideal.

When the sensing elements were tested in salt water (35 parts per thousand NaCl) and simulated ocean water it was discovered that the MSCAT was unable to detect STX in these environments. Wark [129] discovered that the aromatic rings of

the modified CE in the ODAC molecule, in addition to providing fluorescent indication of STX binding, was responsible for the selectivity of the CE in Gawley's work [128]. Wark assessed the possibility of producing the ODAC molecule and attaching it to a MSCAT sensor platform, but found that the synthesis (which requires significant time on the order of a week per yield) is too complex and expensive to be practical. Although the CE MSCAT is sensitive to STX, it is not selective enough to be used *in situ*. Therefore, a new approach was identified.

6.4.2. Antibody Based Selective Sensing Results

Due to the extremely limited supply of STX selective antibodies that were available, it was only possible to perform a "proof of concept" using the MSCAT. The antibody based STX sensing film described earlier was applied to MSCAT sensors. Initial tests were performed in a phosphate buffer saline solution (PBS) which has many ions which fouled the crown ether film. Upon finishing the antibody incubation, a 1mL aliquot of PBS buffer remained on a functionalized MSCAT. The sensor was operated at its fundamental frequency and its response was monitored for approximately 25 minutes with 1 mL of PBS in the MSCAT holder. After approximately 25 minutes, a 10 uL drop of 1.67 mM STX in PBS was added to the sensors resulting in a concentration of approximately 1.65 μ M and the response was recorded (Figure 6.7). As was the case for *E. coli*, the frequency of the sensor with the antibody film initially decreased and then increased over time indicating that STX was binding to the sensing film. The sensor's response increased by approximately 100 Hz over the course of 60 minutes, a significantly larger shift than the

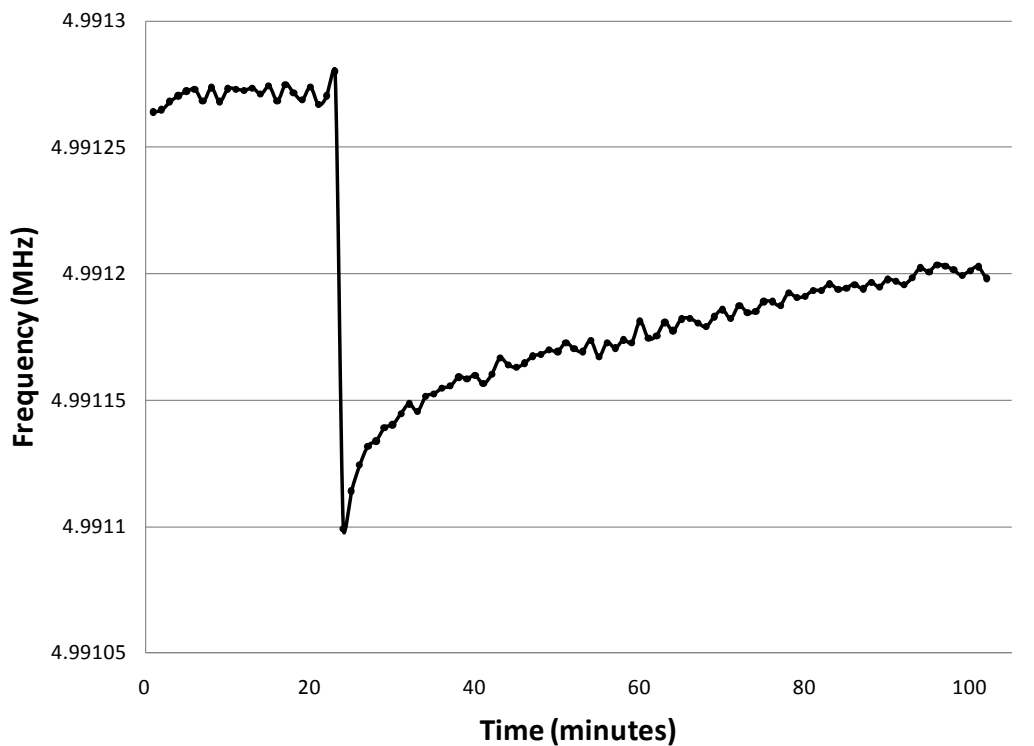


Figure 6.7 Antibody Based MSCAT STX Response to STX

approximately 5 Hz shift observed for a 1 μ M concentration of STX observed for the CE film. The MSCAT's frequency response increased by approximately 40 Hz within the first 5 minutes indicating that a response time on the order of minutes is possible. Although the sensitivity level of the STX antibodies provided by Beacon is proprietary, these results indicate that the STX antibodies are highly sensitive to STX. It is important to remember that these tests were run in PBS which has a high salinity and fouled the CE film.

Previous work on *E. coli* has shown that one can take advantage of the "apparent slip" phenomenon by operating the MSCAT at a critical frequency which can maximize sensitivity. Unfortunately due to the limited supply of STX antibodies that were available this critical frequency has not been found for STX. This work

will be performed once a sufficient supply of STX antibodies is available. However, the promising results utilizing the STX selective antibodies open an avenue for a rapid STX sensor that is capable of operating in complex sensing environments.

Although the feasibility of using a MSCAT sensor platform to sensitively detect STX even in conductive solutions has been shown, more work remains to develop a commercial product. The next steps in realizing a prototype STX sensor are to: determine the optimum operating frequency for the sensor to maximize sensitivity, develop the electronics to collect, process, and store the sensor response, develop the overall sensor system (integration of sample preparation, pre-filtration, sensing element, electronics), test the sensor system in the lab and in the field, comparing the results with established products such as the mouse bioassay.

6.5. Summary

The MSCAT was used to detect the chemical analyte saxitoxin. Shellfish, though a popular food, can carry public health risks. Specifically, paralytic shellfish poisoning (PSP) results from the ingestion of toxic shellfish meat containing algae-produced paralytic shellfish toxins (PSTs). Saxitoxin (STX) is the most potent of over 20 PST chemical derivatives. Two STX selective sensing films, one based on a crown-ether molecule and one based on STX antibodies donated by Beacon Analytical, were developed by Wark and tested with the MSCAT. Although the CE MSCAT it was found to be sensitive to STX, it is not selective enough to be used *in situ*. An MSCAT with the antibody based sensing film was found to be capable of detecting STX even in conductive media. The STX antibody based MSCAT was

found to be highly sensitive to STX and capable of detecting 1 μ M of STX in a matter of minutes.

7 SUMMARY, CONCLUSIONS, AND FUTURE WORK

7.1 Summary

The MSCAT sensor, which uses a gold, photolithographically-deposited, spiral coil antenna, has been developed to improve upon the best aspects of the standard QCM sensor while integrating the positive features of other acoustic wave sensors such as the LFE sensor and EMPAS. The coil on the MSCAT sensor is an antenna that radiates a time-varying electric field that penetrates the AT-cut quartz wafer. As a result of the piezoelectric effect, the time varying electric field sets up a time-varying stress in the wafer. Depending on the wafer thickness and the frequency of excitation, resonant acoustic waves at the TSM fundamental and higher order harmonic frequencies are excited. Like the LFE and QCM, the measurable output of the MSCAT sensor is a change in the resonant frequency shift of the transverse shear mode (TSM) due to changes in the sensing film caused by the measurand.

The MSCAT spiral coil was examined both experimentally and theoretically. Over 40 spirals with different shapes, number of turns, spacing, and widths were designed and tested for the MSCAT sensor. Their maximum operating frequency was determined and a spiral coil design for the MSCAT was selected. The near field behavior of the spiral coil was examined theoretically using FEA software and an understanding of how the electric fields radiated from a MSCAT's spiral coil excite acoustic waves in the substrate was gained.

The MSCAT was also tested for use as a biological and chemical sensor. In order to demonstrate the applicability of the MSCAT platform as a sensor, it was used

to detect two biological analytes which are the leading causes of foodborne illness. The first biological analyte was *Escherichia coli* (*E. coli*) O157:H7, one of the leading causes of food borne illnesses. There are many strains of *E. coli* and although most are harmless to humans, some strains such as serotype O157:H7 can cause serious illnesses. Current methods of evaluating drinking water or food for microorganisms involve collecting samples and transporting them to a central laboratory for analysis. The samples are processed and incubated for 24 to 48 hours before the presence or absence of *E. coli* can be determined. An *E. coli* O157:H7 selective sensing film that can be attached to the MSCAT's quartz surface was developed by Wark. The optimum operating frequency of the MSCAT was determined and the detection time and lowest detection limit for the MSCAT *E. coli* O157:H7 sensor was determined and compared to other BAW sensors.

The second biological analyte examined was *Salmonella*. There are approximately 2400 serotypes of *Salmonella* bacteria, 500 or which are of concern for the food industry due to the possibility of negative health effects in humans. The two most common serotypes in the United States are Typhimurium and Enteritidis. *Salmonella* Typhimurium DT104 is especially dangerous as it is highly virulent and resistant to a number of antibiotics. A *Salmonella* selective sensing film was developed for the MSCAT by Wark and the MSCAT sensing element was tested to determine if it could detect *Salmonella*.

The MSCAT was also used to detect the chemical analyte saxitoxin. Shellfish, though a popular food, can carry public health risks. Specifically, paralytic shellfish poisoning (PSP) results from the ingestion of toxic shellfish meat containing

algae-produced paralytic shellfish toxins (PSTs). Saxitoxin (STX) is the most potent of over 20 PST chemical derivatives. The current AOAC Official Method of Analysis for PST detection is the mouse bioassay. In this procedure samples are extracted from shellfish meat and then injected into mice. The time of death is noted, and using a standard table, the toxin level in the sample is estimated. Two STX selective sensing films, one based on a crown-ether molecule and one based on STX antibodies donated by Beacon Analytical, were developed by Wark and tested with the MSCAT.

A theoretical search and experimental measurements were also performed to identify the existence of high-frequency temperature-compensated TSMs in LiTaO_3 . Prototype LFE LiTaO_3 sensors were fabricated and tested (see Appendix A). Expressions for the near-field electric fields radiated by a spiral coil antenna were also derived (see Appendix B).

7.2 Conclusions

This work is the first demonstration of utilizing a photolithographically deposited antenna to excite bulk acoustic waves in a sensor platform. Although there are limitless numbers of antenna configurations that one may use, the choice has to be carefully made in order to efficiently excite bulk acoustic waves over a wide frequency range. Although all antennas radiate electromagnetic fields which can excite acoustic waves in piezoelectric materials through the reverse piezoelectric effect, most antenna designs only radiate electromagnetic fields efficiently at a single frequency due to the fact that their designs are based on the wavelength of the

electromagnetic wave that is to be excited. There is, however, a class of antennas known as frequency independent spiral antennas that are capable of operating over a wide frequency range. Due to the ability to miniaturize these antennas and the fact that they operate efficiently over a wide frequency range a spiral coil antenna was chosen as the antenna type for the MSCAT.

It was found that a [8 turn, 250 μm spacing, 515 μm width] MSCAT was capable of operating up to the 99th harmonic which is a significant improvement over the 63rd harmonic that was successfully used for the EMPAS. It was found that the parallelism of the AT-cut quartz substrate is critical in order to achieve high frequency operation. Theoretical work was performed in order to gain an understanding of how the MSCAT's spiral coil antenna excites the TSM in AT-cut quartz. An expression for the near-field electric fields radiated by a spiral coil antenna were derived and it was concluded that the spiral coil antenna radiates electric fields in both the lateral and thickness direction in the near field, not just the lateral direction, as was previously believed.

Based on these results, two phenomena relating to the operation of the MSCAT sensor platform using FEA modeling was examined. First, the electric field distribution in the AT-cut quartz wafer when the sensor was loaded with DI water and when it was left in air was examined. It was found that when the sensor was operated in air the electric fields inside the wafer were relatively weak and in several different directions leading to both weak resonances and destructive interference of the TSM due to multiple modes being excited. When a liquid was placed on the sensor surface, however, the distribution of the electric field changed significantly. The

magnitude of the electric field was much stronger than the air case and the electric fields were oriented in the thickness direction leading to only the excitation of the desired TSM. This is in contrast to the EMPAS where the majority of the electric fields are trapped in the air gap between the coil and the AT-cut quartz wafer. This result leads to the conclusion that the MSCAT excites the TSM in AT-cut quartz much more efficiently than the EMPAS does due to the fact that the spiral coil is in direct contact with the substrate. It was also found that an MSCAT platform that has a gold electrode placed on its sensing surface is capable of operating in air and may be applicable to gas sensing applications.

The near-field behavior of several different spiral coil antenna configurations was also examined. It was found that the thickness component of the electric field in the AT-cut quartz wafer varies significantly with the design of the spiral coil. This result leads to the conclusion that it is critical to properly select the spiral coil configuration for the MSCAT in order to efficiently.

The MSCAT was found to be capable of detecting both mechanical (viscosity density product) and electrical (conductivity and relative permittivity) property changes in liquids while the QCM can only detect mechanical property changes. When the MSCAT was operated at elevated harmonics its frequency shift was found to be four orders of magnitude larger than the frequency shift of the LFE or QCM for the detection of relative permittivity changes and five orders of magnitude larger for viscosity density product and conductivity changes. Of more interest, however, is the fact that the sensitivity of the MSCAT varies depending on the operating frequency. The MSCAT was found to be most sensitive to changes in viscosity and conductivity

when it is operated at approximately 300 MHz. The MSCAT was most sensitive to relative permittivity changes when it was operated at approximately 500 MHz although the relative frequency shift at 500 MHz is only approximately 15% larger than when the MSCAT was operated at its fundamental frequency. These results show that the sensitivity to mechanical and electrical property changes is dependent on the operating frequency of the device and the highest possible operating frequency does not necessarily result in the highest level of sensitivity. This is in direct contrast to classical BAW theory such as the Sauerbrey and Kanazawa equations which predict that the sensitivity of BAW devices increases with operating frequency.

MSCAT sensors were also used to detect biological and chemical analytes. MSCAT sensors were used to selectively detect the bacterium *E. coli* O157:H7 in water. The MSCAT sensor was found to be most sensitive when it was operated at its 59th harmonic (295 MHz). At this frequency it was able to detect *E. coli* O157:H7 in concentrations four orders of magnitude lower (10^4 microbes/mL) than the detection limit of the QCM and LFE with half the detection time (4 hours).

MSCAT sensors have also been used to detect the chemical analyte STX, the most dangerous neurotoxin associated with paralytic shellfish poisoning. It was found that although the MSCAT could detect low concentrations of STX using a CE based sensing film; the film was also sensitive to conductivity changes in the medium. An antibody based sensing film was developed and found to be capable of detecting STX even in conductive media. The STX antibody based MSCAT was found to be highly sensitive to STX and capable of detecting 1 μ M of STX in a matter of minutes.

These results show that the MSCAT has an enormous amount of potential as a sensor platform. Due to the fact that the MSCAT has very large frequency shifts to mechanical and electrical property changes when operated at elevated frequencies it may be applicable to applications where small changes in a fluid medium must be measured. It is likely that operating an MSCAT at a wide range of frequencies as an "acoustic spectrometer" will provide additional acoustic impedance information about the analyte being tested. In addition, the MSCAT coated with an antibody based sensing film can be used to sensitively and quickly detect a wide range of chemical and biological analytes and may be a replacement for the ELISA test currently used for chemical and biological detection.

A search was also made for orientations in lithium tantalate that when excited with a lateral electric field would offer improved sensor performance over standard AT-quartz LFE and QCM sensors. Two candidate orientations of lithium tantalate were theoretically identified that showed significant improvements in electromechanical coupling and predicted to have temperature compensated pure TSMs at 25°C, namely the (YXwl) -16.5°, and (YXwl) -84.3° cuts. The (YXwl) -16.5° cut was chosen for further testing based on the separation of interfering modes and the body of literature available on it from its use in RF filtering applications. XRD measurements were performed on the wafer that verified that it was the correct orientation. A LFE sensor with a fundamental frequency of 5.2 MHz was fabricated on this cut and found to be capable of operating at frequencies as high as 1.4 GHz (269th harmonic). The temperature behavior for this cut of LTO was experimentally measured and found to be temperature compensated at 70°C instead of 25°C as

theoretically predicted. When tested as a sensor, the LTO LFE was found to be capable of detecting both mechanical and electrical property changes in liquids unlike the standard QCM. This sensor was used to measure viscosity, conductivity, and relative permittivity changes in liquids and found to have significantly larger frequency changes than AT-cut QCM and LFE sensors when it was operated at high frequencies.

7.3 Future Work

Although the results obtained for the MSCAT are very promising, more work remains. It would be useful to develop portable electronics systems such as an oscillator which would allow real-time measurements of the MSCAT's frequency response. In order to fully optimize the MSCAT spiral coil configuration it will be necessary to develop an equivalent circuit model that incorporates the antenna design. Other antenna designs such as a logarithmic spiral coil where the ratio of the width to spacing varies could also be explored for use with the MSCAT. It is likely that operating an MSCAT at a wide range of frequencies as an "acoustic spectrometer" will provide additional acoustic impedance information about the mechanical and electrical properties of a liquid sample as the sensitivity of the MSCAT to each liquid property changes depending on the operating frequency. However, in order to utilize the MSCAT as a sensitive liquid property sensor, it will first be necessary to develop a strategy to separate the effects of liquid mechanical and electrical property changes from the MSCAT's sensor response. Using the MSCAT for acoustic spectroscopy could also be explored for a wide range of sensing applications including chemical and biological agent detection. The MSCAT could also be explored as a highly

sensitive mass sensor for applications such as a rate monitor for thin film deposition systems.

In order to realize an MSCAT *E. coli* O157:H7 sensor system that can be used in real-world applications several tasks must be accomplished including: utilize an incubation process to improve the sensitivity and response time of the MSCAT immunosensor to *E. coli* O157:H7, develop the electronics to collect, process, and store the sensor response, develop the overall sensor system (integration of sample preparation, pre-filtration, sensing element, electronics), and test the sensor system in the lab and in the field, comparing the results with established products such as Colilert (IDEXX Laboratories, Westbrook, ME).

Although these *Salmonella* results are promising and demonstrate that it is possible to develop MSCAT sensors for a wide range of pathogenic bacteria a significant amount of future work remains. The chemistry to attach non-biotintilated antibodies to the quartz MSCAT surface should be further developed to minimize the noise exhibited by the MSCAT's frequency response. In addition, it will be necessary to determine the optimum operating frequency of the MSCAT for this new film. Finally the new *Salmonella* sensor should be tested to determine its lowest detection limit and to verify that it is able to detect *Salmonella* in real-world sensing environments.

Although the feasibility of using a MSCAT sensor platform to sensitively detect STX even in conductive solutions has been shown, more work remains to develop a commercial product. The next steps in realizing a prototype STX sensor are to: determine the optimum operating frequency for the sensor to maximize

sensitivity, develop the electronics to collect, process, and store the sensor response, develop the overall sensor system (integration of sample preparation, pre-filtration, sensing element, electronics), test the sensor system in the lab and in the field, comparing the results with established products such as the mouse bioassay.

Finally, an MSCAT array could be developed that would be capable of detecting a wide range of chemical and biological analytes using a single sensor system and potentially replace the ELISA sensor platform.

REFERENCES

1. Publication and Proposed Revision of ANSI/IEEE Standard 176-1987 ANSI/IEEE Standard on Piezoelectricity." *IEEE Trans. Ultrason. Ferroelect. Freq. Contr.* **42** (5), 717-771, 1996.
2. B.A. Auld, *Acoustic fields and waves in solids*, 2nd ed., Malabar, FL, USA: Robert E. Krieger Publishing Co., vol. 1, 1990.
3. C. Lu and O. Lewis, "Investigation of film-thickness determination by oscillating quartz resonators with large mass load." *J. Appl. Phys.* **43**, 4385-90, 1972.
4. S.J. Martin, V.E. Granstaff and G.C. Frye, "Characterization of a quartz crystal microbalance with simultaneous mass and liquid loading," *Analytical Chemistry*, **63** (20), 2272-2281, 1991.
5. S.C. Ng *et al.* "Quartz crystal microbalance sensor deposited with Langmuir-Blodgett films of functionalized polythiophenes and application to heavy metal ions analysis." *Langmuir*, **14**, 1748-1752.
6. G. Sauerbrey, "Use of quartz vibrator for weighing thin films on a microbalance," *Z. Phys.*, **155**, 206-210, 1959.
7. B. Morray, Li Suiqiong, J. Hossenlopp, R. Cernosek, and F. Josse, "PMMA polymer film characterization using thickness-shear mode (TSM) quartz resonators," *Proc. IEEE Freq. Control Symp. and PDA Exhibition*, 294-300, 2002.
8. S. Ballantyne, "Electromagnetic excitation of high frequency acoustic shear waves for the study of interfacial biochemical phenomena" PhD dissertation, University of Toronto, Toronto, Canada, 2005.
9. F. Josse, "Acoustic wave liquid-phase-based microsensors," *Sens. Act. A*, **44**, 199-208, 1994.
10. Y. Lee, D. Everhart, and F. Josse, "The quartz crystal resonator as detector of electrical loading: An analysis of sensing mechanisms," *Proc. IEEE Int. Freq. Contr. Symp.*, 577-585, 1996.
11. C. Zhang and J. Vetelino, "Bulk Acoustic Wave Sensors for Sensing Measurand-Induced Electrical Property Changes in Solutions," *IEEE Trans. Ultrason., Ferroelect. Freq. Contr.* **48**, 773-778, 2001.
12. C. Zhang and J. Vetelino, "A Bulk Acoustic Wave Resonator for Sensing Liquid Electrical Property Changes," *Proc. IEEE/EIA Int. Freq. Contr. Symp.*, 535-541, 2001.

13. A. Ballato, E.R. Hatch, M. Mizan, T. Lukaszek, and R. Tilton. "Simple Thickness Modes Driven By Lateral Fields." *Pro. IEEE Int. Freq. Contr. Symp.*, 462–72, 1985.
14. J.R. Vig, U.S. Patent, 5,744,902, "Chemical and Biological Sensor Based on Microresonators," Date of patent: 28 April 1998.
15. J.R. Vig and A. Ballato, U.S. Patent, 6,260,408, "Techniques for Sensing the Properties of Fluids with a Resonator Assembly," Date of patent: 17 July 2001.
16. J.F. Vetelino, U.S. Patent, 7,075,216, "Lateral Field Excited Acoustic Wave Sensor," Date of patent: 11 July 2006.
17. Y. Hu, L.A. French, K. Radecky, M. Pereira da Cunha, P. Millard, J.F. Vetelino. "A Lateral Field Excited Liquid Acoustic Wave Sensor." *Proc. IEEE Ultrasonics Symp.* 46-51, 2003.
18. Y. Hu, L.A. French Jr., K. Radecky, M.P. da Cunha, P. Millard, and J.F. Vetelino, "A lateral field excited liquid acoustic wave sensor," *IEEE Trans. Ultrason., Ferroelect., Freq. Contr.*, **51** (11) 1373-1380, 2004.
19. U. Hempel, R. Lucklum, J.F. Vetelino, and P.R. Hauptmann, "Advanced application of the impedance spectrum of a lateral field excited sensor," *Sens. Act. A*, **142**, 97-103, 2007.
20. D. F. McCann, J. Parks, J.M. McGann, M.P. da Cunha, J.F. Vetelino. "A Lateral Field Excited LiTaO3 High Frequency Bulk Acoustic Wave Sensor." *IEEE Trans. Ultrason., Ferroelect. Freq. Contr.*, **56** (4), 779-787, 2009.
21. W. Wang, C. Zhang, Z. Zhang, Y. Liu, and G. Feng. "Three operation modes of lateral-field-excited piezoelectric devices." *Applied Physics Letters*, **93**, 242906, 2008.
22. W. Pinkham, L.A. French Jr., D. Frankel, Y. Hu, J.F. Vetelino, "Pesticide detection using a lateral field excited acoustic wave sensor." *Sensors and Actuators B*, **108**, 910-16, 2005.
23. C. York, P. Millard and L. French, J.F. Vetelino. "A Lateral Field Excited Acoustic Wave Biosensor," *Proc. IEEE International Ultrasonics Symposium*, 44-49, 2005.
24. US Center for Disease Control. www.cdc.gov/ncidod/dbmd/diseaseinfo/escherichiacoli_g.htm
25. US FDA. <http://www.cfsan.fda.gov/~mow/intro.html>

26. E. Berkenpas, P. Millard, M. Pereira da Cunha. "Detection of *Escherichia coli* O157:H7 with langasite pure shear horizontal surface acoustic wave sensors." *Biosensors and Bioelectronics*, **21**, 2255-2262, 2006.
27. AOAC, *Official Methods of Analysis of AOAC International*, P.A. Cunniff, Ed. Gaithersburg, MD, 1995.
28. D. F. McCann, M. Wark, L. French, J. Vetelino. "Novel Transducer Configurations for Bulk Acoustic Wave Sensors." *Proc. IEEE Sensors*, 1448-1451, 2008.
29. J. M. McGann, K. Sgambato, D.F. McCann, C. Peters, J.F. Vetelino, "Acoustic Mode Behavior in Lateral Field Excited Sensors." *Proc. IEEE Ult. Symp.*, 2009 (in press).
30. K. Sgambato. "Design and testing of a lateral field excited rate monitor for use in thin film deposition systems." M.S. dissertation, University of Maine, Orono, ME, 2009.
31. M. Hirao, H. Ogi, H. *EMATS for Science and Industry*, Norwell, MA, Kluwer Academic Publishers, 2003.
32. R.H. Randall, F.C. Rose, and C. Zener, "Intercrystalline Thermal Currents as a Source of Internal Friction." *Phys. Rev.*, **56** (4), 343-349. 1939.
33. P.R. Mould, T.E. Johnson, Jr., T.E." Rapid assessment of drawability of cold-rolled low-carbon steel sheets." *Sheet Metal Industries*, **50**, 328-333, 1973.
34. G. Alers, "A History of EMATs." *AIP Conference Proceedings*, **975**, 801-808, 2007.
35. M. Pereira da Cunha, J.W. Jordan. "Improved Longitudinal EMAT transducer for elastic constant extraction." *Proc. IEEE Int. Freq. Contrl. Symp.*, 426-432, 2005.
36. H. Ogi, K. Motohisa, Y. Hosono, K. Hatanaka, T. Ohmori, and H. Hirao, "EMATs for Immunosensors," *AIP Conference Proceedings*, **975**, 823-827, 2007.
37. M.K. Kang, R. Huang, and T. Knowles, "Energy-Trapping Torsional-Mode Resonators for Liquid Sensing," *Proc. IEEE Int. Freq. Contrl. Symp.*, 133-138, 2006.

38. H. Ogi, "Field dependence of coupling efficiency between electromagnetic field and ultrasonic bulk waves," *J. Appl. Phys.*, **82(8)**, 3940-3949, 1997.
39. R. B. Thompson, "Physical Principles of Measurements with EMAT Transducers", *Physical Acoustics*, **19**, 157-300, 1990.
40. B.W. Maxfield, A. Kuramoto, and J.K. Hulbert, "Evaluating EMAT Designs for Selected Applications," *Materials Evaluation*, **45** (10), 1166-1183, 1987.
41. A.C. Stevenson and C.R. Lowe, "Noncontact excitation of high Q acoustic resonances in glass plates," *Appl. Phys. Lett.*, **73** (4), 447-449, 1998.
42. H.S. Sindi, A.C. Stevenson, C.R. Lowe, "A strategy for chemical sensing based on frequency tunable acoustic devices." *Anal. Chem.*, **73** (7), 1577-1586, 2001..
43. A.C. Stevenson, B. Araya-Kleinsteuber, R.S. Sethi, H.M. Mehta, C.R. Lowe, "Hypersonic evanescent waves generated with a planar spiral coil." *Analyst*, **128**, 1175-1180, 2003.
44. M. Thompson, R. Nisman, G.L. Hayward, H. Sindi, A.C. Stevenson, C.R. Lowe, "Surface energy and the response of transverse acoustic wave devices in liquids." *Analyst*, **125**, 1525-1528, 2000.
45. A.C. Stevenson, B. Araya-Kleinsteuber, R.S. Sethi, H.M. Metha, C.R. Lowe, "Planar coil excitation of multifrequency shear wave transducers." *Biosensors and Bioelectronics*, **20**, 1298-1304, 2005.
46. F. Lucklum, P. Hauptmann, and N.F. de Rooij, "Magnetic direct generation of acoustic resonances in silicon membranes," *Meas. Sci. Technol.* **17** (4), 719-726, 2006.
47. F. Lucklum, B. Jakoby, P. Hauptmann, and N.F. de Rooij, "Remote Electromagnetic Excitation of High-Q Silicon Resonator Sensors," *Proc. IEEE Int. Freq. Contr. Symp.*, 139-144, 2006.
48. F. Lucklum and B. Jakoby, "Novel Magnetic-Acoustic Face Shear Mode Resonators for Liquid Property Sensing," *Tech. Digest Transducers '07 & Eurosensors XXI*, 1717-1720, 2007.
49. F. Lucklum and B. Jakoby, "Electromagnetic excitation of high-Q silicon face shear mode resonator sensors," *Proc. IEEE Ult. Symp.*, 387-390, 2007.

50. F. Lucklum and B. Jakoby, "Multi-Mode Excitation of Electromagnetic-Acoustic Resonant Sensor Arrays," *Proc. IEEE Int. Freq. Contr. Symp.*, 53-57, 2008.
51. A.C. Stevenson, B. Araya-Kleinsteuber, R.S. Sethi, H.M. Metha, C.R. Lowe, "The acoustic spectrophonometer: A novel bioanalytical technique based on multifrequency acoustic devices." *Analyst*, **128**, 1222-1227, 2003.
52. K. K. Kanazawa, J. G. Gordon, "Frequency of a quartz microbalance in contact with liquid." *Anal. Chim. Acta*, **57**, 1770-1, 1985.
53. A.C. Stevenson, B. Araya-Kleinsteuber, R.S. Sethi, H.M. Metha, C.R. Lowe, "The application of the acoustic spectrophonometer to biomolecular spectrometry: a step towards acoustic 'fingerprinting'." *J. Mol. Recognit.*, **17**, 174-179, 2004.
54. A.C. Stevenson, A.C.A. Roque, B. Araya-Kleinsteuber, E. Kioupritzi, C.R. Lowe, "Wireless excitation of quartz crystals immersed in an aqueous fluid." *Analyst*, **131**, 474-476, 2006.
55. A.C. Stevenson, B. Araya-Kleinsteuber, E. Kioupritzi, A.C. Roque, C.R. Lowe, "Noncontact excitation of quartz crystal resonator chips." *Appl. Phys. Lett.*, **89**, 083516, 2006.
56. A.C. Stevenson and C.R. Lowe, "Noncontact excitation of high Q acoustic resonances in glass plates," *Appl. Phys. Lett.*, **73** (4), 447-449, 1998.
57. B. Araya-Kleinsteuber, A.C.A. Roque, E. Kioupritzi, A.C. Stevenson, C.R. Lowe, "Magnetic acoustic resonance immunoassay (MARIA): a multifrequency acoustic approach for the non-labelled detection of biomolecular interactions." *J. Mol. Recognit.*, **19**, 379-385, 2006.
58. T. Cass, *Immobilized Biomolecules in Analysis: a practical approach*, Oxford University Press: NY, USA, 1998.
59. M. Thompson, S.M. Ballantyne, L.E. Cheran, A.C. Stevenson, C.R. Lowe, "Electromagnetic excitation of high frequency acoustic waves and detection in the liquid phase." *Analyst*, **128**, 1048-1055, 2003.
60. S.M. Ballantyne, M. Thompson, M. "Superior analytical sensitivity of electromagnetic excitation compared to contact electrode instigation of transverse acoustic waves." *Analyst*, **129**, 219-224, 2004.
61. L. Jaehyuk, B. Araya-Kleinsteuber, A.C. Stevenson, C.R. Lowe, "Extending the frequency limits of non-contact acoustic generation." *Proc. IEEE Freq. Contr. Symp.*, 36-39, 2007.

62. T. Schneider, U. Hempel, S. Doerner, P.R. Hauptmann, D. F. McCann, and J. Vetelino. "Compact RF impedance-spectrum analyzer for lateral field excited liquid acoustic wave wensors". *Proc. IEEE Sensors*, 280-283, 2007.
63. J. Vetelino, D. McCann, "Monolithic Antenna Excited Acoustic Transduction Device". Great Britain Patent # GB2439828. May 28, 2008
64. J. Vetelino, D. McCann, "Monolithic Antenna Excited Acoustic Transduction Device". United States Patent Pending, 2007 (11,823,135).
65. J. Vetelino, D. McCann, "Monolithic Antenna Excited Acoustic Transduction Device". German Patent Pending, 2007 (10 2007 029 919.4).
66. J. Vetelino, D. McCann, "Monolithic Antenna Excited Acoustic Transduction Device". Japanese Patent Pending, 2007 (2007-169497).
67. C. A. Balanis, *Antenna Theory, Analysis, and Design*, 3rd ed. Hoboken, NJ: John Wiley & Sons, Inc., 2005.
68. S. Ballantyne, "Electromagnetic excitation of high frequency acoustic shear waves for the study of interfacial biochemical phenomena" PhD dissertation, University of Toronto, Toronto, Canada, 2005.
69. R. Schmitt, *Electromagnetics Explained*, Woburn, MA: Elsevier Science, 2002.
70. S. Doerner, T. Schneider, J. Schroder, P. Hauptman, "Universal impedance spectrum analyzer for sensor applications." *Proc. IEEE Sensors*, 594-596, 2003;
71. T. Schneider, U. Hempel, S. Doerner, P.R. Hauptmann, D. F. McCann, and J. Vetelino. "Compact RF impedance-spectrum analyzer for lateral field excited liquid acoustic wave wensors". *Proc. IEEE Sensors*, 280-283, 2007.
72. H.S. Sindi, A.C. Stevenson, C.R. Lowe, "A strategy for chemical sensing based on frequency tunable acoustic devices." *Anal. Chem.*, **73** (7), 1577-1586, 2001.
73. F. Lucklum, personal conversation, 2005.
74. M. Once, "Effect of energy trapping on performance of QCM." *Proc. IEEE Int. Freq. Contrl. Symp.* 433-441, 2005.

75. A. M. Mehrabani, L. Shafai. "A dual-arm archimedian spiral antenna over a low-profile artificial magnetic conductor ground plane." *Int. Symp. on Antenna. Tech. and Appl. Electromag.*, 1-4, 2009.
76. www.comsol.com
77. D.F. McCann, G. Flewelling, G. Bernhard, and J.F. Vetelino. "A Monolithic Spiral Coil Transduction Sensor." *Proc. IEEE Ultrason. Symp.*, 890-893, 2006.
78. R.F. Schmitt, J.W. Allen, J.F. Vetelino, J. Parks, and C. Zhang. "Bulk acoustic wave modes in quartz for sensing measurand-induced mechanical and electrical property changes." *Sensors and Actuators B*, **76**, 95-102, 2001,.
79. D.W. Branch and T.L. Edwards. "Love Wave Acoustic Array Biosensor Platform for Autonomus Detection." *Proc. IEEE Ultrason. Symp.*, 260-263, 2007.
80. D.F. McCann, M. Wark, P. Millard, D. Neivandt, J.F. Vetelino. "The Detection of Chemical and Biological Analytes Using a Monolithic Spiral Coil Acoustic Transduction Sensor." *Proc. IEEE Ultrason. Symp.*, 1187-1190, 2008.
81. Y. Hu, L.A. French, K. Radecsky, M. Pereira da Cunha, P. Millard, J.F. Vetelino. "A Lateral Field Excited Liquid Acoustic Wave Sensor." *Proc. IEEE Ultrasonics Symp.* 46-51, 2003.
82. U. Hempel. "Lateral field excited quartz crystal resonators – from theoretical approach to sensor application." Ph.D. dissertation, University of Magdeburg, Magdeburg, Germany, 2008.
83. K. K. Kanazawa and J.G. Gordon. "Frequency of a quartz microbalance in contact with liquid." *Anal. Chem.* **57**, 1771-1772, 1985.
84. K. Nortemann, J. Hilland, U. Kaatze. "Dielectric properties of aqueous NaCl solutions at microwave frequencies." *J. Phys. Chem. A.*, **101**, 6864-6869, 1997.
85. Altera, "AN 224: High-Speed Board Layout Guidelines.", <http://www.altera.com/literature/an/an224.pdf>.
86. U. Hempel, "Lateral field excited quartz crystal resonators – from theoretical approach to sensor application." Ph.D. dissertation, University of Magdeburg, Magdeburg, Germany, 2008.

87. C. Peters, "Characterization of lithium tantalite LFE sensors and their responses to liquids." Diploma thesis, University of Magdeburg, Germany, 2009.
88. A.C. Stevenson, B. Araya-Kleinstuber, R.S. Sethi, H.M. Metha, C.R. Lowe, "The acoustic spectrophonometer: A novel bioanalytical technique based on multifrequency acoustic devices." *Analyst*, **128**, 1222-1227, 2003.
89. US Center for Disease Control. www.cdc.gov/ncidod/dbmd/diseaseinfo/escherichiacoli_g.htm
90. US FDA. <http://www.cfsan.fda.gov/~mow/intro.html>
91. IDEXX. <http://www.idexx.com/water/products/compare.cfm>
92. Chandler, J., Maine Health and Environmental Laboratory. Personal Communication. 7 June 2004.
93. IDEXX. <http://www.idexx.com/water/>
94. L. Sang-Hun, D.D. Stubbs, J. Cairney, W.D. Hunt, "Real-time detection of bacteria spores using a QCM based immunosensor." *Proc. IEEE Sensors*, **2**, 1194-1198, 2003.
95. D. F. McCann, M. Wark, P. Millard, D. Neivandt, J.F. Vetelino. "The Detection of Chemical and Biological Analytes Using a Monolithic Spiral Coil Acoustic Transduction Sensor." *IEEE Ultrasonics Symposium*, 1187-1190, 2008.
96. M. Wark, M.S. dissertation, University of Maine, Orono, ME, unpublished.
97. R.P. Johnson, et al., "Detection of Escherichia coli O157:H7 in meat by an enzyme-linked immunosorbent assay, EHEC." *Appl. Envi. Micro*, **61** (1), 386-388, 1995.
98. M.S. Rhee, P.M. Gray, D.H. Kang, "Improvement of selectivity for isolation of *Escherichia Coli* O157:H7 from generic *Escherichia Coli*." *Rapid Meth. And Auto. in Micro*.**10** (1), 27-35, 2007.
99. B. Araya-Kleinstuber, A.C.A. Rouqe, E. Kiupritzi, A.C. Stevenson, C.R. Lowe, "Magnetic acoustic resonance immunoassay (MARIA): a multifrequency acoustic approach for the non-labelled detection of biomolecular interactions." *J. Mol. Recognit*, **19**, 379-385, 2006.

100. E. Berkenpas, S. Bitla, P. Millard, M. Pereira da Cunha. "LGS shear horizontal SAW devices for biosensor applications." *Proc. IEEE Ultrason. Symp.*, **2**, 1404-1407, 2003.
101. E. Berkenpas, M. Pereira da Cunha, S. Bitla, P. Millard. "Shear horizontal SAW biosensor on langasite." *Proc. IEEE Sensors*, **1**, 661-664, 2003.
102. E. Berkenpas, S. Bitla, P. Millard, M. Pereira da Cunha. "Pure shear horizontal SAW biosensor on langasite." *IEEE Trans. Ultrason. Ferroelect. Freq. Cntrl.*, **51** (11), 1404-1411, 2004.
103. E. Berkenpas, T. Kenny, P. Millard, M. Pereira da Cunha. "A langasite SH SAW O157:H7 *E. coli* sensor." *Proc. IEEE Ultrason. Symp.*, 54-57, 2005.
104. E. Berkenpas, P. Millard, M. Pereira da Cunha. "Novel O157:H7 *E. coli* detector utilizing a langasite surface acoustic wave sensor." *Proc. IEEE Sensors*, 1237-1240, 2005.
105. E. Berkenpas, P. Millard, M. Pereira da Cunha. "Detection of *Escherichia coli* O157:H7 with langasite pure shear horizontal surface acoustic wave sensors." *Biosens. Bioelectron.*, **21**, 2255-2262, 2006.
106. <http://www.invitrogen.com/site/us/en/home/brands/Molecular-Probes/Key-Molecular-Probes-Products/Amplex-Red-Enzyme-Assays/amplex-red-technology-overview.html>
107. G. Sauerbrey, "Use of quartz vibrator for weighing thin films on a microbalance." *Z. Phys.*, **155**, 206-10, 1959.
108. K. K. Kanazawa and J.G. Gordon. "Frequency of a quartz microbalance in contact with liquid." *Anal. Chem.* **57**, 1771-1772, 1985.
109. M. Thompson, S.M. Ballantyne, L.E. Cheran, A.C. Stevenson, C.R. Lowe, "Electromagnetic excitation of high frequency acoustic waves and detection in the liquid phase." *Analyst*, **128**, 1048-1055, 2003.
110. W.A. Gee, K.M. Ritalahti, W.D. Hunt, F.E. Loffler, "QCM Viscometer for Bioremediation and Microbial Activity Monitoring", *IEEE Sensors Journal*, **3**, 304-309, 2003.
111. B.A. Cavic, F.L. Chu, L.M. Furtado, S. Ghafouri, H.Su, M. Thompson, "Acoustic waves and the real-time study of biochemical macromolecules at the liquid solid interface." *Faraday Discuss.*, **107**, 159-176, 1997.

112. C. York, P. Millard and L. French, J.F. Vetelino. "A lateral field excited acoustic wave biosensor," *Proc. IEEE International Ultrasonics Symposium*, 44-49, 2005.
113. H. Fujikawa, S. Morozumi. "Modeling surface growth of *Escherichia coli* on agar plates." *Appl. Environ. Microbiol.*, **71** (12), 7920-7926, 2005.
114. D.W. Branch and T.L. Edwards. "Love wave acoustic array biosensor platform for autonomous detection." *Proc. IEEE Ultrason. Symp.*, 260-263, 2007.
115. M.B. Medina, L. Van Houten, P.H. Cooke, and S.I. Tu. "Real-time analysis of antibody binding interactions with immobilized *E. coli* O157:H7 cells using the BIAcore." *Biotech. Tech.*, **11** (3), 173-176, 1997.
116. Device News. <http://www.measurementdevices.com/index.php?name=News&file=article&sid=567>. "R&D: Independent Evaluations of Its New RapidCheck Select Salmonella Test Method."
117. US FDA. <http://www.cfsan.fda.gov/~dms/sprfuto.html>. "Testing Methodologies and Sampling."
118. US FDA. <http://www.cfsan.fda.gov/~comm/mmsalegg.html>. "Detection of Salmonella in Environmental Samples from Poultry Houses."
119. Neogen. <http://www.jsunitech.com/product/fkit/pdf/p-GT-Sal-1001.pdf>.
120. D. Stewart, K. Reineke, M. Tortorello. "Comparison of assurance gold salmonella EIA, BAX for Screening/Salmonella, and GENE-TRAK Salmonella DLP rapid assays for detection of Salmonella in alfalfa sprouts and sprout irrigation water." *Journal of AOAC International*, **85**, 395-403, 2002.
121. M. Gray, B. Wawrik, J. Paul, E. Casper, "Molecular detection and quantitation of the red tide dinoflagellate *karenia brevis* in the marine environment." *Appl. Environ. Microbiol.*, **69** (9), 5726-5730, 2003.
122. C. Hu *et al.*, "Red tide detection and tracing using MODIS fluorescence data: A regional example in SW Florida coastal waters." *Remote Sens. Environ.*, **97**, 311-321, 2005.
123. J. Ishizaka *et al.*, "Satellite detection of red tide in ariake sound, 1998-2001." *J. Oceanog.*, **62**, 37-45, 2006.

124. T. Arnold "Toxicity, Shellfish", eMedicine.com.
<http://www.emedicine.com/EMERG/topic528.htm>.
125. AOAC, "AOAC Official Methods of Analysis –method 959.08."
<http://www.eoma.aoac.org/>, 2007.
126. AOAC, *Paralytic shellfish poison: Biological method. Sec. 35.1.37, Method 959.08*, P.A. Cunniff, Ed. AOAC International, Gaithersburg, MD, 22-23, 1995
127. "The Rapid Test for PSP." http://www.jellet.ca/psp_test.htm.
128. R.E. Gawley, *et al.*, "Visible fluorescence chemosensor for saxitoxin." *J. Org. Chem*, **72**, 2187–2191, 2007.
129. M. Wark, M.S. dissertation, University of Maine, Orono, ME, unpublished.
130. D. Hunter. "Detection of chemical analytes using novel acoustic wave platforms." REU report, 2009, unpublished.
131. www.beaconkits.com.
132. P. Kele *et al.*, "Coumaryl crown ether based chemosensors: selective detection of saxitoxin in the presence of sodium and potassium ions." *Tetrahedron Lett.*, **43**, 4413–4416, 2002.
133. B. Araya-Kleinsteuber, A.C. A. Roque, E. Kioupritzi, A.C. Stevenson, C.R. Lowe. "Magnetic acoustic resonance immunoassay (MARIA): a multifrequency acoustic approach for the non-labeled detection of bimolecular interactions." *J. Mol. Recognit.*, **19**, 379–385, 2006.
134. D. F. McCann, M. Wark, L. French, J. F. Vetelino. "Novel transducer configurations for bulk acoustic wave sensors." *IEEE Sensors Conf.*, 1448-1451, 2008.
135. A. Ballato, E.R. Hatch, M. Mizan, T. Lukaszek, and R. Tilton, "Simple thickness plate modes driven by lateral fields," *Proc. 39th Ann. Freq. Contr. Symp.*, 1985, pp. 462-472.
136. F. Josse, "Acoustic wave liquid-phase-based microsensors," *Sens. Actuators A: Phys.* **44**, 1994, pp. 199-208.
137. M. Rodahl, F. Hook, and B. Kasemo, "QCM operation in liquids: an explanation of the measured variations in frequency and Q factor with liquid conductivity," *Anal. Chem.*, vol. **68**, 1996, 2219-2227.

138. Y. Lee, D. Everhart, and F. Josse, "The quartz crystal resonator as detector of electrical loading: an analysis of sensing mechanisms," *Proc. IEEE Int. Freq. Contr. Symp.*, 1996, pp. 577-585.
139. C. Zhang and J.F. Vetelino, "A bulk acoustic wave resonator for sensing liquid electrical property changes," *Proc. IEEE Int. Freq. Contr. Symp.*, 2001, pp. 535-541.
140. C. York, L.A. French, Y. Hu, P. Millard, and J.F. Vetelino, "A lateral field excited acoustic wave biosensor," *Proc. IEEE Ultrason. Symp.*, 2003, pp. 46-51.
141. W. Pinkham, L. French, Y. Hu, D. Frankel, and J.F. Vetelino, "Pesticide detection using a lateral bulk excited acoustic wave sensor," *Chemical Sensors*, Vol. 20, Sup B, 2004, pp. 262-263.
142. Y. Hu, L.A. French Jr., K. Radecky, M.P. da Cunha, P. Millard, and J.F. Vetelino, "A lateral field excited liquid acoustic wave sensor," *IEEE Trans. Ultrason., Ferroelect., Freq. Contr.*, vol. 51, no. 11, 2004, pp. 1373-1380.
143. S.J. Martin, V.E. Granstaff, and G.C. Frye, "Characterization of a quartz crystal microbalance with simultaneous mass and liquid loading," *Anal. Chem.*, vol. 63, 1991, pp. 2272-2281.
144. J. Detaint and R. Lancon, "Temperature characteristics of high frequency lithium tantalate plate," *Proc. 30th Ann. Freq. Contr. Symp.*, 1976, pp. 132-140.
145. R.W. Weinert, B.R. McAvoy, M.M. Driscoll, R.A. Moore, and H.F. Tiersten, "LiTaO₃ lateral field resonators," *Proc. IEEE Ultrason. Symp.*, 1989, pp. 477-480.
146. J. Detaint, J. Schwartzel, H. Carru, R. Lefevre, C. Joly, B. Cappelle, Y. Zheng, and A. Zarka, "New designs for resonators and filters using lithium tantalate," *Proc. 44th Ann. Freq. Contr. Symp.*, 1990, pp. 337-348.
147. Y. Kim, J.R. Vig, and A. Ballato, "Sensing the properties of liquids with doubly rotated resonators," *Proc. IEEE Int. Freq. Contr. Symp.*, 1998, pp. 660-666.
148. R.T. Smith and F.S. Welsh, "Temperature dependence of the elastic, piezoelectric, and dielectric constants of lithium tantalate and lithium niobate," *J. Appl. Phys.*, vol. 42, no. 6, 1971, pp. 2219-2230.

149. A. Ballato, "Extended Christoffel-Bechmann elastic wave formalism for piezoelectric, dielectric media," *Proc. IEEE Int. Freq. Contr. Symp.*, 2000, pp. 340-344.
150. IEEE Standard on Piezoelectricity, ANSI/IEEE Std 176-1987, pp. 26-28.
151. M.M. Driscoll, C.R. Vale, and R.W. Weinart. "Measurement of Flicker Noise in High-Q, Lithium Tantalate, Bulk Wave Resonators." *Proc. 1987 IEEE Ultrasonics Symp.* 347-52.
152. B. Morray, Li Suiqiong, J. Hossenlopp, R. Cernosek, and F. Josse, "PMMA polymer film characterization using thickness-shear mode (TSM) quartz resonators," *Proc. IEEE Freq. Control Symp. and PDA Exhibition*, 2002, pp. 294-300.
153. S. Ballantyne, "Electromagnetic excitation of high frequency acoustic shear waves for the study of interfacial biochemical phenomena" PhD dissertation, University of Toronto, Toronto, Canada, 2005.
154. D.W. Branch and T.L. Edwards. "Love Wave Acoustic Array Biosensor Platform for Autonomus Detection." *Proc. IEEE Ultrason. Symp.*, 2007, pp. 260-263.
155. R. West, CRC Handbook of Chemistry and Physics. Boca Raton, FL: CRC Press, 1980.
156. E. Prince, Mathematical Techniques in Crystallography and Materials Science. New York, NY: Springer Verlag, 1992, p.29.
157. B.K. Vainshtein, Modern Crystallography. New York, NY,: Springer Verlag, 1994, p.212.
158. J. Detaint and R. Lancon. "*Temperature Characteristics of High Frequency Lithium Tantalate Plates.*" *Proc. IEEE Freq. Control Symp.*, 1976, p. 132-140.
159. O. Madelung, Ed. Landolt-Bornstein Numerical Data and Functional Relationships in Science and Technology. vol. 6, Berlin: Springer-Verlag, 1991.
160. W. Morgan, "Near fields of a monolithic spiral coil acoustic transduction sensor." NSF REU report, University of Maine, 2006 (unpublished).
161. J. Arsenault. Personal Communications, May -August 2006.

162. W. Curtis "Spiral Antennas," *IRE Trans. on Antennas and Propagation*, 298-306; May 1961.
163. S. Ballantyne, "Electromagnetic excitation of high frequency acoustic shear waves for the study of interfacial biochemical phenomena" PhD dissertation, University of Toronto, Toronto, Canada, 2005.
164. C. A. Balanis, *Antenna Theory, Analysis, and Design*, 3rd ed. Hoboken, NJ: John Wiley & Sons, Inc., 2005.
165. J. T. Conway "New Exact Solution Procedure for the Near Fields of the General Thin Circular Loop Antenna," *IEEE Trans. On Antennas and Prop.*, **53** (1), 509-510, 2005
166. P.L. Overfelt, "Near Fields of the constant current thin circular loop antenna of arbitrary radius," *IEEE Trans. Antennas Propag.*, **44**, 166-171, 1996.
167. D. H. Werner, "An exact integration procedure for vector potentials of thin circular loop antennas," *IEEE Trans. Antennas Propag.*, **44** (1), 157-165, 1996
168. L. W. Li, M. S. Leong, P. S. Kooi, T. S. Yeo, "Exact solutions of electromagnetic fields in both near and far zones radiated by thin circular-loop antennas: A general representation," *IEEE Trans. Antennas Propag.*, **45**, 1741-1748, 1997.

APPENDIX A

A LATERAL FIELD EXCITED LiTaO₃ HIGH FREQUENCY BULK

ACOUSTIC WAVE SENSOR

This chapter details an alternative approach to the main goals of this thesis research: to develop a novel bulk acoustic wave (BAW) sensing platform that is capable of operating over a wide range of frequencies. The most popular BAW sensor is the quartz crystal microbalance (QCM) which has electrodes on both the top and bottom surfaces of an AT-cut quartz wafer. In the QCM the exciting electric field is primarily perpendicular to the crystal surface resulting in a thickness field excitation (TFE) of a resonant temperature compensated transverse shear mode (TSM). The TSM, however, can also be excited by lateral field excitation (LFE) in which electrodes are placed on one side of the wafer leaving a bare sensing surface exposed directly to a liquid or a chemi/bio selective layer allowing the detection of both mechanical and electrical property changes caused by a target analyte. The use of LFE sensors has motivated an investigation to identify other piezoelectric crystal orientations that can support temperature compensated TSMs and operate efficiently at high frequencies resulting in increased sensitivity. A theoretical search and experimental measurements were performed to identify the existence of high frequency temperature compensated TSMs in α -quartz and LiTaO₃. Prototype LFE LiTaO₃ sensors were fabricated and found to operate at frequencies in excess of 1 GHz and sensitively detect viscosity, conductivity, and dielectric constant changes in liquids.

Introduction

Bulk acoustic wave (BAW) crystal plate resonators may be classified according to their style of excitation. The “thickness-field-excited” (TFE) resonator (Figure A.1a) has electrodes on both plate faces. The electric field that is induced by the electrodes in the TFE case is impressed across the thickness of the plate, collinear with the acoustic wave propagation direction. The “lateral-field-excited” (LFE) resonators (Figure A.1b) have both electrodes on a single plate face leaving the opposing plate face bare with the exciting electric field impressed mostly across the gap between the electrodes. With thickness field excitation, the choice of a particular crystal and plate orientation completely determines the electro-acoustical properties of the resonator, because it determines both the propagation direction and the excitation direction. Lateral field excitation allows the excitation direction to be chosen independently, which in turn allows a degree of control over the electromechanical coupling to the acoustic modes at a particular plate orientation [135]. This control may be used to optimize LFE resonators for different applications. The respective electrode configurations of TFE and LFE resonators also lead to differences in performance. Neglecting fringing effects, the electric field produced by the TFE resonator electrodes cannot penetrate into the measurand or sensing layer due to the conducting electrode on the sensing surface and thus electrical property changes such as relative permittivity and conductivity cannot be measured [136], [137]. However, in many sensor applications such as biological or chemical analyte detection, it may be desirable to maximize the electrical sensitivity to the environment. Efforts have been made to increase the fringing interactions in TFE

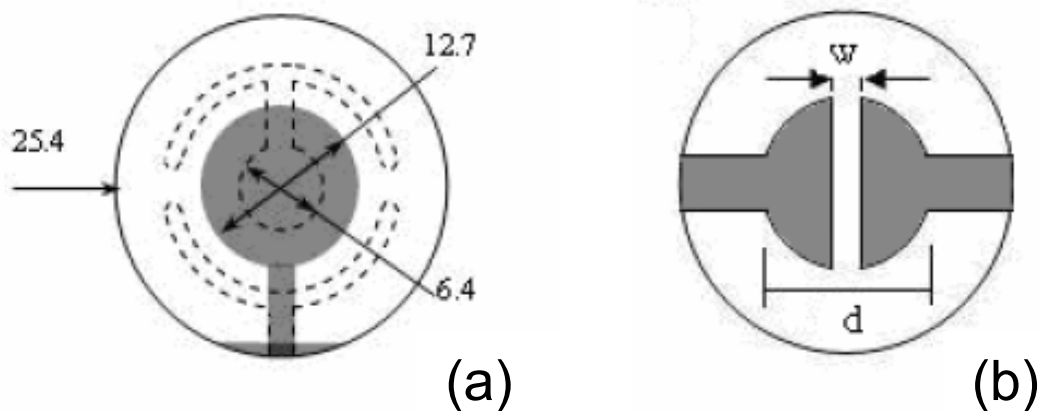


Figure A.1. (a) Top view (sensing surface) of a standard QCM sensor. Shaded (sensing surface) and dotted (bottom surface) regions are gold and all dimensions are in mm.; (b) Bottom view (reference surface) of a LFE sensor. Shaded regions are gold. Typical values for w are 1 mm and 13 mm for d .

resonators [138, 139], but the sensing surface in these devices still has an electrode. Recent reports have noted progress in the development of LFE sensors [140-142]. This work has been performed using the well-known AT-cut of α -quartz. The choice of the AT-cut of quartz has allowed direct comparison to TFE devices of the same material, particularly the quartz crystal microbalance (QCM) [143].

It however, may be possible to enhance the performance of LFE sensors by using another piezoelectric platform. The purpose of this chapter is to present work that has been done to theoretically identify and experimentally investigate orientations in α -quartz and LiTaO_3 (LTO), a material known for its high electromechanical coupling [144-146]. In particular, factors that are desirable for a LFE sensing platform are identified. A theoretical search was then undertaken to identify orientations in α -quartz and LTO suitable for a LFE sensing platform.

LFE Sensor Platform Requirements

Four factors are important in the identification of other possible LFE sensing platforms. It is desirable for an LFE sensor platform to have a piezoelectric active transverse shear mode (TSM) at that orientation; and preferably, a pure TSM at that orientation; that is, an allowable piezoelectrically active acoustic mode for which the mechanical displacements normal to the plate face are zero. While some effort has been made to include and exploit longitudinal displacements in sensor applications [147], such displacements generally degrade performance. Second, given the existence of a pure TSM, it is desirable for one to be able to selectively excite this mode with zero coupling to other modes. Lateral excitation has the advantage of permitting a degree of control over the mode coupling [135]. The challenge is then to identify those orientations that maximize the electromechanical coupling to a pure TSM mode decoupled from interfering modes. Third, the identified TSM should be temperature compensated so that the sensor's frequency response does not fluctuate with temperature changes. Fourth, it is desirable for the TSM to possess larger piezoelectric coupling than that observed for AT-cut quartz, the substrate that has been used in previous LFE work [140- 142].

Search Results

Acoustic bulk wave velocities and their displacement data were computed using the extended Christoffel-Bechmann method [149]. The material constants used for α -quartz were those of James [150], and the material constants used for LTO were those of Smith and Welsh [148]. The loci of orientations with TSMs and the loci of

orientations with zero temperature coefficient of frequency (TCF) were calculated for α -quartz and LTO. Those orientations that lie at the intersections of these loci, namely the temperature compensated TSMs, were studied further. The coordinate systems detailed in the IEEE Standards on Piezoelectricity [16] as seen in Figure A.2 and Figure A.3 were used for the calculations.

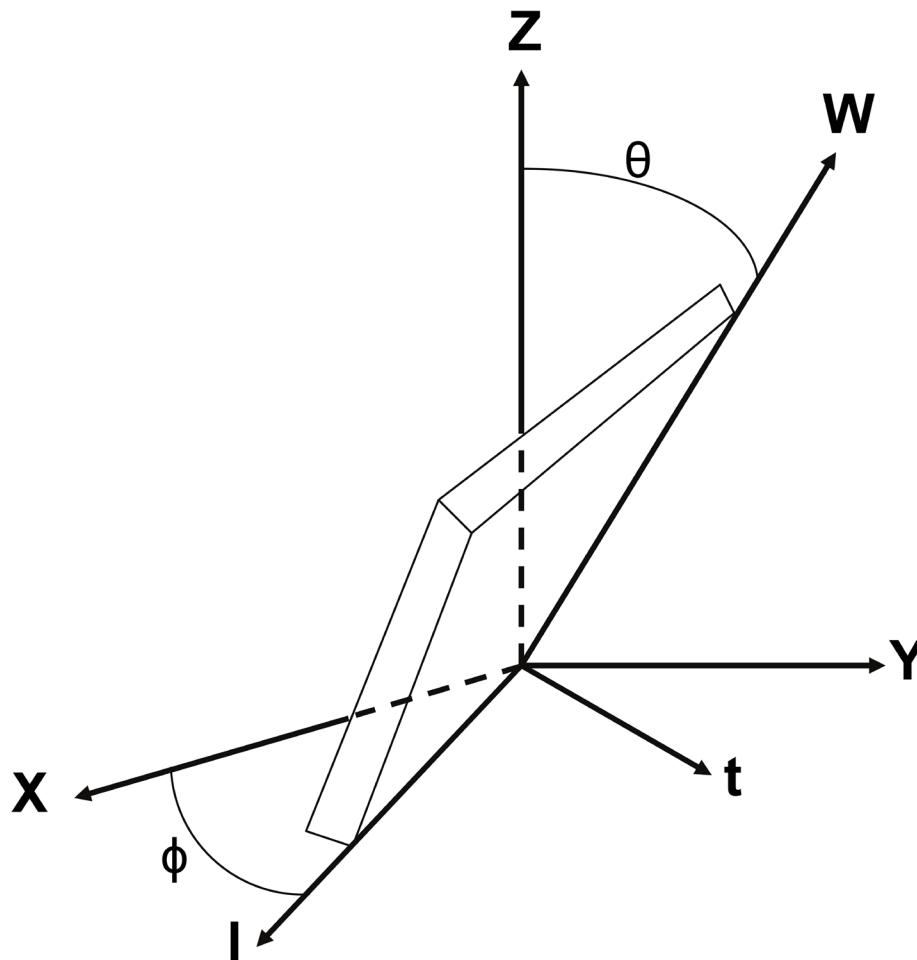


Figure A.2. IEEE Standard on Piezoelectricity [16] coordinate system used to calculate acoustic mode data.

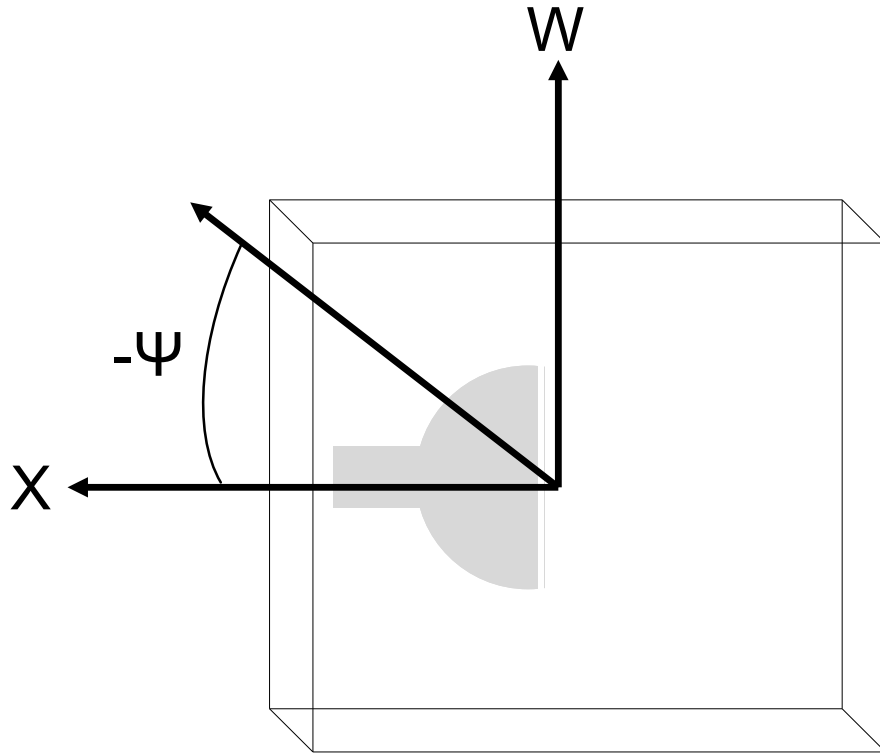


Figure A.3. LFE sensor notation system for electric field direction relative to the crystallographic axes.

Quartz Results

For α -quartz, orientations with temperature compensated TSMs have been identified but the piezoelectric coupling values were similar to those of AT-cut quartz. One cut, however, may be of interest for sensing applications as seen in Figure A.4. The cut given by the IEEE notation (YXwl) [150] $0^\circ/50.3^\circ$ has only slightly higher piezoelectric coupling than AT-cut quartz (6.5% vs. 6.3%) but exhibits a TSM velocity 53% higher than the TSM in AT-cut quartz when the LFE electrodes are oriented such that the electric field is at an angle of 90° relative to the X-axis as seen

in Figure A.4. For a given crystal thickness this would yield a 53% higher operating frequency compared to AT-cut crystal with the same thickness, leading to increased sensor sensitivity. Table A.1 shows the lateral coupling for the other orientations with temperature compensated TSMs identified in α -quartz.

Table A.1. Piezoelectric coupling coefficients for various temperature compensated TSMs in α -quartz.

$[\Phi, \theta]$	$\max(k_{LE})$
$[0, -32.25]$ (At-cut)	6.3%
$[0, 50.3]$	6.5%
$[-60, -44.8]$	6.5%
$[-60, 40.4]$	6.2%

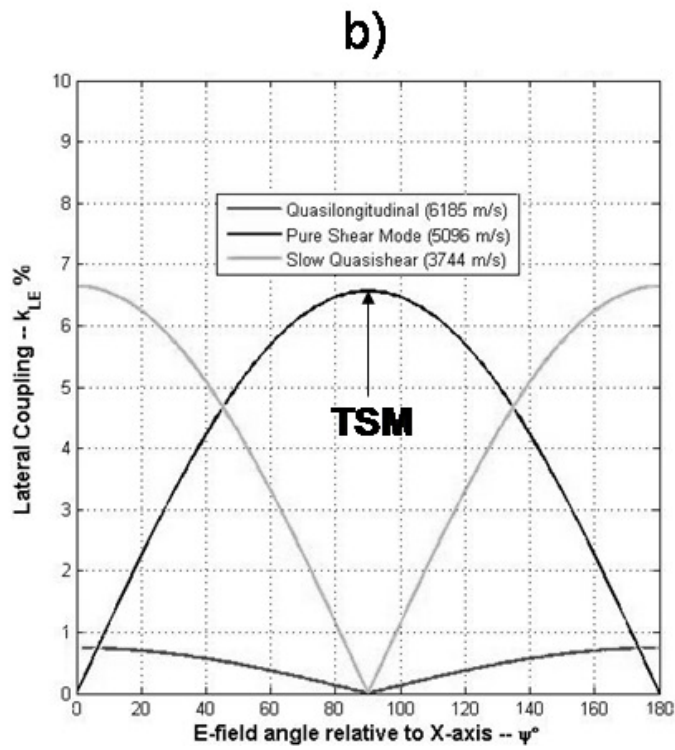
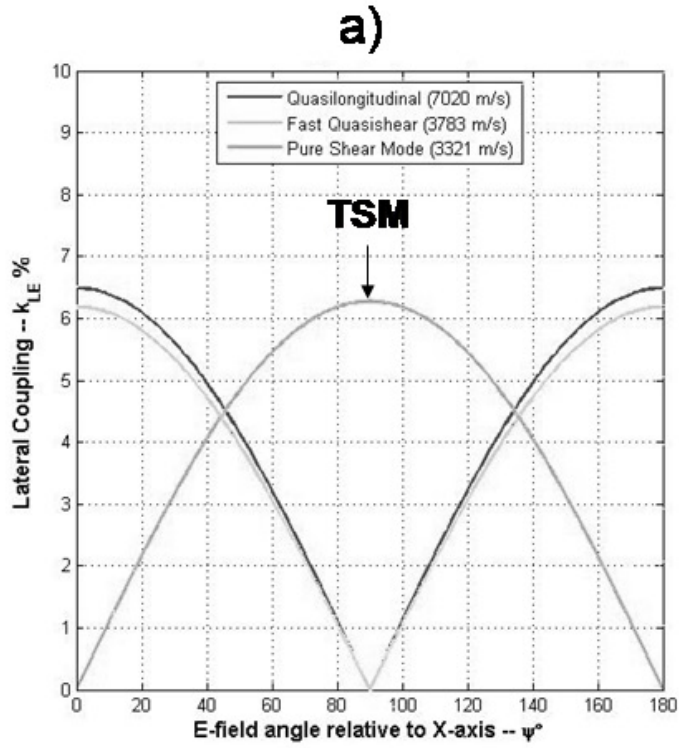


Figure A.4. Lateral field coupling coefficients k_{LE} for a) -32.25° and b) 50.3° rotate-Y cuts of quartz versus electric field angle ψ w.r.t. the X axis.

LTO Results

In LTO two cuts, (YXwl) -16.5° and (YXwl) -84.3° , offering significant improvements in coupling (39% and 47% respectively) compared to AT-cut quartz (6.3%) were identified as possible LFE sensor platforms. As shown in Figure A.5, although the (YXwl) -84.3° exhibits higher piezoelectric coupling than the (YXwl) -16.5° cut, a slight variation in the direction of the electric field would also excite the slow quasi-shear mode which has relatively high piezoelectric coupling, leading to interference. The (YXwl) -16.5° cut has piezoelectric coupling (38.8%) more than 6 times that of AT-cut quartz (6.3%). Also, the (YXwl) -16.5° cut of LTO has been previously investigated for use in RF filtering applications [151] and has theoretically been shown to be temperature compensated at 25°C . This cut of LTO was therefore selected for further testing as a possible LFE sensor platform.

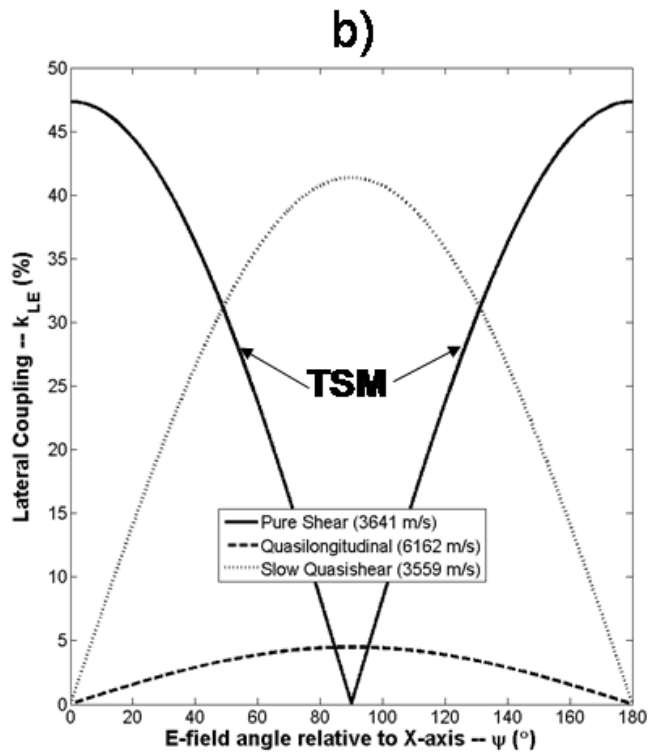
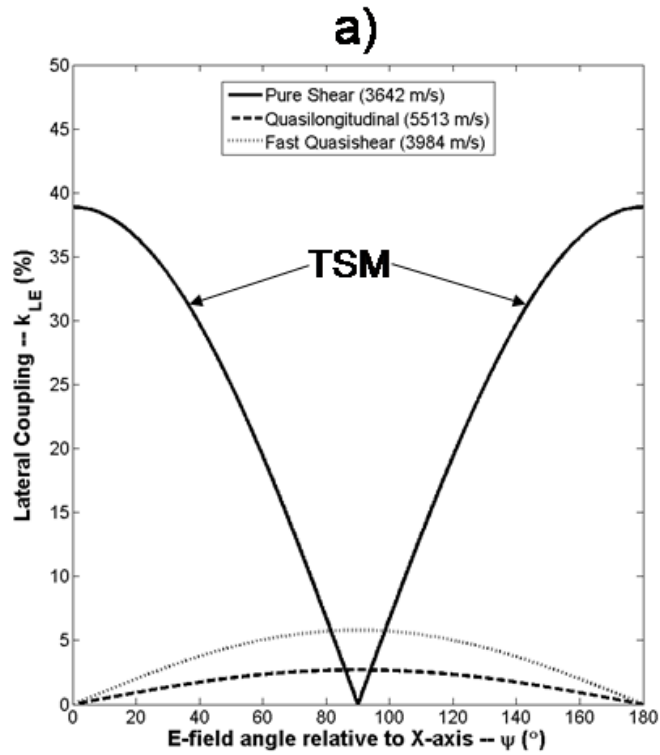


Figure A.5. Lateral field coupling coefficients k_{LE} for a) (YXwl) -16.5° and b) (YXwl) - 83.4° rotate-Y cuts of lithium tantalate versus electric field angle ψ w.r.t. the X axis.

Experiment

LTO wafers were purchased from Sawyer Technical Materials, LLC (Eastlake, OH). X-ray diffraction (XRD) tests were first performed on the wafer to verify that the wafer was the desired (YXwl) -16.5° cut of LTO. Figure A.6 shows the coordinate system with respect to the crystal face used in the XRD tests. Verification of the orientation was performed through the use of pole figures generated by a Panalytical (Westborough, MA) X'Pert PRO MRD Diffractometer using Cu k-alpha radiation configured with an x-ray lens and parallel plate collimator/proportional detector, a MATLAB modeling script, and by a miscut procedure performed by Sawyer Technical Materials, LLC.

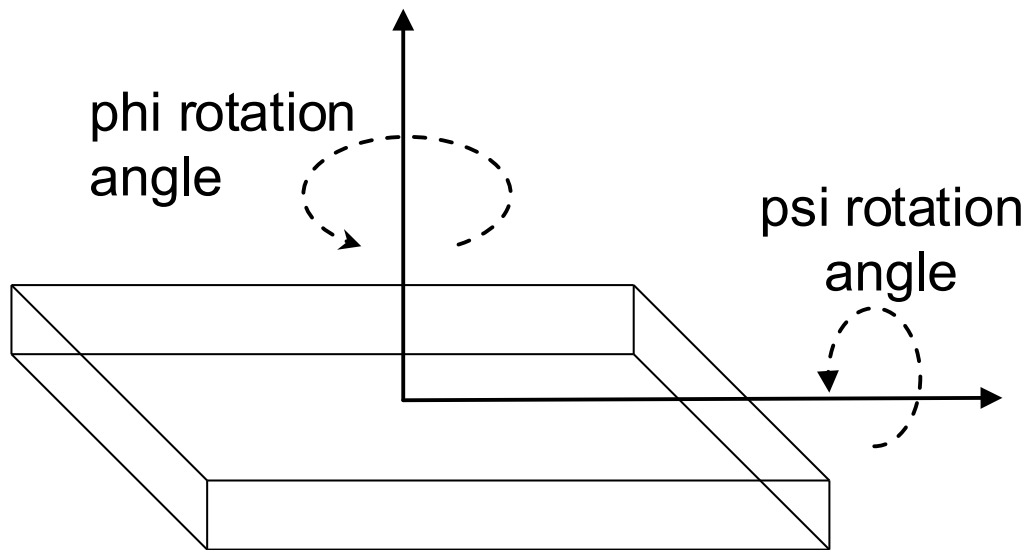


Figure A.6 Coordinate system with respect to the crystal face used in XRD measurements and calculations.

An LFE sensor platform was fabricated by photolithographically depositing thin film gold electrodes with a chromium adhesion layer on one side (Figure A.7) of a LTO wafer. An HP 8571A Network Analyzer was used to monitor the resonant frequency of the LTO LFE sensor platform (referred to as the LTO LFE for the remainder of this paper). The device's fundamental frequency was 5.2 MHz. Due to the high piezoelectric coupling of LTO, it is possible to operate the device at very high frequencies by exciting high order harmonics in the device. Resonances as high as 1.4 GHz (269th harmonic) were detected. Although LFE and QCM sensors fabricated on AT-cut quartz may be operated at elevated harmonics [152], efficiently exciting above the 7th harmonic is difficult due to the relatively low piezoelectric coupling of α -quartz [153].

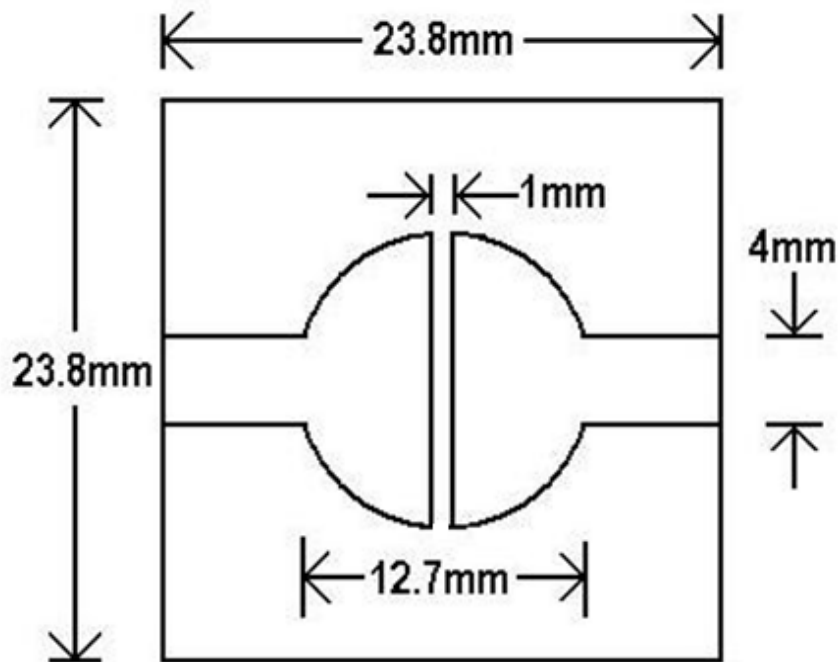


Figure A.7. LTO LFE test crystal with dimensions.

Since the (YXwl) -16.5° cut of LTO is theoretically predicted to be temperature compensated at 25°C [148] the temperature behavior of this cut was experimentally examined. A LTO LFE sensor was placed in a temperature controlled oven and operated at temperatures ranging from 20°C to 90°C . The changes in the resonant frequency of the LTO LFE sensor was monitored over the temperature range at the fundamental frequency (5.2 MHz), 15th harmonic (78 MHz), and 19th harmonic (98.8 MHz).

In order to demonstrate the applicability of the LTO LFE sensor, the mechanical and electrical property changes of liquids were measured and compared to standard AT-cut quartz QCM and LFE sensors. All tests were performed at a constant temperature of 25°C .

The LTO LFE sensor was operated at a different harmonic for each test to demonstrate its ability to operate over a wide range of frequencies. The wide frequency range of operation for the LTO LFE sensor opens the possibility of tuning the LTO LFE's operating frequency for a given application. It has recently been shown that for certain acoustic wave biological sensing applications proper selection of the sensor operating frequency is critical due to the fact that the depth that the acoustic wave penetrates the sensing layer depends on the operating frequency of the sensor [154].

In order to demonstrate the applicability of the LTO LFE sensor, it was first used to detect changes in the viscosity of liquids. The LFE LTO sensor's performance was compared to the performance of standard QCM and LFE sensors, both fabricated on AT-cut quartz with a fundamental frequency of 5 MHz. Eight solutions of varying

viscosities were made by mixing Karo (St. Louis, MO) brand corn syrup with deionized water at varying ratios from 0 to 80% corn syrup. The viscosity of each solution was first measured using a Cannon Instrument Co. (State College, PA) Cannon-Fenske Routine Viscometer. Each solution was applied to a standard QCM, an AT-cut quartz LFE sensor, and a LTO LFE sensor. The change in frequency (from the operating frequency when only de-ionized water was present) was measured for each device. The QCM and AT-cut quartz LFE sensor responses were measured using a Maxtek PLO-10i phase lock oscillator and an EZ FC-705U 100 MHz Universal Counter while the network analyzer was used to monitor the LTO LFE at the fundamental frequency and 63rd harmonic of the TSM. The QCM and AT-cut quartz LFE sensor were fabricated from identical one-inch diameter AT-cut quartz wafers obtained from Maxtek, Inc (Beaverton, OR).

The LTO LFE sensor was also tested to determine its response to electrical property changes in liquids. Its response to the conductivity of NaCl water solutions in the range of 0 to 0.07 wt% was compared to the response of a QCM and quartz LFE. The LTO LFE was operated at the 87th harmonic for the conductivity tests and its resonant frequency was monitored by the network analyzer. The quartz LFE and QCM were operated at their fundamental frequency and their resonant frequency was measured using the Maxtek PLO setup described before.

Permittivity measurements were performed by monitoring the responses of the LTO LFE, AT-cut LFE, and AT-cut QCM to changes in 2- propanol concentrations from 0 to 60 wt% in water. 2- propanol was chosen because its liquid permittivity changes significantly when it is added to water [155]. The LTO LFE was operated at

the 49th harmonic for the permittivity tests and its resonant frequency was monitored by the network analyzer. The quartz LFE and QCM were operated at their fundamental frequency and their resonant frequency was measured using the Maxtek PLO setup described before.

Results and Discussion

Using [16] the desired orientation is described as (YXwl) -16.5° which places the unit plate normal at $[0 \ x, \ +/-\cos(16.5^\circ) \ y, \ +/- \sin(16.5^\circ) \ z]$ in an orthonormal coordinate system. Numerical rotations appropriate for a trigonal 3m type lattice [156] were performed in order to generate the plate normals corresponding to the equivalent crystallographic planes. Since the International Centre for Diffraction Data (ICDD) database for this crystal is defined in terms of Miller-Bravais indices on an $abc \ \alpha\beta\gamma$ [5.147, 5.147, 13.766] [90, 90°, 120°] system a transformation of indices is desirable [157]. Transformation to Miller-Bravais indices for this orientation results in the 3 crystallographically equivalent planes $hk.l \ \langle 0 \ -1.0931 \ 1 \rangle$, $\langle -1.0931 \ 1.0931 \ 0 \rangle$, and $\langle 1.0931 \ 0 \ 1 \rangle$. The $\langle 2 \ 0 \ 2 \rangle$ plane was selected for measurement via XRD as it is in the same family as the $\langle 1 \ 0 \ 1 \rangle$ and nearby the theoretical $\langle 1.0931 \ 0 \ 1 \rangle$ wafer orientation. Figure A.8a shows a $\langle 2 \ 0 \ 2 \rangle$ pole figure obtained with diffractometer set at $2\text{-theta} = 45.569^\circ$. A MATLAB modeling script was created that would simulate a theoretical XRD pole figure for a (YXwl) -16.5° (Figure A.8b). The XRD $\langle 2 \ 0 \ 2 \rangle$ pole figure and results of the modeling script for (YXwl) -16.5° are very similar. It can be concluded that a member of the family of $\langle 202 \rangle$ planes is very close to the cut surface of the sample, (YXwl) -16.5° family (which all possess identical

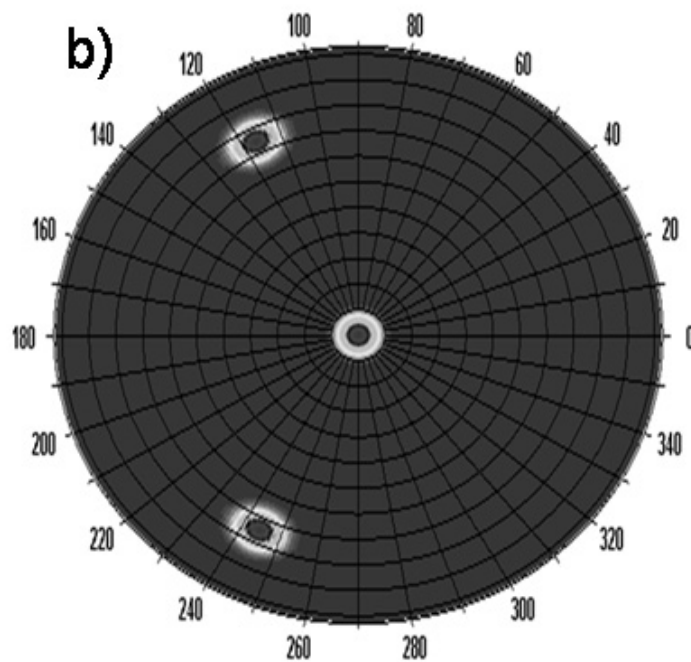
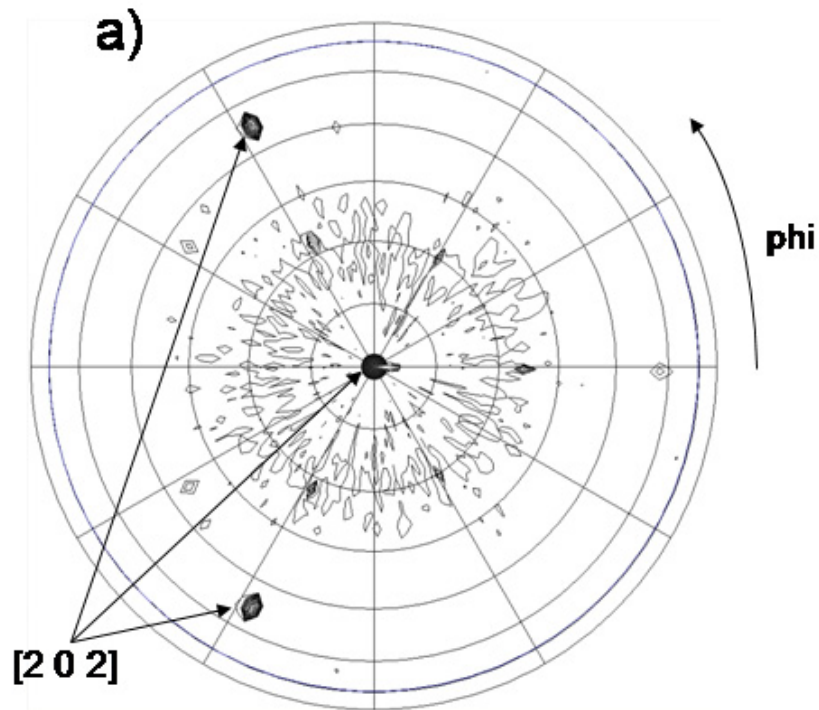


Figure A.8. a) X'Pert Texture generated experimental pole figure of the $\langle 202 \rangle$ plane for (YXwl) -16.5° LTO (concentric circles represent values of ψ ranging from 0° to 90° in 15° increments) and b) Theoretical MATLAB simulation for (YXwl) -16.5° LTO (concentric circles represent values of ψ ranging from 0° to 90° in 10° increments).

characteristics due to crystallographic equivalence [158]) and that the received wafer was in fact cut very close to our desired orientation. For a more precise measurement and confirmation of these conclusions the wafer was sent to Sawyer Technical Materials, LLC for a miscut analysis. Sawyer determined that the orientation was either (YXwl) -16.467° or (YXwl) -19.433° . The (YXwl) -19.433° possibility was excluded through an XRD measurement of the $\langle 0\ 0\ 6 \rangle$ pole figure. In the case of a (YXwl) -16.5° orientation $\langle 0\ 0\ 6 \rangle$ pole would be located at $\psi = 73.5^\circ$ while in the case of the (YXwl) -19.433° orientation the $\langle 0\ 0\ 6 \rangle$ pole would be located at $\psi = 70.467^\circ$. The fact that the $\langle 0\ 0\ 6 \rangle$ pole was observed to be at $\psi = 73.5^\circ$ in the XRD measurements further verified that the wafer was the correct orientation.

The (YXwl) -16.5° cut of LTO is theoretically temperature compensated at 25°C . However, as seen in Figure A.9 experimental measurements show this cut is actually temperature compensated at approximately 70°C , not at 25°C . It is interesting to note that the temperature behavior of the LTO LFE sensor changes very little when it is operated at higher harmonics. I believe that the discrepancy between our predicted and measured temperature behavior for this cut is due slight inaccuracies in the temperature coefficients used for the theoretical calculations as small changes in these values can have significant impacts on the predicted results. Given that the (YXwl) -16.5° cut of LTO is experimentally temperature compensated at 70°C it is possible that an orientation close to the (YXwl) -16.5° cut is in fact temperature compensated at 25°C . These temperature stability results clearly point to a need for updated and more accurate material constants and temperature coefficients for LTO.

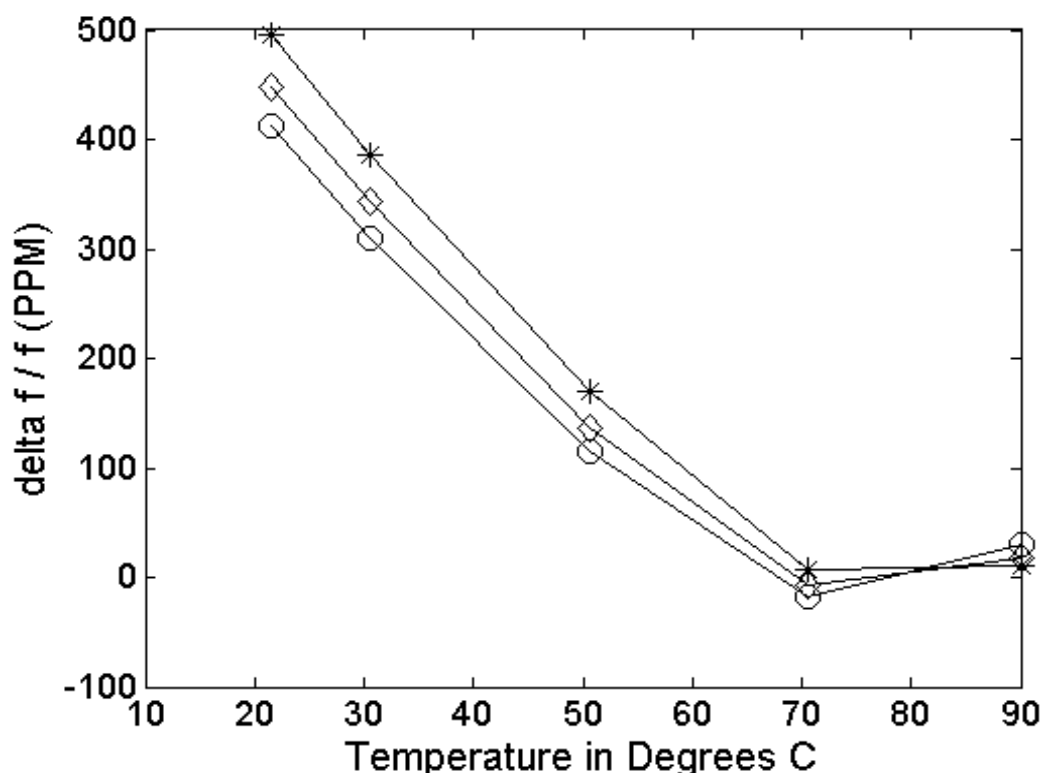


Figure A.9. Experimental temperature behavior for (YXwl) -16.5° LTO at its fundamental frequency (5.2 MHz, connected 'o'), 15th harmonic (78 MHz, connected '*'), and 19th harmonic (98.8 MHz, connected '◇').

Quartz LFE, quartz QCM, and LTO LFE sensors were tested by applying solutions of corn syrup water solutions with viscosities ranging from 1 to 94 cS. As can be seen in Figure A.10a, the LTO LFE sensor had significantly larger responses to viscosity change than either the standard QCM or quartz LFE when it was operated at the 63rd harmonic. Specifically, the LTO LFE sensor showed an approximately twelve times larger frequency shift when compared either the standard QCM or quartz LFE sensors. It is interesting to note that as seen in Figure A.10b LTO LFE and quartz LFE exhibited almost identical frequency shifts when they were both operated at their fundamental frequencies.

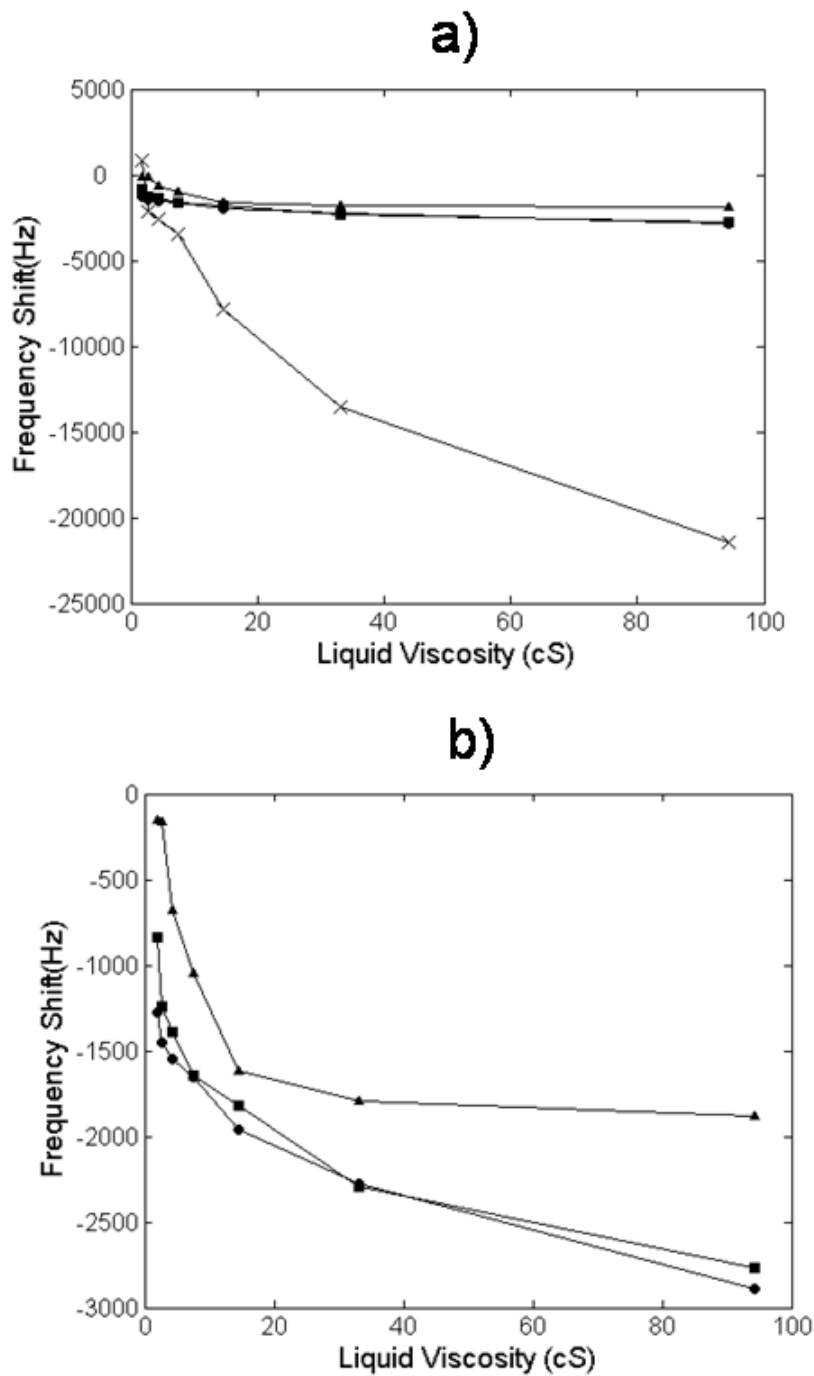


Figure A.10. Sensor response to change in corn syrup viscosities for the a) AT-cut QCM (fundamental frequency, connected '▲'), AT-cut quartz LFE (fundamental frequency, connected '■'), (YXwl) -16.5° LTO LFE sensor (fundamental frequency, connected '●') and (YXwl) -16.5° LTO LFE sensor (63rd Harmonic, connected 'x') and b) AT-cut QCM (fundamental frequency, connected '▲'), AT-cut quartz LFE (fundamental frequency, connected '■'), (YXwl) -16.5° LTO LFE sensor (fundamental frequency, connected '●') only.

As discussed earlier, LFE sensors are also capable of detecting electrical changes since there is no metal layer on the sensing surface as opposed to the QCM where a metal electrode is placed on both surfaces of the plate [140]-[142].

To test the LTO LFE sensor's ability to measure changes in the conductivity of a liquid, the change in resonant frequency of an LTO LFE sensor was monitored using an HP 8751A network analyzer while the sensor was subjected to liquids with various concentrations of NaCl. These measurements were performed at the 87th harmonic of the LTO LFE sensor. The response of a standard QCM and quartz LFE to the same liquids was measured using the PLO setup previously discussed. The resonant frequency changes of the sensors with respect to their resonant frequencies in deionized water as a function of NaCl concentration is shown in Figure A.11a.

Since the resonant frequency change of the LFE sensors is due to both mechanical and electrical property changes in the liquid, the NaCl concentrations chosen for this experiment (0 to 0.07% wt) have very small variations in mechanical property changes such as density and viscosity. The frequency shift for a 0.5 %wt NaCl solution predicted by mechanical perturbation theory was found to be only 5 Hz [138]. It can therefore be assumed that the mechanical properties of the liquid had negligible effects on the frequency response of the sensors.

As can be seen in Figure A.11a and Figure A.11b the LTO LFE sensor was able to measure the changes in the liquid conductivity while the QCM could not. As can be seen in Figure A.11b the quartz LFE exhibited a frequency shift of 434 Hz for

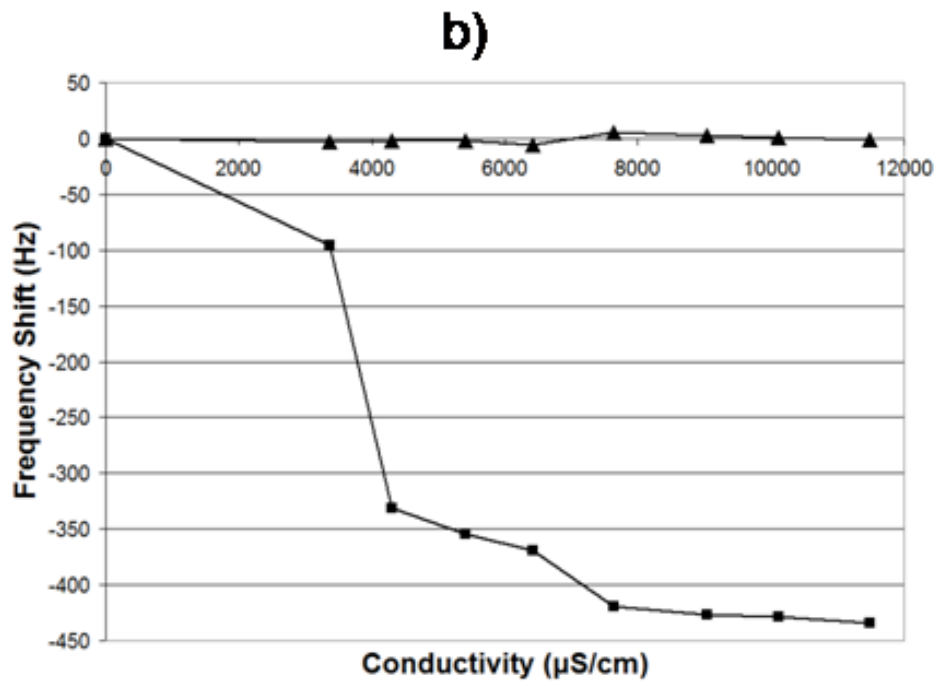
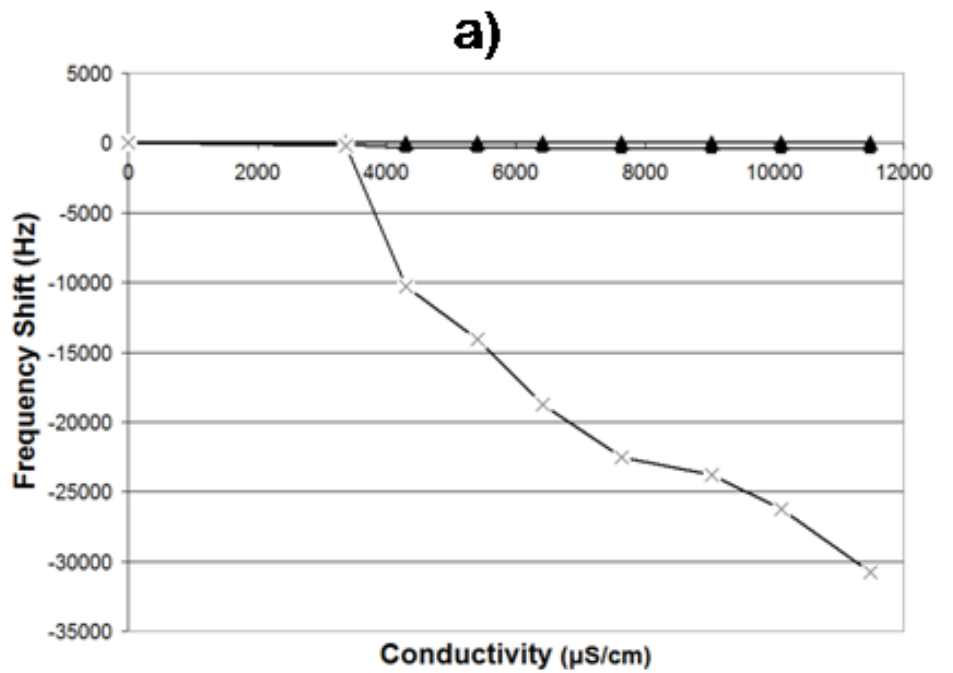


Figure A.11. Sensor response to changes in NaCl concentration for a) AT-cut QCM (fundamental frequency, connected '▲'), AT-cut quartz LFE (fundamental frequency, connected '■') and (YXwl)-16.5° LTO LFE (87th Harmonic, connected 'x') sensors and b) AT-cut QCM (fundamental frequency, connected '▲'), AT-cut quartz LFE (fundamental frequency, connected '■') only.

the 0.07 wt% solution (11,500 $\mu\text{S}/\text{cm}$). The frequency fluctuations of the QCM for all of the liquids were within the noise of the sensor. The frequency change of the LTO LFE sensor was 30.75 kHz for the 0.07 wt% (11,500 $\mu\text{S}/\text{cm}$) solution leading to the conclusion that the LTO LFE sensor is extremely sensitive to small electrical property changes.

The LTO LFE's sensor response to changes in relative permittivity (ϵ_r) was also explored. Figure A.12a shows the resonant frequency changes of the LTO LFE, quartz LFE, and QCM sensors with respect to their resonant frequencies in deionized water to changes in 2-propanol concentrations in water between 0 wt% ($\epsilon_r = 80$) and 60 wt% ($\epsilon_r = 44$). As can be seen in Figure A.12a and Figure A.12b, the frequency of the QCM decreased by 338 Hz at 60 wt% 2-propanol concentration while the frequency of the LTO and quartz LFE sensors increased. Unlike the LFE sensors which respond to both mechanical and electrical liquid property changes, the resonant frequency of the QCM is only influenced by the mechanical properties of the liquid, in this case the product of density and viscosity which reaches a maximum at approximately 50 wt% ($\epsilon_r = 50$) [155]. The LFE sensors also respond to changes in density and viscosity but in the case of the permittivity changes in this experiment, the sensor's frequency response is dominated by the changes in electrical properties. It has previously been reported that relative permittivity decreases approximately linearly with 2-propanol concentrations in water from 0 wt% to 70 wt% [159]. In the case of the LFE sensors the resonant frequency increases as the relative permittivity decreases. The frequency shift of the LTO LFE sensor was approximately 29 times

larger when it was operated at its 49th harmonic compared to the quartz LFE sensor operated at its fundamental frequency.

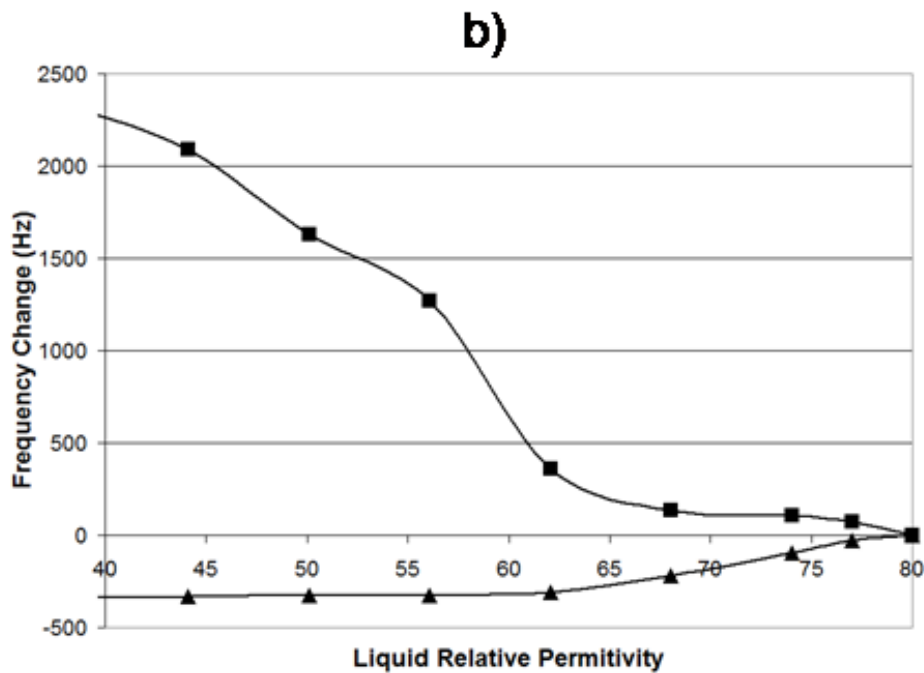
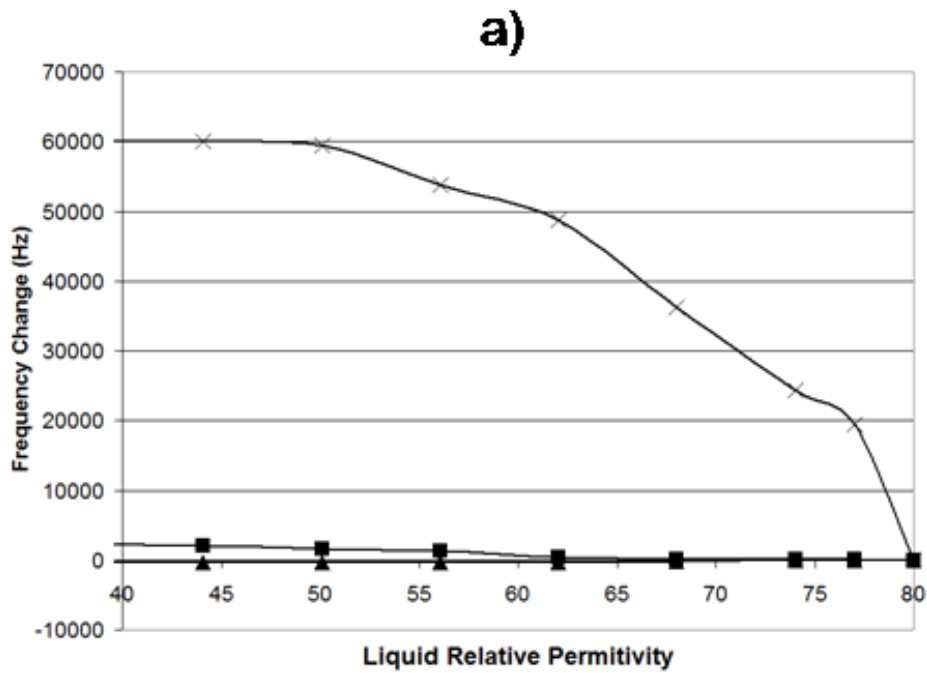


Figure A.12. Sensor response to changes in 2-propanol concentration for a) AT-cut QCM (fundamental frequency, connected '▲'), AT-cut quartz LFE (fundamental frequency, connected '■') and (YXwl) -16.5° LTO LFE (49th Harmonic, connected 'x') sensors and b) AT-cut QCM (fundamental frequency, connected '▲'), AT-cut quartz LFE (fundamental frequency, connected '■') only.

Conclusions

A search was made for orientations in lithium tantalate that when excited with a lateral electric field would offer improved sensor performance over standard AT-quartz LFE and QCM sensors. Two candidate orientations of lithium tantalate were theoretically identified that showed significant improvements in electromechanical coupling and predicted to have temperature compensated pure TSMs at 25°C, namely the (YXwl) -16.5°, and (YXwl) -84.3° cuts. The (YXwl) -16.5° cut was chosen for further testing based on the separation of interfering modes and the body of literature available on it from its use in RF filtering applications. XRD measurements were performed on the wafer that verified that it was the correct orientation. An improperly aligned wafer was then excluded as a possible explanation for the differences observed in the theoretical and measured temperature characteristics. A LFE sensor with a fundamental frequency of 5.2 MHz was fabricated on this cut and found to be capable of operating at frequencies as high as 1.4 GHz (269th harmonic). The temperature behavior for this cut of LTO was experimentally measured and found to be temperature compensated at 70°C instead of 25°C as theoretically predicted. We believe that inaccuracies in the material constants and temperature coefficients used to perform the theoretical calculations are the cause of this discrepancy. This result points to the need for more experimental work to determine exactly the orientation in LTO that is temperature compensated at 25°C. When tested as a sensor, the LTO LFE was found to be capable of detecting both mechanical and electrical property changes in liquids unlike the standard QCM. This sensor was used to measure viscosity, conductivity, and relative permittivity changes in liquids and

found to have significantly larger frequency changes than AT-cut QCM and LFE sensors when it was operated at high frequencies. It is expected that the LTO LFE sensor will yield significant increases in sensor sensitivity for both chemical and biological sensing applications.

APPENDIX B

AN EXPRESSION FOR THE ELECTROMAGNETIC FIELDS

RADIATED FROM A PLANAR SPIRAL ANTENNA

This chapter details the work done in collaboration with Morgan and Arsenault [160, 161] to derive an expression for the near and far electromagnetic fields of a planar spiral coil antenna. Although the behavior of the far-field electric fields for a spiral coil antenna has been analyzed [162] the near-field behavior is not well understood. An understanding of the form of these fields, especially in the near field, is particularly important in understanding the excitation mechanism of the MSCAT.

Previous Work on the Electromagnetic Piezoelectric Acoustic Sensor (EMPAS)

In order to explain the excitation mechanism of the EMPAS, Ballantyne attempted to model the spiral coil as a single rectangular loop of wire [163] and used the expression for the resulting fields that is presented in many antenna text books including [164]. Figure B.1 shows the geometry of the problem Ballantyne solved. He found that the resulting electric field consisted only of an ϕ component in polar coordinates given by:

$$E_{\phi} = \frac{\mu_o \sin \theta}{4\pi} \left[\frac{\omega^2}{rc} \cos \omega t + \frac{\omega^2}{r^2} \sin \omega \right] \quad (\text{B1})$$

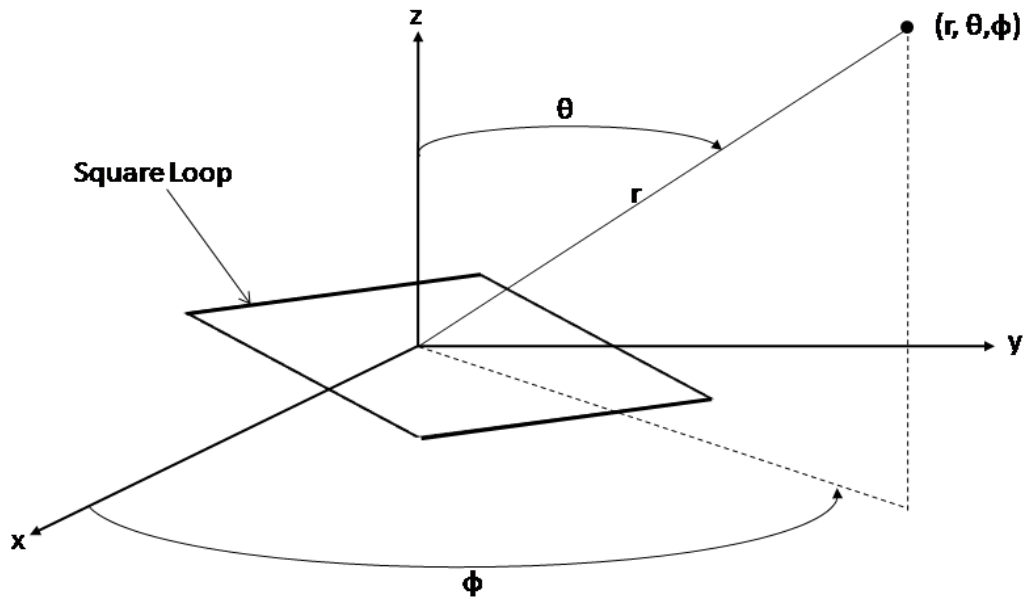


Figure B.1 Geometry of rectangular spiral coil problem solved by Ballantyne.

Ballantyne incorrectly postulates that since the electric field is not perpendicular to the coil and thus the quartz wafer, it cannot be the field that excites the transverse shear mode (TSM) in AT-cut quartz. He hypothesizes that there is a coupling between the magnetic field induced by the coil and the electric field which somehow produces a secondary electric field that is perpendicular to the coil and thus excites the TSM. He further hypothesizes that since coil is a concentric group of single loops this leads to a superposition effect that magnifies this secondary electric field.

This conclusion is flawed for several reasons. First, this evaluation is only valid in the far field and the quartz wafer is clearly in the near field of the antenna. Second, although antenna textbooks approximate a circular coil antenna as a square, this approximation relies on the wavelength of the signal being very long compared to

the length of the coil which is not valid for high frequencies or small coils. Finally, an electric field in the lateral (ϕ) direction can excite the TSM in AT-cut quartz as seen in AT-cut LFE platforms. Figure A.4a shows the coupling to the TSM for lateral electric fields. It is clearly necessary to obtain a more accurate expression for the radiated electric fields from a spiral coil antenna in order to understand how the antenna excites acoustic waves in the MSCAT platform.

Derivation of the Radiated Electric Fields from a Spiral Coil Antenna

Although the behavior of the far-field electric fields for a spiral coil antenna has been analyzed by Curtis [162] the near-field behavior is not well understood. In order to fully analyze both the near and far field behavior of the spiral coil antenna, two methods were used. The first utilized the same techniques that were used to determine the far field behavior of spiral coil antennas by Curtis [162] and the second used the methods that have been developed for analyzing the near-field behavior of single loop antennas [164-168].

As was done by Curtis [162], an approximation was made that a spiral coil has nearly the same geometry as a sum of semicircles. Figure B.2 shows an example for a two turn spiral. The electric field from each semicircle was calculated using the techniques in [164-168] that were developed to solve for the near fields of single loop circular antennas. Once the field from each semicircle was calculated, the principle of superposition was used to determine the total form of the electric field. Figure B.3 shows the coordinate system used for this analysis.

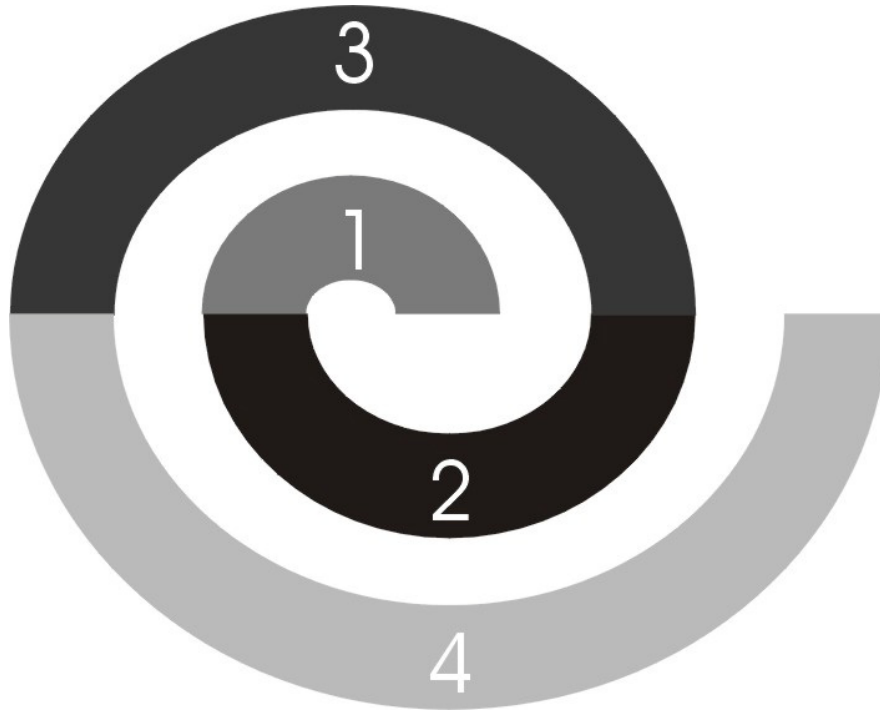


Figure B.2. Diagram showing a two turn spiral coil made up of four semi-circles

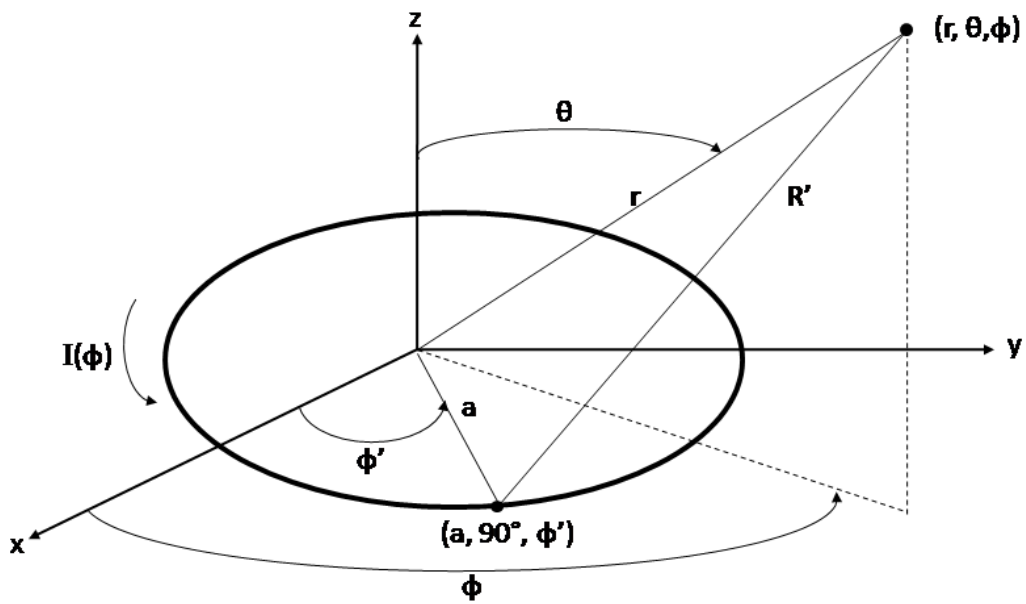


Figure B.3. Coordinate system used in near field spiral coil calculations. The point (r, θ, ϕ) is the observation point.

The inner diameter of the first semicircle d_{in} , diameter of the outer spiral d_{out} , and the number of turns of the spiral l are the only quantities that need to be defined to find the dimensions of each semicircle that makes up the spiral. The quantities a and b are calculated in order to find the radius of the n^{th} semicircle r_n .

$$a = \frac{d_{in}}{2} \quad (\text{B2})$$

$$b = \frac{d_{out} - d_{in}}{2(2l - 1)} \quad (\text{B3})$$

$$r_l = a + (l - 1)b \quad (\text{B4})$$

In previous work to solve for the near-fields of circular loop antennas [164-167] the Helmholtz equation was used to calculate the vector and scalar potentials and then calculate the electric field using the time-varying Maxwell's equations.

$$\nabla^2 \mathbf{A} + k^2 \mathbf{A} = -\mu \mathbf{J} \quad (\text{B5})$$

$$\nabla^2 \varphi + k^2 \varphi = -\frac{\rho}{\varepsilon} \quad (\text{B6})$$

$$\mathbf{E} = \nabla \varphi - \frac{\partial \mathbf{A}}{\partial t} \quad (\text{B7})$$

Where \mathbf{A} is the magnetic vector potential, \mathbf{J} is the electric current density, φ is the scalar potential, \mathbf{E} is the electric field, μ is the permeability, ρ is the total charge density, ε is the dielectric constant, k is the wave number, and t is time. Utilizing the same approach in [164-167] for a spiral coil, however, is problematic due to the fact that these methods utilize the trigonometric symmetry of sine and cosine functions to simplify the integrals since the limits on the integrals range from 0 to 2π . This symmetry does not exist for the semicircle case and the integrals range from 0 to π and π to 2π .

Li *et al.* [168] utilized a different approach to the circular loop antenna problem. They utilized dyadic Green's functions to calculate the near and far fields radiated by the antennas. As Li *et al.* show the volumetric electric current density may be expressed as:

$$\mathbf{J}(r') = \frac{\mathbf{I}(\phi')\delta(r' - a)\delta(\theta' - \frac{\pi}{2})}{a} \boldsymbol{\phi} \quad (\text{B8})$$

Where $\mathbf{I}(\phi)$ is an arbitrary function of ϕ' and a is the radius of the circular loop as shown in Figure B.1. Primed variables indicate the points on the circle and unprimed indicate the observation point (r, θ, ϕ) . It can be shown that the radiated electric field is given by [168]:

$$\mathbf{E} = i\omega\mu \iiint_{V'} \mathbf{G}_o \mathbf{J}(r) dV' \quad (\text{B9})$$

$$\nabla^2 \mathbf{G}(r_1, r_2) + k^2 \mathbf{G}(r_1, r_2) = \delta^3(r_1 - r_2) \quad (\text{B10})$$

Expanding the Green's function yields:

$$\begin{aligned} \mathbf{G}_o = \frac{ik_o}{4\pi} \sum_{n=1}^{\infty} \sum_{m=0}^n (2 - \delta_{m0}) \left\{ \begin{array}{l} [\mathbf{M}^{(1)}(k_o)\mathbf{M}'(k_o)] \\ [\mathbf{M}(k_o)\mathbf{M}'^{(1)}(k_o)] \end{array} \right\} \\ + \left[\begin{array}{l} \mathbf{N}^{(1)}(k_o)\mathbf{N}'(k_o) \\ \mathbf{N}(k_o)\mathbf{N}'(k_o) \end{array} \right] \left\{ \begin{array}{l} \{r > a\} \\ \{r < a\} \end{array} \right\} \end{aligned} \quad (\text{B11})$$

Where $\delta_{mn} = 1$ for $m=n$; and 0 for $m \neq n$ and

$$\begin{aligned} \mathbf{M} = \mp \frac{m z_n(kr)}{\sin \theta} P_n^m(\cos \theta) \sin(m\phi) \boldsymbol{\theta} \\ - z_n(kr) \frac{dP_n^m(\cos \theta)}{d\theta} \cos(m\phi) \boldsymbol{\phi} \end{aligned} \quad (\text{B12})$$

$$\begin{aligned} \mathbf{N} = \frac{n(n+1)m z_n(kr)}{kr} P_n^m(\cos \theta) \cos(m\phi) \mathbf{r} \\ + \frac{d[rz_n(kr)]}{kr dr} \frac{dP_n^m(\cos \theta)}{d\theta} \cos(m\phi) \boldsymbol{\theta} \\ \mp \frac{m}{\sin \theta} \frac{d[rz_n(kr)]}{kr dr} P_n^m(\cos \theta) \cos(m\phi) \boldsymbol{\phi} \end{aligned} \quad (\text{B13})$$

and D_{mn} is a normalization coefficient:

$$D_{mn} = \frac{(2n+1)(n-m)!}{n(n+1)(n+m)!} \quad (\text{B14})$$

In equations (B12) and (B13), $P_n^m(\cos \theta)$ is a Legendre function. In equation (B11), $\mathbf{M}^{(1)}$ and $\mathbf{N}^{(1)}$ $z_n(kr)$ has the form of a spherical Hankel function while for \mathbf{M} and \mathbf{N} $z_n(kr)$ has the form of a spherical Bessel function. For the \mathbf{M}' and \mathbf{N}' , (r, θ, ϕ) are replaced by $(a, \pi/2, \phi')$ [168]:

$$z_n(kr) = \begin{cases} h_n^{(1)}(kr) & r > a \\ j_n(kr) & 0 \leq r \leq a \end{cases} \quad (\text{B15})$$

Substituting equations (B8) and (B11) into equation (B9) yields an equation for the electric field in two regions $\mathbf{E}^>$ (when $r > a$) and $\mathbf{E}^<$ (when $r \leq a$):

$$\begin{aligned}
\begin{bmatrix} \mathbf{E}^{\geq} \\ \mathbf{E}^{\leq} \end{bmatrix} &= -\frac{\eta_o k_o^2}{4\pi} \sum_{n=1}^{\infty} \sum_{m=0}^n (2 - \delta_{m0}) D_{mn} \left\{ \begin{bmatrix} \Phi^{M^{\leq}} \mathbf{M}^{(1)}(k_o) \\ \Phi^{M^{\geq}} \mathbf{M}(k_o) \end{bmatrix} \right. \\
&\quad \left. + \begin{bmatrix} \Phi^{N^{\leq}} \mathbf{N}^{(1)}(k_o) \\ \Phi^{N^{\geq}} \mathbf{N}(k_o) \end{bmatrix} \right\}
\end{aligned} \tag{B16}$$

The variable η_o is the intrinsic impedance ($120\pi\Omega$) and Φ^M and Φ^N are simplified functions corresponding to \mathbf{M}' and \mathbf{N}' :

$$\begin{bmatrix} \Phi^{M^{\leq}} \\ \Phi^{M^{\geq}} \end{bmatrix} = -a \begin{bmatrix} j_n(k_o a) \\ h_n^{(1)}(k_o a) \end{bmatrix} \frac{dP_n^m(0)}{d\theta} \begin{bmatrix} \int_0^\pi \cos(m\phi') I(\phi') d\phi' \\ \int_0^\pi \sin(m\phi') I(\phi') d\phi' \end{bmatrix} \tag{B17}$$

$$\begin{bmatrix} \Phi^{N^{\leq}} \\ \Phi^{N^{\geq}} \end{bmatrix} = \mp a \begin{bmatrix} \frac{d[a j_n(k_o a)]}{k_o a da} \\ \frac{d[a h_n^{(1)}(k_o a)]}{k_o a da} \end{bmatrix} m P_n^m(0) \begin{bmatrix} \int_0^\pi \sin(m\phi') I(\phi') d\phi' \\ \int_0^\pi \cos(m\phi') I(\phi') d\phi' \end{bmatrix} \tag{B18}$$

A cosinusoidal current distribution is assumed:

$$I(\phi') = I_o \cos(p\phi') \tag{B19}$$

When substituting equation (B19) into equations (B17) and (B18), all of the terms outside the integral will remain the same for a given m and n , however the terms inside the integral will become a product of trigonometric terms. Morgan [160] has shown that the integral has the following solutions:

$$\begin{aligned}
\begin{bmatrix} mn \text{ even} \\ mn \text{ odd} \end{bmatrix} &= \int_0^\pi \cos(p\phi) \begin{bmatrix} \sin(m\phi) \\ \cos(m\phi) \end{bmatrix} d\phi \\
&= \left\{ \begin{array}{ll} 0 & \text{if } mn \text{ odd and } p \neq m \\ \frac{\pi}{2} & \text{if } mn \text{ odd and } p = m \\ 0 & \text{if } mn \text{ even and } p = m \\ 0 & \text{if } mn \text{ even and } (p + m) \text{ even} \\ -\frac{2m}{(p + m)(p - m)} & \text{if } mn \text{ odd and } (p + m) \text{ odd} \end{array} \right\} \quad (\text{B20})
\end{aligned}$$

The integrals from π to 2π have the opposite values of the above solution.

Substituting equation (B20) into equations (B17) and (B18):

$$\begin{bmatrix} \Phi^{M<} \\ \Phi^{M>} \end{bmatrix} = -I_o r_l \frac{dP_n^m(0)}{d\theta} C_{mnp} \begin{bmatrix} j_n(k_o r_l) \\ h_n^{(1)}(k_o r_l) \end{bmatrix} \quad (\text{B21})$$

$$\begin{bmatrix} \Phi^{N<} \\ \Phi^{N>} \end{bmatrix} = \mp I_o m P_n^m(0) r_l S_{mnp} \begin{bmatrix} \frac{d[r_l j_n(k_o r_l)]}{k_o r_l dr_l} \\ \frac{d[r_l h_n^{(1)}(k_o r_l)]}{k_o r_l dr_l} \end{bmatrix} \quad (\text{B22})$$

Where S and C are the functional forms of the integral and are given by:

$$\begin{aligned}
C_{mnp} &= \frac{1}{2} \left[((-1)^{mn} - 1)(1 - \delta_{pm})(-1)^{p+m} \left(\frac{-m}{(p + m)(p - m)} \right) \right. \\
&\quad \left. - ((-1)^{mn+1} - 1) \frac{\pi}{2} \delta_{pm} \right] \quad (\text{B23})
\end{aligned}$$

$$\begin{aligned}
S_{mnp} &= \frac{1}{2} \left[((-1)^{mn+1} - 1)(1 - \delta_{pm})(-1)^{p+m} \left(\frac{-m}{(p + m)(p - m)} \right) \right. \\
&\quad \left. - ((-1)^{mn} - 1) \frac{\pi}{2} \delta_{pm} \right] \quad (\text{B24})
\end{aligned}$$

It is now necessary to consider the spiral coil made up of a series of semi-circles. We will consider the first segment to be made up of semicircles r_1 and r_2 , the second segment to be made up of r_3 and r_4 , and so on. New variables will be created in order to evaluate Φ^M and Φ^N for the first through the l^{th} segment:

$$F_l = a + 2(l - 1)b \quad (\text{B25})$$

$$G_l = a + (2l - 1)b \quad (\text{B26})$$

Substituting equations (B25) and (B26) equations (B21) and (B22) and results in:

$$\begin{bmatrix} \Phi_{F+G}^{M<} \\ \Phi_{F+G}^{M>} \end{bmatrix} = -I_o \frac{dP_n^m(0)}{d\theta} C_{mnp} \left[F_l \begin{pmatrix} j_n(k_o F_l) \\ h_n^{(1)}(k_o F_l) \end{pmatrix} \pm G_l \begin{pmatrix} j_n(k_o G_l) \\ h_n^{(1)}(k_o G_l) \end{pmatrix} \right] \quad (\text{B27})$$

$$\begin{bmatrix} \Phi_{F+G}^{N<} \\ \Phi_{F+G}^{N>} \end{bmatrix} = -I_o m P_n^m(0) S_{mnp} \left[\mp F_l \begin{pmatrix} \frac{d[F_l j_n(k_o F_l)]}{k_o F_l dF_l} \\ \frac{d[F_l h_n^{(1)}(k_o F_l)]}{k_o F_l dF_l} \end{pmatrix} \right. \\ \left. + G_l \begin{pmatrix} \frac{d[G_l j_n(k_o G_l)]}{k_o G_l dG_l} \\ \frac{d[G_l h_n^{(1)}(k_o G_l)]}{k_o G_l dG_l} \end{pmatrix} \right] \quad (\text{B28})$$

Equations (B27) and (B28) along with equations (B12) and (B13) can be substituted into (B16) to find the final components of the electric field:

$$\begin{bmatrix} \mathbf{E}_r^> \\ \mathbf{E}_r^< \end{bmatrix} = -\frac{\eta_o k_0^2}{4\pi} \sum_{l=1}^{L_{max}} \sum_{n=1}^{\infty} \sum_{m=0}^n D_{mn} P_n^m(\cos \theta) Z_1 \begin{pmatrix} \Phi_{F+G}^{N<} \frac{n(n+1)h_n^{(1)}(k_o r)}{k_o r} \\ \Phi_{F+G}^{N>} \frac{n(n+1)j_n(k_o r)}{k_o r} \end{pmatrix} \quad (\text{B29})$$

$$\begin{bmatrix} \mathbf{E}_\theta^> \\ \mathbf{E}_\theta^< \end{bmatrix} = -\frac{\eta_o k_0^2}{4\pi} \sum_{l=1}^{L_{max}} \sum_{n=1}^{\infty} \sum_{m=0}^n D_{mn} \left\{ \mp \frac{m}{\sin \theta} P_n^m(\cos \theta) Z_2 \begin{pmatrix} \Phi_{F+G}^{M<} h_n^{(1)}(k_o r) \\ \Phi_{F+G}^{M>} j_n(k_o r) \end{pmatrix} \right. \\ \left. + \frac{dP_n^m(\cos \theta)}{d\theta} Z_1 \begin{pmatrix} \Phi_{F+G}^{N<} \frac{d[rh_n^{(1)}(k_o r)]}{k_o r dr} \\ \Phi_{F+G}^{N>} \frac{d[rj_n(k_o r)]}{k_o r dr} \end{pmatrix} \right\} \quad (\text{B30})$$

$$\begin{bmatrix} \mathbf{E}_\phi^> \\ \mathbf{E}_\phi^< \end{bmatrix} = -\frac{\eta_o k_0^2}{4\pi} \sum_{l=1}^{L_{max}} \sum_{n=1}^{\infty} \sum_{m=0}^n D_{mn} \left\{ -\frac{dP_n^m(\cos \theta)}{d\theta} Z_1 \begin{pmatrix} \Phi_{F+G}^{M<} h_n^{(1)}(k_o r) \\ \Phi_{F+G}^{M>} j_n(k_o r) \end{pmatrix} \right. \\ \left. \mp \frac{m}{\sin \theta} P_n^m(\cos \theta) Z_2 \begin{pmatrix} \Phi_{F+G}^{N<} \frac{d[rh_n^{(1)}(k_o r)]}{k_o r dr} \\ \Phi_{F+G}^{N>} \frac{d[rj_n(k_o r)]}{k_o r dr} \end{pmatrix} \right\} \quad (\text{B31})$$

Where the Z terms, which take into account the varying sine and cosine functions, are given by:

$$Z_1 = \left(-\frac{1}{2}\right) [((-1)^{mn} - 1) \sin(m\phi) + ((-1)^{mn+1} - 1) \cos(m\phi)] \quad (\text{B32})$$

$$Z_2 = \left(-\frac{1}{2}\right) [((-1)^{mn} - 1) \cos(m\phi) + ((-1)^{mn+1} - 1) \sin(m\phi)] \quad (\text{B33})$$

Results and Discussion

Morgan [160] plotted the normalized patterns for the θ and ϕ components of the electric field for one and two turn spirals. He assumed that the wavelength, λ , was equal to one half of the innermost radius. The results can be seen in Figure B.4 and Figure B 5.

Equations (B29) – (B31) are of limited usefulness in optimizing the spiral coil configuration of the MSCAT due to their mathematical complexity, however one important conclusion can be made. In the near-field, the spiral coil does in fact radiate electric fields in all three dimensions. In order to more fully understand the electric fields radiated by a spiral coil antenna and how they excite acoustic waves in the MSCAT sensor platform finite element analysis was undertaken as described in Chapter 3.

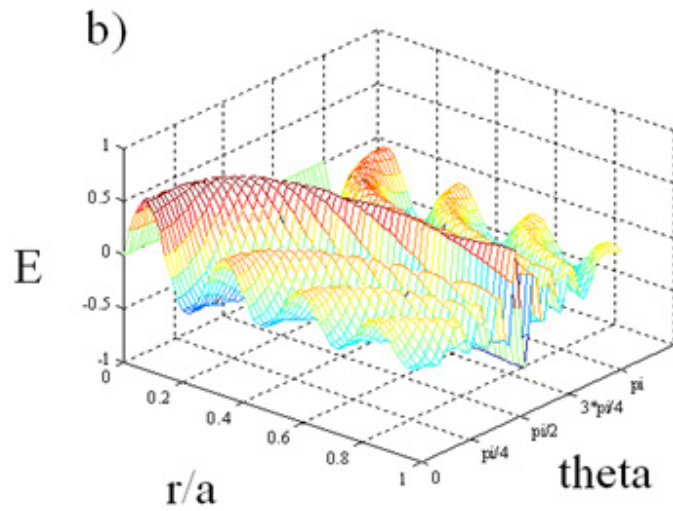
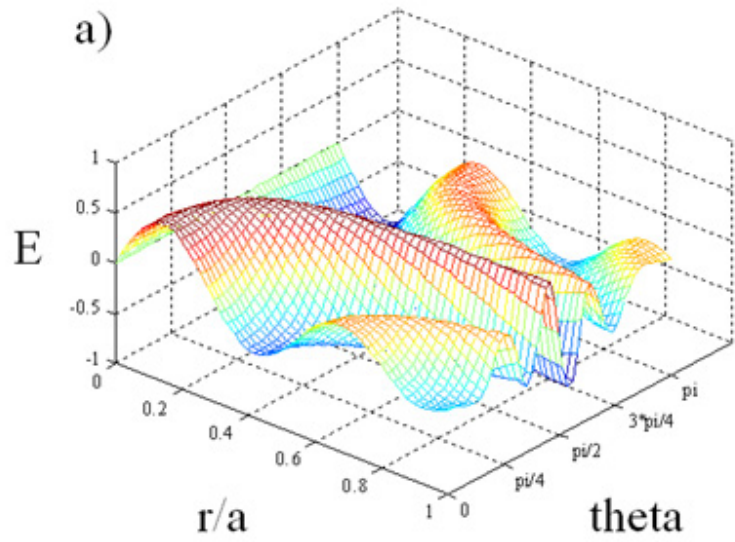


Figure B.4. Three-dimensional normalized pattern of normalized θ component of the electric field as a function of θ for a) single turn spiral and b) two turn spiral

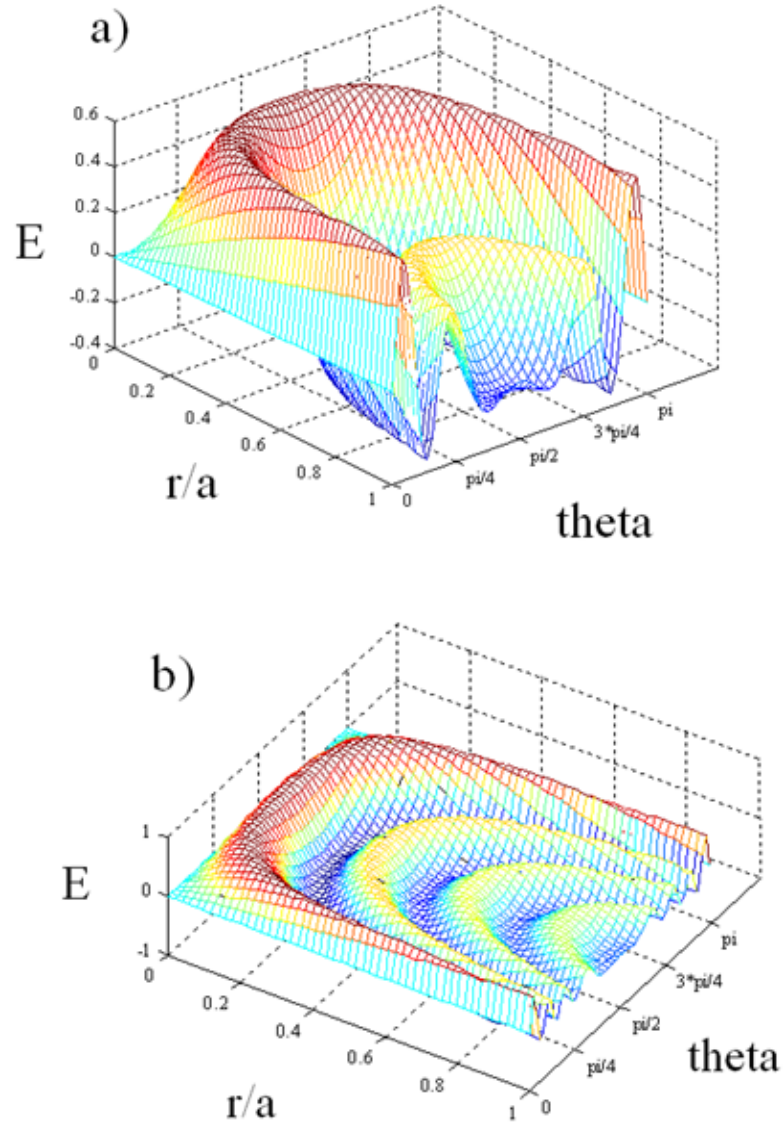


Figure B 5. Three-dimensional normalized patten of normalized ϕ component of the electric field as a function of θ for a) single turn spiral and b) two turn spiral

BIOGRAPHY OF THE AUTHOR

Donald McCann was born in Bangor, Maine on February 9, 1977. He was raised in Bucksport, Maine and graduated from Bucksport High School in 1995. He attended Cornell University and Ithaca College and graduated in 2000 with a Bachelor's degree in Electrical Engineering from Cornell and a Bachelor's degree in Physics from Ithaca College. From 2000-2005 he was the manager of electronic development at Sensor Research & Development in Orono, Maine. In 2005 he entered the Electrical Engineering graduate program at the University of Maine and earned his Master's degree in Electrical Engineering in 2008.

Donald is a candidate for the Doctor of Philosophy degree in Electrical Engineering from the University of Maine in May, 2010.